Study of Gas Phase Kinetics in Arc Plasma Jets

By

NIRUPAMA TIWARI

PHYS 01201304022

Bhabha Atomic Research Centre, Mumbai

A thesis submitted to the
Board of Studies in Physical Sciences

In partial fulfillment of requirements

for the Degree of

DOCTOR OF PHILOSOPHY

Of

HOMI BHABHA NATIONAL INSTITUTE

December, 2018

Homi Bhabha National Institute[1]

Recommendations of the Viva Voce Committee

As members of the Viva Voce Committee, we certify that we have read the dissertation prepared by Nirupama Tiwari entitled "Study of Gas Phase Kinetics in Arc Plasma Jets" and recommend that it may be accepted as fulfilling the thesis requirement for the award of Degree of Doctor of Philosophy.

Designation	Name	Signature	Date
Chairman	Dr. Archana Sharma, OS, APPD, BARC	Archana	24/05/19
Guide/ Convener	Dr. S. Ghorui, SO(G), L&PTD, BARC	Srikumar Ghorui	24/05/19
Co-guide			
Examiner	Prof. Sudha Bhoraskar, Dept. of Physics, S.P. University Pune	S.V. Bhoraskar	24/05/19
Member 1	Dr. T. K. Thiyagarajan, SO(H) L&PTD, BARC	[illegible]	24/05/19
Member 2	Prof. V. L. Mathe, Dept. of Physics, S.P. University Pune	V Mathe	24/05/19
Member 3	Dr. Amitava Roy, SO(G), APPD, BARC	Amitava Roy	24/05/2019
Dean, Physical & Mathematical Sciences	Dr. B.K. Nayak, OS, NPD, BARC	B Nayak	24/05/2019
Technology Adviser (if any)			

Final approval and acceptance of this thesis is contingent upon the candidate's submission of the final copies of the thesis to HBNI.

I/~~We~~ hereby certify that I/we have read this thesis prepared under my/~~our~~ direction and recommend that it may be accepted as fulfilling the thesis requirement.

Date: 24/05/19

Place: Trombay

Srikumar Ghorui

Signature
Co-guide (if any)

Signature
Guide

[1] This page is to be included only for final submission after successful completion of viva voce.

STATEMENT BY AUTHOR

This dissertation has been submitted in partial fulfilment of requirements for an advanced degree at Homi Bhabha National Institute (HBNI) and is deposited in the Library to be made available to borrowers under rules of the HBNI.

Brief quotations from this dissertation are allowable without special permission, provided that accurate acknowledgement of source is made. Requests for permission for extended quotation from or reproduction of this manuscript in whole or in part may be granted by the Competent Authority of HBNI when in his or her judgment the proposed use of the material is in the interests of scholarship. In all other instances, however, permission must be obtained from the author.

N. Devi

Nirupama Tiwari

DECLARATION

I, hereby declare that the investigation presented in the thesis has been carried out by me. The work is original and has not been submitted earlier as a whole or in part for a degree / diploma at this or any other Institution / University.

N. Devi

Nirupama Tiwari

List of Publications arising from the thesis

Journal

1. "Investigations of some aspects of the spray process in a single wire arc plasma spray system using high speed camera", **Tiwari N,** Sahasrabudhe S N, Tak A K, Barve D N, and Das A K *Review of Scientific Instruments*, 2012, *83,* 025110.

2. "Stability and structures in atmospheric pressure DC non-transferred arc plasma jets of argon", **Tiwari N**, Bhandari S, Ghorui S, , nitrogen, and air, *Physics of Plasmas 25*, 2018, 072103

3. "Dynamic behavior of arc voltage and electro-thermal efficiency in atmospheric pressure non-transferred arc plasma torches under different degree of anode cooling", **Tiwari N**, Nath S, Dhamale G D, and Ghorui S, (2018) accepted for publication in *Journal of Thermal Spray Technology*

4. "Multi-Component Diffusion Coefficient in Nitrogen Plasma Under Thermal Equilibrium and Non-Equilibrium Condition", Meher K C, **Tiwari N**, Ghorui S and Das A K, *Plasma Chemistry and Plasma Processing*, 2014, *34*, 949

5. "Axial Evolution of Radial Heat Flux Profile in Atmospheric Pressure Argon and Nitrogen Arcs, Plasma", Meher K C, **Tiwari N**, Ghorui S and Das A K, Plasma Sources Sci. Technol. **23**, 065017, (2014)

6. "Thermodynamic and transport properties of nitrogen plasma under thermal and chemical non-equilibrium, Plasma", Meher K C, **Tiwari N** and Ghorui S, Plasma *Chemistry and Plasma Processing*, 2015, ***15***, 9615.

7. “Direct probing of anode arc root dynamics and voltage instability in a dc non-transferred arc plasma jet”, Ghorui S **, Tiwari N**, Meher K C, Jan A, Bhat A and Sahasrabudhe S N, *Plasma Sources Sci. Technol.* 2015, *24*, 065003.

8. “Unique erosion features of hafnium cathode in atmospheric pressure arcs of air, nitrogen and oxygen”,Ghorui S, Meher K C, Kar R, **Tiwari N** and Sahasrabudhe S N*, J. Phys. D: Appl. Phys.,* 2016, *49*, 295201

9. “In situ probing of temperature in radio frequency thermal plasma using Yttrium ion emission lines during synthesis of yttria nanoparticles”, Dhamale G, **Tiwari N**, Mathe V L, Bhoraskar S V, and Ghorui S, *Journal of applied Physics,* 2017, *122,* 023301

10. Underwater Electrical Discharges: Temperature, Density and Basic Instability Features with Different Anode Materials”, S. Bhattacharya, **N. Tiwari**, A. Mishra,S. Mitra, G. K. Dey & S. Ghorui, Plasma Chem Plasma Process, 2019, 39:1019-1048

Conferences

1. **Tiwari N**, Meher K C, Ghorui S, Study of Structures and Stability in Nitrogen Plasma Jet, 10th Asia Plasma & Fusion Association Conference (APFA2015), Gandhinagar, Gujrat

2. **Tiwari N**, Swati S, Tomar R, Meher, K C and Ghorui, S, Measurement of rotational and excitation temperature in a cascaded DC nitrogen plasma Torch, 30th National Conference on Plasma Science and Technology, SINP, Kolkata, 2015

3. Tiwari N & Ghorui S, In-situ probing of gas phase nucleation dynamics in Yttria-Argon plasma system, 33th National Conference on Plasma Science and Technology, Delhi University, 2018

N. Devi

Nirupama Tiwari

DEDICATIONS

To my late Mother and Husband

who encouraged for higher education

ACKNOWLEDGEMENTS

First of all, I am grateful to Almighty for showering blessings. At the outset, I thank my Ph D guide, Dr. Srikumar Ghorui, for his brilliant guidance and encouragement from conception to completion. I am very fortunate for having a true science loving person as a guide. This thesis is the result of his innovative ideas, restless effort and extraordinary guidance which has led this work to its completion.

I would like to express my gratitude, deep regards and sincere thanks to Dr. A. K. Das, former Head, L&PTD, and Shri R.K Rajawat, Head, L&PTD, BARC, for giving permission to do PhD as well as support and guidance.

I am grateful to Doctoral Committee (Dr Archana Sharma, Dr T. K. Thiyagrajan, Dr V. L. Mathe and Dr Amitav Roy) who critically reviewed my work and took effort in providing me with valuable comments and suggestions.

I am thankful to Dr B. K. Nayak, Dean Academics Physical Sciences for his kind support and valuable guidance.

I would like to thank my mentor Dr N. K. Joshi and Shri. S. N. Sahasrabudhe, Retd. Scientist, L&PTD, BARC for his constant encouragement, help and training on the experimental systems. My heartfelt thanks to Dr P.V.A. Padmnabhan, Dr. D S Patil, Shri D. N. Barve and Shri A. K. Tak, for their unconditional and kind support.

Special thanks to my friends Gayatri, Kailash, Bharati, Rahul and Shubhankar for always being there in all ups and downs.

My thanks are due to my colleagues Chakravarthy, Vandana, Pravat, Sushil, Kiran, Pravin, Vikas, Rajib, Arundhati, Archana, Pawan, Naresh, Chopadeji, Senji, Kedareji, Dilip, Vishal, Vanita and Tushar for their support and suggestions whenever I approached them.

My special thanks to members of Gayatri Parivar for their continuous inspiration and encouragement to complete the work. I would like to thank my friends Rashmi, Suman, Putul, Priya, Rupali, Rekha and Indumati who stood beside me. I would thus like to thank everyone who, knowingly or otherwise, has provided support, encouragement and assistance along the way.

I feel a deep sense of gratitude for my father Dr Ram Chet Pandey who showed me the right path in all fronts of life and encouraged for study. Special thanks to my parents in laws, family members Shri Ram Chandra Pandey, Shri Dharamraj Pandey, Dr Jay Prakash Pandey, Shri Satya Prakash Pandey, Shri Ashok Pandey, Shri Surya Parakash Pandey, Shri Ajay Kumar Pandey, Dr Rajesh Pandey, Krishna Pratap Tiwari, Poonam Tiwari, Santosh Tiwari, Prabhakar Tiwari, Shri Bhaskar Tiwari, Shri Ashok Pandey, Smt Prema Pandey, Smt Kamlesh Pandey, Smt Sharmila Pandey, Dr Babli Pandey, Smt Vandana Pandey, Pratibha Pandey, Smt Vandana Tiwari Saraswati Tiwari, Shardha Tiwari, Smt Gyanmati Chaturvedi, Smt Vimla Pandey, Smt Radhika Pandey, Smt Krishna Dwivedi, Smt Indravati Pandey and all others who were always there in my tough times. I am grateful to my elder sister Dr Gayatri Pandey, brother in law Shri Awedhesh Pandey, my younger brother Dr Satish Pandey, his wife Smt. Sweta Pandey, maternal sister Sangita and her family for their unconditional support.

At last but not the least, I would like to thank to my kids Aaditya and Aashisha for their love and support.

N. Devi

Nirupama Tiwari

SYNOPSIS

Kinetics deals with the effect of forces upon the motions of material bodies or with changes in a physical or chemical system [1]. Kinetics in physics means the study of motion and its causes. Rigid body kinetics deals with the motion of rigid bodies. Chemical kinetics involves the study of chemical reaction rates. Gas phase kinetics in arc plasma jets, the subject of the study, is somewhat special as it involves dynamics of the plasma body as a whole, driven by electromagnetic body forces evolved inside the plasma, directly or indirectly controlled by prevailing chemical kinetics. Chemical kinetics in arc plasma, on the other hand, are controlled by particular operating condition of the plasma torch like plasma current, plasma gas flow rate, type of plasma gas, torch geometry and ionization scenario at the realized temperature. Scope under “Study of gas phase kinetics of in the arc plasma devices” includes both macroscopic kinetics (physical dynamics of the plasma body as a whole) as well as microscopic kinetics (mapping species distribution inside the plasma jet through modelling and emission spectroscopy).

Plasma mainly consists of electrons, ions, neutral particles, excited species and photons, where negative and positive charges balance each other. It is divided in two broad categories classified as thermal plasma and non thermal plasma. In thermal plasma, electron and ion temperatures are nearly equal. Arc plasma devices fall in thermal plasma category [2]. It converts electrical energy into concentrated jet of plasma having very high temperature (>5000K), high velocity (>200 m/s), high electrical and thermal conductivity. Arc plasma torches are used for various applications like plasma gasification (for all types of waste treatment), UF_6-UF_4 conversion, plasma spraying (for thermal barrier coatings), nano-synthesis of high melting point materials, plasma densification (spheroidization, plasma Sintering) etc. [2-7]. Some of the characteristic features of the such systems are steep gradients in plasma quantities (temperature and velocity), extremely high temperature at the core, highly nonlinear variation in plasma properties and mutual interactions among thermal, chemical, electric, magnetic and fluid dynamic fields.

The stability and structure inside plasma jet plays very important role in determining the quality of processing work and its suitability for a particular operation. Depending on operating condition, the devices are always associated with some inherent instability classified as steady, takeover and restrike mode of instabilities [8]. The fluctuations may strongly influence the process involved and strongly affect the lifetime of the devices [4, 5]. Although plasma processing applications are already in use, least is known about the gas phase kinetics of the plasma jet. Some of salient fundamentals in the non transferred arc plasma torches like the transient dynamics of the arc root, stability and structure of the plasma jet affecting the process, effect of anode cooling on the torch performance are poorly understood. A large numbers of investigations have been made in the past [9-13] to study the dynamics in the plasma jet and its origin. However, most of the attempts primarily consider existence of single arc and no current in the external plasma jet.

The present study primarily focuses on physical kinetics of the plasma body including arc root dynamics, plasma jet dynamics, stability and structure in the dc plasma jet for mono-atomic(argon) and molecular gases (nitrogen and air) emanating from a DC plasma torch. Being a molecular gas, nitrogen naturally offer higher voltage drop compared to argon for the same electrode configuration and easily associates higher power. While for air plasma torch, used gas being freely available air, operational cost is significantly lower. However, presence of oxygen doesn't allow use of conventional tungsten cathode, due to very low melting point of oxidized tungsten. One needs to use hafnium or zirconium cathode in such torches. High voltage drop, extremely long plasma jet, and rich variety in external jet dynamics are some of the interesting features. Chemical kinetics inside pure oxygen, nitrogen, air and argon plasma have been investigated through theoretical modelling, whereas the same in slightly sub-atmospheric argon and argon-yttria system have been studied experimentally through emission spectroscopy. The later provides very useful information about homogeneous nucleation process in synthesis of yttria nanoparticles from precursor powder.

Major contributions from the study include (a) Capturing time resolved transient dynamics of anode arc root and its direct correlation with the voltage signal for the first time in arc plasma history (b) Giving direct proof of coexistence of multiple arc roots and revealing their formation, merging and extinction mechanisms (c) Giving first concrete experimental proof of existence of current in the external plasma jet (d) Revealing variety of interesting internal structures of high technological importance inside the external plasma jets for Ar, N_2 and Air (e) Identifying the origin of such structures arising out of interaction between plasma and self generated electric and magnetic field (f) Introduction of a new reliable image analysis technique for easy mapping of gross plasma temperature inside an external plasma jet (g) An enhanced understanding of the evolution of spray particles from molten wire in 'wire arc plasma spray system' and its behaviour under flow driven environment of the arc plasma before deposition on the substrate (h) Developing a unique method in wire arc spray, based on streak length generated by individual particles in CCD, for determination of velocity of the particles getting deposited (i) Obtaining relationship between particle velocity and instantaneous torch power in wire arc spray (j) Contribution of cooling rate on efficiency of the high efficiency low power plasma torch (k) Exploring chemical kinetics of plasma species in argon plasma under thermal non-equilibrium over a wide range of temperature and pressure and direct experimental understanding of chemical kinetics involved in synthesis of yttria nanoparicles in gas phase nucleation process through in-situ emission spectroscopy.

With a brief introduction, **chapter-1** presents the importance, relevance, objective, scope and current status of the problem considered. Different types of plasma devices, their classifications, underlying principles and important application areas are briefly outlined. Various advantages as well as disadvantages of arc plasma devices in comparison to its competing technologies are presented. In summary, the chapter sets the background and the motivation for the work presented in the subsequent chapters.

Chapter-2 presents a detailed literature survey. Physical kinetics changes due to power supply (Hz), arc root movement [few kHz to hundreds of Hz], air entrainment, electromagnetic forces, drag force etc. Entrainment of cold gas into thermal plasma jets using emission spectroscopy, enthalpy probe measurements, shadowgraph, LDA (Laser Doppler Anemometry) and CARS (Coherent Anti-Stokes Raman Spectroscopy) diagnostic techniques were studied by Pfender etal [14]. However, fast imaging techniques and advanced image processing to explore the internal structures of the plumes were not used. Hrabovsky etal. [15] reported the effect of anode attachment on the flow stability in a dc plasma jet. Coudert et al. [16] studied time resolved voltage waveforms in non-transferred arc plasma torch and found it strongly correlated to the instantaneous morphology of arc, which in turn determines the plasma flow structure and temporal behavior. It was concluded that plasma flow includes extinguishing plasma bubbles surrounded by colder layers. The study did not pay attention to explore the dynamic evolution of the structures in the external plasma plume.

Ghorui et al. [17] studied the fluctuating voltage signals generated from atmospheric pressure dc arc discharges and analyzed it to be chaotic, estimated the dynamic properties of attractors observed in the discharge, probed the origin of voltage fluctuations [10] and attempted to quantify the role of inherent arc fluctuations on the properties of synthesized nanostructures [18]. In a single wire arc spray system, particle velocity of the sprayed particle determined using commercially available systems (spray watch, DPV 2000, etc.) focus onto a small area in the spray jet. They are not designed for tracking a single particle from the torch to the substrate.

Literature survey reveals that a thorough experimental investigation of the arc root dynamics for steady, takeover and restrike mode, stability and structure of plasma jet, effect of anode cooling, reaction kinetics, investigation of single particle tracking in spray process under different operating conditions is due for long time.

Chapter- 3 presents experimental setups used in this study. It consists of a DC plasma torch, an IGBT based power supply, water cooling and water supply system, temperature monitoring system, torch positioning system, powder feeder unit, wire feeder unit and various diagnostics systems like high speed camera, high resolution spectrograph with optical fibre, spray watch system, oscilloscope, voltage divider circuit and a computer for data acquisition and control. Details of each component are provided in this chapter. The segmented electrode plasma torch, tungsten electrode spray torch and hafnium electrode air plasma torch served as the key devices for plasma generation. These devices are designed and developed in-house. Fast photography camera was used to capture transient dynamics of arc root, stability and structure in the plasma external jet, investigation of wire arc spray process and jet behaviour during precursor feeding. The high resolution spectrograph was used to capture spectral data required for the measurement of plasma temperature. Spray watch system was used to measure the in flight particle temperature and velocity. The voltage divider circuit together with a multichannel oscilloscope recorded the inherent instability behaviour of the plasma under various operating conditions. This chapter provides a complete details of all the equipments used in different experiments in this study.

Chapter-4 describes the transient dynamics of the anode arc root in a dc non-transferred arc plasma torch through fast photography and directly correlates it with the associated voltage instability for the first time. The coexistence of multiple arc roots, the transition to a single arc root, root formation and extinction are investigated for the steady, takeover and re-strike modes of the arc. Contrary to the usual concept, the emerging plasma jet of a dc non transferred arc plasma torch is found to carry current. An unusually long self-propelled arc plasma jet, a consequence of the phenomenon, is demonstrated.

Chapter-5 investigates the stability of dc non-transferred arc plasma jets and their internal structures through fast photography, emission spectroscopy, and arc dynamics under different operating conditions. A novel method to explore structures inside extremely intense hot plasma jet is conceived and applied for the first time to investigate arc plasma jets. The study revealed distinct interesting structures and their evolution inside the plasma jet, apparently not reported earlier. The associated fundamental mechanisms are identified from direct experimental evidences. Respective steady state jet characteristics with and without air entrainment are obtained from computational fluid dynamic simulation. Arc root motion, air entrainment, and interaction between electromagnetic and fluid dynamic body forces are found to result in a variety of interesting dynamics and structures inside the plasma jet under different operating conditions. Observed behaviors are notably different in argon, nitrogen, and air plasma. While no unusual structures are found over a range of lower flow rates, interesting structures evolve at higher flow rates. Statistical behavior of these structures is found to have a significant dependence on the gas flow rate and torch power. Apart from air entrainment in the downstream, observed isolated temperature islands inside the jet in the upstream have potential to affect particle trajectory, physical processes, and process chemistry in a significant manner.

Chapter-6 presents evolution of spray particles from molten wire as well as particle behaviour in the flowing plasma in a single wire arc plasma spray torch, using high speed camera. Individual particles were tracked and their velocities were measured at various distances from the spray torch. Particle velocity information at different distances from the nozzle of the torch is very important to decide correct substrate position for the good quality of coating. Images of the wire and the arc have been captured for different wire feed rates, gas flow rates, and torch powers, to determine compatible wire feed rates. High speed imaging of particle trajectories has been used for particle velocity determination using time of flight method. It was observed that the ripple in the power supply (thyristor controlled) of the torch leads to large variation of instantaneous power fed to the torch. This affects the velocity of the spray particles generated at different times within one cycle of the ripple. It is shown experimentally that the velocity of a spray particle depends on the instantaneous torch power at the time of its generation. Once the particles leave the plasma jet, their forward speeds were found to be more or less invariant beyond 40 mm up to 500 mm from the nozzle exit.

Chapter-7 presents unusually high electro-thermal efficiency, observed under certain cooling rates of the anode boundary layer in a typical non-transferred arc plasma torch. The behavior is reproducible at different arc currents and gas flow rates. To understand the origin of such behavior, total arc voltage, which bears the overall signature of the internal arc dynamics, has been analysed using tools of dynamical analysis like frequency space behavior, phase space dynamics, correlation dimension and Lyapunov exponent under different rates of anode cooling. Simultaneous emission spectroscopic investigation of the plasma temperature at the nozzle exit and fast photographic study of the anode boundary layer have been carried out for better insight. Observed significant variation in the dominant frequency components under different cooling rates gives concrete signature of distinct changes in the dynamics induced by anode cooling. Vivid differences in the dynamics are brought out in phase space representations. True natures of the dynamics are obtained through the estimated values of correlation dimension and Lyapunov exponents.

Chapter-8 presents the theoretical investigation of chemical kinetics in argon, nitrogen, oxygen and air plasma and experimental investigation of chemical kinetics in yttria-argon plasma. Chemical kinetics of plasma species are presented in argon, nitrogen and oxygen plasma under thermal non-equilibrium parameter ($\Theta=T_e/T_h$)

ranging from 1 to 20, electron temperature ranging from 0 to 50000K and pressure ranging from 0.1 to 5 Atm. The data will be useful in understanding plasma synthesis processes over wide parametric range. Chemical kinetics behind synthesis of yttria nanoparicles in gas phase nucleation process is explored through in-situ emission spectroscopy and high speed camera. It was observed that as soon as precursor is fed to the plasma argon atomic lines disappears and YI, YII, O lines appear. YO band at the nozzle exit was not observed. It starts appearing after 3cm from the nozzle exit. With increase in distance, the band becomes stronger and stronger up to certain distance and then starts falling. The band is clearly visible up to 6cm from the nozzle exit.

Chapter-9 summarizes the important conclusions and the scope for future works.

References

1. https://www.merriam-webster.com

2. Boulos, M. I., Fauchais, P., Pfender, E., "Thermal Plasmas, Fundamentals and applications", Vol1, Plenum Press, New-York(1994).

3. Pfender, E., "Thermal Plasma Technology: Where do we stand and where are we going?", Plasma Chemistry and Plasma Processing, 1-31 (1999)

4. Fauchais, P., and Vardelle, A., "Pending problems in thermal plasmas and actual development", Plasma Phys. Control Fusion 42, B365-B383(2000)

5. Fauchais, P., Montavon, G., Vardelle, M., Cedelle, J., "Developments in direct current plasma spraying", Surface & Coatings Technology 201, 1908–1921(2006)

6. Fauchais, P., "Understanding plasma spraying", J. Phys. D: Appl. Phys. 37, R86–R108 ((2004)

7. Monerie-Moulin F Gitzhofer, F., Fauchais, P. and Boulos, M., “Thermal Plasma Applications in Minerals Metallurgical Processing”, Warrendale, PA: Minerals, Metals and Material Society, 125 (1992)

8. Duan, Z., and Heberlein, J., “Arc instabilities in a plasma spray torch”, J. Therm. Spray Technol. 11, 44–51 (2002)

9. Planche, M. P., Coudert, J. F. and Fauchais, P., “Velocity measurements for arc jets produced by a dc plasma spray torch”, Plasma Chem. Plasma Process. 18, 263–83, (1998).

10. Ghorui, S. and Das, A. K. “Origin of fluctuations in atmospheric pressure arc plasma devices” , Phys. Rev. E, 69, 026408 (2004)

11. Ghorui, S., Vysohlid, M., Heberlein, J. V. R., and Pfender, E., “Probing instabilities in arc plasma devices using binary gas mixtures”, Phys. Rev. E, 76, 016404 (2007)

12. Ghorui, S., Sahasrabudhe, S. N. and Das, A. K., “Current transfer in dc non-transferred arc plasma torches” J. Phys. D:Appl. Phys. 43, 245201 (2010)

13. Krowka, J., Rat, V. and Coudert, J. F., “Investigation and control of dc arc jet instabilities to obtain a self-sustained pulsed laminar arc jet”, J. Phys. D: Appl. Phys. 46 505206,(2013)

14. Pfender, E., Fincke, J. and Spores, R., “Entrainment of cold gas into thermal plasma jets”, Plasma Chemistry and Plasma Processing, I1, 529-543(1991)

15. Hrabovsky, M., “Effect of anode attachment on flow structure in plasma jet generated in dc plasma torch” Annals New York Academy of Science (1999)

16. Coudert, J.F., Planche, M.P., and Fauchais, P., "Characterization of d.c. plasma torch voltage fluctuations", Plasma Chemistry, and Plasma Processing, 16, 211S-227S (1996)

17. Ghorui, S., Sahasrabudhe, S. N., Murthy, P. S. S., Das, A. K., and Venkatramani, N., "Experimental evidence of chaotic behavior in atmospheric pressure arc discharge", IEEE Trans. on Plasma Sci. , 28, 253, (2000)

18. Ghorui, S., Sahasrabudhe, S. N., Tak, A. K., Joshi, N. K., Kulkarni, N. V., Karmakar, S., Banerjee, I., Bhoraskar, S. V. and Das, A. K. et.al., "Role of Arc Plasma Instability on Nanosynthesis", IEEE Transactions on Plasma Science, 34, 121 (2006)

List of Abbreviations

CFR	Cooling Flow Rate
DSO	Digital Storage Oscilloscope
EMF	Electro Motive Force
ETE	Electro thermal Efficiency
FFT	Fast Fourier Transform
FPC	Fast Photography Camera
IGBT	Insulated Gate Bipolar Transistor
LTE	Local Thermodynamic Equilibrium
NTD	Negative Time Derivative
PGFR	Plasma Gas Flow Rate
PLTE	Partial Local Thermodynamic Equilibrium
RPM	Rotation Per Minute
RTD	Resistance Temperature Detector
SCR	Silicon Controlled Rectifier
SIMPLE	Semi-Implicit Pressure Linked Equation
SWAPS	Single Wire Arc Plasma Spray

CONTENTS

LIST OF FIGURES

LIST OF TABLES

Chapter-1
Introduction

Outline of the Chapter

Chapter 1

Introduction

1.1 Kinetics and plasma

Kinetics deals with the effect of forces upon the motions of material bodies or with changes in a physical or chemical system, according to merriam-webster.com [1]. Kinetics in physics means the study of motion and its causes. Rigid body kinetics deals with the motion of rigid bodies. Chemical kinetics involves the study of chemical reaction rates. Gas phase kinetics in arc plasma jets, involves dynamics of the plasma body as a whole, driven by electromagnetic body forces evolved inside the plasma, directly or indirectly controlled by prevailing chemical kinetics. Chemical kinetics in arc plasma, on the other hand, are controlled by particular operating condition of the plasma torch like plasma current, plasma gas flow rate, type of plasma gas, torch geometry and ionization scenario at the realized temperature.

Plasma is energetically the fourth state of matter apart from solid, liquid and gas states. The name fourth state was given basically due to naturally occurrence of the plasma at very high temperature [2]. Fundamental difference among solid, liquid and gases les in the difference between strength of the bonds. Bonds hold their constituent particle together. These forces are strong in solid, weak in liquid and almost absent in gaseous state. State of the matter depends on the random kinetic energy of its atoms or molecules i.e. on its temperature [3]. Range of temperature for all four forms of matter is shown in Figure1.1.

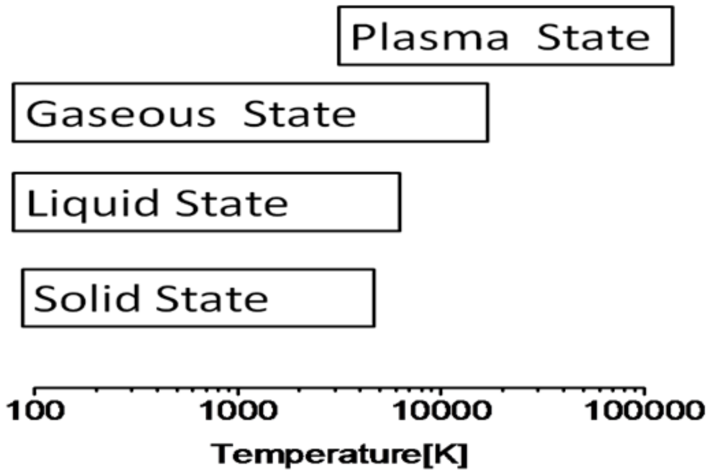

Figure 1.1: State of matter with temperature

State of the matter changes with the energy supplied to the matter. This energy may be thermal or electrical. When solid is heated up it is changed to liquid phase. Further heating of liquid, changes the matter to gaseous state. On further increase in temperature changes the liquid state to gaseous. When energy supplied to the substance is greater than the ionizing potential of atom, then gas is ionized and plasma is formed.

Plasma mainly consists of electrons, ions, neutral particles, excited species and photons, where negative and positive charges balance each other. The term 'plasma' was first applied by Langmuir and Tonks in 1923 to ionized gas in electric discharge. About 99% of the matter in the universe is in plasma state. A body in a non-plasma state like earth is a not common and very less object in the universe. Sun and other stars, galaxies, ionosphere etc. consist of plasma. Few examples of plasmas faced in our daily life are lightning discharge, fluorescent lamp, red neon tubes in advertisements, electrical spark etc.

Plasma is produced by ionizing gases to a certain degree of ionization. Because of the presence of charged particles it possesses electrical conductivity like that of metals. Plasma is mainly characterized by its electron number density (n_e) and electron temperature (T_e). Depending on these two parameters, naturally occurring and laboratory plasma are classified as given in Figure 1.2.

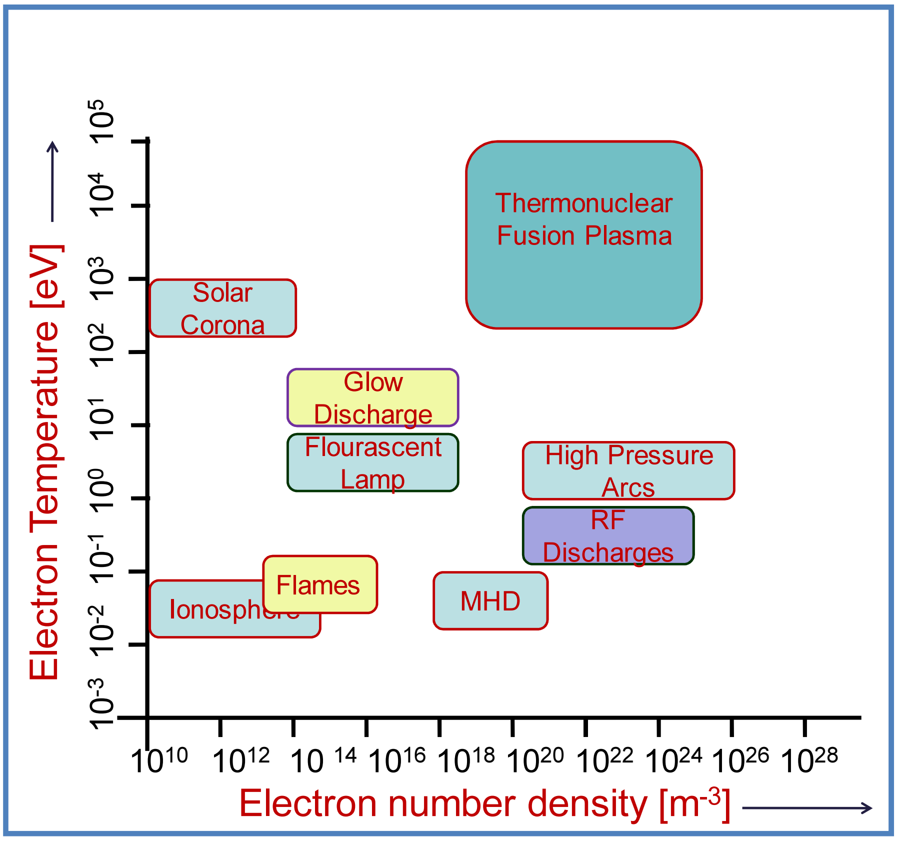

Figure1.2: Categorization of plasma based on electron number density and electron temperature

Plasma produced in laboratory is again classified as thermal plasma and non-thermal plasma depending on their state of thermal equilibrium. In plasma physics, the state of thermal equilibrium is defined in terms of the electron temperature (T_e) and heavy particle (atoms, ions and molecules etc) temperature (T_h). These temperatures are related to the kinetic energy of the electrons and heavy particles respectively. In case of thermal plasma the electron temperature (T_e) is equal to the heavy particle temperature (T_h) while electron temperature (T_e) differs from the heavy particle temperature (T_h) in non-thermal plasma. Plasma generated at lower gas pressure such as RF plasma, glow discharge etc. are non-thermal plasma where as the plasma generated at atmospheric or near atmospheric pressure such as MHD generator, dc plasma, inductively coupled plasma etc. are known as thermal plasma. Hence thermal plasma are characterized by high electron number density and high gas temperature where as non-thermal plasma are characterized by low electron density and low gas temperature.

This study is concerned with DC arc plasma devices falling under thermal plasma category [4]. However in arc plasma systems, in some location such as the vicinity of the anode, the electron temperature may differ from heavy particle temperature leading to thermal non-equilibrium. Variation of the electron temperature (T_e) and heavy particle temperature (T_h) with pressure in arc plasma devices is shown in Figure 1.3.

At low pressure, the electron temperature is much greater than heavy particle temperature. As pressure increases, mean free path decreases and energy transfer from electron to heavy particles increases. This results decrease in electron temperature. The electron and heavy particle temperature reaches to similar values around 100 Torr and plasma becomes arc like. In arcs, at atmospheric pressure the two temperature are equal. When the two temperatures are about the same, the distribution of the species in the plasma can be described by the equilibrium relations, while in the case when Te>>Th, the distribution of active species is governed by electron temperature as given by Grill [5].

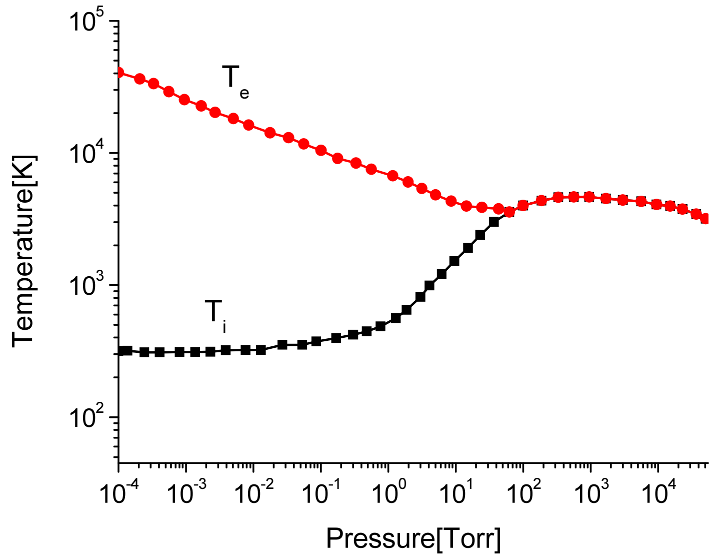

Figure1.3: Variation of electron and heavy particle temperature with pressure.

Thermal plasma devices are again classified into AC plasma devices and DC plasma devices according to the type of electric field applied to produce the plasma. Depending upon the mode of energy coupling the AC arc plasma devices are again divided into two groups: one utilizes electrodes which operate with AC electric current oscillating at a frequency of 50 Hz and the gas is heated by ohmic heating and the other one is electrode less RF inductively coupled plasma devices, where the electrical energy is transferred to the gas by electromagnetic induction as well as through Ohmic heating of the arc formed by the eddy current generated in the plasma. DC plasma devices include the DC plasma generators or gas heaters.

According to the mode of operation they are further classified transferred arc and non-transferred arc plasma devices. In transferred arc plasma devices, the arc is established between the cathode and the job which acts as the anode. However, in non-transferred arc plasma torches, the arc is established between the cathode and a nozzle which behaves as the anode. The classification of the arc plasma devices is shown in Figure 1.4.

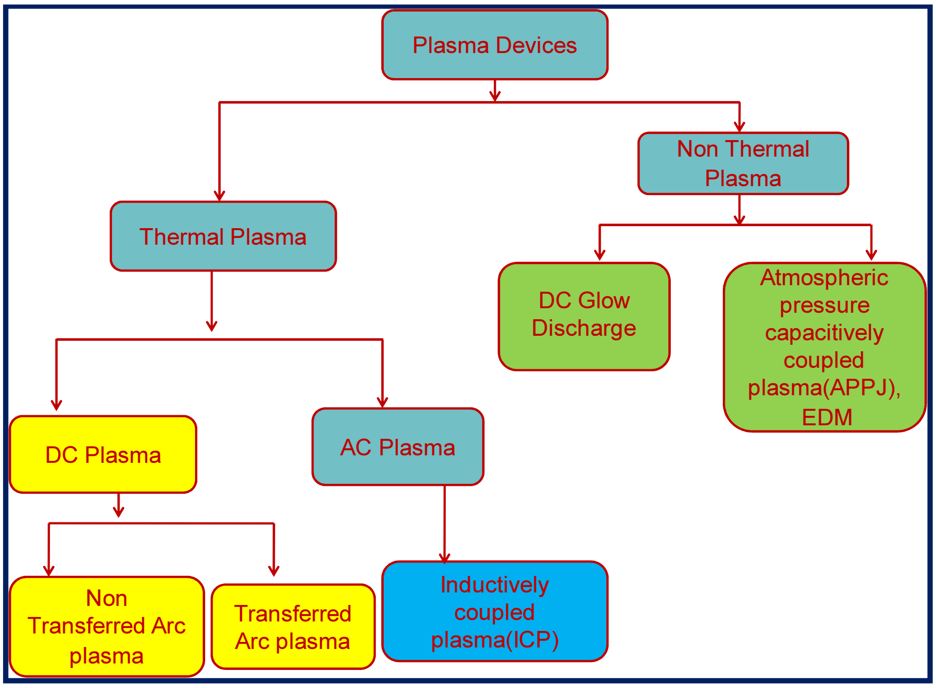

Figure1.4: Classification of arc plasma devices

Figure 1.5 shows the DC plasma torch operating in transferred and non-transferred arc mode respectively.

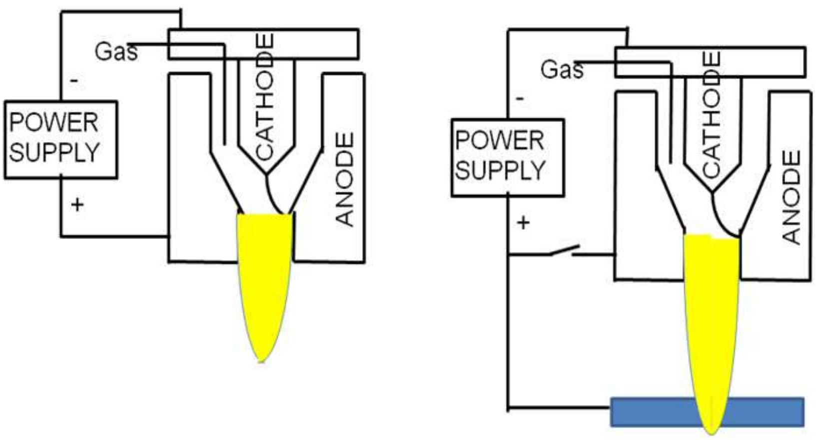

Figure1.5: Non-transferred and transferred arc mode DC plasma torch.

1.2 DC Arc plasma devices

DC plasma torch is a device that converts electrical energy into a concentrated jet of plasma. Temperature, velocity, energy density and enthalpy of this plasma jet are very high. Simplest DC plasma torch shown in Figure 1.6 consists of two concentric electrodes cathode and anode. The cathode is connected to the negative terminal and the anode is connected to the positive terminal of DC power supply respectively. An arc is established between the cathode and anode which heats up the gas passing through the gap between them by ohmic heating and generates the high temperature plasma jet emanating from the nozzle exit. The initial breakdown of the gas between the electrodes is achieved by spark (known as the pilot arc) generated between the two electrodes using a high frequency electric field between them or by a momentary short circuit of the two electrodes. The arc thus formed is known as the pilot arc.

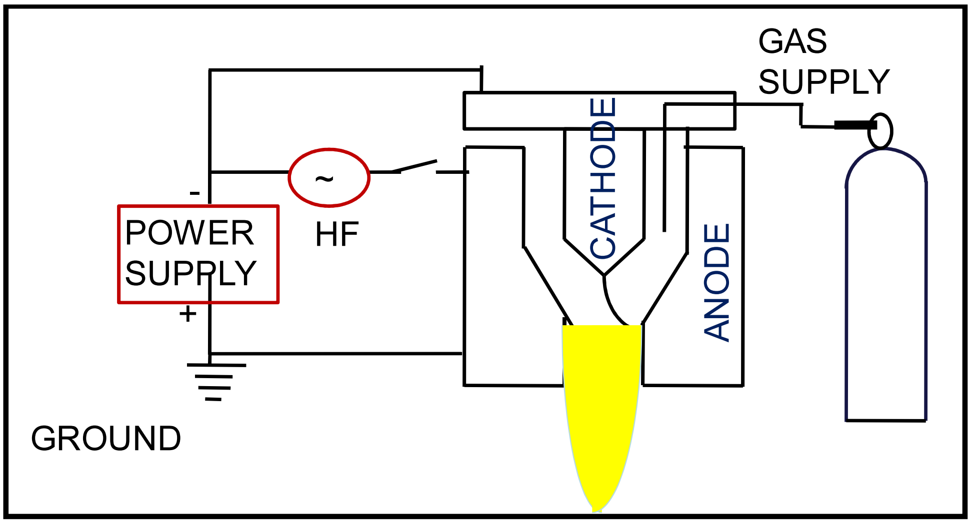

Figure1.6: Design and working of simplest DC plasma torch

The power of the plasma torch can be increased by increasing the voltage drop across the electrodes. This is achieved by increasing the distance between the cathode and anode which needs adding anode like segments between them. Review of a large variety of DC plasma torches operating at different level of electrical power with transferred arc and non-transferred arc mode is provided by Venkatramani [6]. Table 1.1 presents the power level of plasma torch used for various application.

Table-1.1 Power range of plasma torch used for various applications

Sr. No.	Power Range (kW)	Applications
1	0.1 – 1	Welding of foils.
2	1 - 10	Single wire arc spraying, UF_6-UF_4 conversion, Cutting, welding thin plates.
3	10 – 100	Plasma gassification, welding, melting, spraying, machining and material processing
4	100 - 1000	Under water cutting and plasma metallurgy.
5	>1000	High enthalpy sources, wind tunnels and plasma heaters.

There is a wide range of gases used for plasma generation and the choice of plasma generating gas depends on the purpose of application. For example, in plasma gasification process for treating all type of municipal waste, air , nitrogen and oxygen are best suitable, whereas in UF_6-UF_4 conversion, plasma spraying process, chemically inert environment is required so, gases like argon, helium are used. Properties of gases used for plasma generation are given in Table 1.2 [7].

Table-1.2: Properties of gases used for plasma generation

Plasma forming gases	Dissociation energy (eV)	First ionization energy (eV)	Second ionization energy (eV)	Third ionization energy (eV)
Argon	Monatomic	15.75	27.62	40.735
Helium	Monatomic	24.58	54.41	Two electrons
Hydrogen	4.52	13.59	Only one electron	One electron
Oxygen	5.15	13.61	35.12	54.93
Nitrogen	9.77	15.6	29.60	47.44

Material of the electrodes plays very important role for fabricating the plasma torches. For making cathodes, heat-resistant material having high melting point like tungsten, copper, hafnium, zirconium etc are used. Tungsten electrodes works well with non-oxydizing gases. For producing oxidizing plasma, tungsten cathode cannot be used due to immediate oxidation of tungsten in oxidizing environment. For working with air and oxygen, hafnium and zirconium are used. Hafnium also gets oxidized but there is a major difference when compared with tungsten. Tungsten oxide has melting point nearly 2000K lower than that of tungsten metal. On the other hand, hafnium oxide has melting point nearly 500K higher than pure hafnium. Due to lower melting point, oxidized tungsten cathode gets completely eroded away in less than a minute at the arc initiates. Due to high thermal and electrical conductivity copper is used and anode material. Materials used for making the electrodes and their properties are listed in Table 1.3.

Table-1.3: Properties of elements used in plasma torch components

Sl. No.	Element	Thermal conductivity W/m.K at 0^0C	Electrical resistivity Ω·m	Thermal expansion coefficient µm/m.K at 25^0C	Melting point (^0C)
1	Copper (Cu)	400	16.78	16.5	Cu:1084 Cu_2O :1235 CuO :1201
2	Zirconium (Zr)	22.6	421.0	5.7	Zr :1855 ZrO_2 :2715 White
3	Hafnium (Hf)	23.0	331.0	5.9	Hf :2230 HfO_2 :2758
4	Tungsten (W)	173.0	52.8	4.5	W : 3422 WO_3 :1473

In this study four kind of plasma torches will be used.

1) Segmented DC non-transferred arc plasma torch with a tungsten rod type cathode using argon and nitrogen as plasma forming gases
2) Air plasma torch with hafnium insert cathode using air as plasma forming gases
3) Specially designed high efficiency low power plasma torch using argon as plasma forming gas
4) A transferred arc plasma torch named single wire arc spray torch using argon as plasma forming gas

1.3. Definition of the problem

Thermal plasma jets are unique for a number of industrial processes because of its ability to produce high enthalpy, high temperature chemically inert as well as active environment with easier process control. Argon and nitrogen are among the most commonly used plasma generating gases having wide spectrum of applications like cutting, welding, melting, spraying, chemical synthesis, nano-structure production, waste treatment, gasification, densification, metallurgical applications etc. [8]. Mostly argon is used for producing chemically inert environment and air is used for waste treatment while nitrogen is used mainly for a number of plasma assisted chemical processes like plasma nitriding [9, 10, 11] and nanostructure generation [12] preparation of syngas [13] etc.

Use of nitrogen as plasma forming gas has the additional benefits that it can operate with usual tungsten based refractory electrode plasma torches. Being molecular gas, it can provide higher voltage drop with the same electrode configuration. While air is the cheapest, although it requires hafnium cathode, the plasma jet length is very high in case of air plasma. Typical plasma jet in Argon is very short (~ 5 cm), whereas in air and nitrogen plasma length is 6 times higher. This type of long length plasma jet may be very useful for large number of processing applications.

Plasma jet emanating from the DC plasma torches is not stable and fluctuates.

Plasma jet fluctuation arises due to various factors like ripple in the SCR based power supply (300 Hz), arc root movement (few kHz), air entrainment in the plasma jet, drag force due to gas flow, and electromagnetic body forces in the plasma jet[14]. Fluctuation due to power supply ripple is minimized using IGBT (Insulated gate bipolar transistor) power supply. Air entrainment can be optimized using low pressure plasma reactor for precise applications like nanopowder synthesis and fine coating. Fluctuations, arising due to arc root movement mainly depend on operating condition of the torch. Plasma torches primarily operate in three modes: 'steady', 'take-over' and 'restrike' given by Duan et al. [15]. These three modes are identified through measuring arc voltage developed across cathode and anode of the torch. In steady mode, nearly flat behaviour in arc voltage are identified. In take over mode of operation, almost sinusoidal variation in arc voltages of relatively lower amplitude are identified. For restrike mode of operation, large fluctuations in arc voltage having varying saw tooth patterns are observed. Steady mode offers a stable jet but it is harmful for torch health due to continued connection of arc root at a particular anode location. This may puncture the electrode very fast owing to highly concentrated heat flux. On the other hand, the oscillatory behaviour of a moving arc root under takeover and restrike modes may avoid such problems by distributing heat over a wider area but inherently include instability in the plasma jet.

Length, stability and structure of the plasma jet play very important role in the determining the quality of plasma process application and strongly affect the lifetime of the devices [16, 17, 18]. For example in thermal plasma spraying application, quality of coating depends directly on the transfer of heat and momentum from the plasma(high temperature and high velocity) to the powder particles injected into plasma jet. The heat and momentum transfer vary with the velocity and temperature of the plasma, the length of the plasma and the dwelling time of the particles in the plasma. Temperature of the particle should be higher than melting point of the powder to be coated, so that particle should be in molten state before reaching the substrate.

Velocity of the particle should be very high enough to adhere on the substrate. Powder particle should be in molten state before reaching to substrate. If plasma jet is not stable, particles entering into the plasma at the time when jet length is higher, will be overheated and evaporated while particles entering at the time when jet length is less will not melted. Therefore coating will not be of good quality. Similar will be the case for synthesis of nanopowder in dc plasma torch reactor.

Due to extreme brightness of the plasma jet and obstruction because of cylindrical geometry of the anode in non transferred arc plasma torches, direct probing of arc root dynamics for steady, take over and restrike mode of torch operation is a critical problem. Exploring possible mechanism behind a huge length in case of Air plasma jet and nitrogen plasma jet was also a big issue. Thermo physical properties of the gases play role in the luminous volume of the plasma jet but that is not sufficient to get the such huge jet length. It may be possible that plasma jet itself may carry current.

Works done so for on physical dynamics of the arc root, plasma jet, voltage and its origin are given in literature survey of chapter 2. However, most of the attempts primarily consider existence of single arc root. Also it was assumed that there is no current in the external plasma jet.

The problem under the present study is defined as investigation of different macroscopic gas phase kinetics and their origin in (i) nontransferred arc plasma jet of argon, nitrogen and air (ii) transferred arc single wire arc spray system; theoretical investigation of chemical kinetics in Argon plasma; experimental investigation of chemical kinetics in pure argon and argon-yttria plasma through emission spectroscopy and high speed imaging.

1.4 Relevance of the problem

A thermal plasma jet derives its potential from its unique properties like availability of huge concentrated heat flux, extremely high gas temperature and enthalpy and abundant presence of highly reactive nascent atomic and ionic species. Because of such unique properties, the thermal plasma jets find wide usage in variety of application areas. However, one important thing the area is lacking is rigorous analysis of the dynamics of dynamics of anodic arc root and plasma jet behaviour of the plasma torches at different operating parameters. Without this it may not be possible to explore the full potential of these devices for process application. Thermal plasma jets of molecular gasses like nitrogen are important as they possess higher enthalpy, higher power content and much longer jet length compared to plasma jets of monatomic gasses like argon, helium etc. Many of the processing applications require operation at higher power for higher throughput. Studies of arc root dynamics, plasma jet dynamics, structure and stability of the plasma jet, effect of cooling on torch efficiency operating are therefore very much important. For example, in thermal plasma spray process, powder particle (Y_2O_3, Al_2O_3, Zr_2O_3) should be in semi molten state. However if jet is unstable, particle will not melt properly sometimes and sometimes it will be evaporated, therefore coating will not be proper. In processes like spherodization, densification and nanoparticle generation of such high melting point material, the powder particle should properly melt or completely vaporize. Therefore, high power plasma jet with longer length (enough dwell time of the injected particles inside the plasma under high heat flux) are required.

Dynamics of the jet as well as the arc root in arc plasma torches are important factors as it can severely affect the performance of a plasma device for any processing application. This important aspect is addressed in this study by analyzing the arc root dynamics, plasma jet fluctuations, voltage fluctuation behaviour in argon, nitrogen, air plasma, plasma jet in single wire arc spray system and a low pressure dc plasma jet during precursor feeding under different operating conditions.

1.5 Scope of the work:

Scope under "Study of gas phase kinetics of in the arc plasma devices" includes both macroscopic kinetics (physical dynamics of the plasma body as a whole) as well as microscopic kinetics (mapping species distribution inside the plasma jet through modelling and emission spectroscopy). While arc plasma system may include variety of plasma gases and configurations, the study primarily focuses on the kinetics in most technologically relevant ones, namely: DC non-transferred arc plasma jets of argon, nitrogen and air, transferred arc single wire arc spray process.

The present study includes the following:

I. Direct probing of arc root dynamics in DC plasma torches & correlation with voltage instabilities

II. Study of structures and stabilities in atmospheric pressure DC non-transferred arc plasma jets of air, argon and nitrogen

III. Study of arc instabilities driven by thermal state of anode boundary layer and its consequence on overall torch efficiency

IV. Investigation of gas phase kinetics in wire arc plasma spray system in argon jet

V. Theoretical investigation of chemical kinetics in argon plasma under thermal non equilibrium and experimental investigation of chemical kinetics in yttria-argon plasma.

1.6 Structure of the thesis

The thesis is divided into nine chapters. Main contents of the chapters are as follows:

Chapter1: This chapter gives a brief introduction on kinetics and plasma, different types of plasmas and plasma generation processes in DC thermal plasma devices, relevance, status and scope of the work under the present study.

Chapter2: This chapter briefs about few of important works done from 1993-2013 on plasma jet fluctuations, its origin.

Chapter3: This chapter gives detail descriptions of experimental setups used in the study. Different diagnostic technique and equipment used for the study are described

Chapter4: This chapter presents direct probing of arc root dynamics in DC plasma torches & correlation with voltage instabilities. Experimental proof of current in the external plasma jet was established first time in the plasma torch history.

Chapter5: This chapter presents investigation of structures and stabilities in atmospheric pressure DC Non-transferred arc plasma jets of air, argon and nitrogen. Different scenario of the variation of plasma jet length with plasma gas flow rate for air, argon and nitrogen plasma was probed. Supported simulation for Ar, nitrogen and air plasma jet assuming current free jet was reported.

Chapter6: In this chapter, reproducible high electro-thermal efficiency, observed under certain cooling rates of the anode boundary layer in a typical non-transferred arc plasma torch has been reported. To understand the origin of such behaviour, analysis of total arc voltage using tools of dynamical analysis like frequency space behaviour, phase space dynamics, correlation dimension and lyapunov exponent under different rates of anode cooling are reported.

Chapter7: This chapter presents the investigation of kinetics in single wire arc plasma spray system in argon jet. Wire feed rate was optimized and effect of ripple on the velocity of particle was established.

Chapter8: This chapter presents theoretical investigation of chemical kinetics in argon plasma under different degrees of thermal non-equilibrium and pressure, and experimental investigation of chemical kinetics in yttria-argon plasma. Kinetics of argon plasma and argon and Y_2O_3 plasma was probed using emission spectroscopy and fast photography. Possible mechanism of Y_2O_3 nanopowder synthesis was established.

Chapter9: This chapter presents summary of the work done carried out and future scope in the field of various plasma processing application (specially, mechanism of nano-synthesis of Al_2O_3 and Nd_2O_3) in non transferred DC arc plasma.

1.7 References

1. https://www.merriam-webster.com
2. Chen, F.F., "Introduction to Plasma Physics and Controlled Fusion", ISBN 13978-0306413322 (2006)
3. Bittencourt, J.A., "Fundamentals of Plasma Physics", ISBN 978-81-8125-454-9, (2013)
4. Boulos M.I., Fauchais P., Pfender E, "Thermal Plasmas, Fundamentals and Applications", Vol1, Plenum Press, New-York(1994).
5. Grill, A., "Cold Plasma in Material Fabrication", IEEE press, New-York(1994), ISBN 0-7803-1055, 1994
6. Venkatramani, N., Thermal Plasmas in Material Processing, Bull. Mater., Sci.,

Vol. 18, No. 6, 741-754, 1995

7. Tennent, R. M., "Clark's table: Science Data Book", Pearson Education Limited (2006)

8. Boulos, M. I., "Thermal Plasma Processing", IEEE Transactions on Plasma Science, 19, 1078-1089, 1991

9. Tahara, H. and Ando, Y., Study of titanium nitride deposition by supersonic plasma spraying, Vacuum, 83, 98–101, 2009

10 Nayak, B. B., "Arc plasma nitriding of graphite surface towards production of a hard carbon nitride case", Surface and Coatings Technology, 201, 2639-2647 (2006)

11. Yamazato, M., Higa, A., Oshiro, T., Toyama, H., Maehama, T. and Toguchi, M,"Preparation of carbon nitride films by DC arc plasma jet CVD", Diamond and Related Materials, 15, 917-920, (2006)

12. Balasubramanian, C., Godbole, V. P., Rohatgi, V. K., Das, A. K. and Bhoraskar, S. V, "Synthesis of nanowires and nanoparticles of cubic aluminium nitride", Nanotechnology, 15, 370-373 (2004)

13. Yanpeng, S., Yong, N., Angshan, W., Dengxiang, J., Fengwen, Y. and Jianbing, J., "Carbon dioxide reforming of methane to syngas by thermal plasma", Plasma Science and Technology, 14, 252-256 (2012)

14. Tiwari, N. Nirupama Tiwari, Sahasrabudhe, S. N. Joshi, N. K. and Das, A. K. "Study of jet fluctuations in DC plasma torch using high speed camera", Journal of Physics: Conference Series 208, 012134 (2010).

15. Duan, Z. and Heberlein, J. "Arc instabilities in a plasma spray torch" J. Therm. Spray Technol. 11, 44–51 (2002)

16. Fauchais, P. and Vardelle, A., "Pending problems in thermal plasmas and actual development", Plasma Phys. Control Fusion 42, B365-B383(2000)

17. Pfender, E. “Thermal plasma technology: where do we stand and where are we going?”, Plasma Chem. Plasma Process. 19, 1–31 (1999)

18. Fauchais, P., Montavon, G., Vardelle, M., Cedelle, J., "Developments in direct current plasma spraying", Surface & Coatings Technology 201, 1908–1921 (2006).

Chapter-2

Literature Survey

Outline of the Chapter

Chapter 2

Literature Survey

Extensive literature survey on experimental as well modelling and simulation work done on plasma jet dynamics, instabilities, its origin, diagnostics of the plasma, thermal plasma spray process and its effect on thermal plasma spray process have been done in this chapter from the year 1991-2013. Few of the important contributions are presented in a chronological order in this chapter.

Pfender and his co-workers [1] in 1991 studied the entrainment of cold gas into thermal plasma jets using emission spectroscopy, enthalpy probe measurements, shadowgraph, LDA (Laser Doppler Anemometry) and CARS (Coherent Anti-Stokes Raman Spectroscopy) diagnostic techniques. The combined information obtained from the study made a significant contribution in understanding the behavior of plasma plumes and it’s interaction with surrounding cold air. Shear layer instability just after nozzle exit and subsequent development of large scale eddies, rapid drop in the axial jet velocity due to entrainment, reduction in air entrainment at higher current are some of the important observations. Schlieren images were used to characterize the plume structure. However, fast imaging techniques and advanced image processing to explore the internal structures of the plumes were not used.

Coudert et al. [2] in 1996 studied time resolved voltage waveforms in non-transferred arc plasma torch and found it strongly correlated to the instantaneous morphology of arc, which in turn determines the plasma flow structure and temporal behaviour. The analysis of voltage signal and light emission at a point of the plasma jet near to the nozzle exit provided mean electrical field within the plasma column and the mean position of the arc root. It was concluded that plasma flow includes extinguishing plasma bubbles surrounded by colder layers. The study did not pay attention to explore the dynamic evolution of the structures in the external plasma plume.

Investigation by Dyuzhev et al. [3] in 1997 revealed that the anode arc root of a free-burning arc with water-cooled anode is constricted and erosion-free at low currents (<10A). With increase in current, the root was found to split up. A xenon arc was found more prone to such splitting compared to an argon arc. The current density in the anode root was observed substantially lower compared to the same at the cathode. Passing current, specific plasma-forming gas and the width of the electrode gap were found to influence the behaviour in a significant manner. It was suspected that cooling of the arc column by the anode influences the thickness of the anode boundary layer and thereby leads to development of instabilities.

Multiple anode constrictions in atmospheric pressure arcs were further investigated by the Baksht etal. [4] in free burning argon and xenon plasma. The electron temperature and electron density near the anode were investigated under different operating regimes. It was concluded that the constrictions occurred due to overheating instability near the anode, originated from imbalance between Joule heating and cooling via radiation loss.

Planche et al. [5] in 1998 determined the plasma jet velocity from the time of flight measurement of the luminous fluctuations of the wavelength integrated light emission. It was investigated that instabilities may be associated with the movement of arc root. Coupling between fluctuation in the jet velocity, arc voltage and arc instability was explored. Unfortunately, the extreme brightness of the arc and the mechanical obstructions due to the anode wall inhibit direct investigation of the anode arc root dynamics in non-transferred arcs.

Pfender et al. [6] in 1999 and Fauchais et al. [7] in (2000) studied the entrainment of cold gas into thermal plasma jets using emission spectroscopy and enthalpy probe measurements diagnostic techniques.

Hrabovsky et al. [8] in 1999 reported the effect of anode attachment on the flow stability in a dc plasma jet. The plasma torch was equipped with external anode to facilitate direct observation of the plasma dynamics in the arc root region. High speed photographs of the plume and corresponding arc voltage were recorded in a time synchronous manner. Formation of anode jet, strong entrainment of ambient air and the dynamics near the anode arc root were reported. However, the internal details of the exiting plume and associated dynamics were not explored.

Ghorui et al. [9] in 2000 studied the fluctuating voltage signals generated from atmospheric pressure dc arc discharges and analyzed it to be chaotic.

Pan et al. [10] in 2001 produced a long, laminar plasma jets in a DC arc torch by restricting the movement of arc root in the torch channel. The analysis showed that laminar flow plasma with very low initial turbulent kinetic energy can produce a long jet with low axial temperature gradient.

Dorier et al. [11] in 2001 investigated the fluctuating behaviour of a Sulzer Metco F4 dc plasma gun by simultaneous measurement of the arc voltage and end on images of the nozzle interior using a gated camera. The attachment positions over the anode and the intensity profiles around the arc column inside the anode nozzle were visualized using a special image analysis technique. Successive creation and vanishing of multiple attachments and their coexistence were observed. However, the effect of these instabilities on the final structure of the exiting plasma plume was not probed.

Zhao et al. [12] in 2001 examined the chemical, thermodynamic and ionizational state of the plasma in the free stream and inside the thin boundary layer through emission and absorption spectroscopy measurements of an atmospheric pressure DC plasma during diamond growth.

Amanatides et al. [13] in 2001 developed a gas phase and surface simulator of highly diluted silane in hydrogen rf discharges used for the deposition of microcrystalline silicon. Modelling results were in good agreement with experimental data.

Zhao et al. [14] in 2002 investigated the characteristics of the unsteadiness of dc plasma spraying jets through optical emission spectroscopy, high speed photography and voltage signal. Air entrainment was investigated by monitoring intensity of particular nitrogen and argon line in the external jet. Image of the plume was sampled to understand the effect of power supply oscillation on the plume length. Analysis of the results showed that fluctuation in the Argon plasma jet is mainly due to the power supply. However, study to understand the instabilities and structures inside the plasma plume was missing.

Ghorui et al. [15] in 2002 estimated the dynamic properties of attractors observed through dynamical analysis of voltage signal across cathode and anode of dc plasma torch.

Duan and Heberlein [16] in 2002 studied the instabilities in spray torches through high-speed end-on imaging synchronized with voltage signal. Quantitative correlations between the cold-gas boundary layer thickness and the instability mode have been done for different operating parameters. Thickness of the cold-gas boundary layer between the arc and the anode nozzle wall is correlated with operating modes. In restrike mode, boundary layer is thicker, while in steady mode boundary layer is thin. But no investigation was made on effect of instabilities on the plasma jet was probed.

Chen et al. [17] in 2003 presented 3-D modelling of plasma flow and heat transfer characteristics of the thermal plasma systems. It was seen that lateral injection of carrier-gas into a plasma reactor from a port at the side-wall appreciably affects the temperature and velocity fields within the reactor which 2D approaches were unable to predict. Appreciable 3-D flow and heat transfer features exist in the DC non-transferred arc plasma torch, even for the case with completely axi-symmetric geometrical configuration, working gas and the electrical current connection. The 3-D modelling predicted local arc attachment, consistent with the experimental observation.

Ghorui et al. [18] in 2004 probed the origin of voltage fluctuations. The potential of the theory is demonstrated through comparison of theoretical predictions with reported experimental observations

Iwao et al. [19] in 2005 performed experiments with lateral gas flow in transferred arcs to simulate the behaviour of the anode arc root of the non transferred arc. In this configuration, the torch axis was perpendicular to the anode surface with the plasma gas flowing along the arc axis. The configuration had lateral injection of different gases parallel to the anode surface. Such simulations are far from reality as the local environment of the arc root under the planar open geometry of the anode is significantly different from the cylindrical geometry of the anode in a non-transferred arc.

Under two-temperature approximation, the anode layer in a high current atmospheric nitrogen arc was modelled in one dimension by Nemchinsky et al. [20] in 2005. Negligible concentration of the molecular ions and higher concentration of atoms compared to molecules in the anode layer, except for a narrow region near the anode were the major observations. It was found that the electric field in the anode boundary layer is weaker than that in the adjacent arc column but found to be always accelerating. Reactive thermal conductivity was found to play a significant role.

3D time dependent thermal equilibrium CFD model of the anode region of a torch was developed by Trelles et al. [21] in 2006 using finite element method for argon and argon-hydrogen plasma. While use of artificial high electrical conductivity over the anode and appreciable mismatch between experimental and predicted frequency of restrike were the major drawbacks of the model, an interesting speculation was that the reattachment process is driven by movement of the arc rather than breakdown-like process.

Moreau et al. [22] in 2006 have done a three-dimensional (3D) time dependent modelling of the arc and plasma generation in a torch operating under "restrike" mode. The model predicted the effect of operating parameters of the plasma torch on the motion of the anode root attachment over the anode surface and the time-evolution of arc voltage and flow fields in the nozzle.

Using a segmented anode, fast camera and Langmuir probes Yang et al. [23] in 2006 studied the arc behaviour in argon and nitrogen plasma by controlling the thermal state of the anode boundary layer through lateral injection of cold gas.

Another equilibrium model similar to Trelles [21] was developed by Chazelas et al. [24] in 2006. The breakdown model assumed that the anode boundary layer breaks when the arc voltage reaches a fixed threshold value.

Redwitz et al. [25] in 2006 investigated the constricted anode attachments in high intensity discharge lamps filled with inert gases (0.1–1MPa). Anode power input linearly proportional to arc current and higher constriction at lower anode temperature were important observations.

Ghorui et al. [26] in 2006 attempted to quantify the role of inherent arc fluctuations on the properties of synthesized nano-structures.

Peters et al. [27] in 2006 presented the erosion mechanisms of hafnium cathodes at high current. It was achieved by drilling two viewing ports into opposite sides of the nozzle. The ports were at an angle of 45° from the arc axis and have their axes centred on the hafnium insert. A sapphire window was cemented into the port.

Yang and Heberlein [28] in 2007 investigated the anode region of a high intensity argon arc allowing lateral injection of cold ambient gas and categorized the observed arc-anode attachments in four different modes, namely, diffuse, constricted, lift-up and multiple-attachment mode. Using laser Thomson scattering technique and solving the charge continuity equation it was suggested that the electron overheating instability could lead to the formation of multiple arc-anode attachments which eventually merges into a single one. Evaporation–ionization instabilities at the attachment region, stable space-charge relaxation mode, and current and field driven unstable electron thermal modes were suspected to be responsible for the observed behaviour. The fringes of the arc were found to be the favoured locations for arc-anode attachments, similar to experimental observation.

Nogues et al. [29] in 2007 investigated the thickness of the cold boundary layer near the nozzle exit surrounding the arc column for different types of spray plasma torches and studied its influence on the arc voltage instabilities. No attention was paid to understand the structures inside the plasma jet as a consequence of these instabilities.

Later, non-equilibrium model developed by the same group Trelles et al. [30] in 2007 removed the necessity of reattachment model that used artificial high electrical conductivity. However, the fundamental nature of the predicted dynamics differed appreciably from the experimental one in the sense that the theoretically predicted frequency of the dynamics included only limited number of frequencies while the experimental data exhibited presence of strong components at numerous frequencies over a wide range.

3D time dependent thermal non-equilibrium simulation study by Trelles et al. [31] in 2008 included the external plasma jet but could not reproduce instabilities in the external plasma jet similar to that observed experimentally.

Tu et al. [32] in 2008 investigated the arc instability and dynamic behaviour of DC atmospheric double arc argon plasma jet through the fluctuations of electrical signals in combination with the classical tools, like the statistic method, Fast Fourier transform (FFT) and correlation analysis. The FFT and correlation calculation of electrical signals exhibit the only characteristic frequency of 150 Hz, whereas the high frequency fluctuations are totally disappeared. This fluctuations ware due to undulation of tri-phase rectified power supply independent of operating parameter. Each arc root attachment was found to be evenly diffused in spite of a fixed position on the anode surface. In this study, the effect of the arc instabilities on the exiting plasma jet was not explored.

Pan et al. [33] in 2007 compared the Ar, Ar-H_2 and Ar-N_2 DC arc plasma jets and their arc root behaviour at reduced pressure without or with an applied magnetic field. It was found that in the cases without an applied magnetic field, the laminar plasma jets were stable and found to be axi symmetrical. The arc-root attachment on the anode surface was completely diffusive when argon was used as the plasma-forming gas, while the arc-root attachment often became constrictive when hydrogen or nitrogen was added into the argon. As an external magnetic field was applied, the arc root tended to rotate along the anode surface of the non-transferred arc plasma torch.

Again in 2009, Pan et al. [34] studied variation in arc voltage as a function of chamber pressure and gas flow rate. Jet fluctuation near the torch exit was observed using a high-speed video camera. Power supply oscillation at 300 Hz and Helmholtz oscillation at 3 kHz were the primary instabilities detected. Voltage fluctuations owing to movement of arc root were found to be insignificant in their study for their specially designed torch having large anode diameter. Although, typical images of the plasma plume were presented for different atmospheric and sub-atmospheric pressures. This study also paid no attention to explore the internal structures and stabilities of the exiting plasma plume under different operating conditions.

Vilotijevic et al. [35] in 2009, measured the velocity and texture of a plasma jet created in a specially designed plasma torch with fixed minimal arc length. Velocity was measured by measuring the thrust generated by the plasma jet and by photographing the translation of plasma clouds (parts with different brightnesses) in the last third of the length of the plasma plume. Although texture of the plasma jet was presented for two designs, but inside structure and change of the structure of the plasma jet for different parameters were not revealed in this study.

Nunomura et al. [36] in 2009 presented time dependent gas phase kinetics in a hydrogen diluted silane plasma generated by a capacitive coupled 60 MHz very high frequency discharge in a parallel plate cylindrical configuration in a vacuum vessel. Gas Phase kinetics was studied using plasma diagnostic techniques like quadruple mass spectrometry, optical emission spectroscopy, Langmuir probe method and a laser light scattering method for nano particle abundance monitoring.

Ghorui et al. [37] in 2010 investigated arc dynamics inside dc torches using split anodes.

Colombo et al. [38] in 2010 investigated the behaviour of Hafnium cathodes through high-speed camera (HSC) imaging techniques during the low-current pilot arc phase in plasma arc cutting (PAC) of mild steel plates. But the study didn't reveal stability and structure of the plasma jet in non transferred arc.

Mauer et al. [39] in 2010 presented a review of plasma and particle temperature measurements in thermal spray. The enthalpy probe, optical emission spectroscopy, and computer tomography were used for plasma temperature measurements. In-flight particle temperatures was measured using multicolor pyrometry .

Wua C and Pan W [40] in 2011 reviewed the unsteadiness in non-transferred dc arc plasma generators.

Krwoka etal [41] in 2013 investigated the control of dc arc jet instabilities to obtain a self-sustained pulsed laminar arc jet and addressed instabilities mainly originating from Helmholtz oscillation and restrike modes. For unusually low current and a specially designed cathode cavity it was shown that frequencies under both the modes can be matched to generate a pulsed arc jet. Helmholtz frequency was varied by changing the dimension of the plasma cavity.

Meillot et al. [42] in 2013 investigated the interaction between thermal plasma jet of Ar/H_2 and a continuous liquid jet injection of pure water under suspension plasma spraying by modelling. Interactions during the penetration of the liquid into the gas flow were simulated using only Navier Stokes and heat equations. The film of the interactions depicts a complex breakup with a significant variation in WEBER number.

Trelles [43, 45] in 2013, 2014 performed time-dependent three-dimensional modelling of the anode attachment spots in the free-burning arc including thermal non-equilibrium and reported effect of anode cooling on pattern formation and self-organization. Major drawback of these simulation studies is that the pattern formation and self-organization are reported to be highly dependent on the choice of computational grid. For example, as one shifts from base mesh to certain fine mesh, the number of anode attachment points changes from 10 to 27 [Figure9 of Ref.43].

Mantry et al.[45] in 2013 presented on line monitoring of temperature and velocity of the powder particle during yttria stabilized zirconia (YSZ) coatings by plasma spraying process using Spray watch system2i. Spray watch system measures particle parameters in small measurement volume and gives distribution, but it couldn't not track single particle trajectory and measures the velocity upto coating distance.

2.2 Unprobed significant area

It is obvious from literature survey that assumption made so far is the existence of only one anode arc root and observed voltage instabilities is explained as a consequence of the movement of this single arc root. The models assume that no part of the arc extends beyond the exit of the plasma torch and considers the external plasma jet as current free.

Following are the unprobed significant areas so far which need to be addressed which will be useful for process optimization, and benchmarking of future theoretical models:

A) Direct probing of the arc root dynamics in non transferred DC plasma torch

B) Thorough experimental investigation of the arc plasma plume for its stability and structure under different operating conditions is due for long time.

C) Effect of cooling rate on torch efficiency and plasma dynamics of the non transferred torch

D) Plasma kinetics in wire arc spray

E) Chemical kinetics in the thermally non equilibrium Argon plasma jet and mechanism for synthesis of Y_2O_3 nanoparticles in dc arc plasma.

2.3 References

1. Pfender, E., Fincke J. and Spores R., "Entrainment of cold gas into thermal plasma jets", Plasma Chemistry and Plasma Processing, I1, 529-543 (1991)
2. Coudert, J.F., Planche, M.P., and Fauchais, P., "Characterization of d.c. plasma torch voltage fluctuations", Plasma Chemistry, and Plasma Processing, 16, 211S-227S (1996)
3. Dyuzhev, G. A., Mitrofanov, N. K., and Shkolnik, S. M., "Experimental investigation of the anode region of a free-burning atmospheric-pressure inert-gas arc I. General characteristics of the discharge. Low-current regime," Tech. Phys. 42, 30-34 (1997).
4. Baksht, F. G., Dyuzhev, G. A., Mitrofanov, N. K., and Shkolnik, S. M., "Experimental investigation of the anode region of a free-burning atmospheric-pressure inert-gas arc. II. Intermediate current regime—multiple anode constriction," Tech. Phys. 42, 35-38 (1997).
5. Planche M. P., Coudert J. F., and Fauchais P., "Velocity measurements for arc jets produced by a dc plasma spray torch", Plasma Chemistry and Plasma Processing, 18, 261-283 (1998).
6. Pfender, E. "Thermal plasma technology: where do we stand and where are we going ?", Plasma Chem. Plasma Process. 19 1–31, (1999).
7. Fauchais, P. and Vardelle, A., "Pending problems in thermal plasmas and actual development", Plasma Phys. Control Fusion 42, B365-B383 (2000)

8. Hrabovsky, M., "Effect of anode attachment on flow structure in plasma jet generated in dc plasma torch" Annals New York Academy of Science (1999)

9. Ghorui, S., Sahasrabudhe, S. N., Murthy, P. S. S., Das, A. K., and Venkatramani, N., "Experimental evidence of chaotic behavior in atmospheric pressure arc discharge", IEEE Trans. on Plasma Sci. , 28, 253 (2000)

10 Pan, W, Zhang, Wenhua., Zhang, Wenhong and Chengkang, Wu, "Generation of long, laminar plasma jets at atmospheric pressure and effects of flow turbulence" Plasma Chemistry and Plasma Processing, 21, 23-35 (2001).

11. Dorier, J. L., Gindrat, M., Hollenstein, C., Salito, A., Loch, M., and Barbezat, G., "Time-resolved imaging of anodic arc root behavior during fluctuations of a dc plasma spraying torch", IEEE Trans. Plasma Sci., 29, 494-501 (2001)

12. Zhao, M., Owano, T. G. And Kruger, C. H., "Optical diagnostics of an atmospheric pressure diamond – depositiong DC plasma reactor", Diamond and Related Materials 10, 1565-1568 (2001)

13. Amanatides, E. , Stamou, S. and Mataras, D., "Gas phase and surface kinetics in plasma enhanced chemical vapour deposition of microcrystalline silicon: The combined effect of rf power and hydrogen dilution", Journal of Applied Physics, 90, 5786-5798 (2001)

14. Zhao, W., Kuo T., Huangzai T., Di Liu and Guanzhong Z., "Experimental studies on the unsteadiness of atmospheric pressure plasma jet", J. Phys. D: Appl. Phys. 35, 2815–2822(2002)

15. Ghorui, S., Sahasrabudhe, S. N., Murthy, P. S. S., Das, A. K., and Venkatramani, N., "Estimation of dynamic properties of attractors observed in hollow copper electrode atmospheric pressure arc plasma system", PRAMANA

J. Phys.. 59, 143(2002)

16. Duan, Z., and Heberlein J., "Arc instabilities in a plasma spray Torch", Journal of Thermal Spray Technology, 11, 41-51(2002)

17. Chen, Xi. , Ping, Li. He., "Three-dimensional flow and heat transfer in thermal plasma systems", Surface and Coatings Technology 171, 124–133, (2003)

18. Ghorui, S. and Das, A. K., "Origin of fluctuations in atmospheric pressure arc plasma devices", Phys. Rev. E 69, 026408 (2004)

19. Iwao, T., Cronin, P., Bendix, D., and Heberlein, J. V. R., "Anode attachment stability and anode heat transfer for high intensity arcs with lateral gas flow", IEEE Trans. Plasma Sci. 33, 1123–8, (2005)

20. Nemchinsky, A. Valerian., "Anode layer in a high-current arc in atmospheric pressure nitrogen," J. Phys. D: Appl. Phys. 38, 4082–4089 (2005)

21 Trelles, J. P., Pfender, E., Heberlein,J., "Multiscale Finite Element Modelling of Arc Dynamics in a DC Plasma Torch," Plasma Chem. Plasma Process. 26, 557–575 (2006).

22 Moreau, E., Chazelas, C., Mariaux, G. and Vardelle, "A Modelling the restrike mode operation of a dc plasma spray Torch", J. Therm. Spray Technol. 15 524—30(2006).

23 Yang, G., Cronin, P., Heberlein, J. V., and Pfender, E., "Experimental investigations of the anode boundary layer in high intensity arcs with cross flow," J. Phys. D: Appl. Phys. 39, 2764–2774(2006).

24 Chazelas, C., Moreau, E., Mariaux, G., and Vardelle A., "Numerical modelling of arc behaviour in a DC plasma torch",High Temp. Mater. Process. 10, p 393-

406(2006).

25. Redwitz, M., Dabringhausen, L ., Lichtenberg, S., Langenscheidt, O., Heberlein, J., and Mentel, J., "Arc attachment at HID anodes: measurements and interpretation", J. Phys. D: Appl. Phys. 39, 2160–2179 (2006).

26 Ghorui, S., Sahasrabudhe, S. N., Tak, A. K., Joshi, N. K., Kulkarni, N. V., Karmakar, S., Banerjee, I., Bhoraskar, S. V., and Das, A. K. "Role of arc plasma instability on nanosynthesis", IEEE Trans. on Plasma Sci., 34, (2006)

27 Peters, J., Yin, F., Carlos, F,. Borges, M., Heberlein J and Charles, H.,"Erosion mechanisms of hafnium cathodes at high Current" J. Phys. D: Appl. Phys. 38 1781–1794, (2005)

28 Yang, G. and Heberlein, J., "Anode attachment modes and their formation in a high intensity argon arc", Plasma Sources Sci. Technol. 16, 529–542 (2007)

29 Nogues, E., Fauchais, P., Vardelle, M. and Granger, P., "Relation between the arc-root fluctuations the cold boundary layer thickness and the particle thermal treatment", Journal of Thermal Spray Technology, 16, 919-926 (2007)

30 Trelles, J. P., Heberlein, J. V. R. and Pfender, E., "Non-equilibrium modelling of arc plasma torches," J. Phys. D: Appl. Phys. 40, 5937–5952 (2007).

31 Trelles, J. P., Pfender, E. and Heberlein, J. V. R. "Thermal Non-equilibrium simulation of an arc plasma jet", IEEE Transactions on Plasma Science, 36, 1026-1027 (2008).

32 Tua, X., Yana, J.H., Cheronb, B.G., Cena, K.F., "Fluctuations of DC atmospheric double arc argon plasma jet" , Vacuum 82, 468–475 (2008).

33 Pan, W., Meng X., Teng L. , Chen X., Chengkang W., "Comparative observation of Ar, Ar-H_2 and Ar-N_2 DC arc plasma jets and their arc root behaviour at reduced pressure", Plasma Science and Technology, 9, 152-158 (2007).

34 Pan, W. X., Guo, Z. Y., Meng, X, Huang, H. J. and Wu, C. K., "Fluctuation characteristics of arc voltage and jet flow in a non-transferred dc plasma generated at reduced pressure", Plasma Sources Sci. Technol. 18, 045032 (2009).

35. Vilotijevic, M., Dacic, B. and Bozic, D. "Velocity and texture of a plasma jet created in a plasma torch with fixed minimal arc length", Plasma Sources Sci. Technol. 18, 015016, (2009)

36 Nunomura, S.,Yoshida, I. and Kondo, M., "Time dependent gas phase kinetics in a hydrogen diluted silane plasma" Applied Physics letters, 94, 071502, (2009)

37 Ghorui, S., Sahasrabudhe, S. N. and Das, A. K., "Current transfer in dc non-transferred arc plasma torches" J. Phys. D: Appl. Phys.,43, 245201, (2010)

38 Colombo, V., Concetti, A., Ghedini, E. and V Nemchinsky "High-speed imaging investigation of transition phenomena in the pilot arc phase in Hf cathodes for plasma arc cutting", Plasma Sources Sci. Technol. 19, 065025, (2010)

39 Mauer, G., Vaben, R., and Stover, D., "Plasma and Particle Temperature Measurements in Thermal Spray: Approaches and Applications", Journal of Thermal Spray Technology, Volume 20, 391-406, 2011

40 Wua, C., and Pan, W., "Unsteadiness in non-transferred dc arc plasma generators", Theoretical & Applied Mechanics Letters 2, 024001 (2011)

41 Krowka, J., Rat, V. and Coudert, J. F. "Investigation and control of dc arc jet instabilities to obtain a self-sustained pulsed laminar arc jet", J. Phys. D: Appl. Phys. 46, 505206, (2013)

42 Meillot, E., Vincent, S., Caruyer, C., Damiani, D. and Caltagirone, J. P., "Modelling the interactions between a thermal plasma flow and a continuous liquid jet in a suspension spraying process", J. Phys. D: Appl. Phys. 46, 224017, (2013)

43 Trelles, J. P., "Formation of self-organized anode patterns in arc discharge simulations," Plasma Sources Sci. Technol. 22, 025017 (15pp) (2013).

44 Mantry, S., Mishra, B. K. and Chakraborty, M. "Parametric appraisal of process parameters for adhesion of plasma sprayed nanostructured YSZ coatings using taguchi experimental design" Hindawi Publishing Corporation The Scientific World Journal, Volume 2013, Article ID 527491

45 Trelles, J. P., "Electrode patterns in arc discharge simulations: effect of anode cooling," Plasma Sources Sci. Technol. 23, 054002 (16pp) (2014)

Chapter-3
Experimental Setup

Outline of the Chapter

3.1 Introduction

3.2 Experimental Setups

3.3 Plasma Torches

3.4 Power Supply

3.5 Chilled Water Supply Unit

3.6 Diagnostics Systems

- 3.6.1 High Speed Camera
- 3.6.2 High Resolution Spectrograph
- 3.6.3 Spray Watch System
- 3.6.4 Digital Storage Oscilloscope
- 3.6.5 Voltage Divider Circuit
- 3.6.6 RTD and Digital Thermometer

3.7 Feeder Unit

- 3.7.1 Wire Feeder Unit
- 3.7.2 Powder Feeder Unit

3.8 References

Chapter 3

Experimental Setup

3.1 Introduction

Experiments were performed to investigate gas phase kinetics macroscopically (arc root dynamics, plasma jet dynamics, reproducibility of a high electro thermal efficiency at a certain cooling rate, kinetics of arc plasma jet in transferred arc single wire arc spray system) as well as microscopically(identification of species axially in jet of argon plasma and yttria-argon plasma, possible mechanism of synthesis of nanopowder). A simple DC plasma torch consists of two electrodes: a cathode and an anode. Depending on the particular application, plasma torches appear in different designs. Their suitability for a specific application is decided by plasma parameters like temperature, heat flux, plasma dimension, plasma volume, plasma constituent and its enthalpy content. Experimental setups for investigating dynamics of anode arc root, plasma jet of nitrogen, argon and air, plasma kinetic in transferred arc single wire arc spray using different diagnostics are presented in this chapter. Experimental setup mainly consist of DC plasma torches, power supply unit to power the torch, chilled water supply unit to cool the cathode and anode of the torch assembly, gases used for plasma generation (argon, nitrogen gases, air), wire feeder unit, powder feeder unit and diagnostics equipment like high speed camera, high resolution spectrograph, spray watch system, voltage divider circuit to diagnose the plasma. Images of the plasma jet were analyzed using Matlab software [1]. Voltage signal were analyzed using dynamical tools like phase portrait, FFT, Lypunov exponent. Emission spectra were utilized to identification of species and determining temperature using Boltzmann plot technique.

3.2 Experimental setup

Experimental setups mainly consist of plasma generation in dc arc plasma torches and its diagnostics. Plasma generation system includes DC plasma torches, power supply unit to power the torch, chilled water supply unit to cool the cathode and anode of the torch assembly, gases used for plasma generation (argon, nitrogen gases, air), wire feeder unit for wire feed in single wire arc spray, powder feeder unit to feed powder in the plasma jet. Diagnostics comprises measurement of voltage fluctuation using voltage divider circuit, temperature measurement, species identification, particle velocity measurement using Spray Watch System and high speed camera, capturing image of the plasma jet and it image analysis using image analysis, Voltage signal analysis using different dynamical tools.

Experimental setups for probing dynamics of arc root and plasma jet for air, argon and nitrogen plasma, dynamics of jet in single wire arc spray system and low pressure arc plasma jets during precursor feeding using different plasma diagnostics techniques are presented in following sections. Dynamics of spray particle were also investigated in single wire arc spray process.

3.2.1. Set up for direct probing of anode arc root dynamics

Schematic for investigating evolution of arc root and detection of current in the plasma jet are shown in Figure 3.1a and 3.1b respectively.

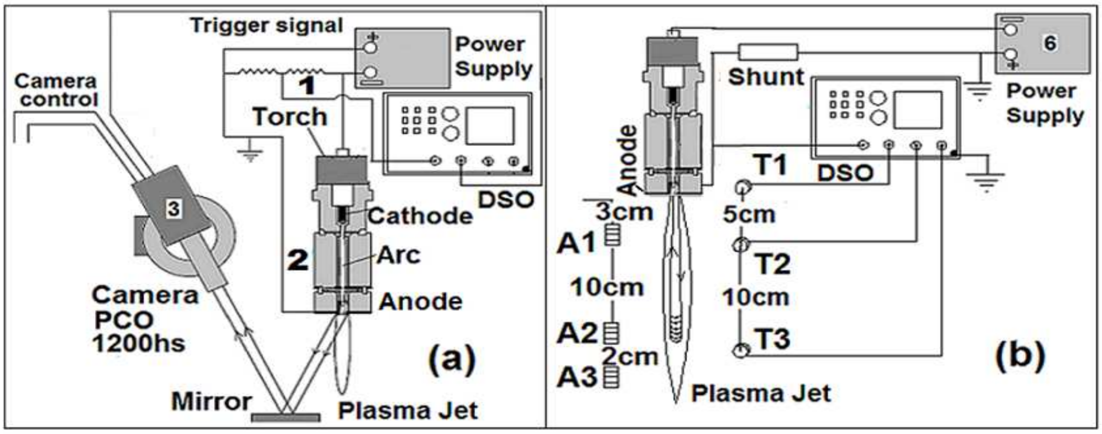

Figure3.1: (a) Schematic of the experimental set up to record the evolution of the arc voltage in a time synchronous manner (b) Setup to detect the current in the exiting plasma jet.

Details of the plasma torch are given in next section [3.3]. With the help of a partially reflecting mirror, part of the interior of the anode exit of a dc non-transferred arc torch is directly viewed by a fast photography camera (FPC) PCO1200hs with a frame rate of 2500 frames s^{-1}. After reduction by the mirror, further reduction in intensity is achieved by reducing the exposure time of the FPC to 20 μs. Being triggered by the camera, a four channel digital storage oscilloscope (DSO, HM03524) recorded the voltage across the arc using a voltage divider circuit ('1' in Figure 3.1(a)) in a time synchronous manner.

For detecting the current in the plasma jet, three transverse coils (T1, T2 and T3: each having 31 turns, length 27 mm, diameter 9 mm, and inductance (L) 70 μH ± 1%) and three axial coils (A1, A1, A3: turns, dimension and L similar to the transverse coils) were placed at specific axial locations, radially 10 cm away from the axis of the jet (Figure 3.2(b)). Inherent instabilities in the current resulted in a change in the associated magnetic flux intercepted by the coils and the generated EMF (electromotive force) in the coils were directly measured by the DSO. With arc current, simultaneous measurements are taken once with the transverse coils and next with the axial coils. The arc current is measured using a shunt (400 A, 100mV), placed in its path. Voltage recorded in the oscilloscope is linearly proportional to the voltage across the shunt.

3.2.2. Setup for investigation of stability and structure in the plasma jet

Schematic of the setup to study stability and structure in the plasma jet for Argon, Air and Nitrogen plasma jet is shown in Figure 3.2. [The plasma torch details are given in section 3.3]. In this setup, instead of imaging arc root, sequence of images of plasma jet, synchronized with voltage signal was captured using high speed camera.

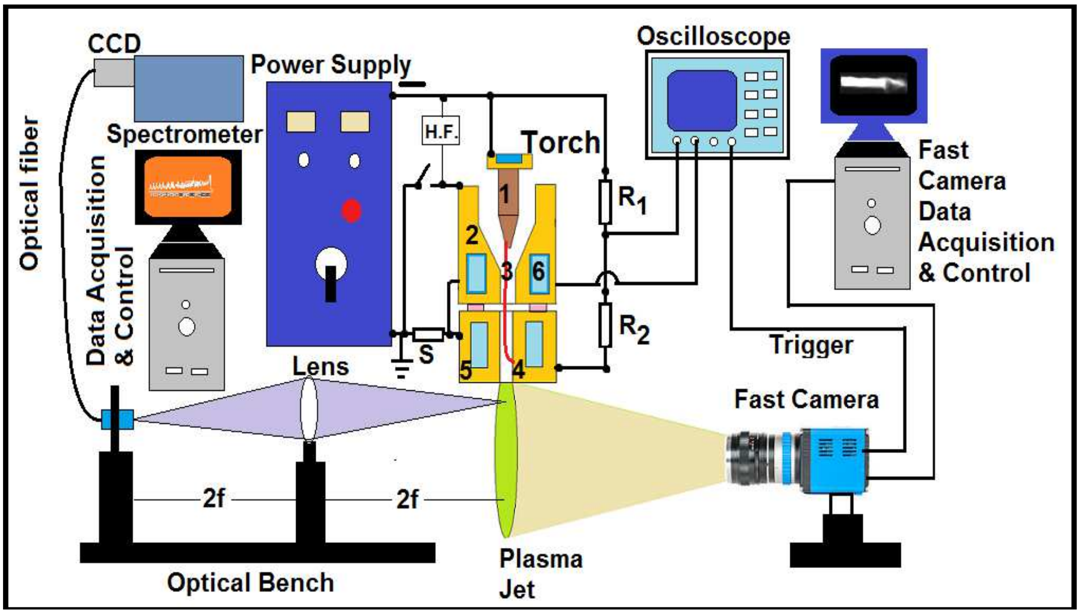

Figure3.2: Schematic of the experimental setup for investigation of plasma jet fluctuation: 1-cathode, 2-auxiliary anode, 3-arc, 4-arc root, 5-main anode, 6-water cooling channels.

Torch uses tungsten cathode for generating nitrogen and argon plasma and hafnium insert cathode for generating air plasma. Emission spectra originating from plasma were captured using optical emission spectroscopy set up given in detail in section 3.6.2. Voltage was measured using potential divider circuit provided in detail in diagnostic section 3.6.6.

3.2.3. Setup for investigation of high electro-thermal efficiency on certain CFR

The experimental setup used to investigate high electro-thermal efficiency at certain water cooling rate in a non-transferred arc plasma torches is shown in Figure. 3.3. The torch details are given in section 3.3. To measure the electro thermal efficiency of the torch, the inlet (T_1) and outlet (T_2) temperatures are measured using RTD (resistance temperature detector) with accuracy better than 0.4%. At some places digital thermometer was also used. The torch is operated with an IGBT based constant current power supply with ripple less than 0.1%. Plasma generation process is same as described in chapter1. To capture kinetics of the plasma, a fast photography camera was used. A four channel digital storage oscilloscope (DSO, HM03524) is used to record the voltage across the arc via a voltage divider circuit consisting of resistances 400 kΩ (R_1) and 11 kΩ(R_2). Details of the oscilloscope and potential divider circuit are given in section 3.6.4 and 3.6.5. The dynamic arc voltage was recorded in a time synchronous manner with the fast photographic snap shots. Trigger signal from the fast camera was used to synchronize the signals. For a given operating power, efficiency of the torch was determined using calorimetric method from the measured water flow rate, inlet and outlet water temperatures. Temperature of the plasma jet was determined from emission spectroscopy. Details of the setup for temperature measurement are described in section 3.6.2.

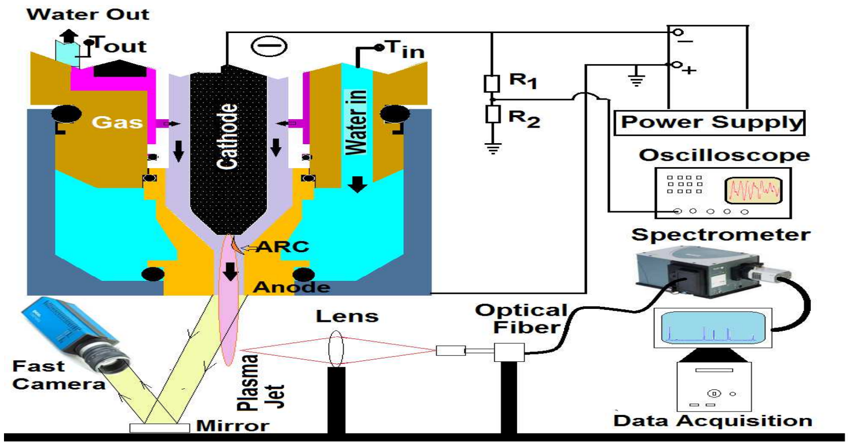

Figure 3.3: Schematic for investigating high electro thermal efficiency.

3.2.4. Set up for kinetic in single wire arc spray process

Schematic of the experimental set up for investigating single wire arc spray process is shown in Figure 3.4a and 3.4b.

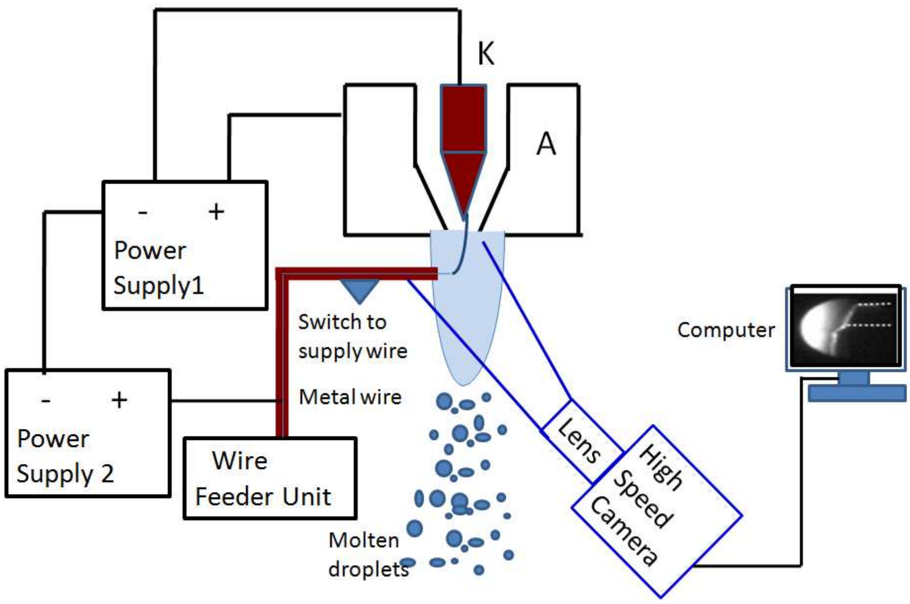

Figure 3.4: (a) Schematic of the Experimental set up for investigating single wire arc spray process.

It is a transferred arc plasma system, used for metallic coating. It consists of a motorized wire feed unit, dc power supplies and a specially designed plasma torch for single wire spray application. Details of the transferred arc single wire arc spray torch are given in plasma torches of section 3.3. In the first part of the experiment, camera was focused on anode wire so that the arc to wire attachment, melting of the wire, detachment of molten mass and formation of liquid metal droplet could be observed.

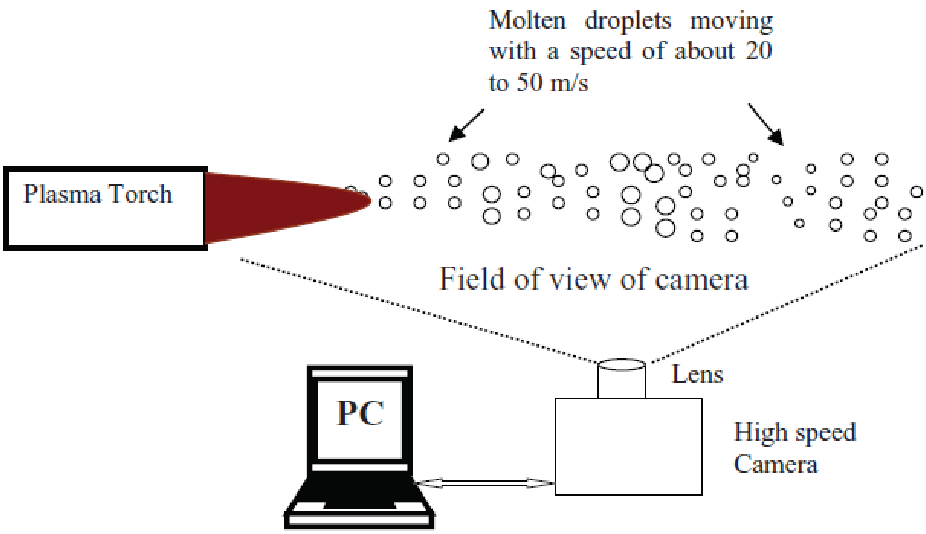

Figure 3.4b: Schematic for measurement of particle velocity.

In the second part of the experiment, sequences of images of the moving, luminous liquid metal droplets were recorded to see particle trajectories as shown in Figure 3.4b. For calibration of the length of the object, a scale was placed near the nozzle and imaged from the camera. Before capturing the images each time, calibration was done.

3.2.5 Setup for in situ probing of chemical kinetics during precursor feeding

Setup for in situ probing of Ar and Ar-Y_2O_3 plasma is shown in Figure 3.5. In this set up, a plasma torch is mounted inside closed chamber and plasma jet is viewed through quartz view port. Pressure of the chamber is kept 10 mbar.A cascaded plasma torch is used to generate plasma. Details of the torch are given in section 3.3. Image of the plasma jet is shown in the inset. Final image of the plasma jet is formed onto a multi-track nine channel fibre (shown in inset separately) using optical lens setup. Emission spectra at nine locations were captured simultaneously using spectrograph (details are in given in section 3.6.)

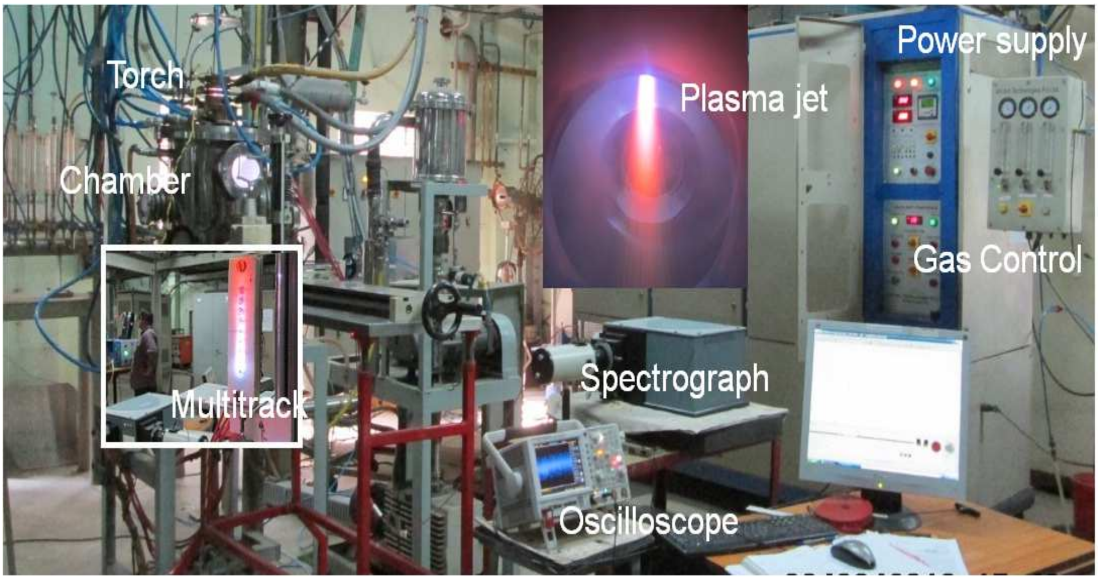

Figure 3.5: Experimental setup for investigation of plasma jet kinetics during precursor feeding in low pressure reactor.

Four channel digital storage oscilloscope (details given in section 3.6.5) was used to capture voltage signal through potential divider circuit (details given in section 3.6.6). High speed camera (details given in 3.6.1) was used to capture the kinetics of the plasma jet during precursor feeding.

3.3 Plasma torches

DC Plasma torch in its simplest form consists of concentric cathode and anode. A gas is passed through the space between the cathode and anode. Initial breakdown of the gas is performed through application of high voltage (kV) at high frequency (~MHz). Bias applied between the electrodes constitutes a current path, called arc. Arc established between the electrodes heats the gas and forms plasma. The plasma comes out from the nozzle exit as a plasma jet. Designs of the torches are different depending on gases used for plasma generation and processing requirement. Study includes four kind of plasma torches developed in L&PTD division. Descriptions of the torches are given in following sections 3.3.1 to 3.3.4.

3.3.1 **Cascaded DC plasma torch**

The torch developed in house was used for generation of nitrogen and argon plasma jet. It consists of seven segments including the cathode and the anode. The intermediate floating anode rings are used to increase the length of the arc between the cathode and the anode. Teflon rings between anode segments were used for insulation. Number of segments was used instead of a single long length anode to avoid double arcing. The tungsten cathode used in the torch can run with non-oxidising plasma gasses like argon and nitrogen. Schematic of the cascaded plasma torch is shown in Figure 3.6.

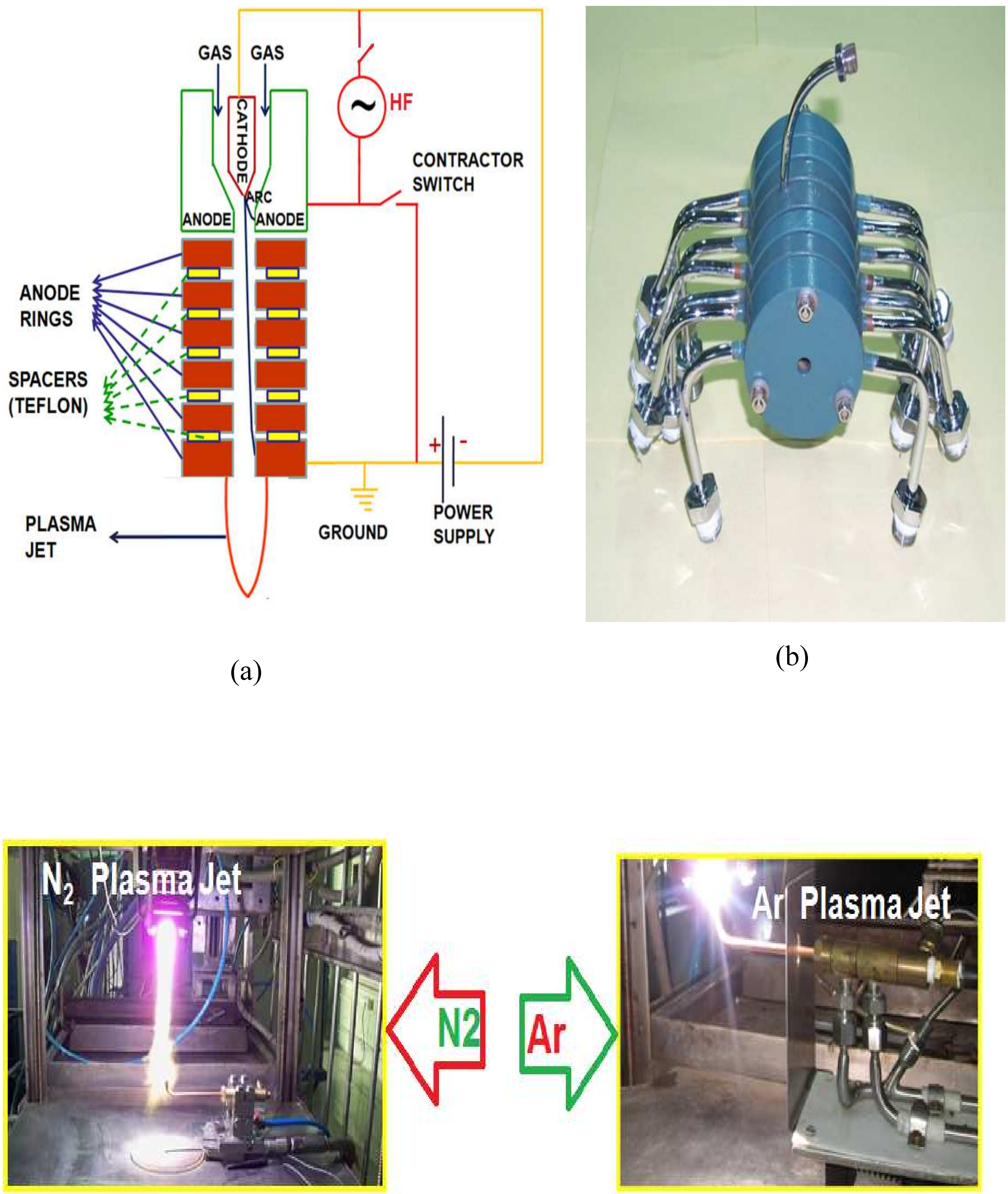

Figure3.6: (a) Schematic of the DC plasma torch (b) Picture of the plasma torch, (c) Torch running with nitrogen (d) Torch operating with argon impinging on the tip of an enthalpy probe.

3.3.2 Air plasma torch

Air plasma torch developed in house is shown in Figure 3.7. Air plasma torch takes filtered air through an air compressor, and converts it into a controlled well-defined jet of air plasma. Low fabrication and operational cost, simple design, use of cheapest gas (air) as the plasma gas, high efficiency (60%-70%), high temperature (7000 K-12000 K at the anode exit), large diameter (20mm-50mm), long plasma jet (150mm-700mm) and ease of control are some of the key features of the present air plasma torch. The design of the air plasma torch and torch in operation is shown in Figure 3.7.

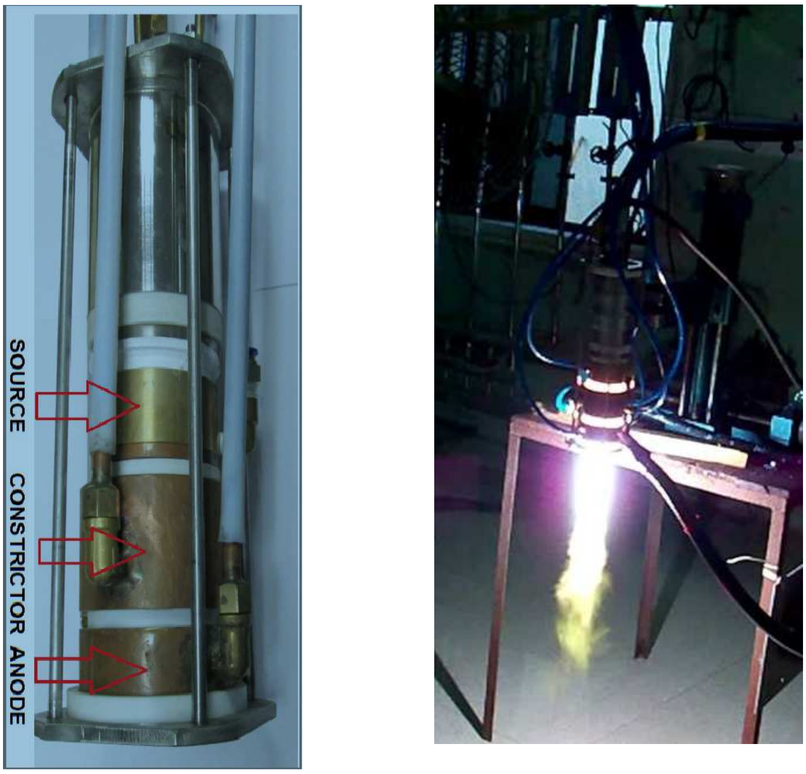

(a) (b)

Figure 3.7: (a) Design of air plasma torch and (b) Air plasma torch in operation.

Air plasma torch has three main sections: (1) plasma source (2) constrictor and (3) main anode. The plasma source section consists of a specially designed hafnium based cathode, gas distributor and coolant distributor. A single coolant loop caters to all the sectors in this section. Plasma (arc) is initiated in this section between the cathode and the nozzle with the help of a radio-frequency igniter (3KV, 3MHz). Once the source is on, the arc is transferred to the constrictor section at low power. The role of the constrictor is to streamline the plasma jet and develop appropriate voltage in the plasma column for operation at a given power level. For a given current and gas flow rate, the power of the plasma jet can be adjusted just by changing length of this constrictor section. The power of the plasma is gradually increased to medium level. Next, the arc is transferred the main anode and full power of the jet is achieved. An extremely bright well formed huge jet comes out from the device as shown in Figure 3.7b.

3.3.3 High efficiency low power (HELP) torch

This is a low power, high efficiency dc plasma torch developed in house. It is specially designed for low power operation. Such torches are suitable for UF_6-UF_4 conversion. The schematic of the torch design and image is shown in Figure 3.8. The torch is operated with argon. It uses 2% thoriated tungsten cathode with diameter 10 mm and tip angle 60^0. The conical anode is made of copper having exit bore diameter of 4 mm and a straight portion of length 12mm in the nozzle exit. The torch possesses a single inlet port and a single outlet port for cooling water, supplied by a chiller unit at a specified temperature. The cooling water first goes to the cathode section and then enters into the anode section. A flow meter measures the water flow rate with accuracy better than ±0.1 lpm (litre per min). The inlet (T_1) and outlet (T_2) temperatures are measured using RTD (resistance temperature detector). The torch is operated with an IGBT (Insulated Gate Bipolar Transistor) based constant current power supply with ripple less than 0.1%. Plasma generation process is same as described in Chapter1.

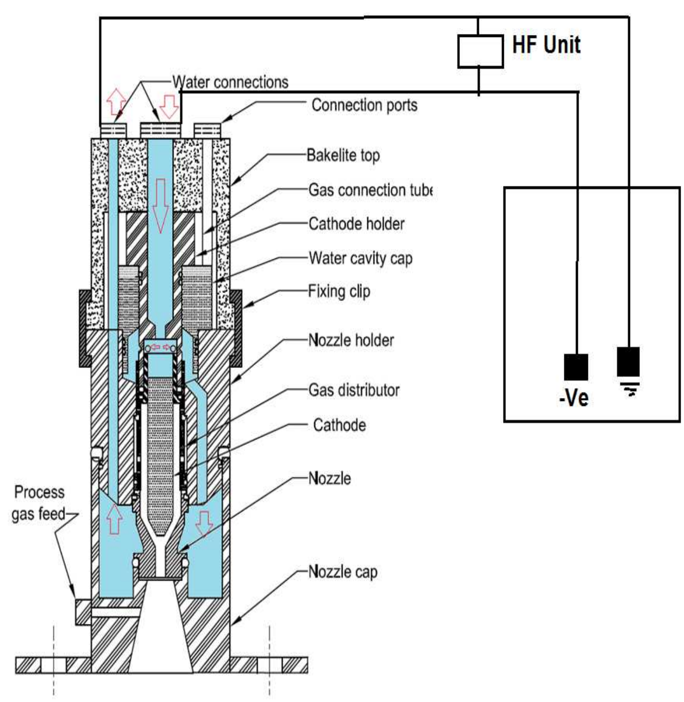

(a)

(b)

Figure3.8: (a) Design of HELP torch and (b) Picture of in house developed torch.

3.3.4 Transferred arc single wire arc plasma spray (SWAPS) torch

SWASP torch is a transferred arc torch in which high current arc is sustained between a continuously fed metal wire and cathode of a plasma torch. The plasma torch is usually started with a pilot arc struck between cathode and an auxiliary nozzle anode and a small low power plasma jet comes out of the torch. After this, a high current arc (called as transferred arc) is established between the cathode and the tip of the wire fed continuously by a wire feeding machine. This transferred arc is sustained by adjusting proper wire feed rate and the arc current. This high current arc rapidly melts the tip of the wire and the high temperature (~ 6000 K to 12000K [8]), high speed (~ 100 to 400 m/s which can be calculated using gas flow rate and its expansion due to high temperature) plasma jet emanating from the nozzle anode, atomizes molten wire mass and accelerates the molten metal droplets ('particles' as popularly termed in spray technology) towards the substrate kept at a distance of few centimetres from the nozzle. Single wire arc spray process and picture of the single wire arc spray torch is shown in the following Figure3.9.

(a)

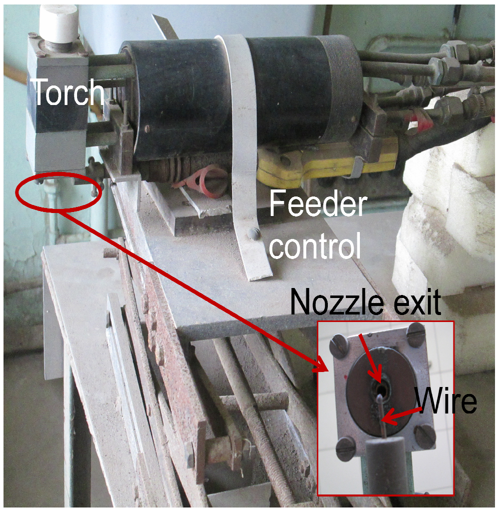

(b)

Figure 3.9: (a) Wire arc spray process and (b) Wire arc spray torch

3.4 Power supply

High power DC power supply embedded with 3kV, 3MHz power supply was used to ignite the plasma. An IGBT based constant current DC power supply is used to provide the necessary power to generate the plasma (Ion Arc Technology Pvt. Ltd.) [2]. Cathode of the torch is connected to negative terminal and anode is connected to positive terminal of the DC power supply. Image of the power supply and its control units is shown in Figure 3.10. The power source can provide 100 kW of DC electrical power at its full capacity. A gas control unit is also attached with the power supply. The power supply has an inbuilt HF electric field generator. The HF unit can produce peak voltage of 3000 V at a frequency of 3 MHz which initiates the pilot arc. The specification of the power upply and the embedded HF electric field generator are given in Table 3.1 and Table 3.2 respectively

Figure 3.10: High power constant current power supply unit.

Table-3.1: Power supply specification

Manufacturer	Ion Arc Technology. Pvt. Ltd.
Power supply output specification	
Maximum power output	100 kW(ripple<2%)
Open circuit voltage	375 V DC
Max load voltage	100V DC
Max load current	1000A DC
Min load current	150A DC
Power supply input specification	
Input voltage	415V AC
Phase	3ø
Frequency	50Hz
Coolant unit specification	
Pump specification	
Input voltage	230V
Frequency	50Hz
Power	0.5 Hp
Compressor Specification	
Input voltage	415V
Phase	3ø
Frequency	50Hz
Capacity	5TR
Coolant tank specification	
Storage capacity	125L

Table-3.2 Specification of HF unit and gas control unit

High frequency (HF) electric field production unit	
Input voltage	230 V
Input current	5A
Type	1 ø
Output voltage	3000 V (3 kV)
Output current	~ 1A
Frequency	3 MHz
Operating mode	Auto and Manual
Time duration for which HF electric field is applied	1 s (In auto mode) and 3 s in manual mode)
Pressure guage (3 numbers)	
Minimum pressure reading	0 psi or 0 kg/cm^2
Maximum pressure reading	200 psi or 14 kg/cm^2
Mininmum pressure measurement	5.0 psi or 0.25 kg/cm^2
Precision	5.0 psi or 0.2 kg/cm^2
Flow meters (3 numbers, two for argon and one for nitrogen)	
Minimum reading	0.0 slpm
Maximum reading	50.0 slpm
Minimum measurable flow rate	5.0 slpm
Precision	1.25 slpm

3.5. Chilled water supply unit

Since plasma temperature is very high. In the core region it goes up to 10000K. At this much high temperature it can melt and evaporate any material even the plasma torch component. Therefore for smooth working of the torch, components of the torch are water cooled. Cooling is provided by a chilled water supply unit. Schematic of the chiller water supply unit and its image is shown in Figure 3.11 and 3.12. It consists of two pumps of capacity 3 Hp and 10 Hp respectively, a water tank of capacity 500 litres and three heat exchangers to cool the water in the tank. This is a centralized coolant supply unit for various experimental systems; one loop of the chilled water supply system is used to circulate chilled water to the torch and other parts of the experimental setup. The possible minimum obtained coolant temperature is 5^{o}C. The inlet water temperature is set at 27^{O}C cool the component of the torch. Technical details of the chilled water supply unit are given in Table 3.3.

Table-3.3: Chilled water supply unit specification	
Parameter	Value
Inlet temperature	35 - 40^{0} C
Outlet temperature	5 ^{0} C to ambient temperature
Temperature stability	± 0.5^{0} C
Refrigeration load	30 TR (105 kW)
Fluid	Demineralised water
Flow rate	50-200 LPM (140 slpm nominal)
Power	25 kW
Electrical specification	
Power supply	415V ± 10%, 3phase, 50Hz

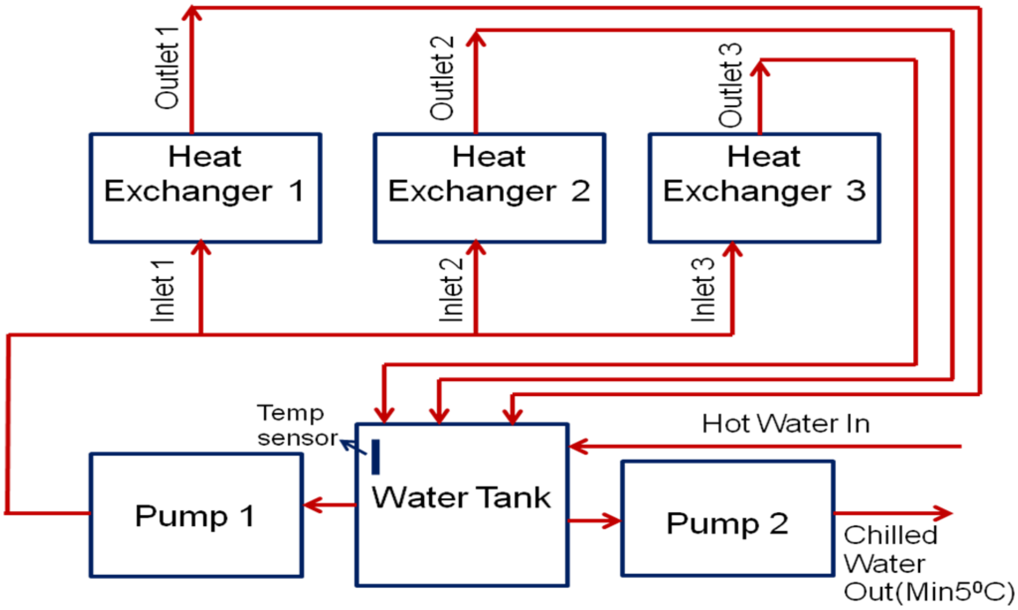

Figure 3.11: Schematic of the chilled water supply unit

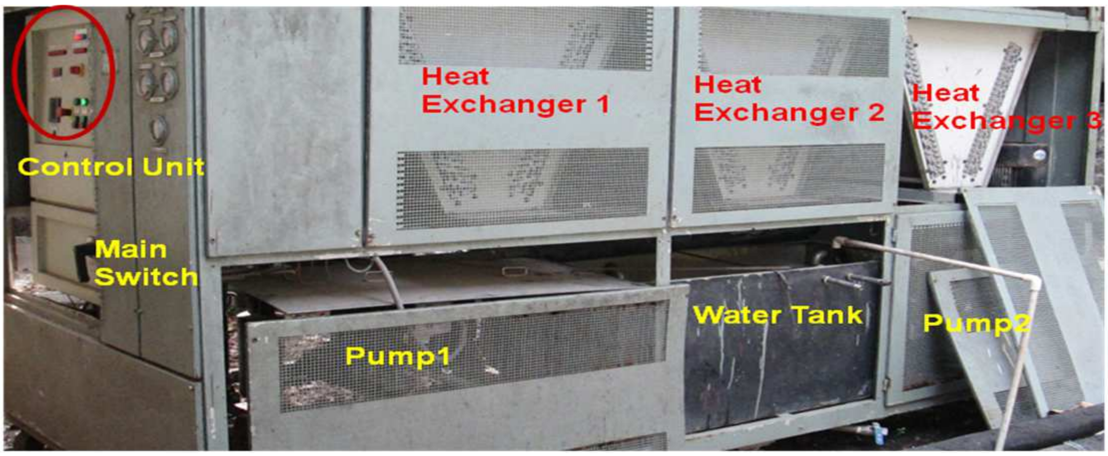

Figure 3.12: Chilled water supply unit

Pump1 circulates water to heat exchanger 1, 2 and 3. Heat exchanger cools the water supplies cooled water to tank from three sides. Using pump1 chilled water is supplied to the system for cooling. Hot water coming from the system is allowed to fall in the water tank where it mixes with cooled water. A temperature sensor is installed in the water tank to set the temperature. As soon as temperature crosses the set limit it gives signal to switch on heat exchangers.

3.6 Diagnostics system

Plasma dynamics were studied using various diagnostic systems like high speed camera, high resolution spectrograph, spray watch system, digital storage oscilloscope, potential divider circuit etc. Details of the diagnostics system is given in following subsections.

3.6.1 High speed camera:

High speed camera (Model No PCO 1200hs, 1280 X 1024 pixels CMOS sensor) was used to visualize fast occurring phenomena in the plasma like plasma jet fluctuation, arc root movement, particle movement in single wire arc spray system etc[3]. Frame rate can be adjusted from 600 FPS to 2000 FPS. The PCO camera system consists of

A) A camera with a digital image output(1394 port is used for interface)

B) Power supply(pco power)

C) Image processing and camera control software named camware

D) A compact lens(Nikon: AF Zoom Nikkor, 28-200mm, f/3.5-5.6D) used to focus, zoom and intensity reduction of the desired image.

A) PCO 1200 camera

A camera with a digital image output(1394 port is used for interface): Inside the camera, photons are converted into charges by the image sensor. After multiple shift process these charges are analogue processed and converted into digital signals. They are then transferred at very high data rates into the primary image memory of the camera(160MB/s). Using data interface(1394 interface) data is transferred to personnel computer. Front and rear view of camera are shown in Figure 3.13A.

(a)

(b)

Figure 3.13A: (a) Front view of camera (b) Rear view

B: Power supply

The power supply provides required voltage to the camera and controls the preset temperature at the image sensor. For exposure control it has all the external trigger connections. Front and rear view are shown in Figure3.13B. Trigger signal of 5V from camera exposure is used to trigger oscilloscope.

(a)

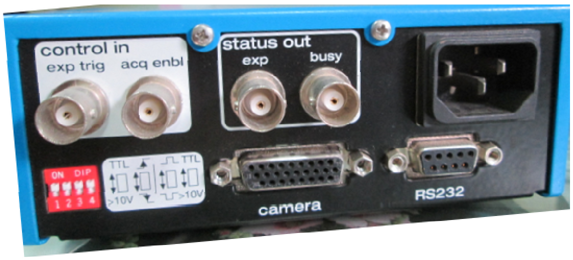

(b)

Figure3.13B: (a) Front view of Power supply (b) Rear view for hardware controls interface.

C: **Image processing and camera control software named camware**

Image processing and camera control is done using camware software. The camera control window is the main interface for all camera settings. Using camera control option in the software, various imaging parameters like exposure time, CCD pixel selection, memory, trigger can be set to desired value. Number of frames per second can be adjusted by number of pixel used for capturing image of CCD. Sequence of images recorded in the camera memory is transferred to the personnel computer.

D: **Compact lens**

Focal length can be varied from 28 mm to 200mm in scale of 28mm, 35mm, 50 mm, 70 mm, 85 mm,105 mm,135 mm and 200 mm. In normal focusing, it can focus from 2m to ∞. For macro focusing, it can focus from 2m to .85m at 28mm and 2m to 1.5m at 200mm. Zoom control and focus control can be done using zoom ring. Image of Nikkon lens used is shown in Figure 3.13D.

Figure 3.13D: Nikkon lens

3.6.2 Spectrograph

Spectrograph (Model Shamrock 303i A, CCD DU and HR4000) are used for identification of species, measurement of temperature and density of the plasma [3, 4].

3.6.2.1 Basic principle: Basic principle for working of spectrograph and actual image are shown in Figure 3.14.

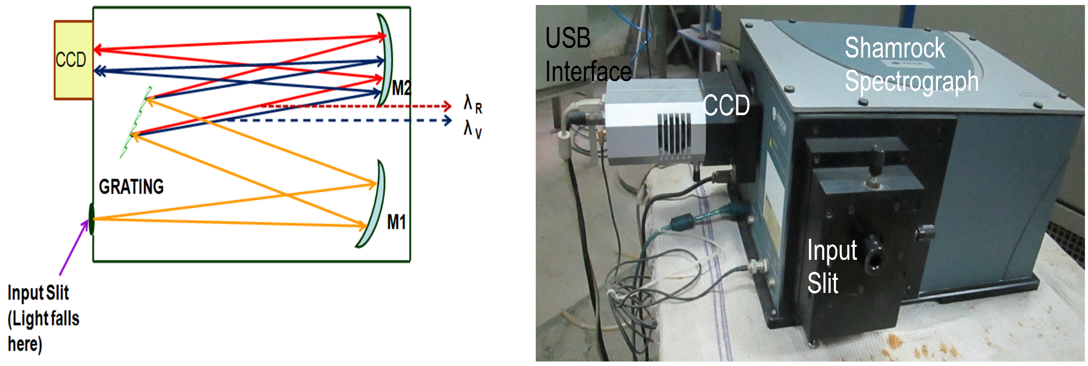

(a) (b)

Figure 3.14: (a) Working of spectrograph and (b) Spectrograph image

It consists of

A) **Input slit:** Light emitted from the source is allowed to fall on the input slit of the spectrograph through lens arrangement. It is fitted on the focal plane of the mirror M1. Slit width can be varied from 10 µm up to 2500µm depending on the optical signal.

B) **Mirror M1:** This mirror is at the focus of the slit. This mirror is tilted so that it reflects parallel light to the grating.

C) **Grating:** Grating diffracts light of different wavelength at different angle (according to Braggs law $2d\sin\theta = n\lambda$, where θ is the angle of diffraction and λ is wavelength) falls on mirror M2.

D) **Mirror M2:** Light from the grating falls at different angle on the focusing mirror M2. Mirror M2 focuses the light of different wavelength at the different location on Charge Coupled Device(CCD).

E) **Charged Coupled Device (CCD):** A charge coupled device is placed at the focal plane of the mirror M2. A charge coupled device is used to convert optical signal into electrical signal.

F) **Signal processing and spectrograph control software named AndorIdus**

After signal processing, the emission spectra are collected on PC using USB interface and software controlling spectrograph. Software facilitates controlling the various parameters of the spectrograph. These parameters include online selection of input slit width, gratings, exposure time and viewing online and capturing emission spectra etc.

For carrying the optical source information to the input slit, optical fibre is used. There are two operating modes for operation

(i) **Spectrograph with single fibre setup:** It is simple and optical signal is directly allowed to fall on the input slit. It is used for capturing signal at one particular location at a time.

(ii) **Spectrograph with Multi-track fibre set up:** In this mode, signal from different locations can be collected simultaneously. Setup for multi track is shown in Figure 3.15 for experimental set up. In multi track fibre assembly set up, image of the optical source falling on the multi track is magnified using F# matcher. F# matcher reduces stray light by matching the output angle of the fibre to the input angle of the spectrograph. It magnifies the image keeping quality intact in terms of spectral and spatial. Image of the source at different locations is formed on the CCD plane as shown in the following Figure 3.15. Dimensions of the track (pixels) need to be defined for images capturing in image mode of the software. After defining the tracks emission spectra is captured in multi track mode. This set is excellent for investigating kinetics in the highly unstable plasma.

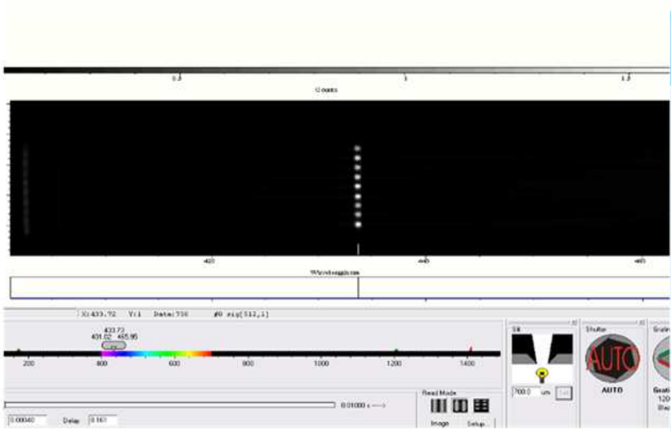

Track	Y1	Y2
1	44	54
2	60	70
3	75	85
4	89	99
5	106	116
6	122	132
7	137	147
8	152	162
9	168	178

Figure 3.15: Image of multi track on CCD and track location (pixel position). Y1 and Y2 are lower and upper position of a fibre on Y axis.

In Figure 3.15, difference between Y1 and Y2 gives numbers of pixel covering the area of the single fibre tip. Track 1, 2, 3 are the fibre numbers. One tip of the fibre covers almost 10 pixel height. Gap between two fibres is 5 pixels on CCD. This 5 pixel gap corresponds to 9 mm on actual scale. So there is no overlapping between two locations. Distance between two locations of the fibres is 9mm**.**

3.6.2.2 Calibration of spectrograph

For identification of proper emission lines, calibration of the spectrograph is required. Calibration of spectrograph was done using a standard Hg-Ar lamp. There are standard lines in the emission coming from Hg-Ar lamp. The wavelengths of these spectral lines from a standard Ar-Hg lamp were recorded by the spectrograph for different gratings 300l/mm, 1200l/mm and 2400l/mm. Difference in the wavelength between standard lines and recorded line give the wavelength shift. This shift was measured in the entire wavelength range of the lamp (400 to 900 nm). Wavelength shifts for different grating used are given in the Table-3.4.

Table-3.4: Shift in wavelength

Grating used	Shift
300 l/mm	2.4 nm
1200 l/mm	1.7 nm
2400 l/mm	0.7 nm

3.6.2.3 Principle of plasma temperature measurement

Intensity emitted by the plasma is given by

$$I_{ul} = \left(\frac{1}{4\pi}\right) A_{ul} n_u h v_{ul} L \qquad 3.1$$

where I_{ul} is the intensity of the line radiation, A_{ul} is the transition probability from E_u to E_l, n_u is the population of upper energy level E_u, ν_{ul} is the frequency of the radiation emitted, h is Plank's constant, L is the size of the plasma

Population density n_u in a state 'u' is related to the population density of the ground state n_0 by

$$n_u = \frac{n_0 g_u e^{\left(-\frac{E_u}{kT}\right)}}{Q} \qquad 3.2$$

Here Q is the partition function defined as sum over all the states and is given by

$$Q = \sum_u g_u e^{\left(-\frac{E_u}{kT}\right)} \qquad 3.3$$

Substituting Value of n_u

$$I_{ul} = \frac{hLn_o g_u A_{ul} e^{\left(-\frac{E_u}{kT}\right)}}{4\pi Q \lambda_{ul}} \qquad 3.4$$

Where λ_{ul} is the wavelength of emission line.

Taking log on both sides

$$ln\left(\frac{I_{ul}\lambda_{ul}}{g_u A_{ul}}\right) = ln\left(\frac{Lhn_0}{4\pi Q}\right) - \frac{E_u}{kT} \qquad 3.4$$

If we take several lines from the same species, Q is common, L (size of plasma) is common and they will cancel out in the ratios of their intensities. Plot of ln $\{(I_{ul}\,\lambda_{ul}) / (g_u\,A_{ul})\}$ and E_u will be a straight line with slope $-1/kT$.

Once the slope is determined experimentally, the temperature T can be determined.

Typical argon spectra and Boltzmann plot is shown in Figure 3.16 and 3.17

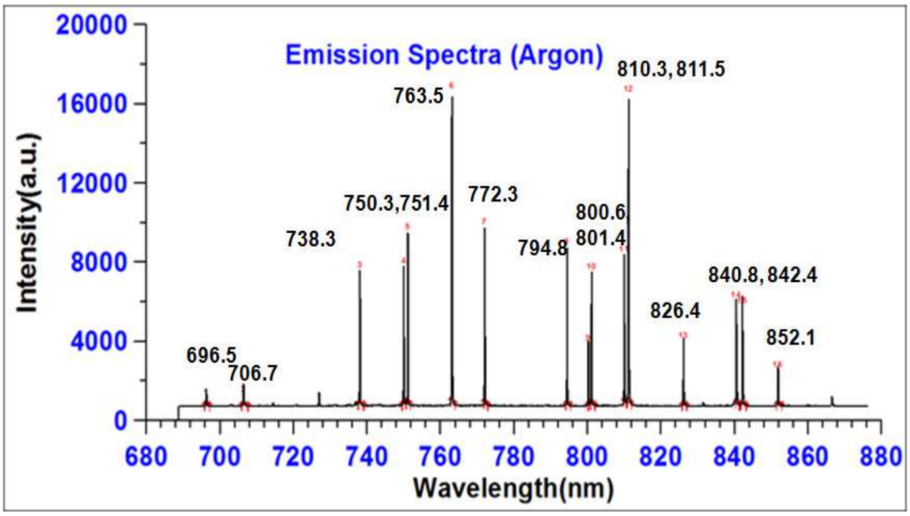

Figure3.16: Emission spectra for Argon atomic lines.

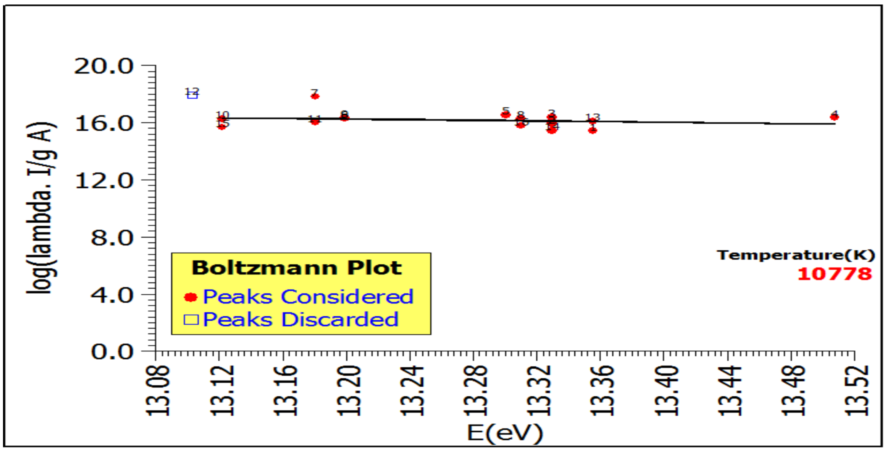

Figure 3.17: Typical Boltzman plot.

3.6.3 Spray watch system

Spray watch system (Model spray watch 2i, Oseir Finland) is an on-line, in-process measurement of most important spray and particle parameters of thermal spray process [5]. Image of the particle is focused on the CCD using focusing arrangement. It images the particle flow and measures the most important parameters velocity and surface temperature of the particles just before they form the coating on the target surface. The system is based on modern CCD camera and image processing technology. It consists of

A) Camera unit and

B) PCI card to be installed in PC and Spray Watch software-2i and

C) Air preparation unit

A) Camera unit: This is main part of the system. It is a special type of CCD camera. The CCD chip size is 1392X1024 pixel sizes. CCD is divided into two parts. One part is used for velocity measurement and Second part is used for surface temperature measurement. Double filter is used to get the intensity for those wavelengths only. Particle is imaged by CCD camera. Optical Stripe Filter enables simultaneous measurement of particle velocity and temperature using a single CCD camera.

B) PCI card and Spray Watch software2i: Control card is fixed into the PCI slot of the computer and Spray Watch software is installed. The software is used to display, and record the spray parameter online. The distance between the spray and the camera unit can be adjusted from 185 mm to 400 mm using software. Depth of field, exposure time for velocity measurement and temperature measurement can be adjusted using software. CCD of the spray watch system is divided in two parts. First part is used for measurement of velocity of the particle and second part is used for measurement of surface temperature of the particle. A Digital image processing algorithm developed by Oseir detects the particles.

D) Air preparation unit: This unit is used to cool the electronics inside the camera and purge the window. It is a two stage filtration unit. It consists of a pre-filter (used to remove wet and dry particles bigger that about 30 μm) and a fine filter used to remove particles down to 0.01 μm. Oil free air compressor is used to supply oil free air to input of pre-filter.

Schematic of the particle velocity and temperature measurement using spray watch and a photograph showing set up of the camera are shown in the following Figure 3.18.

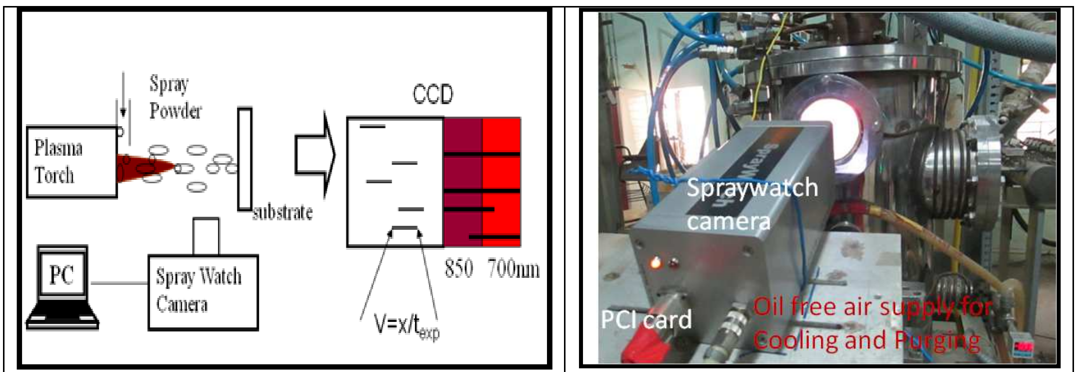

(a) (b)

Figure 3.18: (a) Schematic of the particle velocity and temperature measurement using spray watch. (b) Camera in operation for a low pressure plasma spray system

(i) Particle velocity measurement: Velocity of particle is measured by time-of-flight method. Particle forms a streak in a set exposure time. Distance travelled in set exposure time divided by the exposure time gives the particle velocity. Range of measurement is 10 - 1000 m/s and resolution ~ 0.5 m/s.

(ii) Particle surface temperature measurement: Optical stripe filters (wavelengths 850nm and 700nm) enables measurement of particle temperature. The spray is imaged through the filters using 1-10 ms exposure time. Average temperature of particles is measured by two-color pyrometry at wavelenghts 700 and 850 nm. Intensity emitted by the partcile is collected through theses two wavelength filters. Surface temperature of the particle is detremined by follwing formula:

$$T_p = \frac{(\lambda_1 - \lambda_2)}{\lambda_1 \lambda_2 ln[\left[\left(\frac{\lambda_1}{\lambda_2}\right)^5 \frac{I_{\lambda_1}}{I_{\lambda_2}}\right]} \qquad 3.5$$

Where, λ_1 and λ_2 are wavelengths of emission. I_{λ_1} and I_{λ_2} are I_{λ_2} are the corresponding intensities. Measurement range is 1000 – 3500 °C . The resolution of the system is ~ 5° C. No re-calibration needed.

3.6.4 Digital storage oscilloscope

Digital storage oscilloscope is used to record the voltage, current signal and trigger signal. A 350 MHz four channel digital storage oscilloscope (DSO) (Model HMO3524 Hameg Instruments) was used to record the voltage and current fluctuations [7]. The image of the oscilloscope is shown in Figure 3.19. For collecting data different sampling rates were chosen according to requirement. The corresponding time bases are 1 ms and 2 ms respectively. The total time for which the data has been recorded is 12 ms and 24 ms respectively.

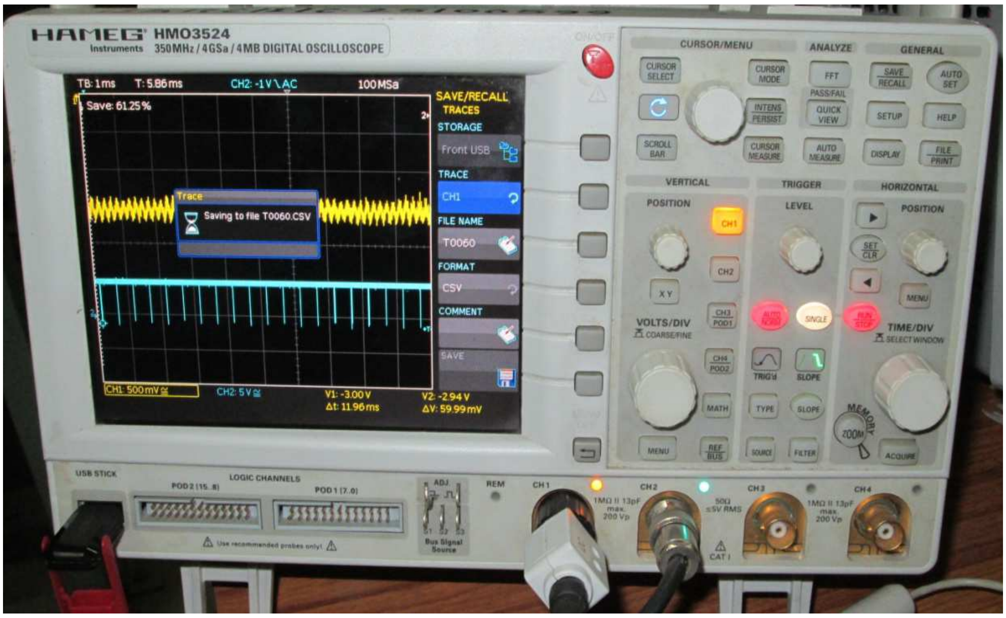

Figure 3.19: Digital storage oscilloscope in operation

During the experiment, total 24000 data points are collected. Time interval between two consecutive data points is 2.5 µs and 5.0 µs respectively. Since the frequency of voltage fluctuation is of the order of kHz, the above settings are appropriate to reliably reconstruct the signal as per Nyquist's criteria. To synchronize the signal with the image of the camera, trigger signal from camera was used as external trigger input to the oscilloscope and all data trigger from camera, voltage signal and current signal were recorded in single sequence mode. To analyze the signal further, all signals were recorded in CSV mode. Data were then transferred in USB pen drive for further processing.

3.6.5 Potential divider circuit

Due to very high voltage across cathode and anode, voltage can’t be directly measured through oscilloscope and it can damage the oscilloscope also. A voltage divide circuit as shown in the Figure 3.20A was designed to measure the fraction of the voltage. Actual voltage across cathode and anode was obtained by multiplying the dividing factor. Terminal 1 and terminal 3 are connected to the cathode and anode of the plasma torch respectively. Frequency response of the resistive voltage divider circuit is shown in figure 3.20B. Total arc voltage drop is divided between 11 kΩ and 400 kΩ in series and voltage signal is received across 11kΩ. Circuit was tested for 5 kHz and 50 kHz frequency and no distortion in the output signal was observed over th frequency range. The amplitude of the fluctuating component of voltage signal was found to be different for different type of plasma gases. It is low for Argon and high for nitrogen and air plasma.

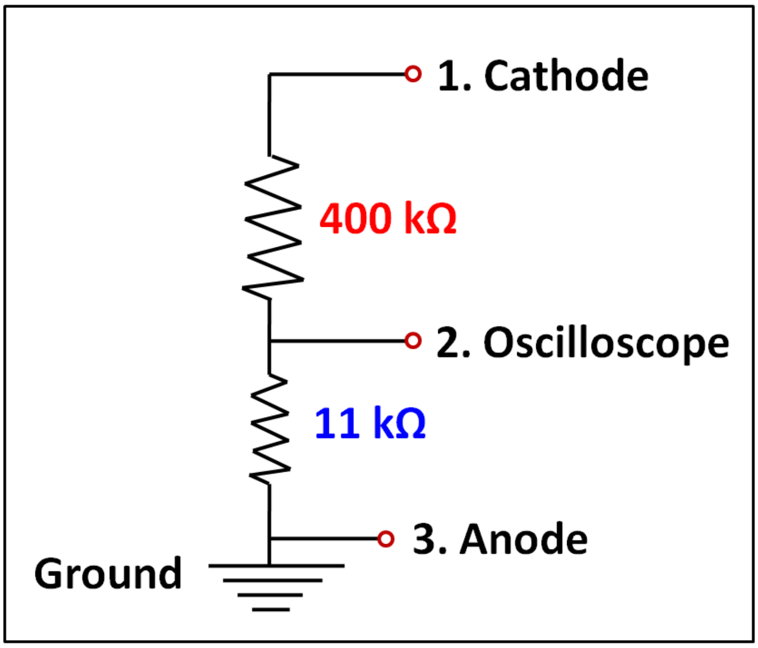

Figure 3.20A: Potential divider circuit

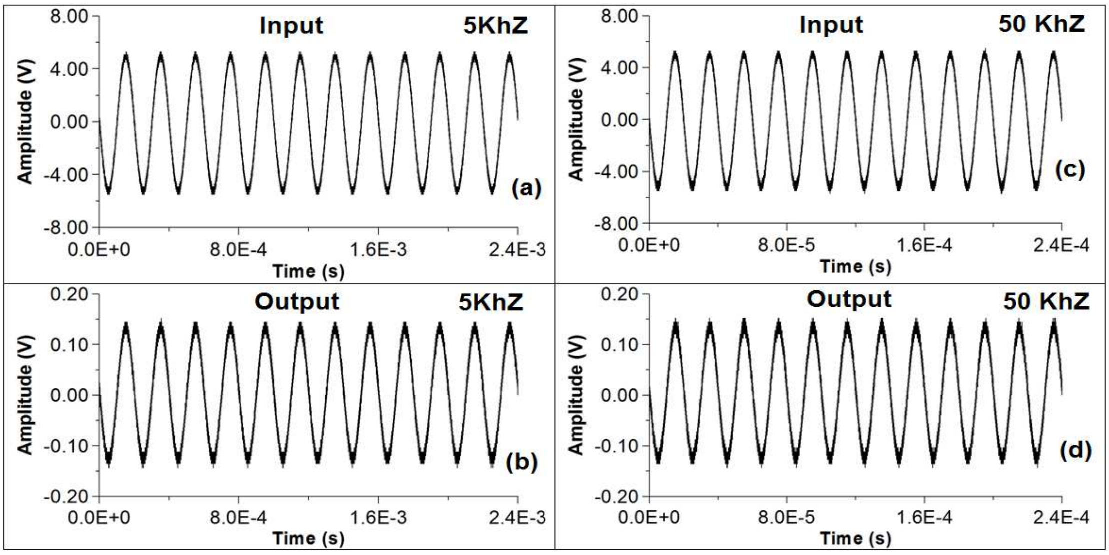

Figure 3.20B: Frequency response of the resistive voltage divider circuit: (a) Input signal at 5 kHz; (b) Output signal corresponding to input signal of (a); (c) Input signal at 50 kHz; (d) Output signal corresponding to input signal of (c). No significant distortion in the voltage signal is observed over the entire range of interest in frequencies. Exact reduction in the amplitude is observed [total arc voltage drop is divided between 11 kΩ and 400 kΩ in series and voltage signal is received across 11kΩ].

3.6.6 Resistance Temperature Detector (RTD)

Measurement of the temperature of the cooling water flowing through the torch is very important for safe operation of the device. For the safety of the arc devices, the inlet and outlet temperature should be in safe limit. Limit of safe operation is from 20^0-45^0C. The water running through the system should neither be very low (condensation) nor high enough (boiling). Temperature of the cooling water at the inlet and outlet of torch segments was monitored using resistance temperature detectors (RTD). In this study, RTD PT 100 (Model Omega Engineering) and digital thermometer were used for measuring the temperature. It is based on the principle that resistance of material changes with change in the surrounding temperature. Technical specifications are provided in Table-3.5. Photographs of the RTDs and thermometer used in the experiments are shown in Figure 3.21a and 3.21b.

Table-3.5 Technical specification of RTD and thermometer

Specification for RTD	
Manufacturer	Omega Engineering
Type	PT100
Accuracy	+/- 0.1 C at 0 ^{o}C
Temperature range	-200 to 600 ^{o}C
Specification for Thermometer	
Manufacturer	MEXTECH
Type	Digital
Accuracy	+/-0.1^{0}C
Temperature range	-50 to 300 ^{o}C

(a)

(b)

Figure 3.21: (a) RTD PT100 (b) MEXTECH DT-9 Digital thermometer

3.7 Feeder unit: Feeder unit is used to feed the material to be coated on a substrate using thermal spray. Two types of feeder assembly were used:

3.7.1 Wire feeder unit

This unit (ADORE, model NO:VCG B-203) was used in single wire arc spray system. The unit is capable of feeding 0 – 18 m/min of wire. It consists of a wire spool pay-off spindle assembly, a wire straightner, and a precision-driven motorized wire drive assembly. It is connected to the torch unit which is provided with a wire feed control switch actuated only during spraying by the operator. It uses nickel and copper wire of diameter 1.6 mm, 1.2 mm. Its range varies from 1m/min to 10m/min. Picture of the wire feeder unit is shown in the following Figure 3.22.

Figure 3.22: Wire feeder unit.

3.7.2 Powder feeder unit

This unit (Model No: MEC Powder feeder 3350) was used in low pressure dc plasma reactor[8]. Powder to be coated is fed to plasma. Picture of the powder feeder unit used is shown below Figure 3.23. Working of the powder feeder unit is based on the principle of pressurization and constant volumetric feeding. Canister is partially filled with the powder. It is pressurized by the carrier gas used to carry the powder. At the bottom of canister, a slotted metal disc mounted off-center at the bottom. This allows the powder particle to move down to the powder hose in a control manner. The powder feed rate(g/min) is governed by the rotation speed(rpm) of the metal disc. Depending onto the set feed rate, equivalent volume of powder fits into the slots made in the disc.

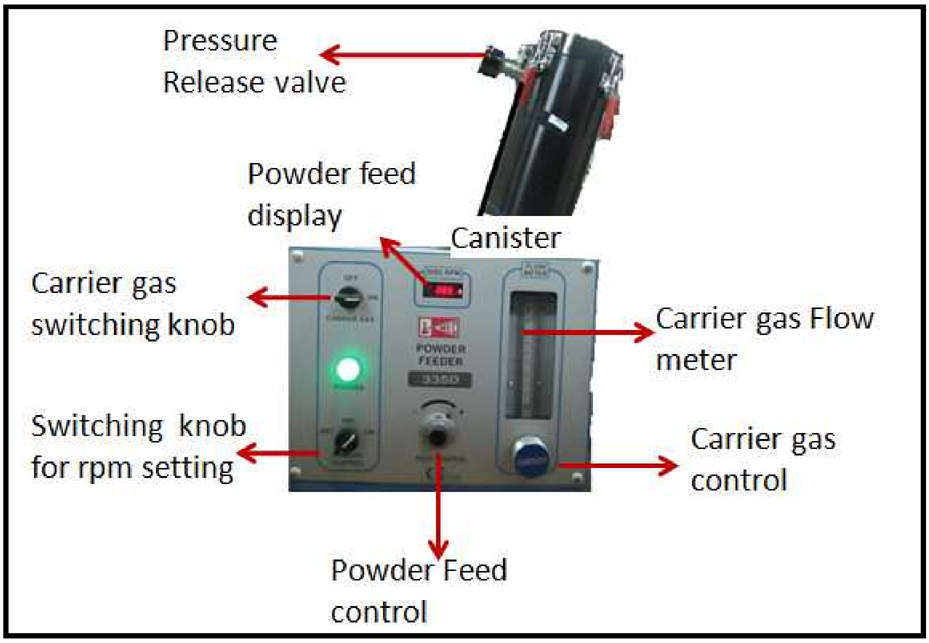

Figure 3.23: Powder feeder unit in working condition.

As the disc rotates with predetermined rate, the given amount of powder is fed into the powder hose and carried away by the carrier gas to the plasma torch.

3.8 References:

1 See https://www.mathworks.com for image processing.

2 Ion Arc Technology Pvt. Ltd., Coimbatore, India.

3 PCO Germany https://www.pco.de/highspeed-cameras/pco1200-hs.

4 Ocean Optics, USA, www.oceanoptics.com.

5 Andor https://andor.oxinst.com.

6 Spray Watch2i www.oseir.com.

7 Hameg Instruments, Germany, www.hameg.com.

8 Powder feeder unit www.mecpl.com.

Chapter-4

Direct Probing of Anode Arc Root Dynamics and Voltage Instability in a DC Non-transferred Arc Plasma jet

Outline of the Chapter

Chapter 4

Direct Probing of Anode Arc Root Dynamics and Voltage Instability in a DC Non-transferred Arc Plasma Jet

4.1 Introduction

In this chapter, dynamics of the arc root in a non-transferred arc is investigated through fast imaging and simultaneous measurement of the arc voltage. It was revealed that the existing models of non-transferred arc are partially correct. While the observed instability is essentially caused by the movement of the arc root, there may well be multiple arc roots at the same time and that the arc current may extend well beyond the exit of the plasma torch. Existence of current in the external plasma jet was experimentally proved by judicious positioning of several independent axial and transverse coils along the length of the external plasma jet and correlating the received signals with the instabilities in the total arc current. The findings elaborated in this chapter are important as the external jet current may highly enhance the temperature of the plasma jet through continued ohmic heating and substantially influence the plasma chemistry. It is also demonstrated that the external jet current is capable of initiating a plasma thruster action to generate a self-propelled plasma jet of a huge length. Such unusually long high energy density plasma jets may find wide applications owing to their large volume, greatly enhanced particle residence time and enhanced particle heating. Different modes (steady, takeover and restrike) of arc depend on anode diameter, nature of gas, flow rate of gas and arc current. The arc attachments are strongly linked to the cold boundary layer surrounding the arc column, and depend on the thermo-physical properties of plasma forming gas as well as torch geometry like anode nozzle diameter and gas injection design. For a given geometry and arc current, the general tendency is to exhibit steady mode at lower gas flow rate, restrike mode at higher gas flow rate and takeover mode in between. Depending on geometry and plasma gas, once a specific mode sets in for a particular operating condition, the anode arc root behaviour is mostly independent of the history of formation of the arc (like cathode geometry and cathode type). Presented results in this paper are obtained with an air plasma torch having only one electrically isolated segment of length 50 mm ('2' in Figure 3.1(a) of chapter3) between cathode and anode. This floating segment is made of copper having inner diameter, same as that of the anode. Possible arcing between cathode and anode with this electrically insulated tube (segment) was inhibited by a curtain of shroud gas. Scope of the present study is limited to direct probing of the anode arc root behaviour when a certain mode is established in an arc. The operating conditions to achieve extremely long, laminar plasma jets in atmospheric pressure argon are available in [1]. The conditions leading to gradual transition from one arc mode to another in argon and nitrogen are available in [2, 3]. Experimental details are presented in section 4.2. Results and discussions are presented in section 4.3. Summary and conclusions are presented in section 4.4.

4.2. Experimental details

Schematic of the set up used for investigating evolution of arc root over the anode surface and detecting the current in the exiting plasma jet are shown in Figure 3.1 of Chapter 3. Properly aligned partially reflecting mirror in combination with a fast photography camera with reduced exposure time of the shutter, allowed us to capture a real-time development of arc root over the anode surface and corresponding evolution of the arc voltage in a time-synchronous manner. Inherent instabilities in the current in the plasma jet resulted in a change in the associated magnetic flux intercepted by the coils and the generated EMF (electromotive force) in the coils were directly measured by the DSO. With arc current, simultaneous measurements are taken once with the transverse coils and next with the axial coils. Voltage recorded in the oscilloscope is linearly proportional to the voltage across the shunt. Operating conditions are given in table 4.1.

Table-4.1: Operating parameter

Parameters	Measures
Inner diameter(ID) of anode nozzle	6,10,15 mm
Arc current	90–450 A
Plasma forming gas	Argon, Nitrogen, Air
Gas flow rate	10–40 slpm
Cathode type	For argon and nitrogen: 2% thoriated tungsten cathode (rod type, diameter—8 mm, tip angle—60°). For oxygen and air: button type hafnium embedded copper cathode (diameter 9 mm).

4.3. Results and discussion

Different operating modes of voltage instability and associated arc root dynamics are presented in Figures 4.1 - 4.4. In each frame of the FPC (Figures 4.1–4.4), the relatively thicker and longer luminous zone shows the hot core of the plasma jet exiting through the anode, aligned along the axis of the torch (the brighter edge points towards the cathode). The relatively faint, comet-like structure in each frame shows the zone where the arc connects over the anode surface, the head of the comet being the arc root. If the exposure time is less or the arc undergoes significant expansion immediately after the arc root, the tail of the structure may not be visible and the arc roots may simply appear as bright spots over the anode surface. Tiny faint line(s) at fixed location(s) in the frames (boxed in Figure 4.4) correspond to image(s) of the jet(s) formed by reflection at the inner wall of the anode. The 'takeover mode' of voltage instability and associated arc root dynamics are presented in Figures 4.1 (a) and (b) respectively. The voltage oscillations were too fast and capturing frames at every cycle was beyond the limit of the FPC. Instead, frames were captured at instants marked by arrow indexed '1'–'25' on the voltage trace. Frame-1 captured the arc with only one root. Visually, a jet from the anode arc root meets another jet nearly perpendicular to it coming from the cathode side (upstream). The meeting zone is named as the 'return region (RR)'. Energetic electrons excite the atoms in their path and make their path visible when the excited atoms emit. Possibly, the electrons from the cathode, guided through the cylindrical electrodes, spread over a wider zone before they again reunite and enter into the anode arc root. This makes the RR relatively less intense. The arc was near its voltage minima when frame '1' was captured (Figure 4.1(a)). Frame-2 and corresponding arc voltages were similar.

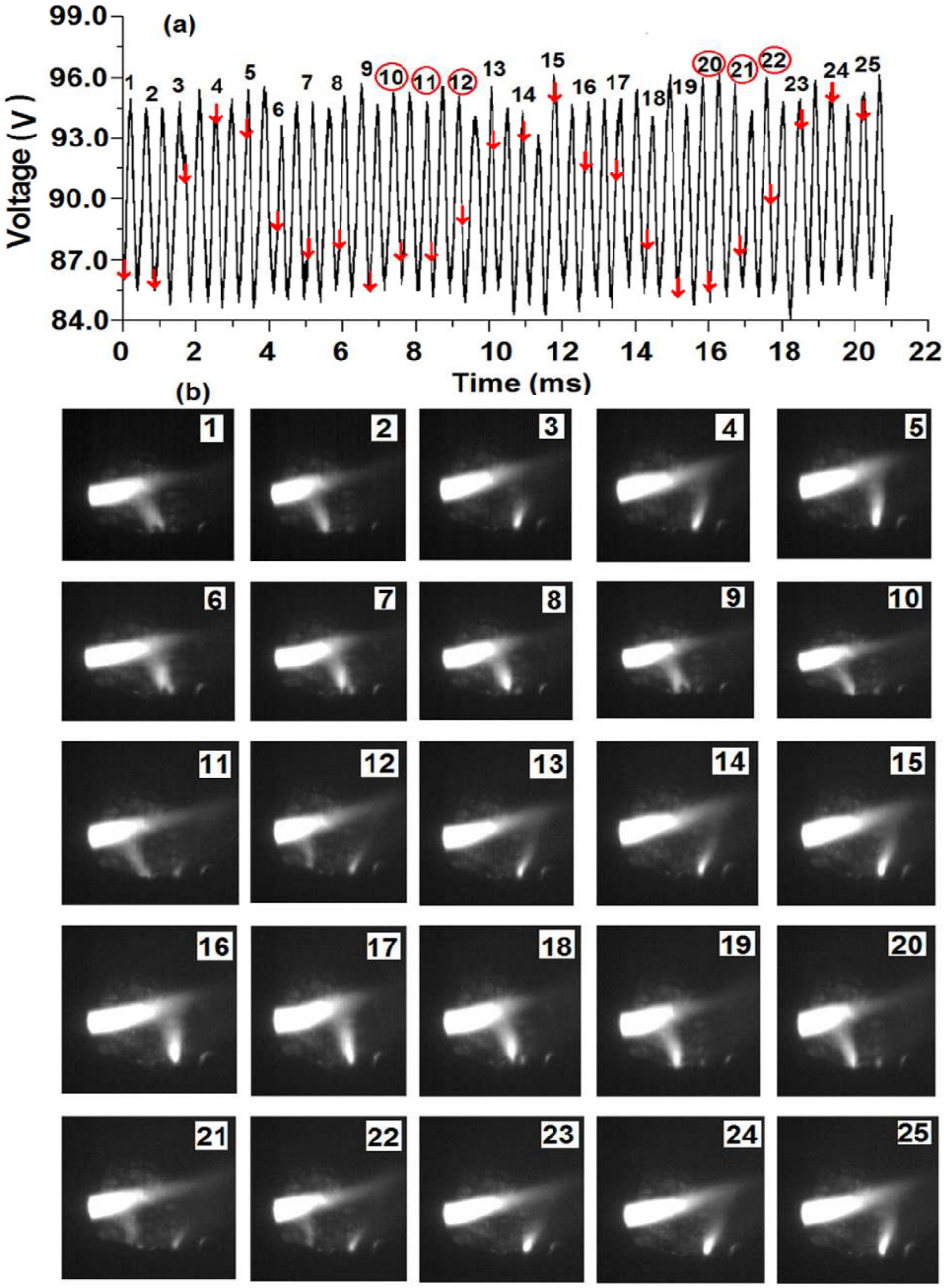

Figure 4.1: (a) Voltage waveform in 'take over' mode of voltage instability. (b) Evolution of the arc root in takeover mode. Frame numbers correspond to the instants marked on the voltage trace. (Operating conditions—anode nozzle i.d: 15 mm, plasma gas: air, gas flow rate: 15 slpm, arc current: 200 A).

However, frames 3, 4 and 5 intercepts increased arc voltages. The earlier obtuse angled short current path in the RR is now transformed into hairpin shaped acute angled long current path producing a higher arc voltage. Frames 6–9 again intercept lower arc voltages and the current paths in the RR were similar to frames 1 and 2. However, special features are observed while the arc elongates from its minimum voltage configuration. A second arc root (R2) forms below the first arc root (R1) and they exist together (frames (10, 11, 12) and (20, 21, 22)). With time, R1 decays and R2 strengthens. Finally, R2 becomes the only arc root near the maxima of the arc voltages. As time continues, the scenario repeats. Under the 'steady mode', the arc voltage varies little from its mean. Figures 4.2(a) and (b) captured the behaviour as it undergoes a transition from steady to re-strike mode. Frames 1–8 exhibit nearly constant arc voltage and almost a stationary arc root. The observation of a double arc root even in the 'steady mode' is interesting (frame-5). It has been observed that a 'ringing' pattern is associated in the corresponding voltage oscillation with double arc root. The saw-tooth like voltage oscillations in the 'restrike mode' and corresponding arc dynamics are nicely depicted in Figure 4.3. Near the peak of the oscillation, the 'V'-shaped current path of frame-1 becomes nearly 'U'-shaped (frame-2) as the voltage increases. In the next frame, a sudden upstream reconnection (restrike) of the arc takes place, the 'U' loop disappears, the RR goes deep inside the anode bore and the arc voltage drops down to an minimum (frame-3). Past this minimum, the arc voltage starts increasing again and two arc roots appear in frame-4.

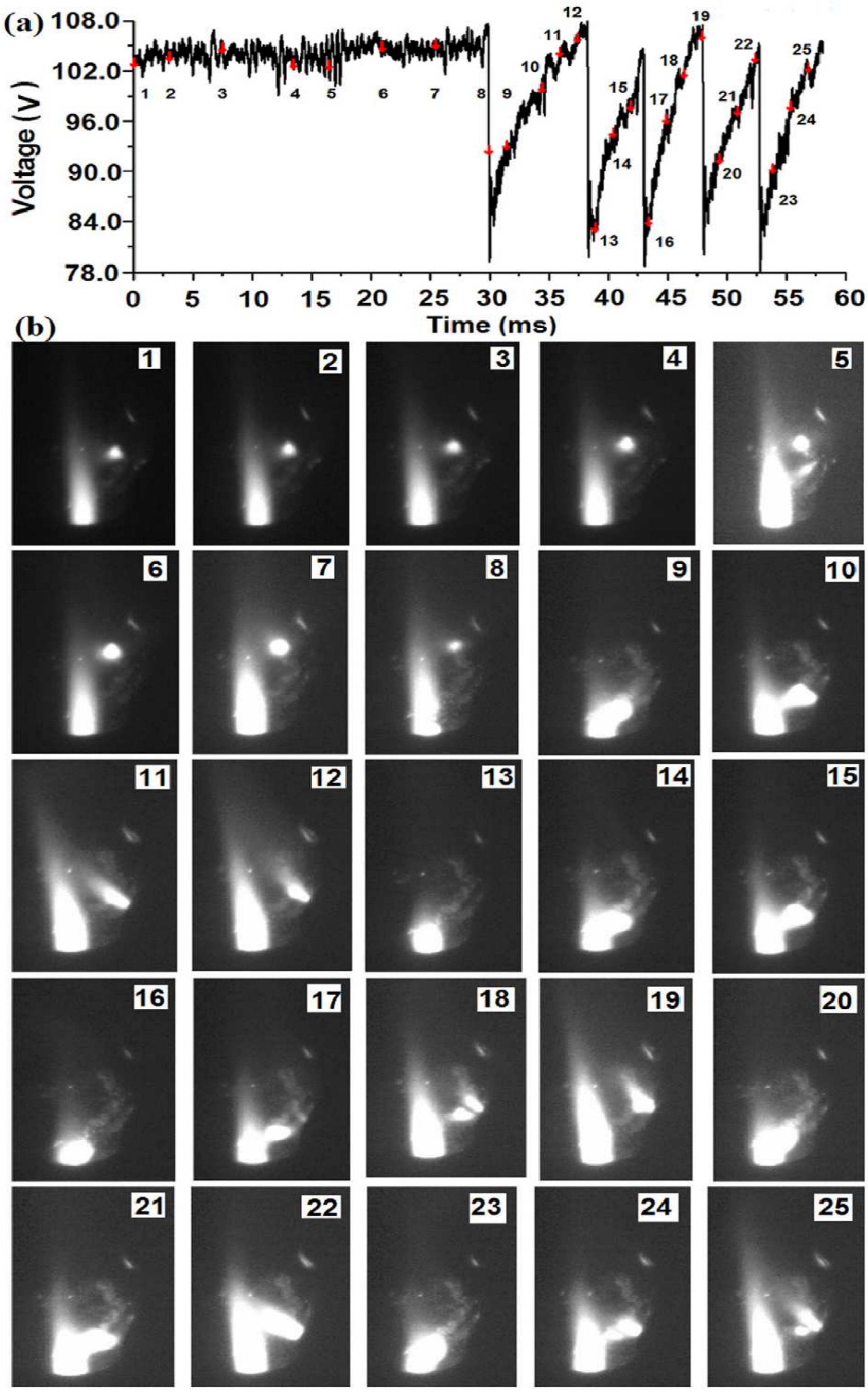

Figure 4.2: (a) Time series of steady mode of voltage instability (followed by restrike mode). (b) Associated evolution of the arc root. Frame numbers correspond to the instants marked on the voltage trace. (Operating conditions—anode nozzle i.d: 15 mm, plasma gas: air, gas flow rate: 17.5 slpm, arc current: 200 A).

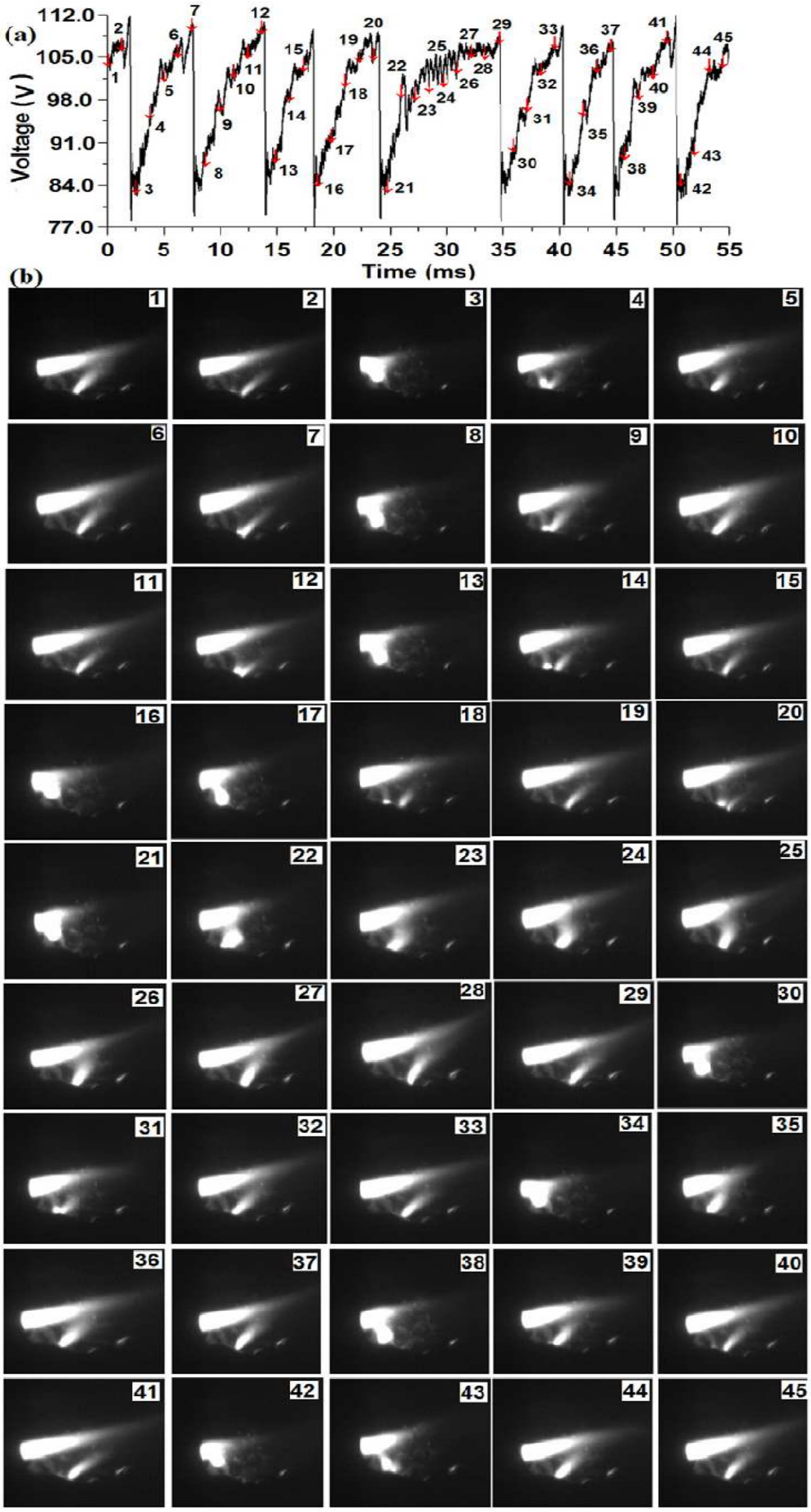

Figure 4.3 (a) Time series of restrike mode of voltage instability. (b) Evolution of the arc root in restrike mode. Frame numbers correspond to the instants marked on the voltage trace. (Operating conditions—anode nozzle i.d: 15 mm, plasma gas: air, gas flow rate: 25 slpm, arc current: 200 A).

The RR includes a shorter and a longer arc path simultaneously. With further increase in arc voltage, the shorter path gradually disappears and the longer current path gradually changes from a ‘V’ shape to a ‘U’ shape and finally goes for the next restrike. The same scenario repeats throughout the restrike time series (frames 4–8, 9–13, 14–17, 18–22, etc). Multiple arc roots captured during the transition from a shorter to a longer arc are presented in Figure 4.4. As many as seven simultaneous arc roots of different intensities have been observed (frame-3). Possibly, due to enhancement of the local electric field at micro projections, eroded anodes exhibit more number of simultaneous arc roots compared to new one. Explicit shorter and longer current paths under double arc root configuration are captured in frame-4 of Figure 4.4.

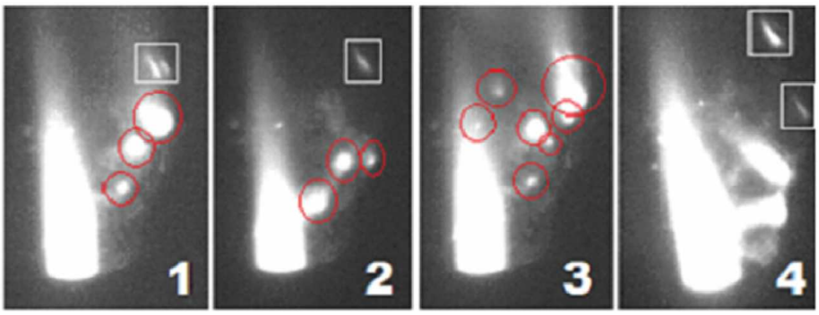

Figure 4.4: Observation of multiple arc roots. Explicit shorter and longer current paths are seen in frame-4.

Forward and return current paths, beyond the exit of the torch are obvious from the captured FPC images of the plasma jet. It has been observed in the experiment that the presence of such current in the external jet may lead to formation of self propelled plasma jet of huge length.

To explain this unique behaviour, the observed long jet of plasma, a schematic of the possible current path inside the jet and corresponding FPC image of the jet are presented in Figure 4.5(a), Figure 4.5(b) and Figure 4.5(c) respectively.

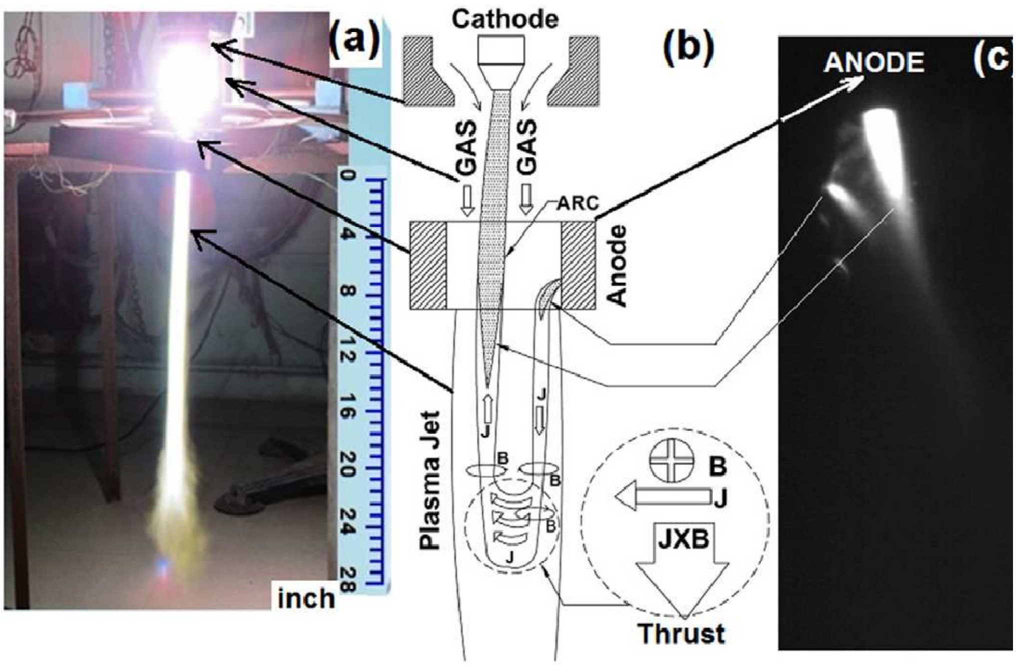

Figure 4.5: (a) Self propelled plasma jet. (b) Schematic of possible current path inside the plasma jet and associated electromagnetic body forces. (c)

Different sections of the plasma jet and that of the FPC image are correlated in the schematic for clarity. To minimize the contribution from pressure linked thermal expansion related thrust, the middle part of the torch (part-2, Figure 3.1(a) in chapter3) is removed in this demonstration. Only 'open space' exists between the cathode and the anode. The arc column is self constricted in this open space by radially inward compressive force originating from the interacting arc current and the self magnetic field. As explained below, it is primarily the electromagnetic magnetic body force that propels the arc forward and forms the huge jet of plasma after the anode exit.

On the basis of the well-known Steenbeck's voltage minimum principle given by Ecker G [4], an arc always tries to find a path that will offer it the lowest possible arc voltage. However, the chosen arc path also depends on other factors like prevailing electromagnetic and fluid dynamic environments. As a consequence, the ultimate arc path may follow any of the configurations presented in Figures 4.6(a)–(d).

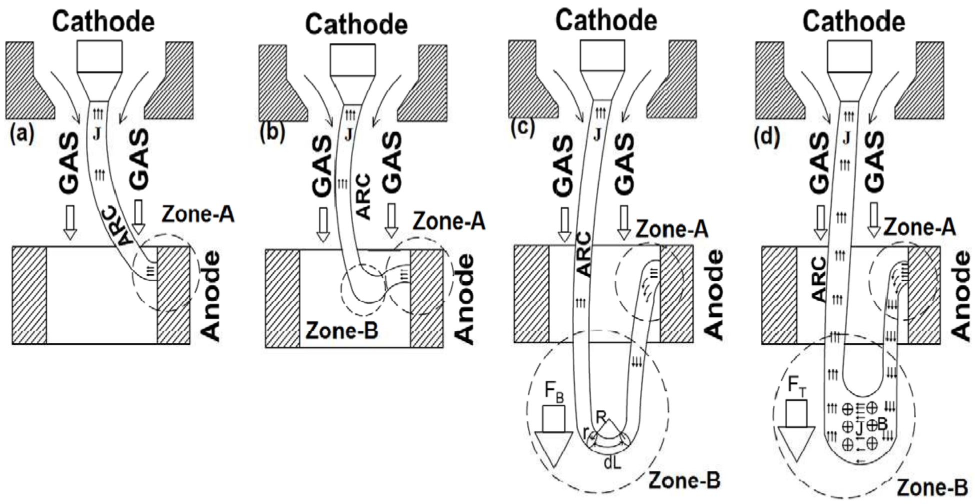

Figure 4.6: Possible current connections in non-transferred arc plasma devices. (a) Arc connection without loop. (b) Initiation of arc loop by viscous drag force. (c) Arc connection with a simple loop in the downstream. (d) Arc connection

A cylindrical arc segment of length ‘dL’ and radius ‘ro’, exposed to a transverse free stream flow of velocity ‘v’ and density ‘ρ’ experiences a downstream viscous drag force [5]:

$$F_D = C_D ro\, \rho v^2\, dL \tag{4.1}$$

Here C_D is the viscous drag coefficient, a function of the Reynolds number and heat transfer to the cold gas. When F_D is not strong enough, typical path followed by an arc maintaining Steenbeck’s minimum voltage principle is close to the one shown in Figure 4.6(a). It is obvious that ‘v’ goes to zero near the wall (no slip boundary) of a cylindrical anode, and consequently F_D becomes zero there. However, as ‘v’ is highest near the core, F_D may become significant there, and force the arc path to take a shape as shown in Figure 4.6(b). This type of arc paths are widely discussed in literature and it has been estimated that a curved arc path of length dL, radius of curvature 'R' and radius 'ro' experiences a magnetic body force, F_B given by [5–7]:

$$F_B = \left(\frac{3\mu_0 I^2}{16\pi R}\right)\left[1 - \frac{7}{8}\left(\frac{r_0}{R}\right)^2\right] dL \qquad 4.2$$

Here, μ_o corresponds to permeability and F_B acts in a direction away from the centre of curvature of the arc. It may be noted that in Figure 4.6(b), the curvatures of the arc in zone-A and zone-B are opposite to each other. This makes FB to act upward in zone-A, and downward in zone-B. However, it may also be noted that both of FB and FD act downwards in zone-B. It may be further noted from equation (4.2) that magnitude of FB increases as curvature increases (i.e. 'R' decreases). Therefore, it is natural that the arc takes a curved path in zone-B. However, appreciable resistivity of the arc at moderate and high flow rate of plasma gas causes a significant rise in the arc voltage with increase in curvature (as the total length of the arc increases). Effort to stay at minimum voltage configuration (Steenbeck principle) finally decides the ultimate path chosen by an arc. The present study employs a relatively low flow rate of gas, for which it has been observed through FPC images (Figure 4.5 for example) that FB alone is strong enough to push the arc deep downstream in zone-B forming an arc path like that shown in Figure 4.6(c) or (d). For example, under the configuration of Figure 4.6(c), choice of I = 120 A, R = 2.5 mm and r = 2.0 mm, gives a numerical estimate of FB as:

$$F_B = 0.324 \text{ Nm}^{-1} \qquad 4.3$$

The magnitude of the force is strong enough to push the arc deep down stream in the external jet. However, a scrutiny of the FPC images (Figure 4.5(c), for example) reveals that most possibly the current transfer between the forward and the return current path takes place in a diffused region like zone-B in Figure 4.6(d), where both axial and transverse currents exist together and forms a configuration close to that of a plasma thruster. The magnetic field created by the axial current may directly interact with the transverse current in this zone and create a huge axial thrust as:

$$F_T = j_T \times B_x \tag{6.4}$$

where j_T and B_X are the transverse current density and the magnetic field at the location 'x' respectively. F_T acts in axial direction and the strong axial thrust so generated may be responsible for the formation of the huge plasma jet. The presence of axial and transverse currents in the external jet is further confirmed through the following experiment.

For any dc arc, the total arc current always includes a small ac component owing to dynamic plasma load as well as associated electronics. By Faraday's law, the electromotive force (EMF) induced in a coil, placed perpendicular to some passing current, is proportional to the negative of the time derivative (NTD) of the passing current. Therefore, in the setup of Figure 3.1(b) in Chapter 3, the EMF generated in each transverse coil is proportional to the NTD of associated axial current and the same in each axial coil is proportional to the NTD of associated transverse current. In the experiment, the transverse coils were placed closer to the forward current (compared to the return current) through FPC observation to avoid the nullifying effects of opposite currents. For the typical current signals, the negative of its numerical derivative looks like a mirror image of the current signal itself. Therefore, whenever the EMF induced in a coil roughly follows the mirror image of the current signal, it is confirmed that the same current is passing the nearby region in the jet. It was observed that T1 located near the arc roots sometimes cleanly senses the arc current (t >4ms) and sometimes not (t <4ms) (Figure 4.7(a)).

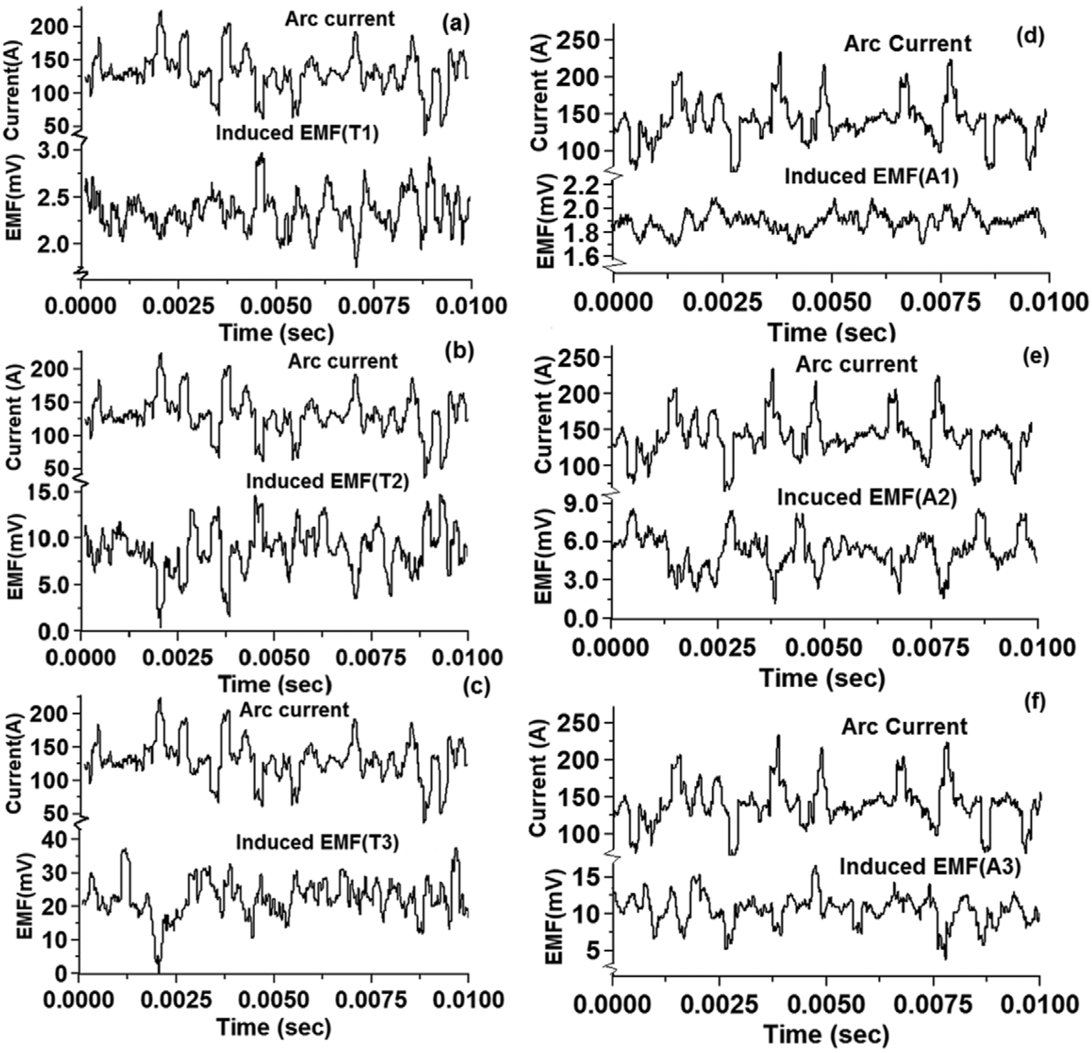

Figure 4.7: Induced currents in the transverse (a)–(c) and axial coils (d)–(f).

This is possibly due to the fact that after reaching the anode, the current takes an arbitrary path through it before finally returning to the power supply [7]. Interestingly, T2, located quite away from the anode exit, always accurately senses the arc current without fail (Figure 4.7(b)). Therefore, the plasma jet possesses a well defined forward and return current path in this region. However, T3, located in the tail fringe of the plasma jet detects the arc current intermittently (Figure 4.7(c)). Being a highly turbulent region, possibly the arc current extends up to this zone only in an intermittent fashion. For the axial coils, it is observed that A1, positioned close to the anode exit, does not sense any transverse current (Figure 4.7(d)). However, A2, located just above the tail region, accurately senses it all the time without fail (Figure 4.7(e)). The observation suggests that a transverse current exists in this region and possibly the arc current bend in this region to take its return path. A3, placed slightly below the tail region, rarely detects the arc current (Figure 4.7(f)). Current transport in this highly turbulent tail region of the jet is interesting and may be a subject of further investigation.

4.4. Summary and conclusion

Non-transferred arc plasma devices find wide usage in numerous technological applications. An important and fundamental aspect in these devices is the presence of inherent instabilities, manifested through so called ‘steady’, ‘takeover’ and ‘restrike’ modes of arc. Such instabilities have profound impact on the process qualities as the typical time period of the instabilities fall in the range of dwell time of particles inside the jet. While these modes are characterized through measured fluctuations in arc voltage, the actual dynamics of the arc inside the devices, giving rise to the observed instabilities could not be probed earlier in actual geometries. Presence of extremely high temperature, extreme brightness and the mechanical obstruction posed by the physical wall of the device itself barred direct probing of the arc dynamics. The study presented in this article is possibly the first of its kind giving vivid details of the arc root dynamics in non-transferred arc plasma devices under different possible arc modes in actual device geometry. Apart from directly capturing the arc dynamics and correlating it with associated voltage instabilities, the study revealed that the existing models of non-transferred arcs are only partially correct. Contrary to usual concepts, it has been found that the existence of multiple arc roots is common and the arc current may extend well beyond the exit of a non-transferred arc plasma torch. The external jet current may continue ohmic heating, highly enhance the temperature of the exiting plasma jet, and significantly affect the jet chemistry and jet dynamics. While the evidence of jet current extending the nozzle exit was obtained through fast photography itself, its presence in the external jet was further confirmed through a novel experiment by positioning different transverse and axial induction coils along the length of the plasma jet. Passing currents through various sections of the jet was detected by these coils and induced EMFs in individual coils were correlated with the current passing through the arc. Strong correlation between induced EMF in the transverse coils and arc current over a sizable length of the external jet confirmed existence of arc current in the external plasma jet. The extreme edge of the current carrying zone in the plasma jet unavoidably includes a region having current direction transverse to the length of the jet. The existence of such regions in the external plasma jet is successfully detected in the experiment through appropriately positioned induction coils. The study also revealed that it is possible to produce a self propelled plasma jet of huge length having enhanced temperature, better confinement, and higher efficiency. Possible mechanisms involved in the evolution of such huge jets are explored. While viscous drag force and electromagnetic body force both may contribute in the ultimate jet dynamics, the unusual jet length appeared to be primarily an attribute of associated electromagnetic body forces. The findings are expected to bear a significant impact on future modelling and development of novel non-transferred arc plasma devices.

4.5 References

1. Pan, W., Zhang, W., Zhang, W. and Chengkang, W., "Generation of long, laminar plasma jets at atmospheric pressure and effects of flow turbulence" Plasma Chem. Plasma Process. 21*,* 23–35 (2001).
2. Duan, Z., and Heberlein, J., "Arc instabilities in a plasma spray torch" J. Therm. Spray Technol. 11, 44–51 (2002).
3. Iwao, T., Cronin, P., Bendix, D., and Heberlein, J. V. R., "Anode attachment stability and anode heat transfer for high intensity arcs with lateral gas flow", IEEE Trans. Plasma Sci.33, 1123–8 (2005).
4. Ecker, G., "Theoretical aspects of the vacuum arc Vacuum Arcs" ed J M Lafferty (New York: Wiley) chapter 7, 228–320 (1980).
5. Schrade, H. O. and Soehngen, E. E., "On arc pumping and the motion of an electric arc in a transverse magnetic field" *ARL,* 65–178 (1965).
6. Wutzke, S. A., Pfender, E. and Eckert, E. R. G., "Symptomatic behavior of an electric arc with a superimposed flow" *AIAA, J.* 6 1474–82 (1968).

Chapter-5

Study of Structures and Stabilities in Atmospheric Pressure DC Non-Transferred Arc Plasma Jets of Air, Argon and Nitrogen

Outline of the chapter

Chapter 5

Study of Structures and Stabilities in Atmospheric Pressure DC Non-Transferred Arc Plasma Jets of Air, Argon and Nitrogen

5.1 Introduction

This chapter deals with investigation of stability of dc non-transferred arc plasma jets and their internal structures. DC non-transferred arc plasma jets are widely used in numerous processing applications including plasma spraying, novel material synthesis, chemical conversion, nano-synthesis, waste treatment and special applications in the area of aerospace, biomedical, semiconductor, electronic and automotive industries. Improved wear resistance, enhanced biocompatibility, longer life span, higher strength, and better chemical compatibility are some of the important benefits that led to impressive developments in the area over last several decades. In spite of these outstanding developments, some of the salient fundamentals in the thermal plasma jets of non-transferred arc plasma torches are still poorly understood. This applies to the wide variation in the jet characteristics under different operating conditions in terms of thermal and entrainment behaviour. They influence the interaction of powder particles with the plasma as well as affect the process efficiency and process quality in a significant manner.

Arc plasma torches primarily operate in three different modes classified as 'steady', 'take-over' and 'restrike' depending on operating condition. While steady mode offers a stable jet, it may be detrimental for torch health as continued connection of arc root at a particular anode location may puncture the electrode very fast owing to highly concentrated heat flux. On the other hand, the oscillatory behavior of a moving arc root under takeover and restrike modes may avoid such problems by distributing heat over a wider area but inherently include instability in the plasma jet. While instabilities under different arc modes have been subjected to investigation over many decades, investigation on external jet stability and evolution of different internal structures inside the plumes under different operating conditions are limited.

A thorough experimental investigation of the arc plasma plume for its stability and structure under different operating conditions was done. While vivid details of the jet dynamics will be extremely useful for process optimization, generated data will help in benchmarking of future theoretical models. The present chapter explores variety of interesting structures and instabilities in the external plasma jet under different operating conditions, captured through high speed camera. Image analysis was done using standard image processing software. Distribution of temperature inside the plasma jet was determined from CFD simulation as well as analysis of emission spectroscopic data. Thorough analysis of the intensity contours were carried out to understand the salient processes. Contributions from arc dynamics were estimated through synchronous record of arc voltage fluctuations and fast photography images. Radical differences in the stability of plasma jets of atomic and molecular gases were explored.

5.2 Experimental Details

Schematic of the experimental setup used is shown in the Figure 3.2 of Chapter3. The plasma torches used in the study with different plasma forming gases had straight nozzles of identical diameter (10mm) in all the cases. For operation with argon and nitrogen, tungsten (2% thoriated) cathodes were used. Whereas for air plasma, hafnium cathodes, inserted in a copper matrix were used. However, the hafnium electrode torch was capable of operating with nitrogen as well and similar jet characteristics were noted. Details of such operations are available elsewhere [1, 2]. Sequence of plasma jet images synchronized with voltage signal were captured using high speed camera for Argon, Nitrogen and Air plasma jet. Emission spectra for Argon, Nitrogen and Air were recorded. Rotational spectra of N_2^+ band were found in the nitrogen plasma using 2400 l/mm grating having resolution $0.7A^0$. Experiments were performed for torch current from 100A - 225A and gas flow rate from 10 lpm to 40 lpm.

5.3 Results and Discussion

Fast photographic studies of the argon as well as air and nitrogen plasma jets were performed near the nozzle exit, primarily to understand the location of the arc root and possible current paths. For argon plasma, only a single jet was observed and no arc root could be detected. Possibly, either the arc electrode connection was diffused or the arc root was formed well inside the nozzle and could not be imaged due to mechanical obstruction. The observation is in agreement with the studies reported earlier.

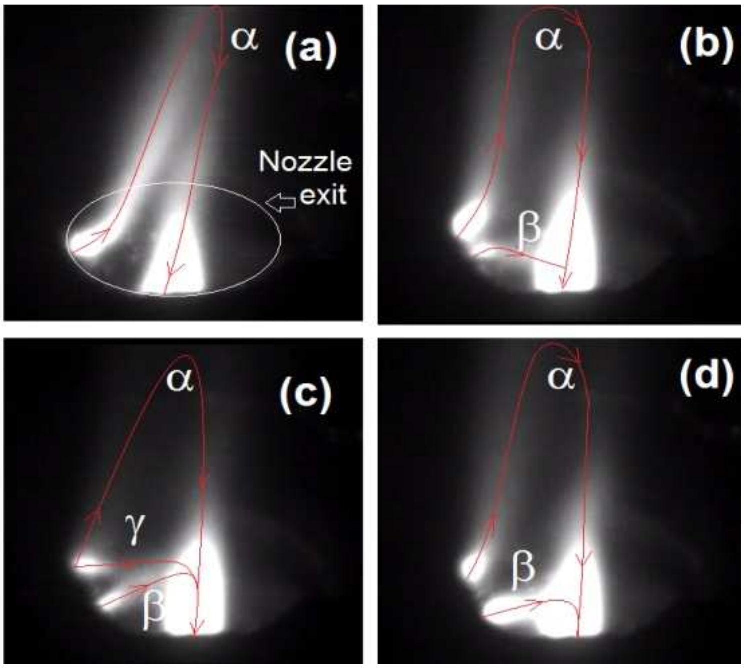

Figure.5.1: Typical fast photographic images of air plasma jet exiting from nozzle exit, depicting single as well as double arc roots. Tentative current paths are drawn in red. α, β and γ are the locations of different current paths, transverse to the plasma flow: (a) single current path (b) two simultaneous current paths (c) three simultaneous current paths. (d) two simultaneous current paths with clear uneven sharing of currents.

However, for nitrogen and air plasma, very interesting features were observed. Figure 5.1 presents the fast photographic images, filtered in a manner that only the extreme intensity regions are visible. Without filtering they look like typical extremely luminous strong jets, coming out from the nozzle exit. In chapter 4, details of the dynamics and correlation with arc voltage fluctuation have been explored. The highest luminosity paths indicate the path of arc current. As seen in Figure 5.1, the jet external to the nozzle exit carries current. Many of the times multiple arc roots are also formed and multiple current paths are detected in the same jet. Typical images observed are presented in Figure5.1. Figure 5.1 (a) presents observation of a single arc root. The current path forms a single loop and extends deep inside the external jet. Figure 5.1 (b) exhibits two arc roots with two different current paths detected. In Figure 5.1 (c) there are two arc roots but three obvious current paths. Luminosity of these current paths depends on the sharing of current among these paths. Figure. 5.1 (d) shows existence of two strong arc roots with nearly equal luminosity.

While several of the earlier studies discuss about the jet instabilities, they mostly address current free jets. Instability features in a current carrying jet may be distinctly different from that in current free jets in three respects: (a) Unlike current free jet, the ohmic heating continues in the external jet. (b) Ohmic heating in the external jet is more than that in the core as heating takes place due to both forward and return currents in the later. (c) There are locations in the external jet like 'α', 'β', 'γ' (see Figure 6.1) where current paths are transverse to the exiting plasma jet. The transverse current produces magnetic field which is perpendicular to the propagating plasma beam consisting of high density of charged particles. The magnetic field so produced may trap the charged particles and act as a rigid barrier to the plasma flow. The present investigation explains the distinct behaviour observed in such jets taking into account the aspects mentioned.

The study first takes a note of the possible specific features in the steady state jet behaviour, without any current present in the external jet. This is done through computational fluid dynamic (CFD) simulation of the external jet. The study is important as similar features observed in a current carrying jet may be regarded as a contribution not from the specific current carrying aspect. Then the experimental results are analyzed keeping this into consideration.

5.3.1 CFD simulation

A 2D axi-symmetric code has been used for CFD simulation of the current free plasma jet under steady state. Navier-Stokes equations involving conservation of mass, momentum, and energy have been solved using SIMPLE [3] algorithm assuming plasma to be optically thin and local thermodynamic equilibrium (LTE) holds. Necessary thermodynamic and transport properties have been taken from literature [4, 5, 6]. Computational domain for the assumed current free jet is shown in Figure 5.2.

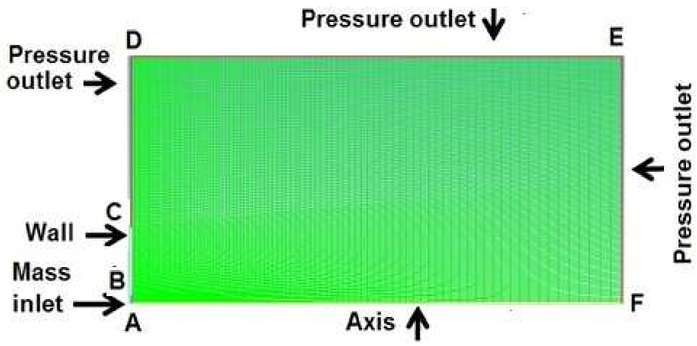

Figure 5.2: Computational domain used in the simulation of current free external jet.

Dimensional details are [A(0,0), B(0,5mm) C(0,40mm), D(0,150mm) E(300mm,150), F(300mm,0)]. Computation starts from the nozzle exit (AB). Axi-symmetric boundary condition is applied along the central axis (AF). Pressure outlet boundary condition is assumed at all other boundaries of the computational domain except for top flange wall (BC) where no slip boundary condition is used and the nozzle exit (AB) where mass inlet boundary condition is set. Temperature profile at the nozzle exit has been specified through conservation of total power, mass flow rate and measured efficiency of the torch. No swirl component is considered. Upwind scheme is used for interpolation. Standard k-ε turbulence model has been used for turbulence. Grid independence of the obtained results has been verified by choosing grids of different sizes.

For discharge of argon and nitrogen in air, as soon as the plasma jet exits from the nozzle exit, entrainment of cold atmospheric air into the plasma begins. In such situation, the thermodynamic and transport properties of the plasma jet are decided by the parent plasma gas as well as the amount of atmospheric air entrained. Mixing law is applied for determination of respective properties in such cases. Volume-weighted mixing law for density and mass-weighted mixing law for rest of the properties have been adopted [7].

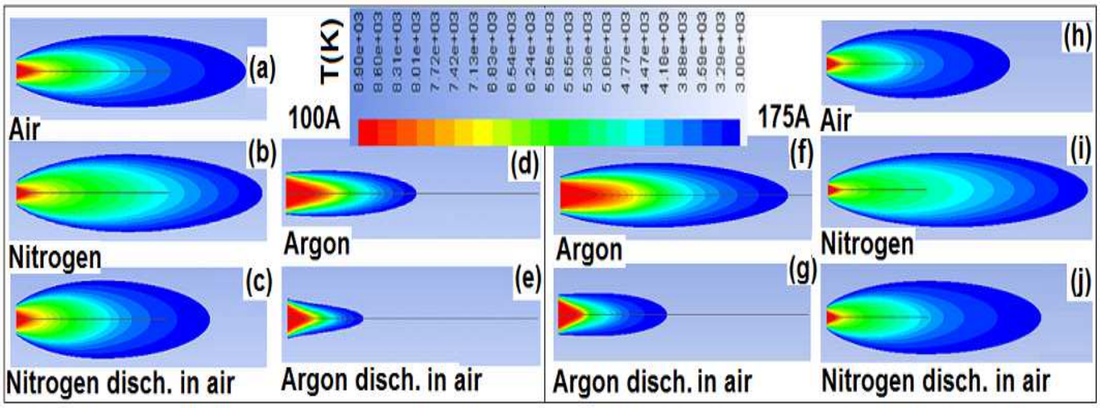

Figure 5.3: Simulated temperature profiles in argon, air and nitrogen plasma: (a)-(e) for current=100A; (f)-(j) for current 175A.

Distribution of temperatures in the simulated jets of argon, nitrogen and air, discharging in their own environments are presented in Figure 5.3. Argon and nitrogen jets discharging in air environment are also presented. Figure 5.3 (a)-(e) presents the results with arc current of 100A and Figure 5.3 (f)-(j) presents the results with arc current of 175A. In the plots the upper bound of temperature is 8900K whereas the lower bound of temperature is intentionally limited 3000K so that it can closely mimic the luminous part of the jet observed during torch operation. The black solid line along the axis in each Figure is the fixed reference length (100mm) with respect to which, length of the jets in respective Figures may be compared. It is observed from Figure 5.3 (a) and Figure 5.3(b) that at 100 A, the length of nitrogen jet is slightly longer than the length of air jet.

However, in the core the high temperature zone extends much longer along the axis in nitrogen compared to that in air. Similar plots [Figure 5.3 (h) and 5.3 (i)] for 175A exhibit that at higher current the observations become more prominent. Now, jet length in nitrogen is significantly longer than that in air and the core temperature extends further longer. It is observed from Figure 5.3 (d) and 5.3 (f) that jet length in argon plasma is much less compared to that in nitrogen or air plasma under similar operating conditions. The differences arise purely from the differences in the thermodynamic and transport properties of the respective gases. Interesting effects are observed for discharge of argon and nitrogen in air. Jet length shrinks significantly for all currents. Entrainment of cold air into the plasma may be primarily responsible for this.

Apart from jet length, degree of turbulence in the jet is a parameter of interest as long as stability and structures are concerned. Differences in the turbulent intensities arising purely due to differences in the fundamental nature of the gases are presented in Figure 5.4 for arc current 175A. It is observed that turbulent intensity initially increases, becomes maximum few cm away from the nozzle exit and then decreases monotonically. Among argon, nitrogen and air, the turbulent intensity is highest for air and almost comparable for argon and nitrogen. However, for argon and nitrogen discharging in air, turbulent intensity is higher in nitrogen compared to that in argon under similar operating conditions. Similar features are observed for arc current 100A.

As argon and nitrogen jet discharges in air, entrainment of air takes place and mass fraction of air entrained in the jet increases. Mass fraction of entrained air in the plasma jet as a function of distance from the nozzle exit is plotted in Figure 5.4 (f) for nitrogen. It is observed that significant entrainment takes place within a distance of 5 cm. Similar results are obtained with argon as well. It may be remarked that the observations agree well with the earlier experimental studies done by Pfender et al. [8].

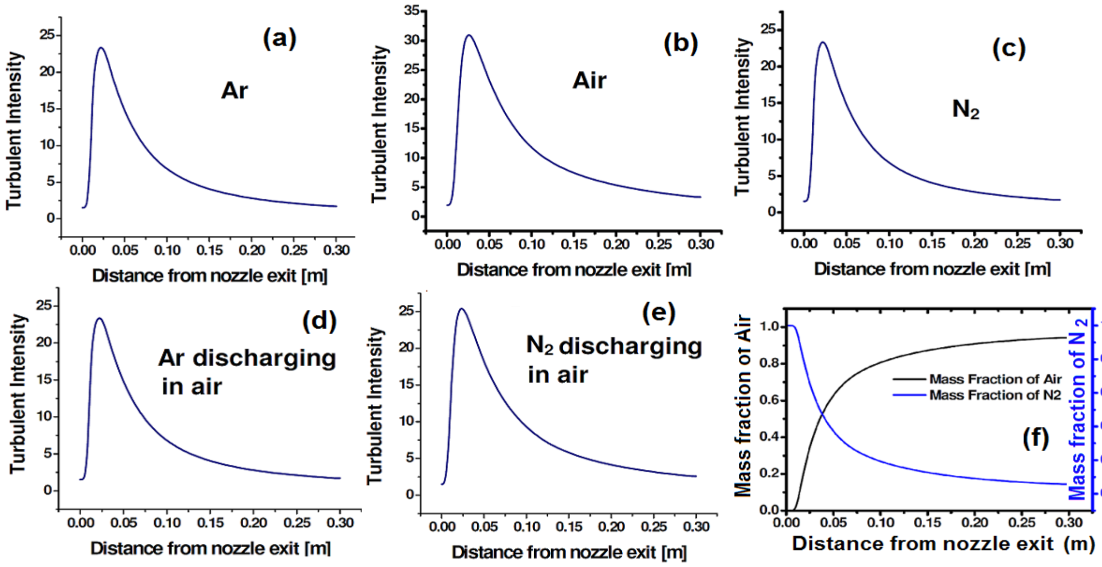

Figure 5.4: Simulated turbulent intensities and mixing effects in plasma jets of different gases (arc current 175A).

5.3.2 Experimental results

To analyze the instability features of the external plasma jets under a given operating condition, the gray scale images captured by fast photographic camera were analyzed for intensity contours using standard image analysis technique readily available in the computer program MATLAB [9]. Program is written in ‘m-editor’ for reading the grayscale images and plotting the intensity contours. Grey scale images are first read using inbuilt MATLAB function ‘Imread’. Then the colored intensity contours are obtained from the gray scale image using MATLAB function ‘imcontour’ where the number of equally spaced contour levels in the plot can be set and color scheme can be chosen. In the present study, the colour scheme chosen is ‘jet’. It ranges from blue to red, and passes through the colors cyan, yellow, and orange as presented in Figure 5.5. Identical scheme with same number of levels has been used throughout the study so that intensity of different jets may be compared. If intensity of any zone goes beyond the red level, it appears as white. Method used to obtain a rough correspondence between the intensity based ‘Jet’ colour scheme and actual gas temperature is explained in Figure-5.5.

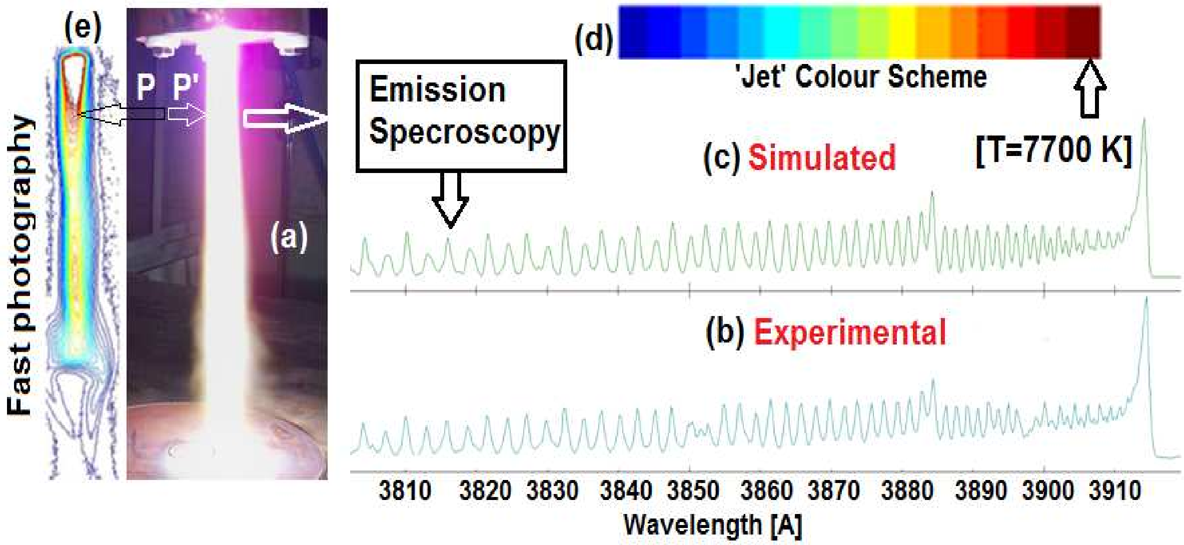

Figure 5.5: ‘Jet’ colour scheme and correspondence with gas temperature (red corresponds to maximum intensity and blue corresponds minimum intensity): (a) A nitrogen plasma jet (b) experimentally measured band spectra at location P' in the actual jet (c) simulated band spectra matching with experimental spectra at gas temperature 7700K. (d) Jet colour scheme (e) Iso-intensity contours of the fast photographic image under ‘Jet’ colour scheme: Red corresponds to the zone where measured temperature is 7700K.

The intensity contours of a nitrogen plasma jet [Figure 5.5(a)] under the chosen color scheme, is extracted from the gray scale image captured by the fast camera and presented in Figure 5.5(e). The location of the highest level of intensity (red) near the torch exit is identified. The optical bench is now adjusted to collect light from that particular zone. The spectrometer identifies a band spectra (first negative system N_2^+ B-X) as presented in Figure 5.5(b). This band is originated from the transition between excited state of molecular ion N_2^+ $B^2\Sigma_u^+$ and the ground state of N_2^+ $X^2\Sigma_g^+$ [10] where (0, 0) band head is located at 391.44 nm. Now, temperature input to the spectral simulation software 'LIFBASE'[11] is tuned until for nitrogen plasma the simulated spectra [Figure 5.5(c)] gives a very close match with the spectra obtained experimentally [Figure 5.5(b)]. In the present study the closest match is obtained at a temperature of 7700K..

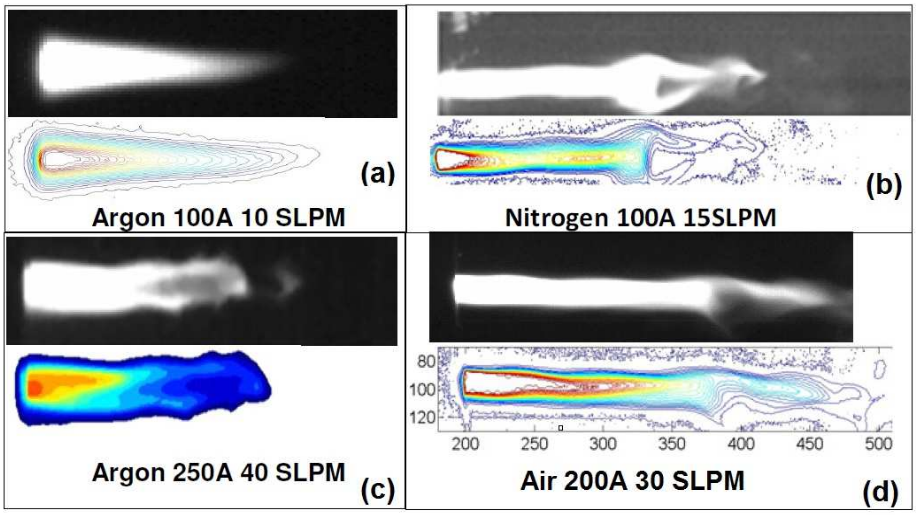

Figure 5.6: Interesting dynamics observed in the external plasma jet through fast photography (a) Typical laminar plasma jet in argon (b) observed sudden termination of the jet in nitrogen plasma (c) Observed bifurcation of the external jet in the middle in argon (d) sudden termination in the air plasma jet with highly uniform jet structure.

Hence the ‘red’ in the colour scheme roughly corresponds to 7700K and the lowest level corresponds to ambient temperature. Typical gray scale image of a plasma jet, usually addressed in literature is presented in Figure 5.6(a). The image is for an argon plasma jet, carrying current of 100A under gas flow rate of 10 slpm. It exhibits smooth axi-symmetric laminar behaviour. Because of drastic intensity cut imposed on the camera, only the extremely luminous core region of the jet is visible. Plenty of studies have been made on behavior of this type of jets and its downstream air entrainment through schlieren, shadowgraphy and CARS techniques [8]. However, it is interesting to note that none of these studies reported about the jet characteristics presented in Figure 5.6 (b),(c) or (d), although they are found to be very common and originates from the very nature of the arc itself as explained in the subsequent sections. Possibly the kind of structures existing inside the core of an extremely intense jet could not be revealed by schlieren or shadowgraph due to extreme luminosity in the region of interest. Thanks to the features of fast camera where intensity of the captured image can be reduced to an appropriate level keeping only the regions above certain luminosity level visible.

Figure 5.6 (c) presents the gray scale image and intensity contours of an argon plasma jet only but at higher current. Rather surprisingly, it is observed that the extremely intense core is now divided into two parts from the middle. Obviously, such bifurcation is not due to air entrainment as that happens only in the downstream region and not in the core, immediately after the nozzle exit. Figure 5.6 (b) presents a nitrogen plasma jet with current of 100A and flow rate of 15 slpm. It is observed that the jet exhibits sudden termination after some length as if the jet is facing a rigid barrier at that location on its path. However, it is observed that the hot luminous plasma is allowed to pass through either side of the barrier giving the jet the shape of a crab's claw. Figure 5.6 (d) presents an air plasma jet with current of 200A and flow rate of 30 slpm. Unlike usual shape like Figure 5.6 (a) it is strikingly rectangular in structure with nearly uniform intensity. While sudden termination of the jet as in Figure 5.6 (b) is observed here as well, the hot plasma passes through only one side of the structure in this case. Needless to say that the features observed in these Figures may have profound impact on the processing applications. In the following, we investigate the features in detail and probe origin of these structures of technological importance.

5.3.2.1 Instability features in argon plasma jet

Existing literature usually classifies instabilities in conventional dc non-transferred arc plasma torches into two broad categories: Helmholtz oscillations and restrike mode instabilities [12]. The first one is a resonant type, believed to occur due to mechanical coupling between pressure oscillations inside the cathode cavity and the arc voltage. While the second one is a random or chaotic type, usually present in most of the torch operations due to movement of the anode arc root. The resultant instability is considered as a superposition of these two oscillations. It has been reported in literature that the restrike mode instability is usually associated with the formation of plasma blobs in the moving jet which have potential to seriously affect the processing jobs [13]. Typical frequency of Helmholtz oscillation, suspected to be related with the volume of the cathode cavity, is an order of magnitude less compared to the frequency of restrike mode oscillations. However, it has been reported that geometry of the torch and operating parameters can be adjusted to match frequencies of these two oscillations [12]. The instabilities are reflected in the overall arc voltage which can be measured and analyzed. Similar observations are noted in the present study also specifically in the regimes of low arc currents and low gas flow rates [Figure 5.6(a)]. However, at higher current and higher gas flow rates very interesting behaviour is observed, not reported in these earlier studies. Observations apparently do not directly follow the mechanisms described above and need further investigation for explanation. In the following we specifically present the results obtained in the later cases.

Twenty one consecutive images of an argon plasma jet, operating at an arc current of 250A and flow rate of 40 slpm are taken at an interval of 55 μs and presented in Figure 5.7 (b). Corresponding voltage, current and camera trigger instants are presented in Figure 8(a).

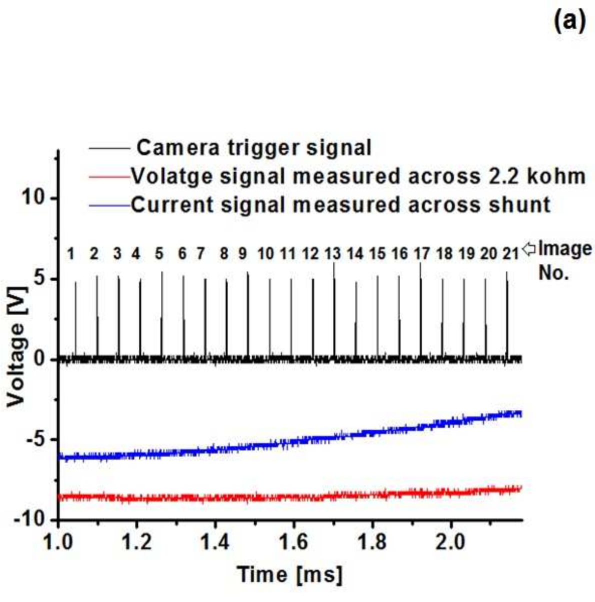

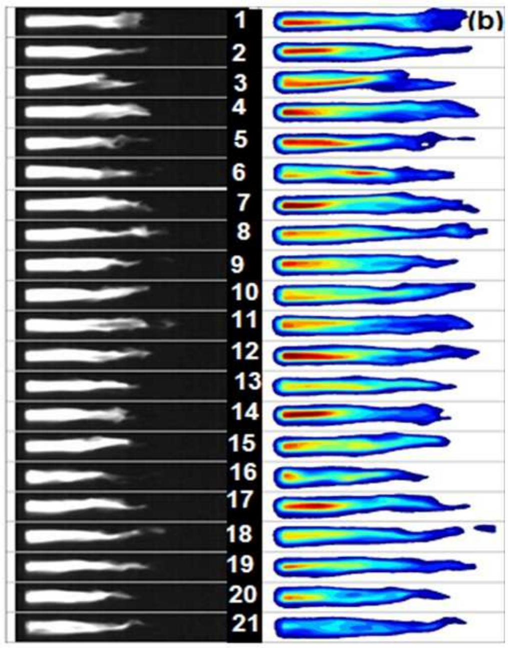

Figure 5.7: (a) Voltage and current signal during fast photographic acquisition in argon plasma jet [250 A, 40 lpm]. (b) Instability features observed in consecutive 21 frames (t=1.04 ms to t=2.14 ms) at an interval of 55 microseconds. Corresponding image numbers are printed on both.

The trigger instants are numbered in both Figure 5.7(a) and Figure 5.7(b) for easy identification. The specialty of this data set is that the arc voltage remained nearly constant [see Figure 5.7(a)] throughout the shots. Interesting point to note is that although the arc voltage remained fairly steady and exhibited no instability, the external plasma jet exhibited wide range of instabilities in this period [Figure 5.7(b)]. For example, apart from the instabilities in the downstream, clear formation of plasma blob is observed in 6^{th}, 15^{th} and 16^{th} frames and vivid bifurcation in the middle of the jet is observed in 7^{th}, 9^{th}, 11^{th}, 12^{th} and 20^{th} frames

Possible mechanism of the observed behavior is presented in Figure 5.8. The explanation is based on the direct observation of the arc paths presented in Figure 5.1. It is observed in Figure 5.1 that part of the arc path may extend into the plume region beyond the nozzle exit as shown in Figure5.8 (a) or it may stay inside the nozzle bore as shown in Figure 5.8(b). Degree of extent of the current path into the plume may vary depending on the particular nature of the gas, operating current and geometry of the torch. For example, while we successfully recorded the external current paths in nitrogen and air plasma [Figure 5.1], we failed to record the same in argon. However, phenomenological evidences as described above indicate that such current paths, transverse to the plasma flow exist in case of argon plasma as well. Possibly the path stays well inside the nozzle bore in case of argon, keeping it outside the field of view of the fast camera.

When the current path extends into the plume region [Figure 5.8(a)], it inevitably includes a region in the plume where current path is transverse to the flow direction. This is because the current path which has entered in to the plume region must return back to the anode for current continuity.

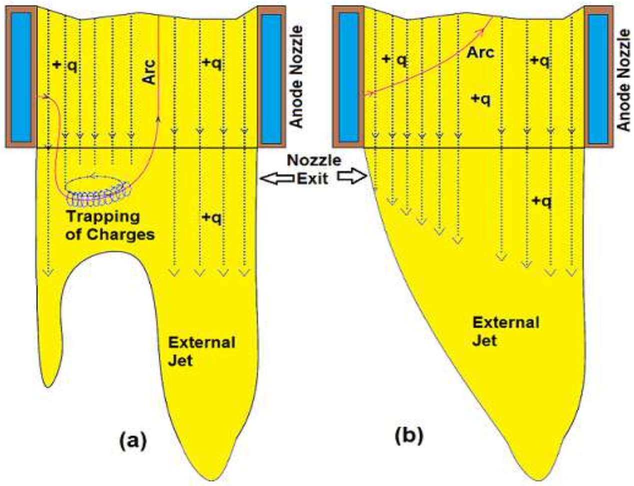

Figure 5.8: Possible mechanism of formation of structures inside an arc plasma jet (a) current path extending into the plume region (b) current path inside the nozzle bore.

The current path, transverse to the plasma flow produces magnetic field which is normal to the plasma flow (pointing out of the paper in Figure 5.8 (a)). When the charged particles in the flowing plasma face this magnetic field transverse to their path they simply get trapped by the field and start orbiting around the magnetic field [Figure 5.8 (a)]. In course of time they may produce more ionization in the region through collision but they do not move further in the direction of the plasma flow. The field lines act as a solid barrier to the flowing plasma. However, gases near the nozzle wall have relatively lower temperature and low degree of ionization. It must be noted that the magnetic field is not a barrier at all to the gas particles which are neutral. Therefore, while the magnetic field acts as a solid barrier to the plasma flow in the central region owing to availability of high degree of ionization, it is not so in the region close to the nozzle wall. Hot luminous but neutral gas may leak from either side of the central region. Observed 'crab's claw' shape of the plasma jet, bifurcating from the central region may be explained from this. The formation of plasma blob observed in Figure 5.8(b) may have contribution from the increase in plasma conductivity in the region through collisional ionization by the trapped rotating charged particles. Detachment of blob might have occurred to ascertain minimum arc voltage configuration.

There is another possible current configuration where the current path does not extend into the plume region as shown in Figure 5.8(b). This configuration also can generate component of magnetic field transverse to the flow on one half of the flow path (left side in Figure 5.8(b)) but the magnetic field component will have much weaker strength compared to that discussed for Figure 5.8(a). Resulting flow may have asymmetry due to the barrier imposed by the generated field component as presented in Figure 5.8(b).

5.3.2.2 Instability features in nitrogen plasma jet

Observed instability features for nitrogen plasma are presented in Figure6.9. Behaviour of the external jet has been studied under different flow rate of the plasma gas as well as different arc currents. While observed behaviour is found to be substantially different from that in argon in many respects, underlying mechanism, responsible for different observed structures inside the plasma jet, appears to be the same. Notably, observed behaviour in nitrogen plasma is found to be very similar to that exhibited by air plasma.

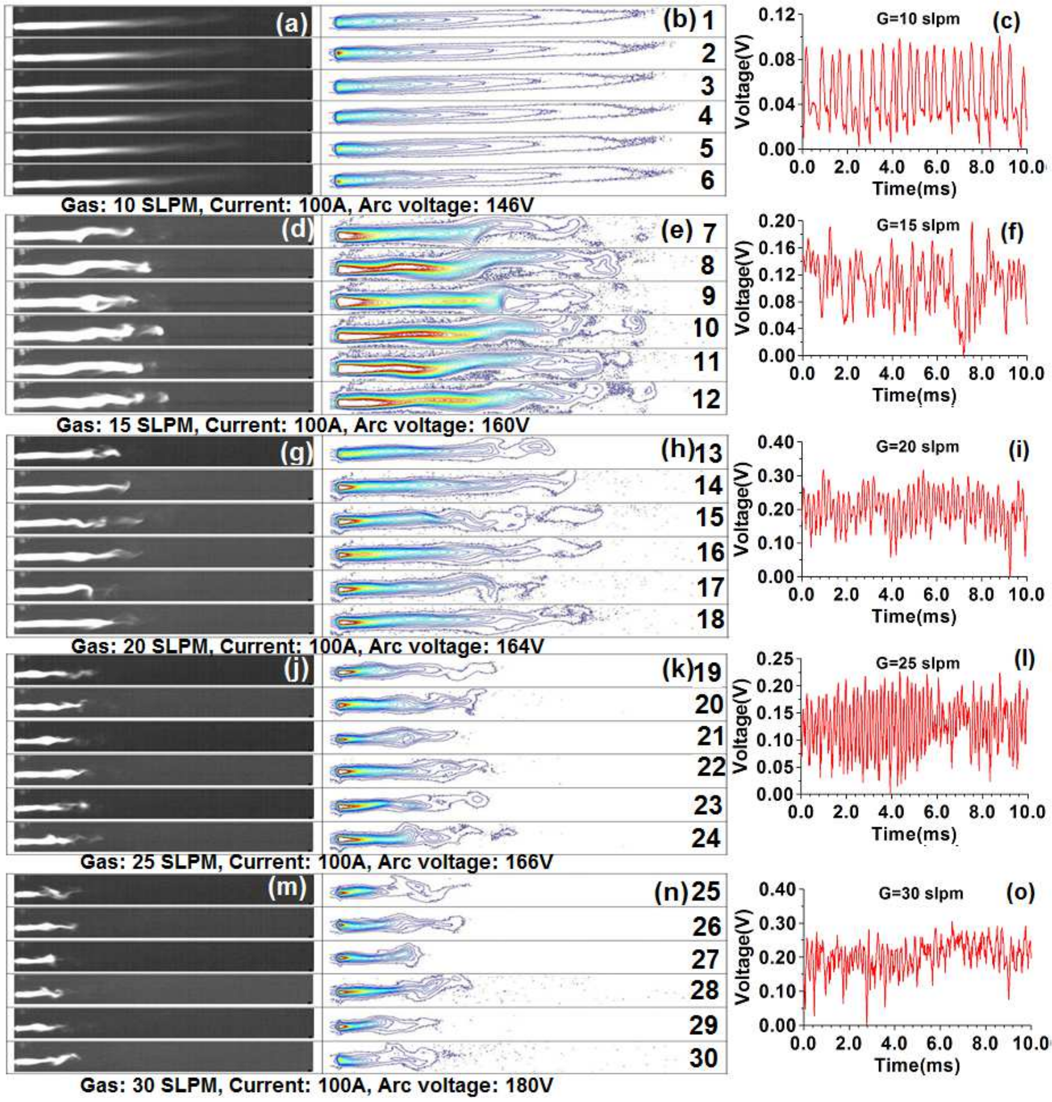

Figure 5.9: Instability features in nitrogen plasma jet under different flow rates.

Due to this, behaviour of nitrogen plasma with gas flow rate alone is presented in this section for a fixed arc current, and in the next section behaviour of air plasma for a fixed gas flow rate is presented under different arc currents.

In Figure 5.9, the flow rate of nitrogen varies from 10 slpm to 25 slpm in step of 5 slpm for a fixed current of 100A. In each row the first Figure presents the gray scale images captured by the fast camera at five different instants under the same operating condition, the second one gives their intensity contours and the third one gives the arc voltage waveform captured while the fast photographic images were taken. It is observed that for gas flow rate of 10 slpm, the external plasma jet is fairly laminar [Figure 5.9 (a) & (b)]. The voltage instability exhibits highly periodic behaviour with low amplitude [Figure 5.9 (c)]. However, as the flow rate increases by 5 slpm, the behaviour changes drastically as reflected in both jet structures and voltage waveforms [Figure 5.9 (d), (e) & (f)]. Length of the hot core of the plasma jet increases by many folds and features similar to argon plasma like sudden termination of the jet become clearly visible. For example, the third snap (#9) in Figure 5.9 (d) assumes the 'crab's claw' like structure discussed earlier, while the first snap (#7) assumes a shape as if the jet is impinging on a slanting surface. We have examined that under such conditions the current path extends deep into the external jet and mostly assumes 'α' configuration [Figure 5.1] and evolves continuously. Under 'α' configuration, relatively colder gas near the wall of the exit nozzle has enough possibility to enter into the middle of the external current loop. This in turn has potential to change in the angle of the transverse current path with respect to the direction of plasma flow. Depending on the angle, the imposed barrier may or may not be normal to the plasma flow. In the first case, the jet may assume a 'crab's claw' like configuration, whereas, in the second case the jet may assume shape as if impinging on a slanting surface. However, in all the cases the flow of hot gas is noticed either from one or both the sides of the barrier. Here it may be pointed out that the phenomenon is fully three dimensional in nature and evolving with time. The fast camera is looking at it only from one side. In case, the jet poses in a way that the camera grabs the flow from the sides of the barrier, the barrier effect may not be observed distinctly. Instead, images like (#8,#10,#11,#12) of Figure 5.9(e) may be observed, where the effect of barrier is observed only partially. Corresponding instability in the arc voltage [Figure 5.9 (f)] indicates that amplitude of voltage oscillation as well as its frequency is increased and it is more erratic in nature.

Figure 5.9 (g), (h) and (i) represent the results when nitrogen gas flow rate is increased further by 5 slpm. While features similar to previous case is observed, distinct differences are observed in the length of the hot core and dominant frequencies in the voltage instability. As gas flow rate increases under constant current operation, larger amount of gas gets heated by nearly similar power. Energy balance demands lower temperature of the plasma. This in turn reduces its electrical conductivity, especially in the downstream region and shifts current path towards 'β' configuration from 'α' [Figure 5.1], causing decrease in the jet length. Also, as curvature of the current path substantially decreases under 'β' configuration, the forward thrust due to magnetic pressure decreases "Ghorui et al. (2015)." favoring decrease in the jet length. Figure 5.9 reveals that as gas flow rate increases further, the effect shows it influence and average length of the plasma jet decreases monotonically while reverse was obtained for the case of argon plasma. To see the variation in length, image was calibrated. Calibration and variation of luminous jet length for argon and nitrogen plasma at fixed current 175A are shown in Figure 5.10. Figure 5.10(b) shows that length of the argon plasma jet increases from 29 mm to 40 mm by increasing gas flow 10 to 30 lpm, further increase of gas flow rate decreases length of the plasma jet, while for nitrogen plasma, luminous length of the plasma jet decreases with increase in gas flow rate as shown in the Figure 5.10c.

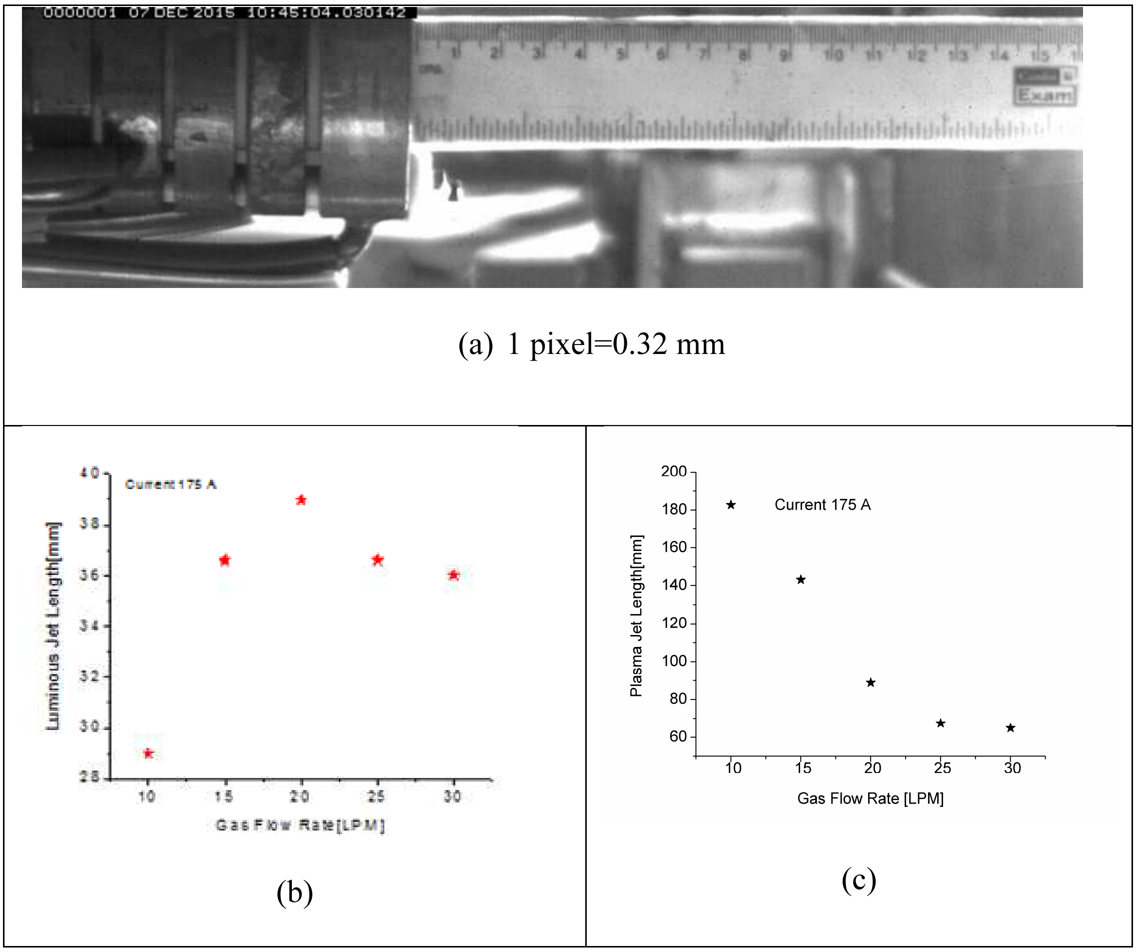

Figure 5.10: Variation of luminous jet length with gas flow rate (a) Calibration of length (b) For argon plasma (b) For nitrogen plasma

5.3.2.3 Instability features in air plasma jet

Instabilities in air plasma jet are presented in Figure 5.11 for a fixed gas flow rate of 30slpm and arc currents of 125A, 175A, 200A and 225A. Sudden termination of the arc at barriers posed by transverse magnetic field, similar to previous cases has been observed at all currents. Most of the time, the barrier is observed as if the jet is impinging on a slanting surface. With increase in arc current, the length of the hot core is found to increase significantly without much change in the features of voltage instability up to an arc current of 200A [Figure 5.11(a)-(i)]. Enhanced magnetic pressure at higher current results in higher forward thrust, which might be responsible for the increased length of the external plasma jet observed [14]. However, after current around 200A, the average length of the hot core of the plasma jet start decreasing again as observed in Figure 5.11(j) at an arc current of 225A. Through fast photography, it has been observed that most of the time the jet operates with current path in 'α' configuration [Figure 5.1].

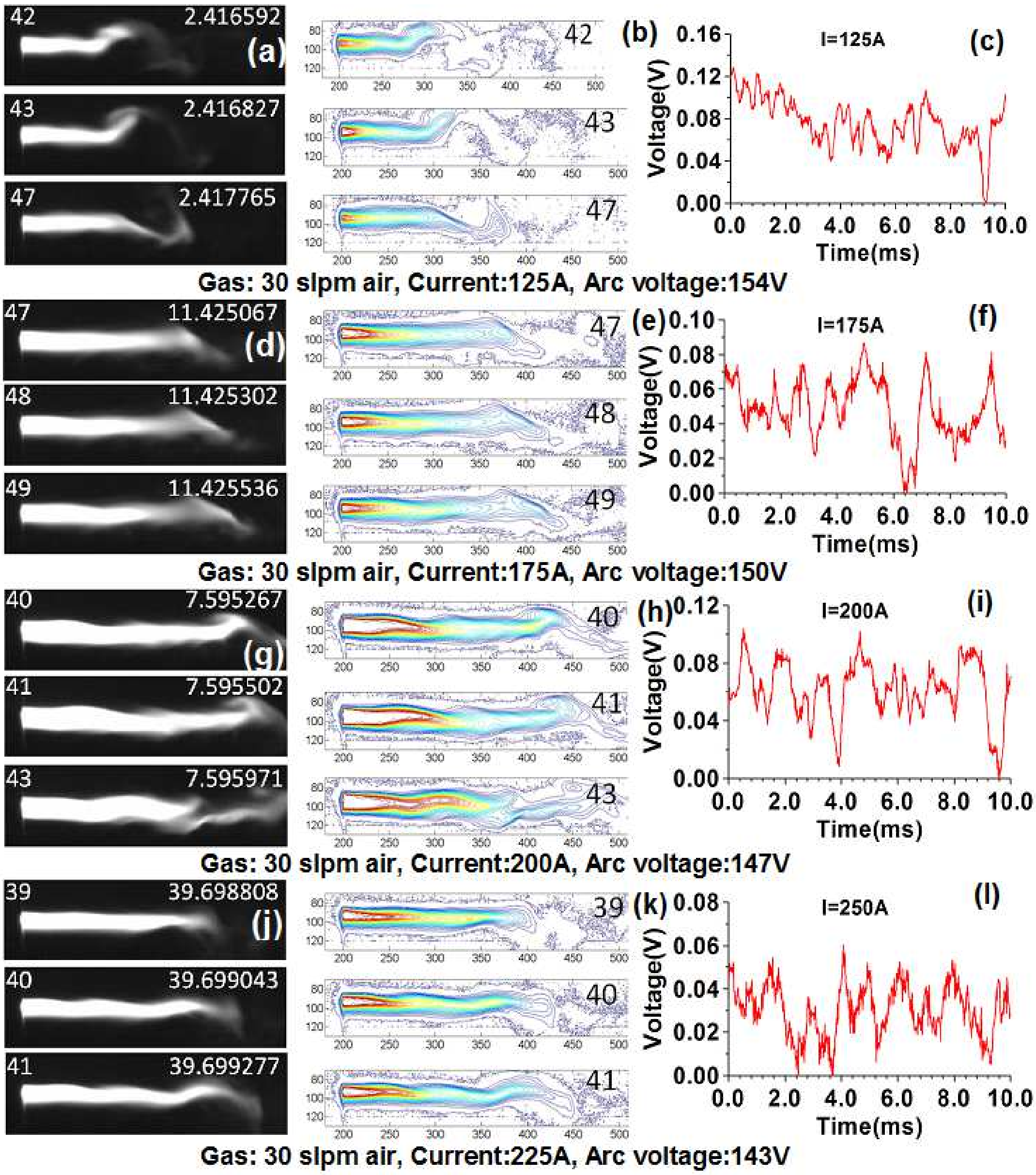

Figure 5.11: Instability features in air plasma jet under different arc currents. (a)-(c): 125A, (d)-(f):175A, (g)-(i):200A and (j)-(l): 225A.

In this configuration there exists one forward and one return current path nearly parallel to each other. Since opposite currents repel, the bending curvature at the return point gets reduced when higher electrical conductivity of the plasma favors that at higher temperature. Once the curvature gets reduced, the forward thrust due to magnetic pressure reduces and so does the length of the plasma jet at higher current. Fast photography has revealed that while most of the time the current path in 'α' configuration exists, sometimes the jet may operate with simultaneous current paths in 'α', 'β' and 'γ' configuration together or with any combination of them. In the later cases three dimensional shape of the jet may assume some irregular shape depending on the type of current paths established. In the voltage wave form it has been found that a high frequency but low amplitude voltage oscillation get superimposed on the usual re-strike type behaviour of arc voltage at 225A [Figure5.11(i)]. That may be an indicative of higher stiffness of the current path at higher current.

5.4 Summary and conclusion

Structures and stabilities in the external plasma jet of argon, nitrogen and air have been investigated through numerical simulation as well as experimental study. Emission spectroscopy, fast photography and record of voltage instability in a time synchronous manner revealed number of interesting features of the external jet, previously unexplored. Standard image processing techniques have been used to investigate internal structures of the external plasma jet. A calibration procedure is established for a rough estimate of temperature distribution inside the jet. While most of the earlier studies assume a current free external jet and naturally do not consider its effects, the present study establishes that arc current may extend into the external jet region and significantly influence its structure and stability, one of the most important concerns for technological applications. Behaviour in monatomic gases like argon is found to be significantly different from that in molecular gases like nitrogen and air. Whereas, nitrogen and air are found to exhibit nearly similar features. It has been observed that presence of transverse current in the external jet acts as a rigid barrier to the ionized part of the plasma, mainly occupying the central region of the jet. The effect has been vividly seen in all the gases studied. A new type of instability, apart from the usual Helmholtz and restrike type, originating from the current carrying feature of the jet has been observed in argon plasma and investigated thoroughly. Carried out numerical simulation of the current free jets in argon, nitrogen and air revealed that the external jet length in argon is expected to be much smaller than that in nitrogen and air under identical operating conditions. It is also revealed from simulation that highest instability (turbulent intensity) is expected in air and lowest in argon. Reduction in jet length as an effect of air entrainment in the external plasma jet has also been established from simulation for all the gases. The differences originate purely from intrinsic thermodynamic and transport properties of the plasma gases alone and observed experimentally as well. However, features in the actual experimental behavior of the plasma jets are found to be drastically different from that predicted by numerical simulation of the current free jets. Instead of expected typical laminar structure with effect of turbulence in the downstream, sudden termination of the plasma jets, bifurcation of the external jet from the middle, jet structure with highly uniform intensity over a long length are some of the interesting aspects observed. Both in nitrogen and air plasma the jet length is found to monotonically decrease with increase in gas flow rate. With increase in current, it has been observed that there is an optimum current up to which the jet length increases with increase in current and after that it starts decreasing again. Possible explanation of all the observed phenomena has been given from current carrying features of the external jet established from fast photography. It is believed that the obtained results will contribute significantly towards enhanced understanding of the external plasma jets for process applications and theoretical developments.

References:

1. Ghorui, S., Tiwari, N., Meher, K. C., Jan, A., Bhat, A., and Sahasrabudhe, S. N,. "Direct probing of anode arc root dynamics and voltage instability in a dc non-transferred arc plasma jet", Plasma Sources Sci. Technol. 24, 065003, (2015).

2. Ghorui, S., Meher, K. C., Kar, R., Tiwari, N. and Sahasrabudhe, S. N., "Unique erosion features of hafnium cathode in atmospheric pressure arcs of air, nitrogen and oxygen", J. Phys. D: Appl. Phys. 49, 295201 (2016).

3. Patankar, S. V., "Numerical heat transfer and fluid flow", New York : McGraw-Hill, ISBN No.: 0-89116-522-3 (1980).

4. Meher, K. C., Tiwari N., Ghorui S., "Thermodynamic and transport properties of nitrogen plasma under thermal equilibrium and non-equilibrium conditions", Plasma Chem Plasma Process, 35, 605–637 (2015).

5. Ghorui, S., Heberlein, J. V. R., Pfender, E. "Thermodynamic and transport properties of two-temperature nitrogen-oxygen plasma" Plasma Chem Plasma Process, 28, 553–582((2008).

6. Boulos, M.I., Fauchais P., and Pfender E., "Thermal plasmas: fundamentals and applications," 1, ISBN0-306-44607-3 (1994).

7. Te, Ba, Chang, W. K., and Heong, W. N., “Numerical study of the plasma flow field and particle in-flight behaviour with the obstruction of a curved substrate”, Journal of Thermal Spray Technology, 18, 859-874, (2009).

8. Pfender, E., Fincke J. and Spores R., “Entrainment of cold gas into thermal plasma jets”, Plasma Chemistry and Plasma Processing, I1, 529-543(1991).

9. See https://www.mathworks.com for image processing.

10. Lofthus, A., and Paul, H. K., “The spectrum of Molecular Nitrogen”, J. Phy. Chem. Ref. Data, vol.6., No1, (1977).

11. http://www.sri.com/psd/lifbase/24.05.12.

12. Krowka, J., Rat, V. and Coudert, J. F., “Investigation and control of dc arc jet instabilities to obtain a self-sustained pulsed laminar arc jet”, J. Phys. D: Appl. Phys. 46, 505206 (2013).

13. Coudert, J. F., Planche M. P., and Fauchais, P., “Velocity measurement of dc plasma jets based on arc root fluctuations” Plasma Chemistry and Plasma Processing, 15, 47-70 (1995).

14. Trelles, J.P., Pfender E. , Heberlein J., “Multiscale finite element modelling of arc dynamics in a DC plasma torch”, Plasma Chem Plasma Process 26, 557–575 (2006).

Chapter-6

Study of Arc Instabilities Driven by Thermal State of Anode Boundary Layer and its Consequences on Overall Torch Efficiency

Outline of the Chapter

Chapter 6

Study of Arc Instabilities Driven by Thermal State of Anode Boundary Layer and its Consequence on Overall Torch Efficiency

6.1. Introduction

This chapter presents possibly the first experimental data revealing significant dependence of electro-thermal efficiency (ETE) on degree of anode cooling. Maximum temperature handled by typical arc plasma torches may easily exceed tens of thousands of degree Kelvin. External cooling of the thermally stressed components of the torch is unavoidable. In doing so, significant amount of energy is lost by the plasma to the cooling fluid. Efficiency of a plasma torch is determined by the amount of energy retained inside the plasma. Depending on operating regime and torch configuration, typical efficiency of a non-transferred arc torch may vary within 30%-70 %. While the same in transferred arc torches may go beyond 90%. Any commercial application naturally attracts torches with higher efficiency. Even a slight increase in the efficiency may prove substantially beneficial. Although, numerous researches are done on plasma torches, little attention is paid to the desired rate of electrode cooling for maximum efficiency. In most of the applications, it is grossly decided by the maximum allowable outlet temperature of the coolant.

Unusually high ETE was observed for a specific range of cooling rates of the anode. Observed behaviour was examined under different PGFRs as well as different arc currents and found to be highly reproducible. The effect was more pronounced at lower arc currents, and gradually diminishes as arc current increases. Anode cooling significantly influences the thickness of the anode boundary layer, which in turn influences the instability features of the arc. While, thickness of the anode boundary layer itself may have appreciable effect on anode heat transfer, the dynamic pattern formation of arc foots over the anode also may have significant bearing on the overall heat transfer. Direct access of the anode region to investigate the pattern formation is not possible in actual devices, primarily due to mechanical obstruction and uncertainty in the location of the highly dynamic arc foot. However, as the location of the arc foot or its nature (diameter, temperature, electrical conductivity etc.) changes, it keeps a signature of that in the total arc voltage, which is precisely measurable. It is noted that in case of simultaneous multiple arc roots (as in pattern formation), there is certain possibility that effect due to one gets compensated by the other and not reflected in the total arc voltage. In spite of such possibilities, the arc voltage is expected to bear the best signature of the internal arc dynamics and its analysis may reveal the origin of high electro-thermal efficiencies observed.

Observed fluctuations in the total arc voltage under different rates of anode cooling were analyzed in the present study using standard tools of dynamical analysis like time series, frequency spectrum, phase portrait, dimension, and Lyapunov exponent. Accurate estimation of dynamic properties of a nonlinear system is a complex task. In literature, there are examples of claims and counterclaims in establishing a particular nature of dynamics due to improper application of the tools, lack of benchmarking standards and rigorous analysis schemes[1-4]. A time series alone cannot identify whether a signal is periodic, chaotic, or random. While part of the time series of a chaotic system may well look like a periodic signal, a random looking signal may actually be a chaotic signal [5-6].

Phase portrait of a system is the gateway to look into its dynamical aspects. It can clearly identify periodic and aperiodic systems but fails to distinguish multi-periodic and chaotic systems. In the latter two cases, the dynamics in phase space occur within a well-defined basin of attraction having peculiar structure called strange attractor. The strange looking structures (phase portraits) in phase space exhibit integer dimension for multi-periodic systems but fractal dimension for chaotic systems. However, observing strange attractor with fractal dimension is not a definitive test for chaotic dynamics. Attractors are reported with fractal dimensions but non-positive Lyapunov exponent, a criterion necessary for a system to be chaotic [7-9].

Underlying nature of a complex signal becomes surprisingly vivid when signal is analyzed in frequency space. A very complex looking multi-periodic time series may offer only few distinct spikes in the frequency space. Random signals exhibit continuous band spectra with highest power at zero frequency. On the other hand, chaotic signals exhibit continuous, broadband spectra, spiked at predominant frequencies.

Lyapunov exponent gives the rate of expansion of the nearby trajectories in phase space. A deterministic system may have as many Lyapunov exponents as the dimension of the phase space in which the dynamics is being analyzed. If at least one of these exponents is definite positive, the system is chaotic. Unfortunately, sometimes random noise also exhibits finite positive value of Lyapunov exponent [10-12]. Noise being an infinite dimensional process, an infinite dimensional reconstruction phase space is required to achieve the ‘zero’ value of the exponent, which never comes out in practice. However, it may be clearly observed that the exponent value tries to reach its exact theoretical value as analysis is carried out in higher and higher dimensional state space. Any experimental signal always carries some noise component which may contribute towards false positivity of the exponent value. Analysis must be done in state space of various dimensions to check for its stationarity. As contribution from noise component dies down fast as state space dimension increases, the stationary positive value of the exponent, if any, becomes prominent at higher dimensional state space.

Given a continuous dynamical system in n dimensional state space, an infinitesimal n-sphere of initial conditions will evolve with time to an n-ellipsoid due to locally deforming nature of the flow. The i^{th} one dimensional Lyapunov exponent is then defined in terms of length of the ellipsoidal principal axis $p_i(t)$ given by [13-14]

$$\lambda_i = \lim_{t \to \infty} \frac{1}{t} \log_2 \frac{p_i(t)}{p_i(0)} \qquad 6.1$$

For computation of the largest Lyapunov exponent from experimental time series, a direct algorithm proposed by Wolf et. al. [15] has been used. This algorithm is widely used, robust, completely general, capable of computing all the exponents, and well suited for a variety of dynamical systems [16, 17]. However, for detection of chaos, only largest Lyapunov exponent (λ_1) needs to be computed and the use of the fixed evolution time program of Wolf [15] is sufficient for this. Details of instruction for computation of this exponent and listing of the code are available in Ref.[15]. Implementation of the algorithm in the present case is presented in the experimental part.

Similar is true for estimation of dimension of attractors. The assumption that deterministic dynamics yields convergence of the slope of the correlation integral at a finite and small value, indicating a low dimensional attractor is not always true. Insufficient number of data points and linear correlation in the data may lead to false convergence, which creates illusion of proof of chaos where there is none [1-4]. An algorithm developed by Ghorui et.al. [14], benchmarked against standard systems, has been used in estimation of correlation dimension.

Section-6.2 gives the experimental details. Result and analyses of the signals are presented in section-6.3. Summary and conclusions are presented in section-6.4.

6.2. Experimental details

The experimental setup used in the study is presented in Figure 3.3 of chapter 3. The torch is operated with argon. It uses 2% thoriated tungsten cathode with diameter 10 mm and tip angle 60^0. The conical anode is made of copper having exit bore diameter of 4 mm and a straight portion of length 12mm in the nozzle exit. The torch possesses a single inlet port and a single outlet port for cooling water, supplied by a chiller unit at a specified temperature. A flow meter measures the water flow rate with accuracy better than ±0.1 lpm (litre per min). The inlet (T_1) and outlet (T_2) temperatures are measured using RTD (resistance temperature detector) with accuracy better than 0.4%. The torch is operated with an IGBT (Insulated Gate Bipolar

Transistor) based constant current power supply with ripple less than 0.1%. Arc current can be continuously varied up to 500A and precisely controlled. For a given operating power, efficiency of the torch is determined using calorimetric method from the measured water flow rate, inlet and outlet water temperatures. Temperature of the plasma jet is determined from emission spectroscopy. Measurements were taken for torch current ranging 100A-200A in steps of 50, Gas Flow Rate from 10 lpm to 40 lpmin steps of 10 and water cooling flow rate from 4 lpm to 9 lpm in steps of 1.

6.3. Results and Analysis

6.3.1 Impact of CFR on efficiency of the plasma torch

The electrical energy input to the plasma torch is estimated as:

$$P_{in} = V_{arc}.I_{arc} \tag{6.2}$$

The energy loss due to cooling of the torch components is estimated as:

$$P_{out} = m.s.(T_{out} - T_{in}) \tag{6.3}$$

m and s are mass flow rate and specific heat of water respectively. T_{out} and T_{in} are the outlet and inlet water temperatures.

Efficiency of the torch is estimated as:

$$\varepsilon = \frac{P_{in} - P_{out}}{P_{in}} \times 100\% \tag{6.4}$$

For a given operating condition, efficiencies were calculated from six independent measurements and average of them is taken as the ETE corresponding to that particular operating condition. Observed average deviations from the mean value out of the six measurements are indicated by the bars attached to respective data points in the graphs. In the experiment, cooling flow rate (CFR) is varied from 4 lpm to 9 lpm in step of 1 lpm. Plasma Gas flow rate (PGFR) is varied from 10 slpm to 40 slpm in step of 10 slpm and arc current is from varied 100A to 200A in step of 50A.

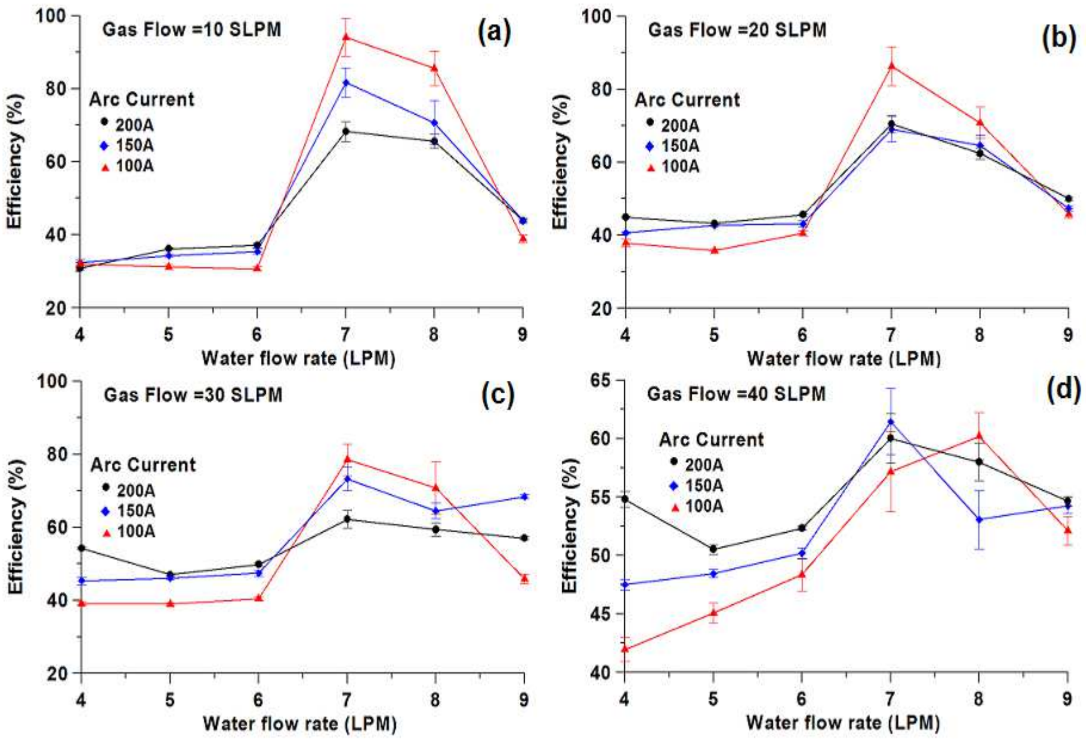

Figure 6.1: Variation of torch efficiency with CFR under different arc currents (a) plasma gas: 10 slpm (b) plasma gas: 20 slpm (c) plasma gas: 30 slpm (d) plasma gas: 40 slpm

Figure 6.1 (a) presents the estimated efficiencies at different arc currents for a PGFR of 10 slpm. It is observed that as long as anode cooling water flow rate is below 6 lpm, the torch consistently shows its usual efficiency (<40%) at all currents. It also exhibits the trend of higher efficiency at higher arc currents. The values and the trends are very typical to non-transferred arc plasma torches. However, as CFR increases to 7 slpm, the efficiency of the torch suddenly shows a big jump. The trend with current reverses and now higher efficiency is observed at lower arc currents. As presented in the graphs, such increase in efficiency at this particular flow rate has been observed at all currents through independent measurements. Notably, the jump is relatively smaller at higher currents. As CFR increases further to 8 lpm, efficiency still remains very high but shows a decreasing trend. However, the trend of higher efficiency at lower arc current is still maintained. When CFR is increased further to 9 lpm, efficiency shows a sharp fall and reaches again to the values, typically observed in such devices. The trend with current also is now reversed, i.e. higher efficiency is observed at higher arc currents.

Similar studies for other PGFRs (20, 30 and 40 slpm) are presented in Figures 6.1 (b), (c) and (d) respectively. It is observed that the jump in efficiency after certain particular flow rate (6 lpm of cooling water) is observed in all the cases. However, the effect is seen to be less prominent at higher PGFRs [Figure 6.1(d)].

A general observation is that as gas flow rate increases, overall efficiency of the torch increases (except the region where the jump in efficiency occurs). This is expected since increased gas flow rate increases the rate of convective heat transfer, lowers the plasma temperature for a given input power, and increases the thickness of the anode boundary layer. As difference in temperature (between boundary layer and electrode) decreases and thickness of the boundary layer increases, conductive heat loss to the anode, as well as radiative heat loss also decreases. Similarly, higher efficiency at higher arc current is also expected as more heat is generated compared to that lost through loss mechanisms. These are some simple explanations for the enhanced efficiency observed at higher gas flow rates and higher arc currents. However, they fail to explain the jumps in efficiency observed at certain CFRs where relatively lower efficiency is observed at higher PGFRs contrary to what generally expected. Being hinted by the theoretical studies and experimental indications, discussed elaborately in the introduction section, it is suspected that such unusual behaviour at particular water flow rates may have its origin to the internal arc dynamics. This led to investigate the total arc voltage signal in more detail using the tools of dynamical analysis, particularly in the region where such jump in efficiency occurs. Results are presented in the following sections.

6.3.2 Impact of CFR on arc dynamics

Instabilities in arc voltage are inherent in arc plasma devices. Observed steady, takeover and restrike mode of instabilities (Duan et al.18), Helmholtz oscillations (Krowka & Rat et. al. 19), and restrike behaviour of arc are well investigated in literature (Ghorui et.al. 20). Influence of thickness of the cold boundary on arc voltage instabilities in spray plasma torches was investigated by Nogues et al. [21]. The effect of pressure and gas flow rate on the same was studied by Pan et al. [22]. In this section, we have presented the changes in the observed behaviour of arc voltage instabilities as CFR to the anode changes under different PGFRs and arc currents.

In Figures 6.2, 6.3 and 6.4 behaviour of arc voltage is presented for an arc current of 100A, 150A and 200A with CFRs of 5lpm, 7 lpm and 9 lpm. PGFR was varied from 10 slpm to 30 slpm in step of 10 slpm. The specific CFRs were chosen with the facts in mind that efficiency studies in the previous section indicated typical low values for CFRs of 5 lpm and 9 lpm but a significant increase in the efficiency for a CFR of 7 lpm. General observation from Figure 6.2 is that the arc exhibits typical restrike kind of behaviour. Some high frequency oscillations in the arc voltage are superimposed on low frequency oscillations. While some changes in the time series were noticed with change in CFR, they are not very much distinct. In such situation, phase space representation of the dynamics (phase portrait) were resorted, where the differences in the dynamics become vividly visible.

Phase portrait in two dimension may be obtained by plotting any two canonically conjugate quantities of a system, like 'position and momentum' or 'current and voltage' etc. However, such idea fails in unknown systems, where, the canonically conjugate quantities are not known a priori and only a single observable of the system is measured with time. Method of delay coordinate [23, 24] is a powerful technique that can be used in such cases for construction of phase space diagrams from a single time series. In this method, the time series corresponding to a particular signal is constructed by sampling the signal at regular interval (Δt). For an observable $S(t)$ and time delay δt, a m-dimensional phase portrait is constructed from the vectors $[S(t_i), S(t_i + \delta t), \ldots\ldots\ldots, S(t_i + (m-1)\,\delta t)]$, where $t_i = i\Delta t$, $i = 1, 2, \ldots, \infty$. If analysis is done in low dimensional state space, proper unfolding of corresponding attractor may not take place and the computed value of dimension, Lyapunov exponent etc. may not be accurate. For m, greater than minimum required, computed values of dynamical properties start exhibiting their proper values. Choice of δt in the reconstruction is almost but not completely arbitrary [23]. For an extremely low value of δt, folding regions of the attractor become obscured and total extent of the attractor becomes too poor for correct computation. For very large values of δt, consecutive data points in phase space become uncorrelated.

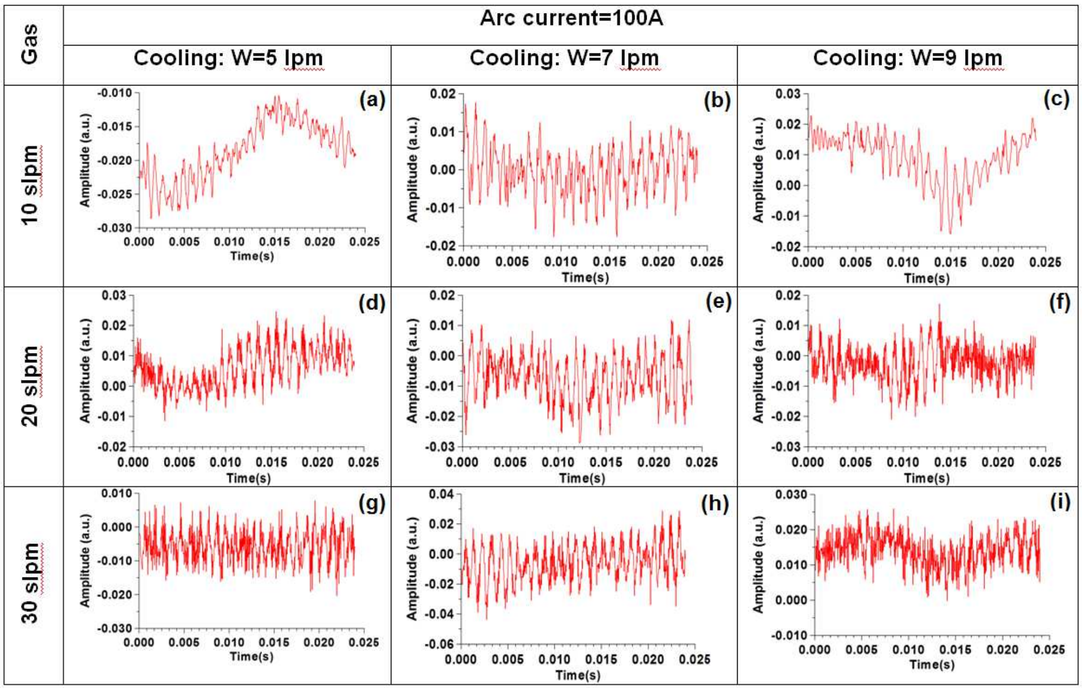

Figure 6.2: Behaviour of arc voltage with different flow rates of coolant for an arc current of 100A. (a)-(c): plasma gas flow=10 slpm; (d)-(f): plasma gas flow=20 slpm; (g)-(i): plasma gas flow=30 slpm.

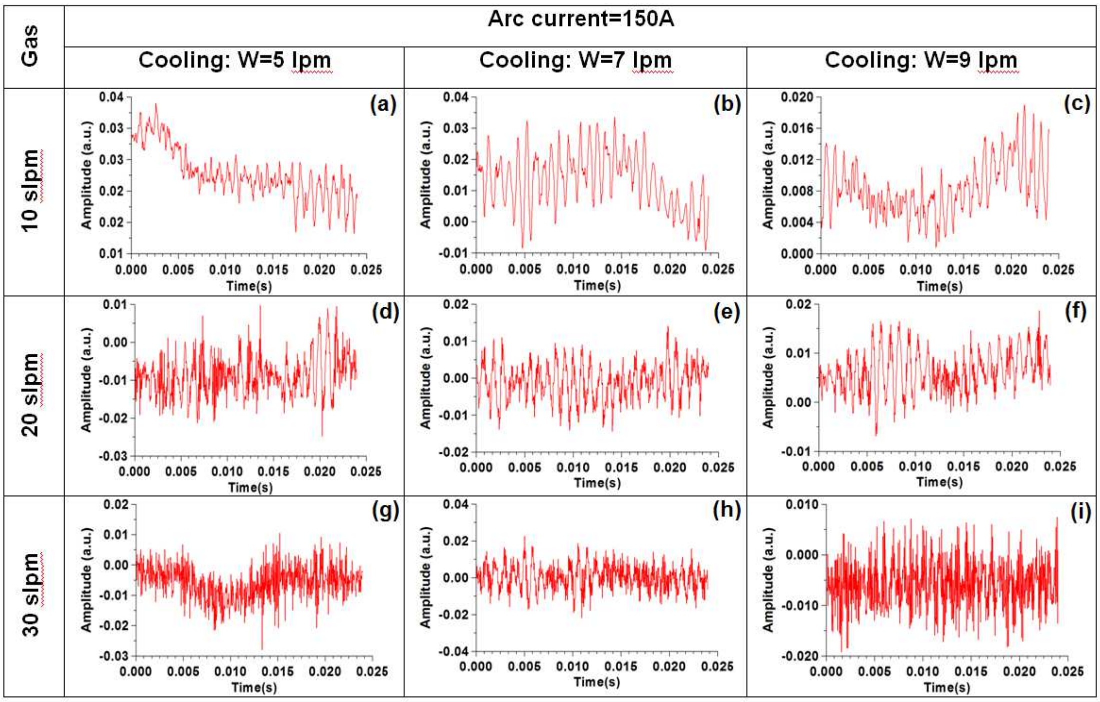

Figure 6.3: Behaviour of arc voltage with different flow rates of coolant for an arc current of 150A. (a)-(c): plasma gas flow=10 slpm; (d)-(f): plasma gas flow=20 slpm; (g)-(i): plasma gas flow=30 slpm.

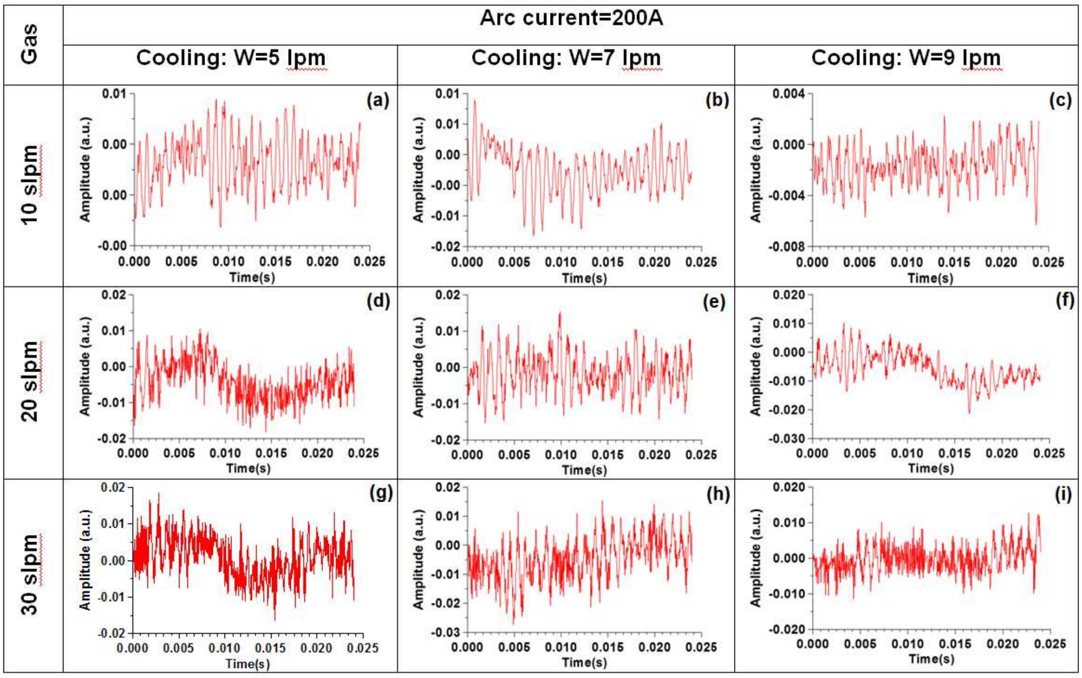

Figure 6.4: Behaviour of arc voltage with different flow rates of coolant for an arc current of 200A. (a)-(c): plasma gas flow=10 slpm; (d)-(f): plasma gas flow=20 slpm; (g)-(i): plasma gas flow=30 slpm.

Phase portraits corresponding to dynamics observed in Figures 6.2, 6.3 and 6.4 are presented in Figures 6.5, 6.6 and 6.7. The differences in the dynamics under different operating conditions are now distinct. It is observed that for an arc current of 100A, as gas flow rate varies from 10 slpm to 30 slpm, associated attractors occupy larger and larger volume in the phase space. However, under a given flow rate of plasma gas and arc current, as CFR increases from 5 lpm to 7 lpm, the phase space volume of the attractor shrinks. Corresponding ETE is found to increase drastically. Interestingly, as CFR increases further to 9lpm, phase space volume of the attractor increases again, corresponding which a sharp decline in the ETE is observed. Nearly similar behaviour is observed for other arc currents 150A and 200A.

While a phase portrait is able to give the exploded view of the dynamical details, exact nature of the dynamics come out when analysis is done in frequency space and values of dimension and Lyapunov exponents of the dynamics are estimated. For general readability, we briefly introduce use of these tools for nonlinear analysis in the next section, and evaluate the credibility.

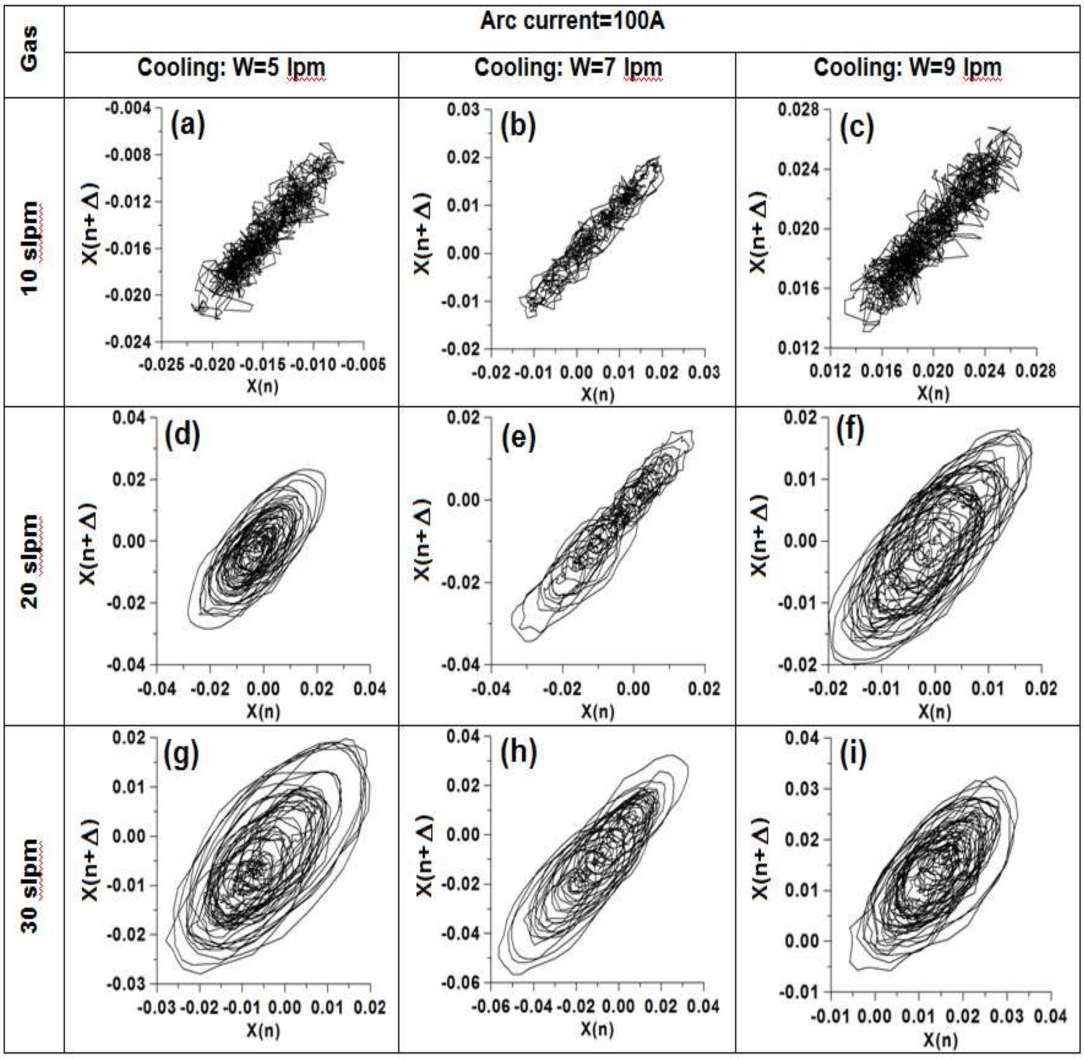

Figure 6.5: Phase space behaviour of arc voltage with different flow rates of coolant for an arc current of 100A. (a)-(c): plasma gas flow=10 slpm; (d)-(f): plasma gas flow=20 slpm; (g)-(i): plasma gas flow=30 slpm.

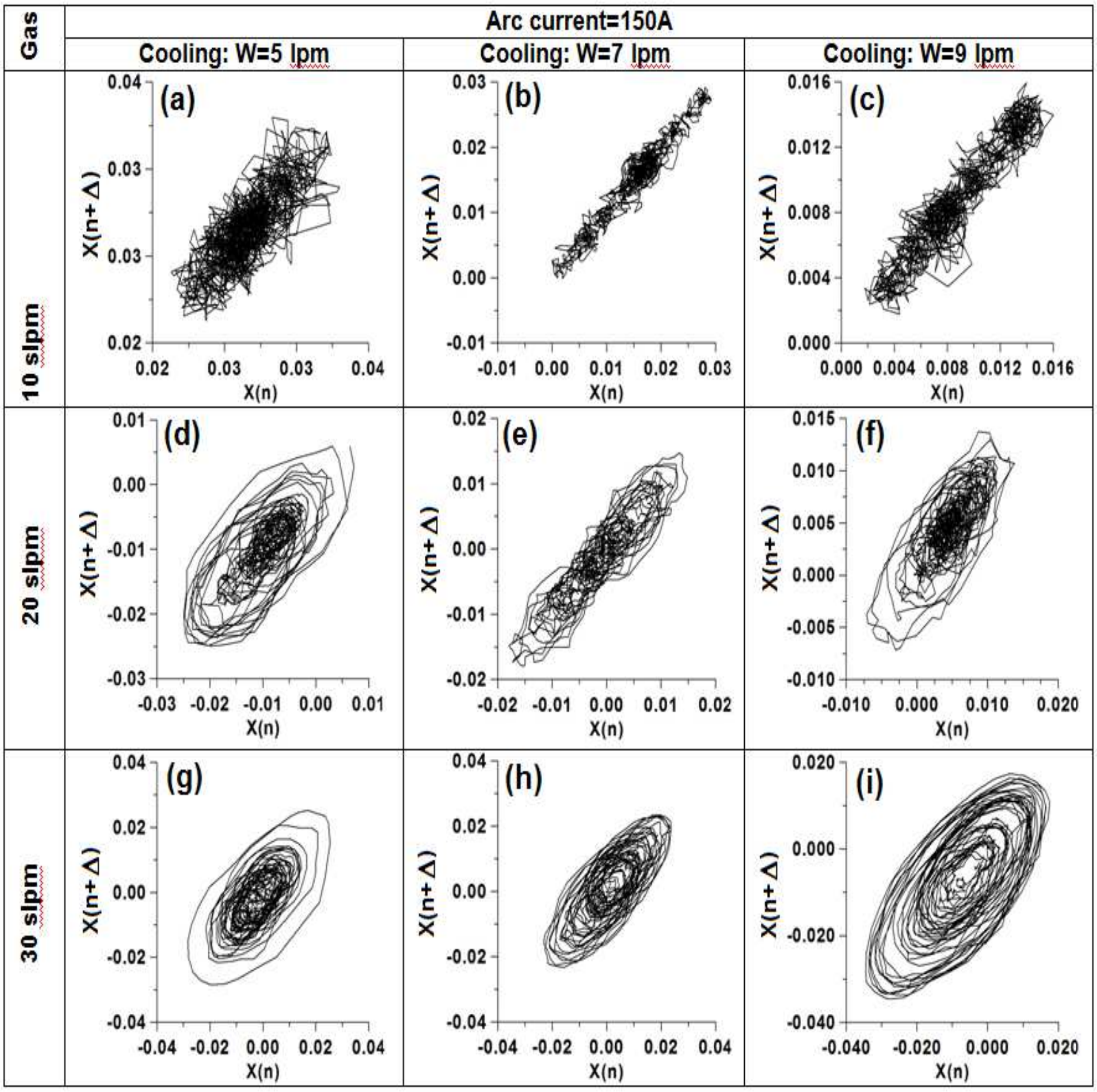

Figure 6.6 Phase space behaviour of arc voltage with different flow rates of coolant for an arc current of 100A. (a)-(c): plasma gas flow=10 slpm; (d)-(f): plasma gas flow=20 slpm; (g)-(i): plasma gas flow=30 slpm.

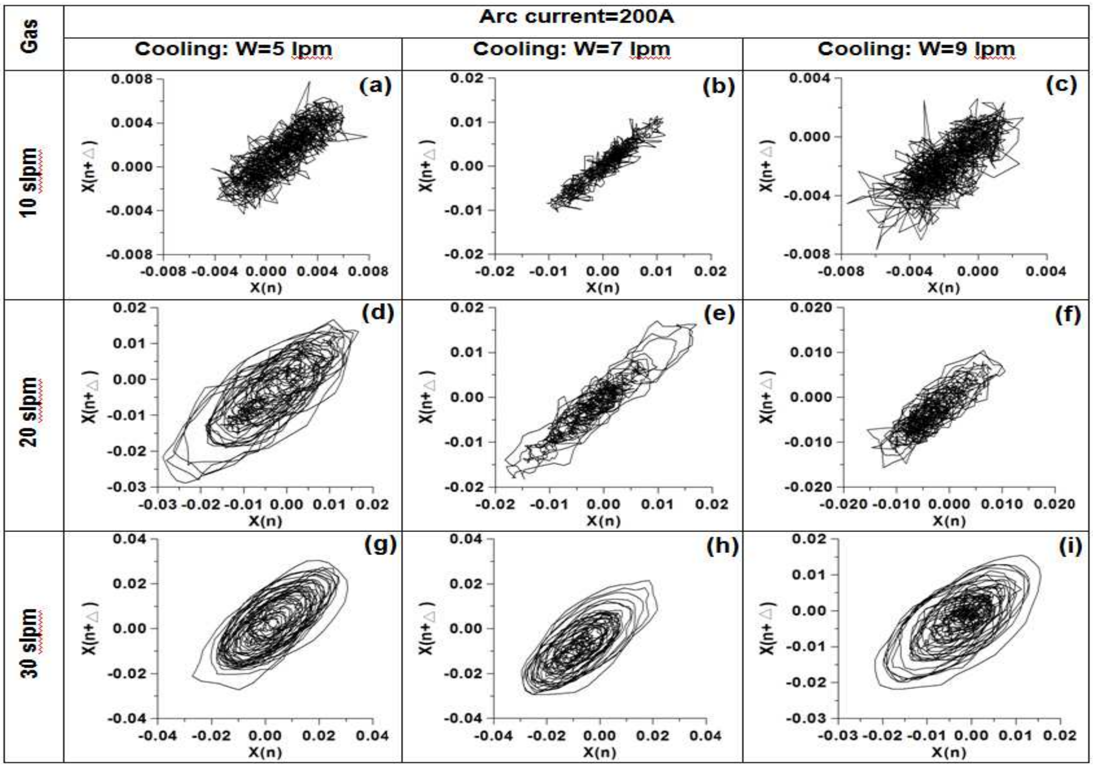

Figure 6.7: Phase space behaviour of arc voltage with different flow rates of coolant for an arc current of 200A. (a)-(c): plasma gas flow=10 slpm; (d)-(f): plasma gas flow=20 slpm; (g)-(i): plasma gas flow=30 slpm.

6.3.3 Benchmarking of the non-linear dynamic tools

For a quick familiarity with the tools used, we considered a very specific time series with known attributes, apply the tools and understand how accurately they predict the embedded features like underlying frequencies, dimension and value of the highest possible Lyapunov exponents. While we explain the details of the calculation methodology in relevant sections, here we give only the results for a time series originated from the precise equation [See Figure 6.8(a)]:

$$y(t) = A_1 \sin 2\pi f_1 t + A_2 \sin 2\pi f_2 t \tag{6.5}$$

To keep the analysis in the same frequency domain as the arc instabilities, f_1 and f_2 as 5 kHz and 20 kHz were chosen respectively so that the dynamics at both low frequency as well as high frequency ends are well represented. Amplitudes of both the components (A_1 and A_2) were chosen as 10. Total number of samples (20000) and sampling interval (2μs) are chosen same as that in the experiments.

Upon analysis in frequency space [Figure 6.8(b)], it was observed that both the embedded frequencies are accurately reproduced. Typical structure of the attractor in phase space constructed using delay coordinate technique [23-24] is presented in Figure 6.8(c). Correlation dimension of the attractor in phase space of dimension 4 and 7 were obtained from the linear slope of the plots in Figure 6.8(d) and 6.8 (e) respectively [details of the quantities plotted are given in section 6.3.5]. It is observed that exact dimension (1.0) of the dynamics are accurately obtained in both the cases. Figure 6.8(f) presents the remarkable stationarity of the estimated dimension of the attractor in state spaces of various dimensions (>3). Estimated value of highest Lyapunov exponent in state space of dimension 4 and 7 are presented in Figure 6.8(g) and Figure 6.8(h) respectively. It is observed that expected zero value of the exponent is reached asymptotically as more and more data points participate in the computation. Figure 6.8(i) presents the stationarity of the estimated exponent value in state spaces of various dimensions. With this confidence, we now apply the tools to the actual experimental signals in the next section.

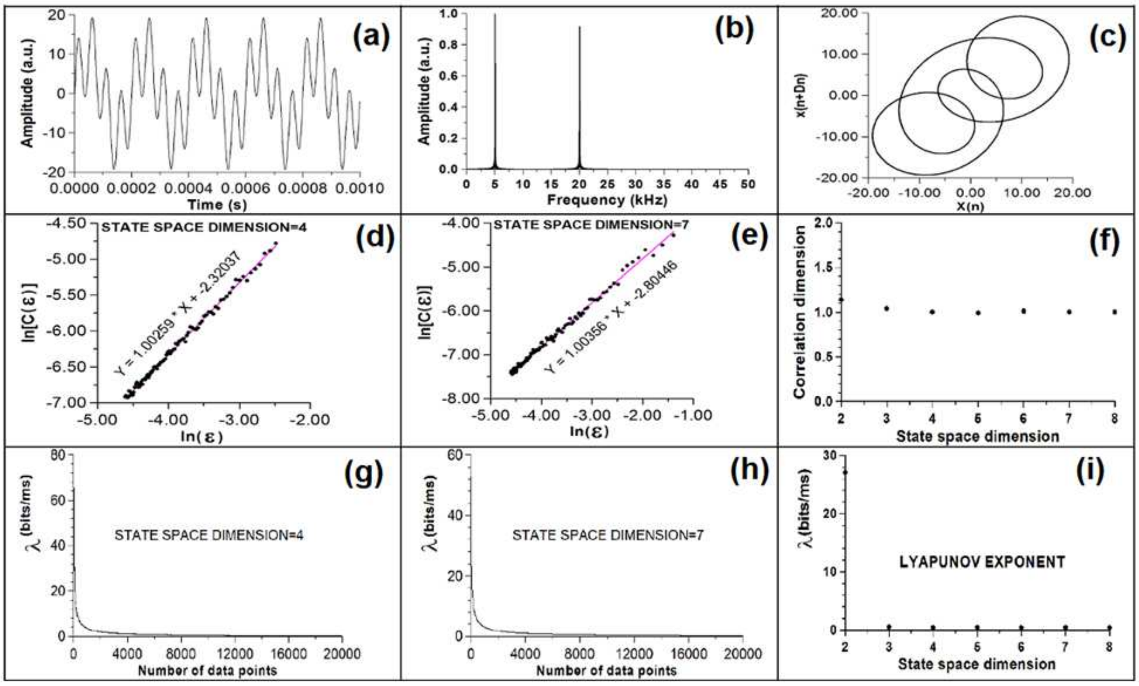

Figure6.8. Benchmarking of the used nonlinear dynamic tools: (a) a doubly periodic precise time series comprising of frequencies at 5kHz and 20kHz (b) Estimated behaviour in frequency space accurately extracts the existing frequencies (c) The phase space representation of the dynamics (attractor) (d) Calculation of correlation dimension (CD) in state space of dimension 4 (e) Calculation of CD in state space of dimension 7 (f) Variation of computed CD with dimension of used state space (g) Calculation of Lyapunov exponent (LE) in state space of dimension 4 (h) Calculation of LE in state space of dimension 7 (i) Variation of computed LE with dimension of used state space.

6.3.4 Frequency space behaviour of arc voltage at different arc currents and PGFRs under different degree of anode cooling

Fast Fourier Transforms (FFT) of the voltage instability signals under different cooling rates of anode are presented in Figure 6.9 with different flow rates of plasma gas and arc current of 100A. Figure 6.9(a) shows the behaviour observed with PGFR of 10 slpm and CFR of 5 lpm. Observed highest spectral amplitude near zero frequency, continuous distribution, gradually decreasing trend in amplitude and no prominent peak are some typical features of random and chaotic systems. In chaotic systems, low dimensional attractors with positive Lyapunov exponents are observed, which are markedly different from random systems. While such tests are carried out in the next sections, it is observed that as CFR increases from 5 lpm to 7 lpm (with PGFR of 10 slpm), strong new dynamics sets in around two distinct frequencies 1.2 kHz and 16 kHz [Figure 6.9(b)]. It may be noted from previous sections that corresponding ETE shows a sharp jump. We refer to these new dynamics as D_1 and D_2, which are very specific to this device and appear always around the particular frequencies mentioned. With further increase in CFR, it was observed from Figure 6.9(c) that D_2 vanishes and D_1 loses its strength significantly. Corresponding ETE also decreases. This indicates that D_1 and D_2 might have some role in the enhanced efficiencies.

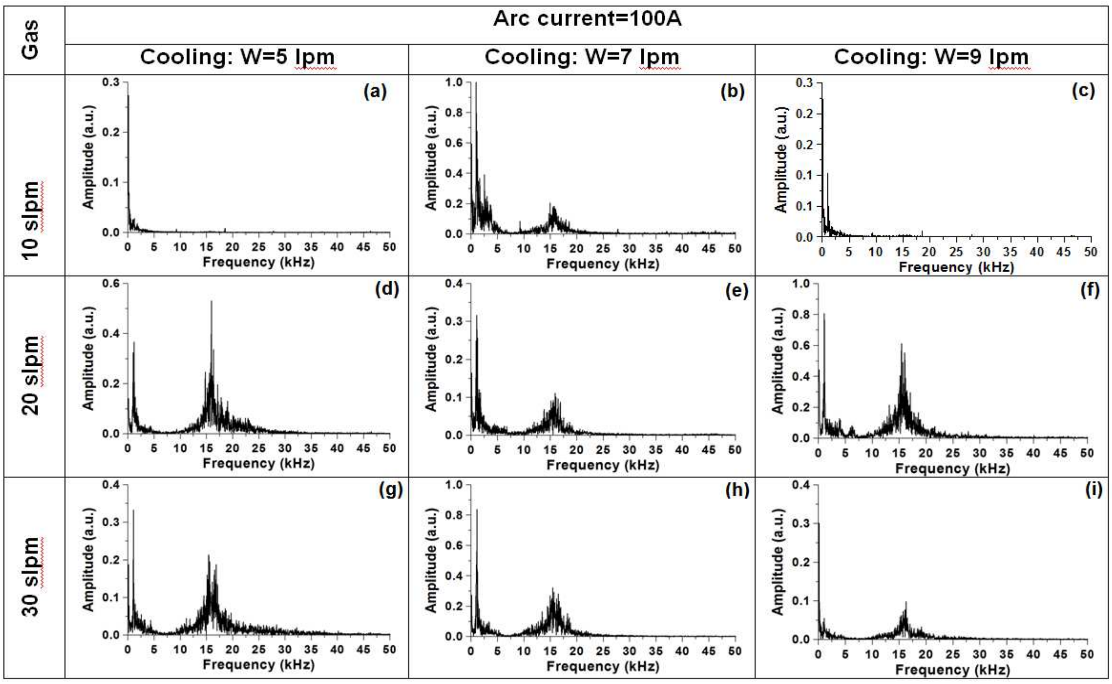

Figure 6.9: Frequency space behaviour of arc voltage with different flow rates of coolant for an arc current of 100A. (a)-(c): plasma gas flow=10 slpm; (d)-(f): plasma gas flow=20 slpm; (g)-(i): plasma gas flow=30 slpm.

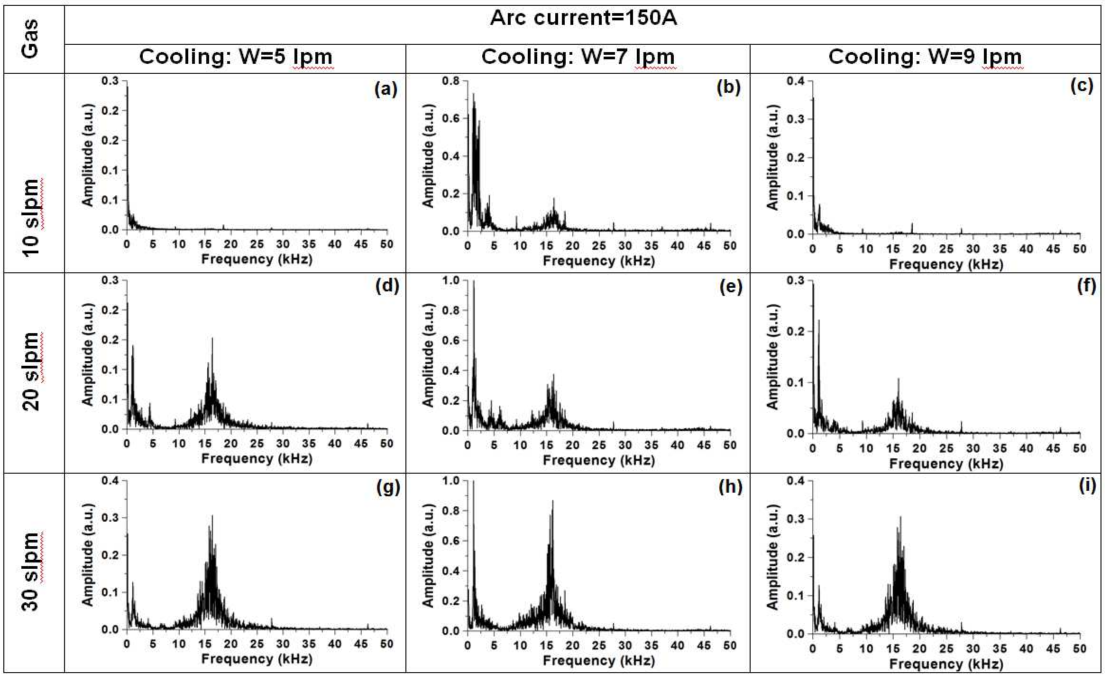

Figure 6.10: Frequency space behaviour of arc voltage with different flow rates of coolant for an arc current of 150A. (a)-(c): plasma gas flow=10 slpm; (d)-(f): plasma gas flow=20 slpm; (g)-(i): plasma gas flow=30 slpm.

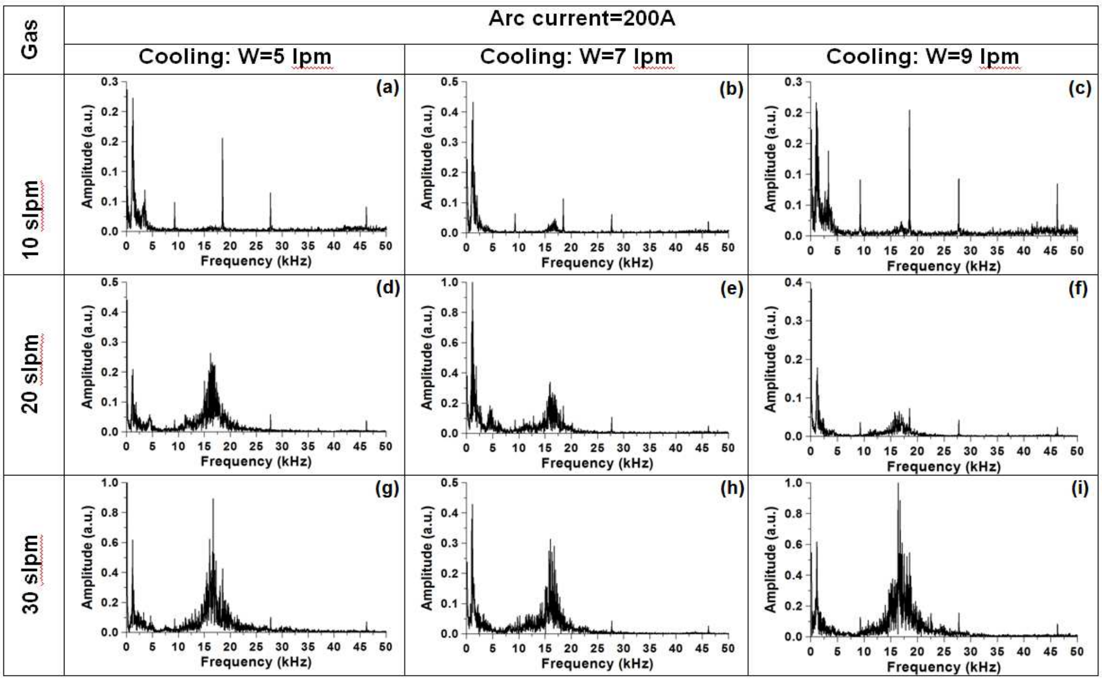

Figure 6.11: Frequency space behaviour of arc voltage with different flow rates of coolant for an arc current of 200A. (a)-(c): plasma gas flow=10 slpm; (d)-(f): plasma gas flow=20 slpm; (g)-(i): plasma gas flow=30 slpm.

When PGFR increases to 20 slpm [Figure 6.9(d) - Figure 6.9(f)], it is observed that both of D_1 and D_2 are always present irrespective of the CFRs. However, ratio (R_D) of spectral amplitudes of D_1 and D_2 significantly increases as CFR increases from 5 lpm to 7 lpm. The same decreases when CFR increases further from 7 lpm to 9 lpm [Figure 6.9(f)]. For further increase in the PGFR to 30 slpm, we again observe that increase in R_D occurs when CFR increases from 5 lpm to 7 lpm and the reverse happens when CFR increases further to 9 lpm [Figure 6.9(g) – Figure 6.9(i)]. Corresponding ETE follows R_D. It is noted that increase and decrease in R_D is associated with increase and decrease in corresponding ETE. As may be seen from the results presented in Figure 6.9, Figure 6.10 and Figure 6.11, the fact was always observed without fail when D_1 and D_2 both are present in the dynamics, irrespective of plasma gas flow and arc current.

Figure 6.10 and Figure 6.11 presents the behaviour in frequency space for arc currents of 150A and 200A respectively. Similar to case of 100A, disappearance of D_2 is observed at low PGFRs for CFR of 5lpm and 9lpm. Here also we note that R_D nicely maintains its relationship with ETE as before. While features for 150A are highly similar to that observed for 100A, the behaviour observed with 200A is markedly different at low flow rates of plasma gas [Figure 6.11(a) – Figure 6.11(c)]. New multi-periodic dynamics appear at completely new frequencies represented by the sharp distinct peaks in the frequency spectra. It is conjectured that the behaviour may correspond to the periodic pattern formation indicated in the previous theoretical and experimental studies done by Yang et al. [25, 26, 27] and Trelles et al. [28, 29]. Dynamics at some of the frequencies [9kHz, 18 kHz, 28kHz and 46kHz] continue to exist even as PGFR increases to 20 slpm and 30 slpm [Figure 6.11].

6.3.5. Dimension of the arc voltage attractor under different current, PGFR and degree of anode cooling

Dimensions of an object relates to the way the points inside the object are distributed in the configuration space. In differential topology, dimension of a manifold is same as the dimension of the Euclidean space that the manifold resembles locally. It represents the minimum number of state variables required to describe the dynamics in a dynamical system. Usually these dimensions are integers. However, in many physical systems involving chaotic dynamics, they are fractal. As a measure, variety of dimensions like 'capacity dimension (D_{cap})', 'information dimension (D_I)', 'correlation dimension (D_C)' etc. are defined in literature in a way that all of them give identical integer dimension for regular objects like circle, sphere, torus, ellipse, line etc. In this context, an entire family of dimensions is defined by Renyi [30] in which D_{cap}, D_I, D_C appear as special cases:

$$D(q) = \underset{\varepsilon \to 0}{Lt} \frac{H_q(\varepsilon)}{\ln(1/\varepsilon)} \qquad q = 0,1,2... \tag{6.6}$$

where,

$$H_q(\varepsilon) = \frac{1}{1-} \quad \sum_{i=1}^{N(\varepsilon)} P_i^q(\varepsilon) \qquad q \neq 1 \tag{6.7}$$

$$H_q(\varepsilon) = -\sum_{i=1}^{N(\varepsilon)} P_i(\varepsilon) \ln P_i(\varepsilon) \qquad q = 1 \tag{6.8}$$

N(ε) represents the number of hypercubes of dimension ε required to completely fill the attractor (A hyper cube is a line in one dimension, a square in two-dimension, a cube in three-dimension and so on). P_i is the relative frequency of visiting a typical trajectory to the i^{th} volume element. H_q represents the generalized entropy. D_{cap}, D_I and D_c appears for q equal to 0, 1 and 2 respectively [30]. Although, for same number of data points and under identical conditions, computed capacity dimension of a system comes much closer to its actual dimension. Most widely used dimension in literature is the correlation dimension (possibly due to its simplicity in calculation) [31]. For a collection of N points of a trajectory, finding correlation dimension ultimately reduces to finding the number (N_p) of pair of points (X_i,X_j) such that:

$$\left\| X_i - X_j \right\| < \varepsilon \tag{6.9}$$

The correlation dimension is then calculated as:

$$D_c = \underset{N \to \infty}{Lt} \frac{1}{N^2} \left[N_p \right] \tag{6.10}$$

For calculation of correlation dimension, an algorithm developed by Ghorui et. al. [14] was used in the present study. Benchmarking of the algorithm is already presented in section 6.3.3 [Figure 6.8].

Estimated correlation dimension of the exhibited dynamics for 100A arc current are presented in Figure 6.12 for different PGFRs and CFRs. Dimensions are estimated in state spaces of dimension ranging from 2 to 8 in each case. Noise, an infinite dimensional process, is an integral part of any experimental signal. Fortunately, its effect comes down as analysis is carried out in higher dimensional state space and true value of dimension of the underlying dynamics, which is independent of dimension of state space starts appearing.

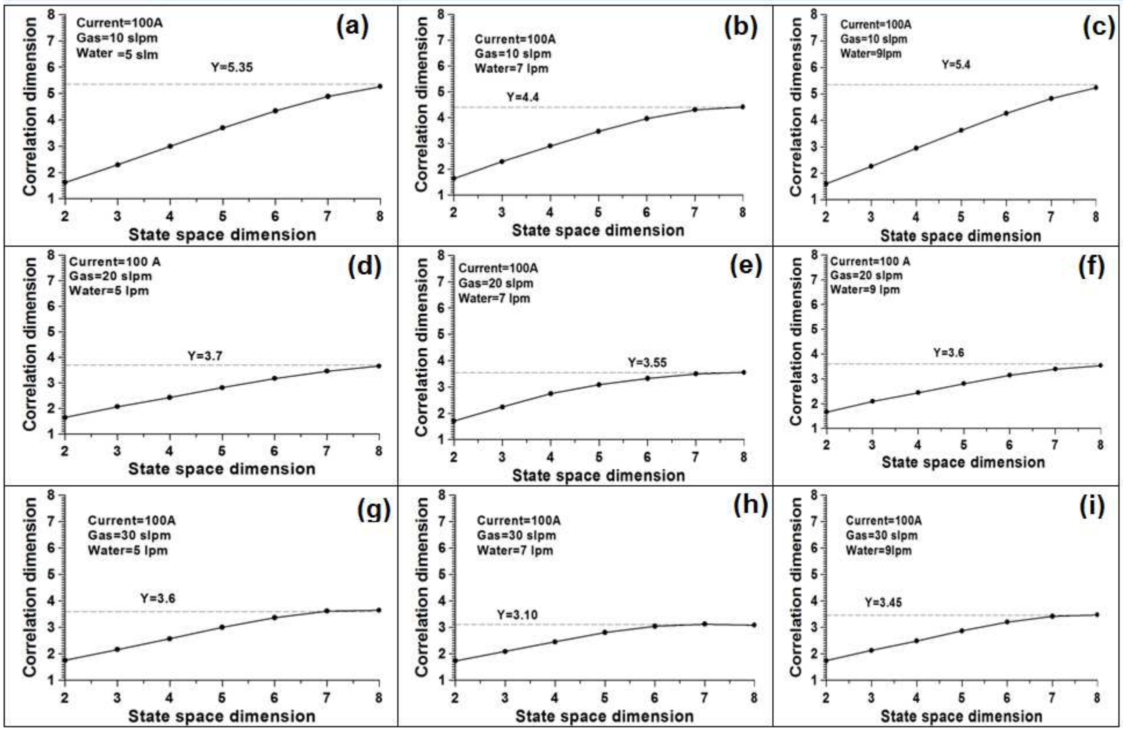

Figure 6.12: Dimension of the voltage attractor at an arc current of 100A with different anode cooling, calculated in state space of dimension 2 to 8. (a)-(c): Plasma gas 10 slpm, (d)-(f): plasma gas 20 slpm, (g)-(i): plasma gas 30 slpm. Dotted lines present the probable value of correlation dimension.

It was observed that the associated dynamics involved low dimensional attractors. Under a given arc current, dimension of the attractor reduced as plasma gas flow increased. For a given PGFR and arc current, as CFR increased from 5 lpm to 7 lpm, dimension of the attractor reduced [Figure 6.12(a) and (b)]. It was also noted that corresponding to this, a jump in the ETE was observed [Figure 6.1]. For further increase in CFR to 9 lpm, dimension of the attractor increased again and corresponding ETE showed a drop [Figure 6.1]. Regarding the plots in Figure 6.12, the computed dimension asymptotically tried to reach its actual value as the state space dimension increased. However, when the effect of noise was strong [e.g. Figure 6.12(a), (c)] such values were not prominent enough but surely above the value indicated by the dotted lines in respective graphs. At higher gas flow rates, the effect of noise was less and exact values of the dimension could be clearly judged [Figure 6.12(g),(h),(i)].

Similar behavior was observed for other arc currents [150A and 200A] also. The estimated values of dimension were mostly fractals, indicating possibility of chaotic dynamics. A definitive test of such possibilities is evaluation of corresponding Lyapunov exponent, positivity of which ensures presence of chaotic dynamics. Advantage of chaotic dynamics is that when it sets on, the dynamics is controllable as it originates from precise governing equations. In the next section, we present the analysis of Lyapunov exponents.

6.3.6. Lyapunov exponent of the voltage instability under different arc current, PGFR and degree of anode cooling

For analysis of Lyapunov exponent of the dynamics, arc voltage was sampled at a regular interval (Δt) to construct a time series of length (N). An m-dimensional phase portrait constructed from the sampled data points using delay coordinates [23,24] allowed to calculate the Lyapunov exponent. An algorithm, developed by Alan wolf [15] was used in determination of the highest positive Lyapunov exponent (λ_1). In this algorithm, the evolution of a single pair of nearby orbits is followed in phase space. Let $\zeta_1 \ldots \zeta_n$ are the sampled voltage values $\zeta(t)$, scaled in the interval [0,1] for convenience. A point in the m dimensional phase portrait, is denoted by $\{\zeta(t), \zeta(t+\tau) \ldots . \zeta(t+[m-1]\ \tau)\}$, where τ is the delay time (τ). A minimum Length scale (L_{min}) is defined such that lengths below this scale will not be entertained. Since the computation is based on infinitesimal length scales, the maximum distance between two points for which they will still be considered to be in a common infinitesimal neighbourhood is defined as L_{max} ($0< L_{max}\leq 1$).

The computation followed the following steps [30]:

(i) At $t=t_0$, an initial point (fiducial point) was chosen arbitrarily in phase space

(ii) Distance of its nearest neighbor $L_I(t_0)$ was determined from the data set.

(iii) The system was then allowed to evolve for a certain time (T_{ev}), within which the initial separation element $L_I(t_0)$ was evolved to $L_f(t_1)$.

(iv) At $t=t_1$, the data set was searched for a new nearest neighbor such that the separation between the two points was a minimum one as well as the angular separation between the evolved and replacement elements [$L_f(t_1)$ and $L_I(t_1)$] also remained within maximum allowable angular separation θ_{max}.

(v) The points being used were retained if an adequate replacement point was not available.

(vi) The procedure was repeated to cover the entire available data and the value of λ_1 was calculated as:

$$\lambda_1 = \frac{1}{t_M - t_0}\sum_{k=1}^{M}\log_2\frac{L_f(t_k)}{L_i(t_{k-1})} \tag{6.11}$$

($t_k - t_{k-1}$) is the evolution time T_{ev}, which remains constant throughout the computation. M is the total number of replacement steps. The estimation process has dependence on number of parameters like ΔT, m, τ, T_{ev}, L_{max}, L_{min}, and θ_{max}. For correct estimation, used values of the parameters must be appropriate. However, the choice is not very critical. There is a range of the parameter values over which the estimated exponent remains nearly constant. Set of parameter values used in the study is listed in Table 6.1. Invariance of the estimated exponent value around these set of parameters have been checked. A typical computation of λ_1 set out as shown in Figure 6.9.8. In the beginning, high fluctuation in the exponent value was observed due to scarcity of included data points. As more and more data points were included, the fluctuation died down fast and true value of the exponent settled in.

For estimation of correct value of the exponent, it is necessary to examine stationarity of the obtained value in state space of various dimensions. Similar to dimension calculation, true value of the exponent becomes apparent as the analyzing state space dimension increases. For 100A of arc current, the results are presented in Figure 6.13. It was observed that for low flow rate of plasma gas, the exhibited exponent values were positive and nearly independent of the dimension of state space in which the analysis was carried out [Figure 6.13(a)-(c)]. The dynamics so exhibited may be truly chaotic. It was noted that estimated fractal dimension in Figure 9 and corresponding frequency space behaviour in Figure 6.11 also supported the fact. However, as plasma gas flow increases [20 slpm and 30 slpm], no stationarity of the estimated exponent values was observed when computed in state spaces of various dimensions. Instead, it was observed that as dimension of state space increased, the exponent value exhibited an unambiguous decreasing trend towards zero value, indicative of random behaviour. Similar features were found at other arc currents [150A and 200A]. Observed onset of strong multi-periodic behaviour at 200A for 10 slpm of plasma gas, discussed in the previous section, also diagnosed to be non-chaotic for 5 lpm and 9 lpm of CFR. However, for 7 lpm the dynamic showed nearly constant value in all state space dimensions considered and appears to be chaotic.

Table-6.1. Parameter values used in estimation of Lyapunov Exponent λ_1

N	m	ΔT	τ	L_{min}	L_{max}	θ_{max}	T_{ev}
20000	4	.002ms	$5\Delta T$	.0004% of horizontal extent	20% of horizontal extent	.3 radian	$10\Delta T$

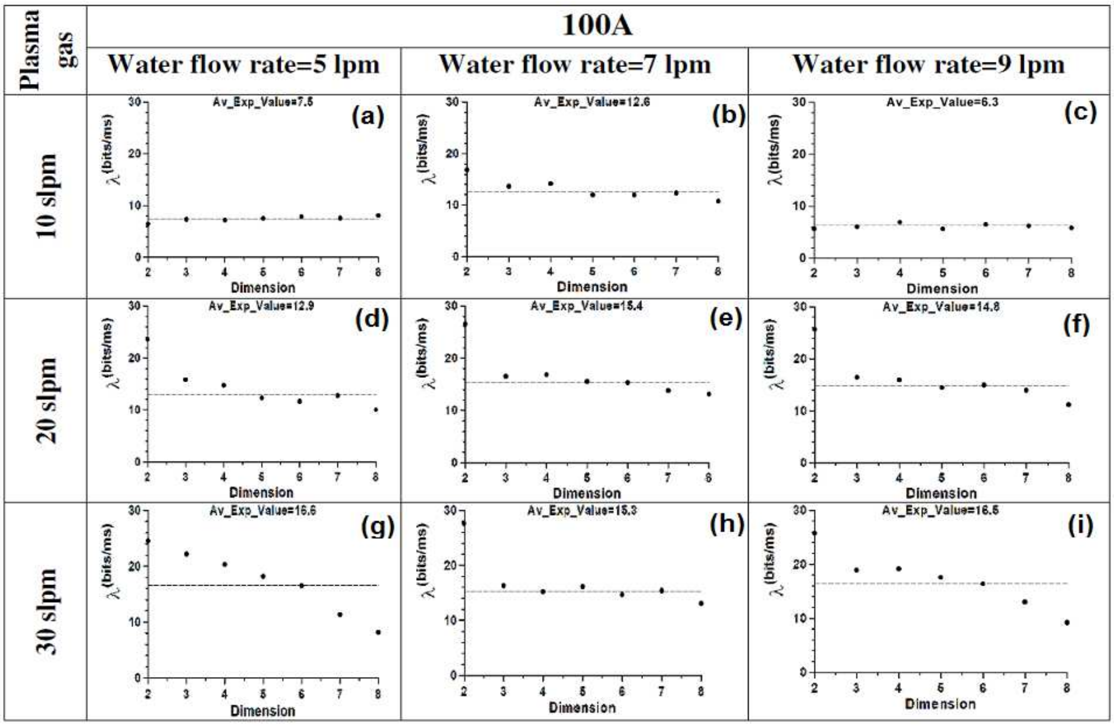

Figure 6.13: Lyapunov exponent of the voltage instability at an arc current of 100A with different anode cooling, calculated in state space of dimension 2 to 8. (a)-(c): Plasma gas 10 slpm, (d)-(f): plasma gas 20 slpm, (g)-(i): plasma gas 30 slpm.

6.3.7 Impact of anode cooling on plasma temperature at the nozzle exit

While the effect of anode cooling has substantial effect on efficiency of the plasma torch, in this section, its influence on the plasma jet temperature at the nozzle exit, if any was studied. In the experiment, PGFR is varied from 10 slpm to 40 slpm in step of 5 slpm under CFR of 5 lpm, 7 lpm and 9 lpm and arc current of 100A, 150A and 200A. In each case, the nozzle exit temperature was determined from the emission spectroscopic data using Boltzmann plot method.

When a system is in thermal equilibrium, various energy levels are populated according to Boltzmann distribution. Under such condition, the intensity (I_{ui}) of radiation of wavelength (λ_{ui}) due to transition from level 'u' to 'i' follows the relation given by Griem[32]

$$\ln\left(\frac{I_{ui}\lambda_{ui}}{g_u A_{ui}}\right) = -\frac{E_u}{k_B T} + C \tag{6.12}$$

Where, k_B is the Boltzmann constant, A_{ui} is the 'transition probability' for the specific transition. E_u and g_u are the excitation energy and statistical weight factors of the upper level 'u'. It is obvious from equation (6. 12) that at a given temperature 'T', a plot of $\ln(I_{ui}\lambda_{ui} / g_u A_{ui})$ along vertical axis and E_u along horizontal axis for different λ_{ui} will result in a straight line, and the excitation temperature 'T' can be determined from the slope of the straight line [given in detail in chapter3]. It may be remarked that in most of the laboratory plasmas complete local thermal equilibrium (CLTE) does not hold good [32]. There exist few levels which are not populated as per Boltzmann distribution due to lack of enough collisions. Apart from these levels, rest of the energy levels follow Boltzmann distribution and the system exhibits partial local thermal equilibrium (PLTE) [32]. Different transition lines considered in the study and relevant spectroscopic parameters are listed in Table-2. It has been ensured that the LTE followed by the lines used. Typical emission spectra and Boltzmann plots obtained in the present case are presented respectively in Figure 6.14(a) and (b). Correlation coefficient for the applied linear fit to the experimental data in Figure

6.14(b) was better than 0.95 in each case. Variation in the average temperature as a function of PGFRs under different CFR is presented in Figure 6.15 (a), 6.15(b) and 6.15(c) for arc currents of 100A, 150A and 200A respectively. Average temperature was determined from five independent measurements using the same set of emission lines. Observed scatter in each measurement were presented by the error bars associated in the graphs.

It is expected that higher CFR will result in higher conductive loss, resulting in lower temperature of the plasma jet. This was essentially observed at 100A and 150A for most of the PGFRs used [Figure 6.15(a) and Figure 6.15(b)]. However, it was also observed that highest plasma temperature did not correspond to the lowest CFR [4 lpm] at relatively higher PGFRs. Instead, it was observed that some intermediate CFR [7 lpm] gave the highest plasma temperature. It was interesting to note that highest torch efficiency was also obtained at this particular CFR value. At high current of 200A [Figure 6.15(c)], the scenario changed and except for very high PGFRs, similar behaviour was not observed.

For physical examination of the boundary layer thickness, the nozzle exit zone was imaged using fast photographic camera. Typical images observed were presented in Figure 6.15(d). Strong asymmetry in the jet observed at CFR of 4slm indicated existence of thin boundary layer at one side. Whereas with CFR of 7 lpm, relatively thicker but uniform boundary layer was observed. Such thicker cold boundary layer may give better isolation to the heat transfer and result in higher ETE as observed.

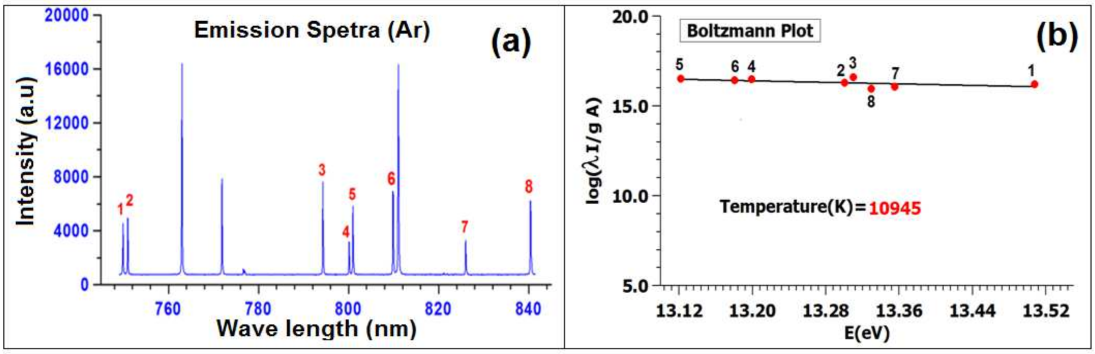

Figure 6.14: (a) Recorded emission spectra: wavelengths considered are marked in red. (b) Typical Boltzmann plot observed with the emission spectroscopic data.

Table-6.2. Details of the lines used in Boltzmann Plot

Sl No.	Wavelength (A^0)	E_u (cm^{-1})	A_k($x10^{-8}s^{-1}$)	g_k
1	7503.869	108722.6	4.45e-1	1
2	7514.652	107054.2	4.02e-1	1
3	7948.176	107131.7086	1.86e-1	3
4	8006.157	106237.55	4.90e-2	5
5	8014.786	105617.2700	9.28e-2	5
6	8103.693	106087.2598	2.50e-1	3
7	8264.522	107496.4166	1.53e-1	3
8	8408.210	107289.7001	2.23e-1	5

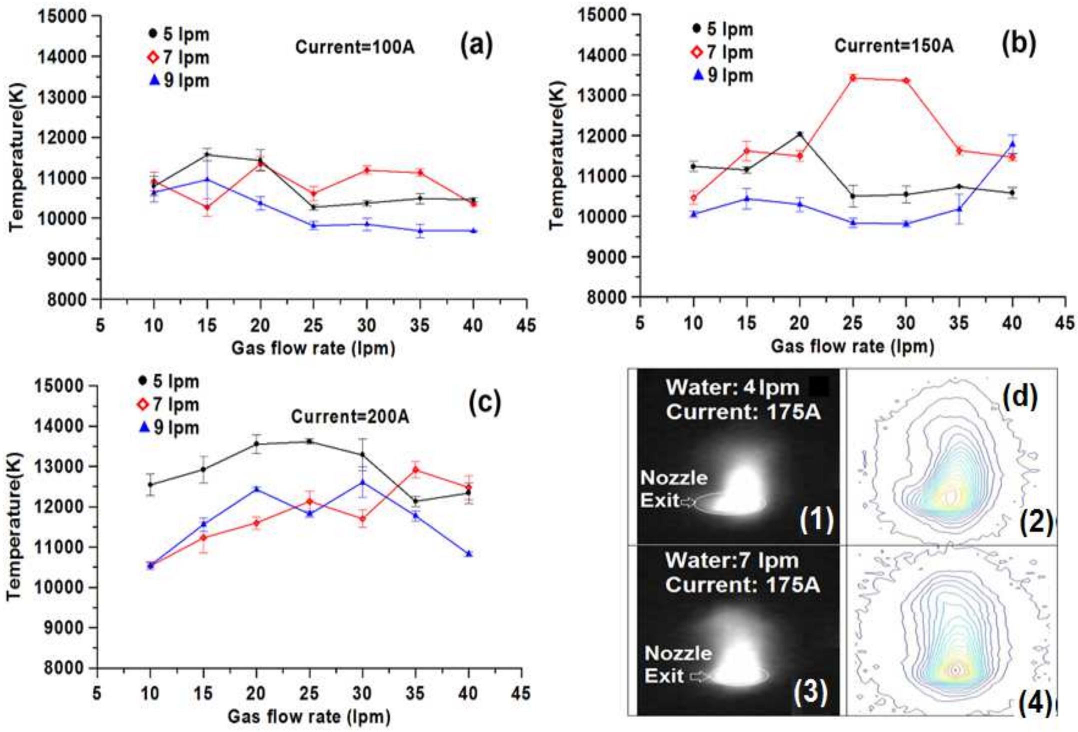

Figure 6.15. Effect of anode cooling on the plasma temperature at the nozzle exit under different PGFRs (a) arc current 100A (b) arc current 150A (c) arc current 200A (d) fast photographic snapshots: (1)-image and (2)-iso-intensity contours for CFR 4 lpm; (3)-image and (4)-iso-intensity contours for CFR 7 lpm.

6.4 Summary and Conclusions

Unusually high electro-thermal efficiencies in non-transferred arc argon plasma torches, induced by certain cooling rates of the anode have been reported under various flow rates of plasma gas and arc currents. Instabilities induced in the arc-anode attachment region involving fluid dynamic boundary layer with steep gradient in velocity and temperature and electrical boundary layer having sheath and pre-sheath regions were suspected to play a key role. Such instabilities, directly manifested through arc voltage have the potential to affect the performance of a torch to a significant extent. While it was understood that a torch with different design may manifest such observation of high efficiency in a different regime of electrode cooling, the phenomena exhibited in the present case under different currents and plasma gas flow rates are found to be highly repeatable. Considering substantial technological impact of the observation, a thorough investigation of the observed behaviour has been carried out using tools of dynamical analysis.

Time series, phase portraits, fractal dimension, and highest positive Lyapunov exponent exhibited by the system have been investigated together with analysis of the behaviour in frequency space. It has been consistently observed in the present device that whenever the torch enters into the regime of high efficiency onset of instabilities at two distinct frequencies occur. These specific instability components continued to show their presence at other operating conditions as well. Importantly, the ratio of spectral amplitude at these two frequencies was found to be highest when highest efficiency occurs. Low dimensional attractors presented by the system exhibited definite positive Lyapunov exponents for low flow rates of plasma gas, indicating occurrence of chaotic dynamics. However, for higher gas flow rates and higher arc currents the system apparently did not enter into chaotic regime. It has been observed that the attractor shrinks in phase space when the system starts exhibiting highest efficiency. Fractal dimension of the attractor also decreases at this time. With higher arc current, the instability included distinct multi-periodic behaviour at specific frequencies together with other features. These newly developed components of instability continued to show their presence under different plasma gas flow rates and rates of anode cooling. The phenomena may correspond to systematic pattern formation in arc-anode attachment region, reported in literature.

To understand the linkage among instability, electro-thermal efficiency and plasma temperature, an emission spectroscopic study together with fast photographic measurements have been carried out. Temperature was determined from atomic Boltzmann plot technique. It was observed that for low flow rates of plasma gas, the highest efficiency did not correspond to highest temperature of the plasma jet at the nozzle exit. However, at relatively higher flow rates it did. The fast photography measurement revealed presence of thin asymmetric boundary layer for lower flow rate of coolants and uniform thick boundary layer for coolant flow rates giving maximum electro-thermal efficiency. It is believed that the new revelations may have significant impact on future technology developments in the area.

6.5 References

1. Nicolis, C. and Nicolis, G., "Is there a chaotic attractor", Nature. 311, 529 (1984).

2. Grassberger, P., "Do climatic attractor exists", Nature. 323, 609 (1986).

3. Nicolis, C., Nicolis, G., "Evidence for climatic attractor", Nature. 326, 523 (1987).

4. Procaccia, I., "Complex or just complicated", Nature. 333, 498 (1988).

5. Parker, T. S. and Chua, L.O., "Practical Numerical Algorithms for Chaotic Systems", Springer Verlag, NewYork, (1990).

6. Hao, B. L., "Chaos", World Scientific, Singapore (1984).

7. Grebogi, C., Ott E., pelican S. and Yorke J.A., "Strange attractors that are not chaotic", Physica 13D, 261(1984).

8. Romeiras, F. J., Bondeson, A., Ott E., Antonsen, T. M., Grebogi, C., “Quasiperiodically forced dynamic systems with strange nonchaotic attractors”, Physica, D, 27, 277 (1987).

9. Ditto W.L., Spano M.L., Savage H.T., Rauseo S.N., Heagy J. and Ott E., “Experimental observation of strange non chaotic attractor”, Phys. Rev. Lett. 65, 533(1990).

10. Dammig, M., Mitschke, F., “Estimation of Lyapunov exponents from time series: the stochastic case”, Phys. Lett. A. 178, 385 (1993).

11. Broeck, C. V., Nicolis, G., “Noise induced sensitivity to the initial conditions in stochastic dynamical systems”, Phys. Rev. E. 48, 4845 (1993).

12. Tanaka, T., Aihara, K. and Taki, M., “Analysis of positive Lyapunov exponents from random time series”, Physica D. 111, 42 (1998).

13. Grassberger, P. and Procaccia, I., “Characterization of strange attractors”, Phys. Rev. Lett. 50, 346 (1982).

14. Ghorui, S., Das, A. K., Venkatramani, N., “A simpler and elegant algorithm for computing fractal dimension in higher dimensional state space”, PRAMANA-J PHYS. 54, L331 (2000).

15. Wolf, A., Swift, J. B., Swinney, H. L. and Vastano, J. A., “Determination of Lyapunov exponent from a time series”, Physica D, 16, 285 (1985).

16. Abarbanel, H. D. I., Brown, R. and Kennel, M.B., Int. J. Mod. Phys. B. 5, 357 (1991).

17. Grassberger, P., Schreiber, T. and Schafrath, C., Int. J. Bifurc. Chaos. 1, 521(1991).

18. Duan, Z., and Heberlein J.,” Arc instabilities in a plasma spray Torch”, J. Therm.

Spray Technol. 11, 41-51 (2002).

19. Krowka, J., Rat, V. and Coudert, J. F., "Investigation and control of dc arc jet instabilities to obtain a self-sustained pulsed laminar arc jet", J. Phys. D: Appl. Phys. 46, 505206 (2013).

20. Ghorui, S., Tiwari, N., Meher, K. C., Jan, A., Bhat, A., and Sahasrabudhe, S. N., "Direct probing of anode arc root dynamics and voltage instability in a dc non-transferred arc plasma jet", Plasma Sources Sci. Technol. 24, 065003 (2015).

21. Nogues, E., Fauchais, P., Vardelle, M., and Granger, P., "Relation between the arc-root fluctuations, the cold boundary layer thickness and the particle thermal treatment" J. Therm. Spray Technol. 16, 919-926, (2007).

22. Pan, W., Wenhua, Z., Wenhong, Z. and Chengkang, Wu., "Generation of long, laminar plasma jets at atmospheric pressure and effects of flow turbulence", Plasma Chem. Plasma Process., 21, 23-35 (2001).

23. Roux, J. C., Simoyi, R. H. and Swinney, H. L, "Observation of a strange attractor", Physica 8D, 257 (1983).

24. Packard, N. H., Crutchfield, J. P., Farmer, J. D. and Shaw, R. S., "Geometry from a time series", Phys. Rev. Lett. 45, 712 (1980).

25. Yang, G., Cronin, P., Heberlein, J. V., and Pfender, E., "Experimental investigations of the anode boundary layer in high intensity arcs with cross flow," J. Phys. D: Appl. Phys. 39, 2764–2774 (2006).

26. Yang, G., and Heberlein, J., "Anode attachment modes and their formation in a high intensity argon arc," Plasma Sources Sci. Technol. 16, 529–542 (2007).

27. Yang, G., and Heberlein, J., "Instabilities in the anode region of atmospheric pressure arc plasmas," Plasma Sources Sci. Technol. 16, 765–773 (2007).

28. Trelles, J. P., "Formation of self-organized anode patterns in arc discharge simulations," Plasma Sources Sci. Technol. 22, 025017 (2013).

29. Trelles, J. P., "Electrode patterns in arc discharge simulations: effect of anode cooling," Plasma Sources Sci. Technol. 23, 054002 (2014).

30. Renyi, A., "Probability Theory", North-Holland, Amsterdam, 1970.

31. Block, A., Bloh, W. V. and Schellnhuber, H. J., "Efficient box-counting determination of generalized fractal dimensions", Phys. Rev. A, 42, 1869 (1990).

32. Griem, H. R., "Plasma Spectroscopy", McGraw-Hill (New York) 1964.

Chapter-7

Plasma Kinetics in Single Wire Arc Plasma Spray System

Outline of the Chapter

Chapter 7

Plasma Kinetics in Single Wire Arc Plasma Spray System

7.1 Introduction

This chapter deals with the physical kinetics of the plasma jet in a single wire arc plasma spray system due to ripple in SCR based power supply. Single Wire Arc Plasma Spray (SWAPS) torch is a transferred arc torch in which high current arc is sustained between a continuously fed metal wire and cathode of a plasma torch [1]. The plasma torch is usually started with a pilot arc struck between cathode and an auxiliary nozzle anode and a small low power plasma jet comes out of the torch. After this, a high current arc (called as transferred arc) is established between the cathode and the tip of the wire fed continuously by a wire feeding machine. This transferred arc is sustained by adjusting proper wire feed rate and the arc current. This high current arc rapidly melts the tip of the wire, and the high temperature (6000–12 000 K) [2], high speed (100–400 m/s which can be calculated using gas flow rate and its expansion due to high temperature) plasma jet emanating from the nozzle anode atomizes molten wire mass and accelerates the molten metal droplets ("particles" as popularly termed in spray technology) towards the substrate kept at a distance of few centimeters from the nozzle.

In the present study, individual particles were tracked by imaging the entire "spray zone," i.e., from torch nozzle to 500 mm distance from it. The substrate to be coated is usually kept at a much smaller distance than this. Kinetics of the spray process are investigated using a high speed camera [3]. In the first part, a close up lens was used to record initial stages of the spray process. Using these images, a range of wire feed rate in which the arc sustains properly was determined and thus optimization of the feed rate for that torch power was done. In the second part, images of particles-in-flight were recorded. A moving luminous particle is seen as a streak on the image plate, i.e., CCD of the camera. The length of the streak gives the distance it travels in the exposure time of the frame. The velocity of the particle is then determined by time of flight method. It was observed that the particles have widely different velocities even when the dc power fed to the torch was held constant. The cause of this variation was traced to the ripple in the power supply of the torch. The power supplies used for single wire arc spray torch were Silicon Controlled Rectifier (SCR) based and have a large amount of ripple in the output voltage. This is due to the fact that the currents in the torch are of the order of hundreds of amperes and it is very difficult to filter the ripple at power frequency. Instantaneous voltage and current variation due to the ripple in the power supply causing power fed to plasma torch to vary, which in turn affects plasma temperature[4], flow velocity of plasma, particle velocity, and the rate of melting of wire in higher extent. It was observed that particles have different velocities depending on the time of their generation in one cycle of the ripple. A particle generated, when instantaneous torch power was maximum, attains higher velocity as compared to a particle generated when instantaneous torch power was minimum within a cycle of ripple. It is of interest to know the variation in the velocity of particles with distance from the nozzle. For this purpose, individual particles were tracked in images taken in quick succession. As the particle travels downstream, the velocity is expected to decrease due to viscous drag of the air and it is also expected to be influenced by the force of gravity. Instantaneous velocity of particle was measured in subsequent images as the particle travels downstream and thus its axial velocity was measured at different distances from the anode nozzle. For this, double exposure mode of the high speed camera was used. Particle velocity and temperature were also measured using Spray Watch System 2i system but this system cannot track individual particles. The details are given in Section 7.2 and Section 7.3.

7.2 Experimental details:

Schematic of the experimental set up is shown in Figure 3.4 in Chapter3. In first part of experiment, camera was focused on anode wire so that the arc to wire attachment, melting of the wire, detachment of molten mass, and formation of liquid metal droplet could be observed. Images were recorded for different torch parameters as given in Table 7.1.

Table-7.1: Operating parameters for SWASP

Parameters	**Values**
Pilot arc power	1- 4 kW
Transferred arc power	3 -8 kW
Total torch power	4 kW-12 kW
Wire feed rate	1 – 5 m/min
Gas flow rate (Ar)	10- 25 lpm

In the second part of the experiment, sequences of images of the moving, luminous liquid metal droplets were recorded to see particle trajectories. For calibration of the size of the object, a scale was kept near the nozzle. There is double exposure mode in PCO camera as depicted in Figure 7.1.

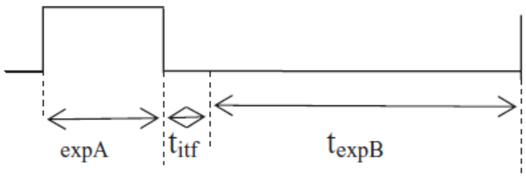

Figure7.1: Timing diagram for double exposure mode

Using double exposure mode, two sub frames A, B with inter frame time 75 ns can be recorded. The exposure time $t_{exp}A$ for the first sub frame is set by the user. Exposure time $t_{exp}B$ for the second sub frame is determined by the software. The inter frame time t_{itf} is the time interval between end of first exposure and start of second exposure and is 75 ns. Exposure time for frame A was kept 50 μs. This exposure time was selected for the determination of location of the particle. A particle with 50 m/s speed (which is on the higher side of velocities of the particles in SWAPS) travels a distance of 2.5 mm in 50 μs. Taking into account the distance at which substrate is kept (few cms), the particle can be considered to be localized. Reducing the exposure time for first frame leads to a low signal. Exposure time for sub frame B was 718 μs as determined by the software. In this exposure time, particle with 50 m/s speed travels a distance of 35.9 mm and forms a streak on the CCD of the camera. In sub frame A, location of the particle can be determined and in sub frame B its speed can be measured using streak length and exposure time. Consecutive images of the particles taken in double exposure mode show how a marked particle travels downstream. Its velocity at different locations in its journey can be measured as described earlier.

7.3. Results and discussions

7.3.1 Melting behaviour and molten mass detachment

Sequence of images of the plasma jet, arc attachment to wire, melting of the wire and detachment of the molten mass from the tip are shown in Figure 7.2. Here, torch power was kept at 10 kW, Wire feed rate was kept at 3 meters/minute, gas feed rate was kept at 20 lpm, frame rate was kept at 5000 FPS. Initially, pilot arc was struck between cathode and nozzle anode and then arc was transferred to the wire. To sustain the arc, the wire has to be fed continuously. The feed rate of the wire has to properly match the torch power and gas flow rate so that the liquid droplets are formed and are carried away by the jet. The process could be divided in three regions as follows:

a) First region: Solid metal wire electrode is straight and in uniform motion marked as 1. The dotted lines show the wire. One can see the melting of the wire at the tip and the liquid being formed.

b) The second region: Molten mass starts flowing down, marked as region 2.

c) The third region: Molten metal detaches from the wire and flows along with the jet marked as region 3.

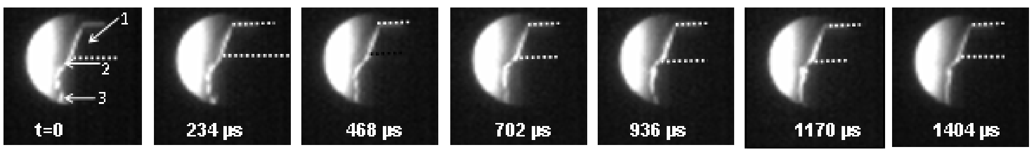

Figure 7.2: Wire melting process recorded at inter frame time 234 μs.

In the above sequence, process of arc to the wire attachment, melting of the wire and detachment of the molten mass can be clearly seen.

7.3.2 Effect of wire feed rate

For a fixed input torch parameter (Pilot arc power 2 kW, Transferred arc power 7 kW, Argon flow rate 15 lpm), effect of wire feed rate is shown in the Figure 7.3(a-i). If the wire feed rate is proper, the arc sustains, the wire melts and gets consumed.

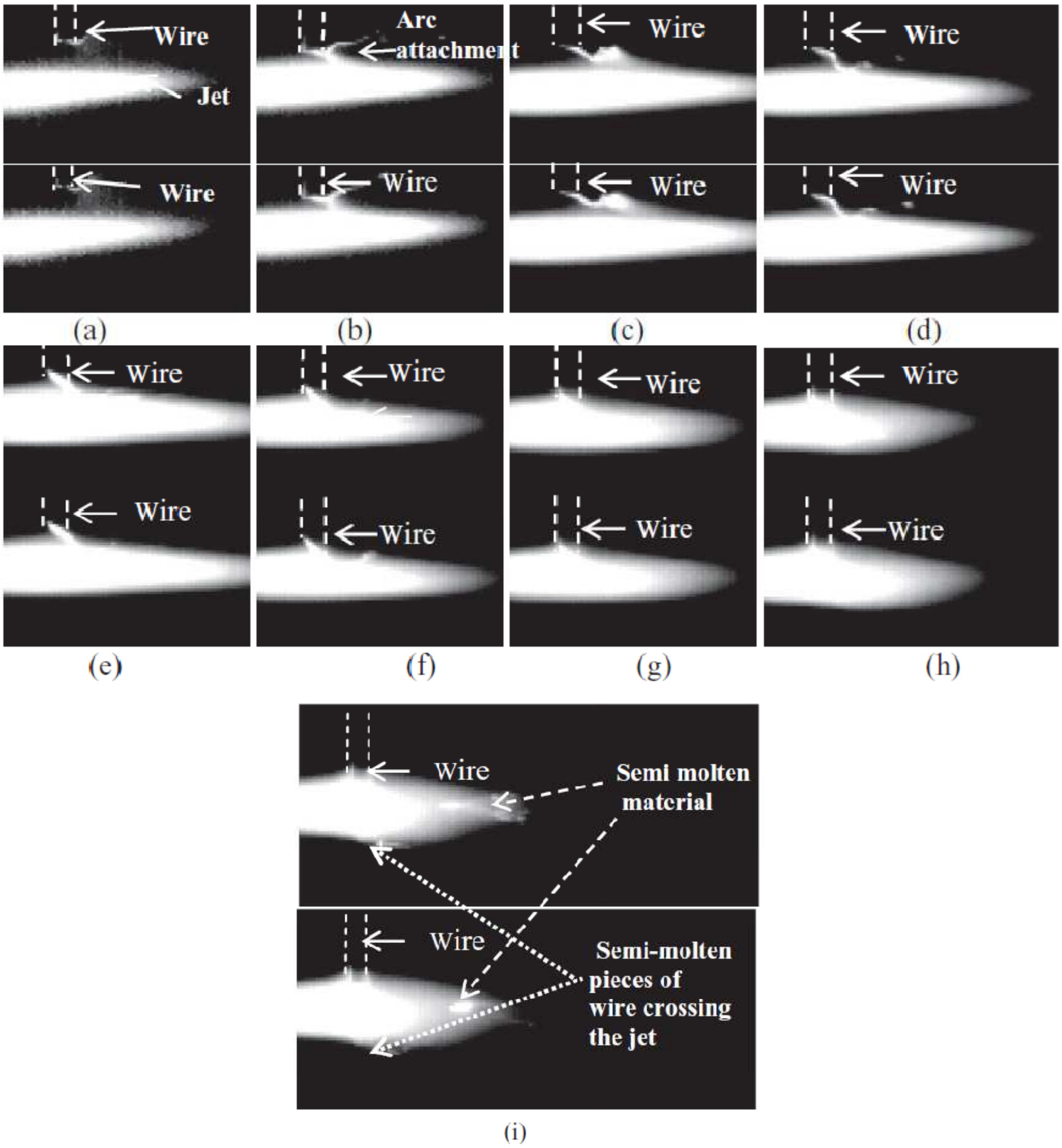

Figure 7.3: Two consecutive frames (inter frame time 0.5 ms) for different wire feed rates: (a) 1 m/min. (b)1.5 m/min (c) 2.0 m/min (d) 2.5 m/min (e) 3.0 m/min (f) 3.5 m/min (g) 4.0 m/min (h) 4.5 m/min (i) 5.0 m/min. Dotted lines show the wire.

It was observed that when wire feed rate is below 2.5 meter/minute (Figure 7.4 a, b & c); arc cuts off intermittently. As soon as wire feed rate is increased to 2.5 m/min and up to 4.5 m/s (Figure 7.3d, e, f, g & h), arc sustains continuously. Wire goes on melting and the molten mass is atomized. When the feed rate of the wire is further increased to 5 m/min and above (Figure 7.3 i), it does not melt properly. One finds pieces of solid wire crossing the jet as shown in the Figure 5i. It was observed that as the wire feed rate is increased (Figure 7.3 a to i), the luminous length of the jet decreases due to cooling by the cold wire. Width of the jet increases due to the obstruction by the solid wire as seen in Figure 7.3 h & i. Sequence of images as shown in appendix of the chapter showed the dynamics of the plasma jet in details at different feed rate 1m/min, 2m/min and 3m/min respectively. Iso-intensity contours of the jet drawn using image processing software Matlab [5] are shown in Figure 7.4. One can roughly correlate the local plasma jet temperature to the local intensity of the jet. Three pictures for different wire feed rate are shown in Figure 7.4a, 7.4b and 7.4c. Left hand side pictures show the black and white image taken by the high speed camera and right hand side pictures show the processed image showing different colors to different intensity zones. Figure 7.4a shows that the hot zone at the tip of the wire is separated from the body of the plasma jet indicating that the arc is cut off at the time of taking the image. Figure 7.4b shows that the hot zone has merged with the body of the jet indicating the wire melting rate and feed rate are adjusted so that the arc sustains continuously. The jet length in this case is seen to be reduced as the heat in the jet is taken away by the melting wire. Figure 7.4c shows that the hot zone length of the jet is reduced and it is slightly broadened when the wire feed rate is 5 m/min or more. This is due to the cold wire taking away the heat from the jet.

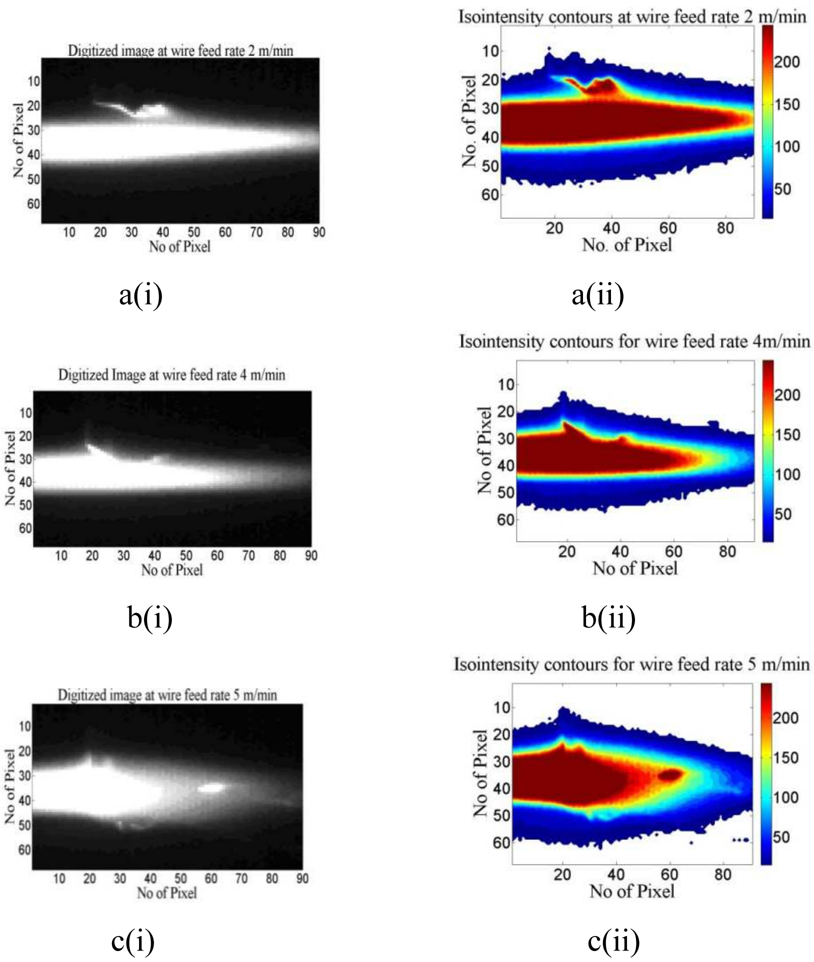

Figure 7.4: Iso-intensity contours for different wire feed rates (a) 2 m/min (b) 4 m/min (c) 5 m/min

Wire feed rate versus torch power is shown in Figure 7.5. The current setting of the power supply was kept constant and the wire feed rate was varied. The dc currents and voltages shown by the meters on the power supply were noted. It is evident from the Figure that when wire feed rate is lower, the arc puts off intermittently and smaller average power is extracted from the power supply. As the feed rate increases, arc sustains continuously and large power is extracted from the power supply resulting in a good spray. Increasing wire feed rate further leads to formation of large chunks of solid wire falling out from the jet and results in constant shifting of the arc and subsequent reduction in power.

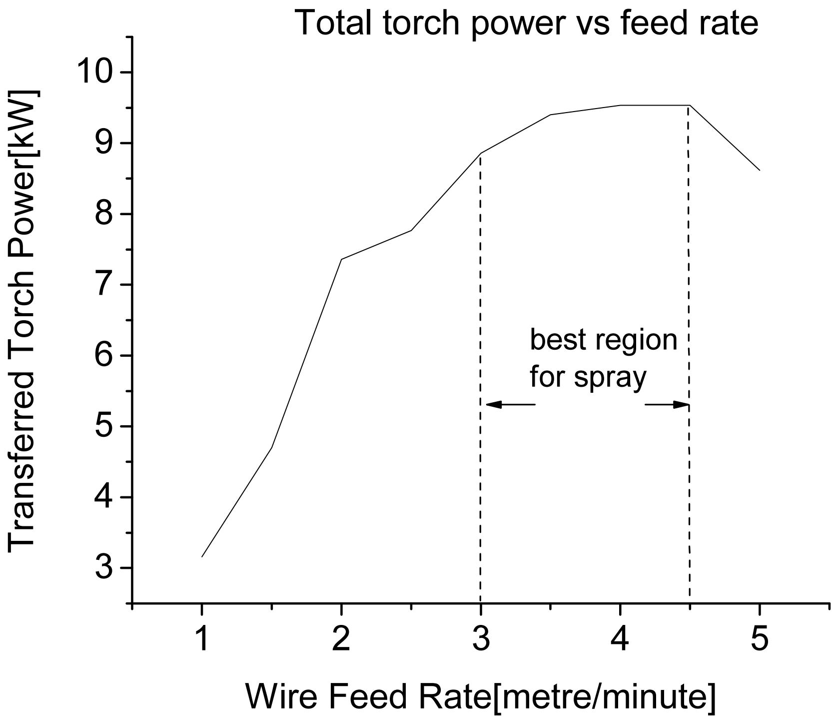

Figure 7.5: Power extracted from the power supply Vs wire feed rate

This graph shows that for a torch power of 9 kW (electrical) and 15 lpm gas flow rate, optimum wire feed rate of 3.0 m/min to 4.5 m/min for proper melting and spray.

7. 3. 3 Total power required in wire arc spray

It is shown in the earlier section that the optimum feed rate of the wire for a total torch power of about 8 - 9 kW was 3 to 4 m/min. To get molten copper droplets, the copper wire temperature has to be raised to melting temperature, then latent heat of melting is to be provided.

Heat required to melt copper (H) = m Cp (T_2-T_1) + m L, where m is the mass of copper wire fed in one second, Cp is the specific heat, T_2 is the melting point of copper, T_1 is the room temperature and L is latent heat of melting.

Taking mass of wire getting melted in one second at the feed rate of 3 m/min to be 897 g, specific heat of copper (Cp) = 385 J/Kg. K and latent heat of melting L = 210000 J/Kg, heat supplied by the arc to the wire for just melting it, is 553 J. It is well known that power transferred to the anode is about 10 to 15% of the electrical power fed to the transferred arc plasma torch. Out of 6 kW of transferred arc power (pilot arc power 2kW is subtracted from 8 kW of total electrical power), that transferred to the wire anode is ~ 600W to 900 W (10 to 15 % of 6 kW). This Figure roughly matches with 553 W calculated above. Molten droplets are entrained in the hot jet and get heated to ~ 2000 K (as measured by two color pyrometry of hot particles [6]). This energy comes from the plasma jet resulting from transferred and non transferred part of the arc.

7. 3. 4 Particle velocity

It was observed that molten particles have widely different velocities depending of the time of their generation within one cycle of ripple (~ 10 mS) in our power supply. As shown in Figure 7.9a, instantaneous torch power varies from 6.7 kW to 14 kW. Due to this, the plasma jet temperature also varies a lot leading to different expansion and thus different flow velocity within a cycle of the ripple. The molten particles entrained in the jet experience the acceleration due to the drift velocity of the plasma jet. Particles having higher velocities and generated at later time overtake the particle having lower velocities and generated at earlier time as shown in Figure 7.6. These images were recorded at 8kW torch power, wire feed rate 3.0 m/min and gas flow rate 15 lpm.

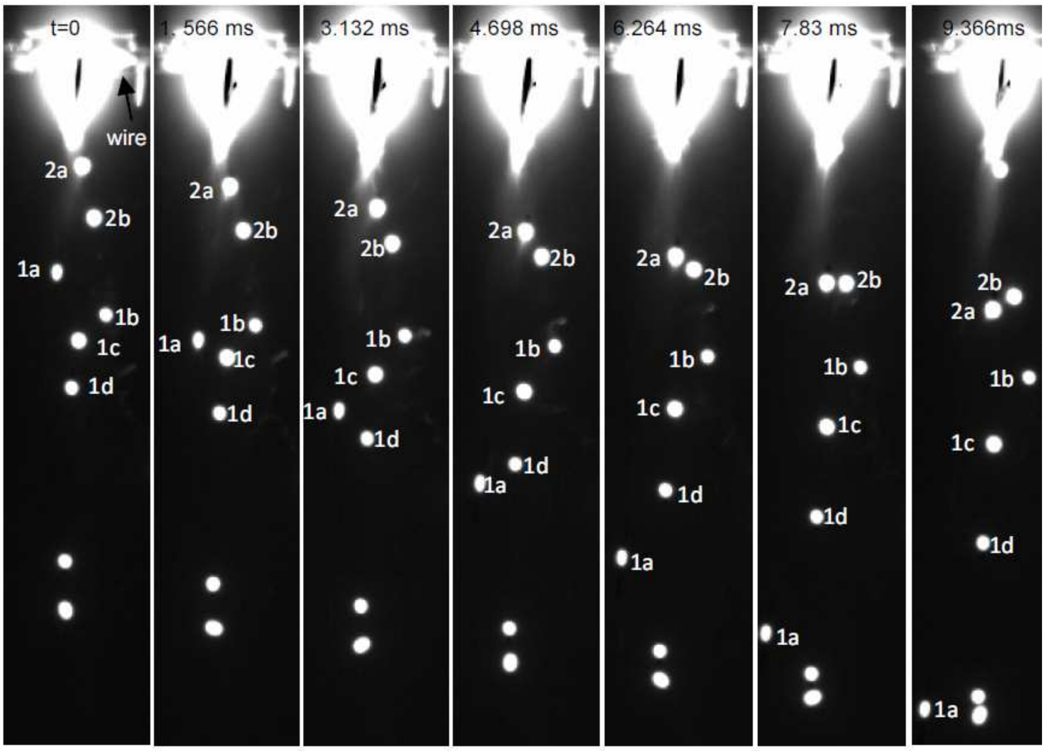

Figure 7.6: Sequence of images of the particle showing different velocities. The particles having higher velocities marked as1a and 2a in above images are overtaking the particles having lower velocity marked as 1b, 1c, 1d and 2b. The dark streak seen in the center of the image of the jet is due to hardware setting of the camera which shows over exposed pixels as dark ones.

7.3.4.1 Particle flow towards substrate

Typical image of particle flow recorded in double exposure mode is shown in Figure 7.7. Sub frame A shows the position of the particles (50 μs exposure time) and sub frame B shows the distance covered by them in 718 μs as explained earlier. Axial velocity component of the particle is calculated by distance travelled by it divided by the exposure time. We studied several consecutive images taken in double exposure mode and determined velocities of particles as they travel downstream.

Figure 7.7: Particle images recorded in double exposure mode

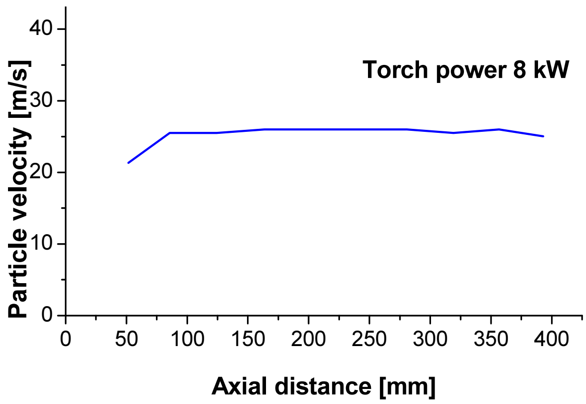

Figure 7.8: Variation of velocity Vs distance for a particle

It was observed that velocity of particles increase initially (near the torch), reaches a maximum and remains almost constant up to 50 cm from the torch nozzle as shown in Figure 7.8. Numerical simulation using a CFD code was carried out to estimate the particle velocity for different torch powers.

7.3.4.2 Variation of particle velocity due to ripple in the power supply

Particle velocity was found to vary greatly due to ripple in the power supply. To record this variation, high speed camera was synchronized with a Digital Storage Oscilloscope (DSO) which recorded the voltage and current signals from the torch. It was observed that the velocity of the particles generated when instantaneous power was high, was higher than the particle generated when instantaneous power was low in one ripple cycle. The jet length was about 25 to 40 mm depending on the power fed and the gas flow rate. The particles experience acceleration when it is entrained in the high velocity jet. Their velocity remains almost constant after 40 mm from the nozzle as seen in Figure 7.9. One can estimate the time of the generation of a particle with an accuracy of about 1 ms using the laws of motion. For this one needs to know its velocity when it is at a distance of 40 mm from the nozzle of the torch. The graph presented in Figure 7.9 b is drawn using this method

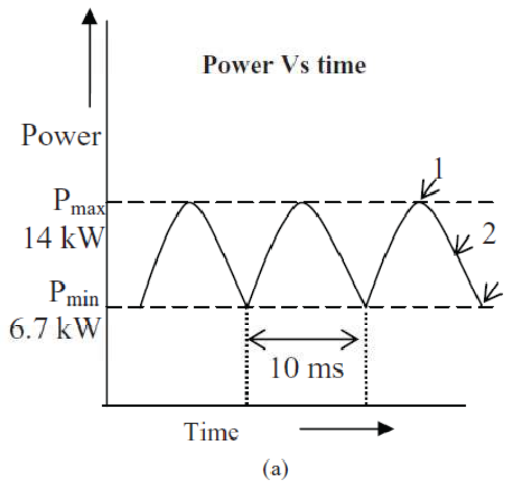

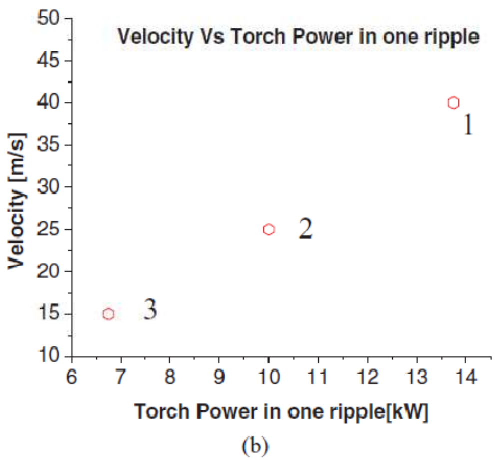

Figure 7.9: Correlation of the particle velocity with the ripple of the power supply. Particles generated at times marked as 1, 2 and 3 in (a) have velocities as shown in the graph in (b)

7.3.4.3 Numerical simulation

Variation of particle velocity with power: To understand the reasons for variation in velocity of droplets that emanate from the wire at different times, we have carried out computational fluid dynamic simulation of the fluid and particle flow using a commercial software FLUENT [6]. Computational domain consists of torch and a section of open atmosphere in which plasma jet expands. Schematic of the computational domain is shown in Figure 7.10. The plasma gas enters through a circular section A-I. Energy produced by the arc between cathode and the wire heats the plasma gas. Plasma gas expands into open atmosphere through the torch nozzle PU. Relevant dimensions of the computational domain are listed in Table 7.2.

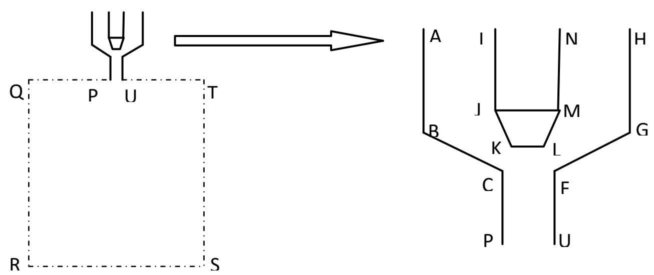

Figure 7.10: Schematic diagram of computational domain

Table-7.2: Dimensions of the computational domain

Boundary	Dimension (mm)
QR, ST	500
RS	100
PU	4
AI	5
AH	20
CP	20

Energy, mass and momentum conservation equations were solved. Turbulence equations were solved using 2-equation, standard k-ε model. To compute the velocity of copper droplets of 200 micron size (which is a typical size of the particles in SWAPS) in the expanding plasma flow and measured by spray watch system-2i[7], we have used discrete phase model. Mass transfer between droplet and plasma gas is neglected. To simulate the thermal effects of electric arc, we modelled it by replacing with a cylindrical volumetric heat source of radius 1 mm and length 20 mm. As the interaction of droplets with the fluid is limited to the region outside the torch, we have neglected the effect of electromagnetic forces on the flow. Argon is taken as the plasma gas. Variation in transport properties of argon with temperature were taken into account as per Murphy and Patankar [8, 9]. All the torch walls were taken as water cooled boundaries. The boundary PQRSTU is taken as pressure boundary condition. Spherical droplets of molten metal start with zero velocity from the centre of nozzle. Power supply ripple and variation in the size of the droplets could be the two factors affecting the droplet velocity. Effect of gravity on droplet velocity is found to be negligible. Variation in the velocity of the particle with distance is plotted in Figure 7.12.

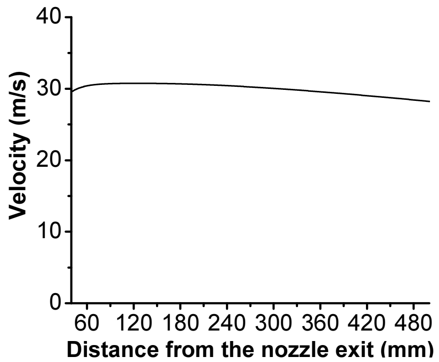

Figure 7.11: Variation of the velocity of the particle with distance using simulation for torch input power 8 kW.

It is clear from the graph that the velocity of a single particle does not change much from 4 cm up to 50 cm from the nozzle exit.

7.4 Conclusions

The plasma spray process in a single wire plasma arc spray system was investigated through high speed imaging. It was observed that initially arc is transferred to the wire, melts it, liquid droplets get detached from wire and is accelerated towards the substrate. Whole process was video graphed with a high speed camera. It shows how the above processes depend on the wire feed rate if the torch power and gas flow rate are held constant. Proper range of wire feed rate for a constant torch power was determined by the image analysis of the video recording. Particle velocity was measured by time of flight method. Particle velocities vary greatly and the variation was correlated to the ripple in the DC power supply. In one cycle of ripple, particle velocity is high when instantaneous torch power is high and it is low when instantaneous torch power was low. It was observed that particle velocity does not change appreciably from 4 cm up to 50 cm from the nozzle exit even in the presence of drag due to atmospheric air. Effect of gravity was found to be negligible. These investigations were not possible with the commercially available systems like Spray watch System, DPV 2000 etc. Numerical simulation for velocity of the particles at various powers and distances was done using commercially available software. It was found that experimental results match well with results of numerical simulation. Further experiments will give more insight into details of the wire arc spray process.

7.5 References

1. Chakravarthy, D.P., Barve, D. N., Patil, D. S., Mishra, P., Prasad, C. S. R. and Rout R. K., "Development and characterization of single wire-arc-plasma sprayed coatings of nickel on carbon blocks and alumina tube substrates", Surface & Coatings Technology 202, 325–330 (2007).
2. Joshi, N. K., Sahasrabudhe, S. N., Sreekumar, K. P. and Venkatramani, N., "Variation of axial temperature in thermal plasma jets" Meas. Sci. Tech., 8(10), 1146-1150, (1997).
3. PCO Germany https://www.pco.de/highspeed-cameras/pco1200-hs.
4. Sahasrabudhe, S. N., Kulkarni, N. V., Ghorui, S., Barve, D.N., Joshi, N. K. and Bhoraskar, S. V., "Time resolved temperature measurements in thermal plasma jet", Proc. Symp. Power Beams & Material Processing, Sept. 25-28, BARC, Mumbai, (2002).
5. See https://www.mathworks.com for image processing
6. Ansys Fluent 13.000
7. Spray Watch2i www.oseir.com.
8. Murphy, A. B. and Arundelli, C. J. "Transport coefficients of argon, nitrogen, oxygen, argon-nitrogen, and argon-oxygen plasmas", Plasma chemistry and plasma processing, 14, (1994).
9. Patankar, S. V., "Numerical heat transfer and fluid flow", New York : McGraw-Hill, ISBN No.: 0-89116-522-3, 1980.

Appendix

Sequence of images for attachment process at wire feed rate 1m/min, 2m/min and 3m/min are shown in Figure A, B and C. It is clearly seen that at low feed rate, attachment is intermittent, while at 3 m/min attachment is continuous, which is important for coating. Inter-frame time was kept 0.144 ms.

A) Feed rate 1m/min:

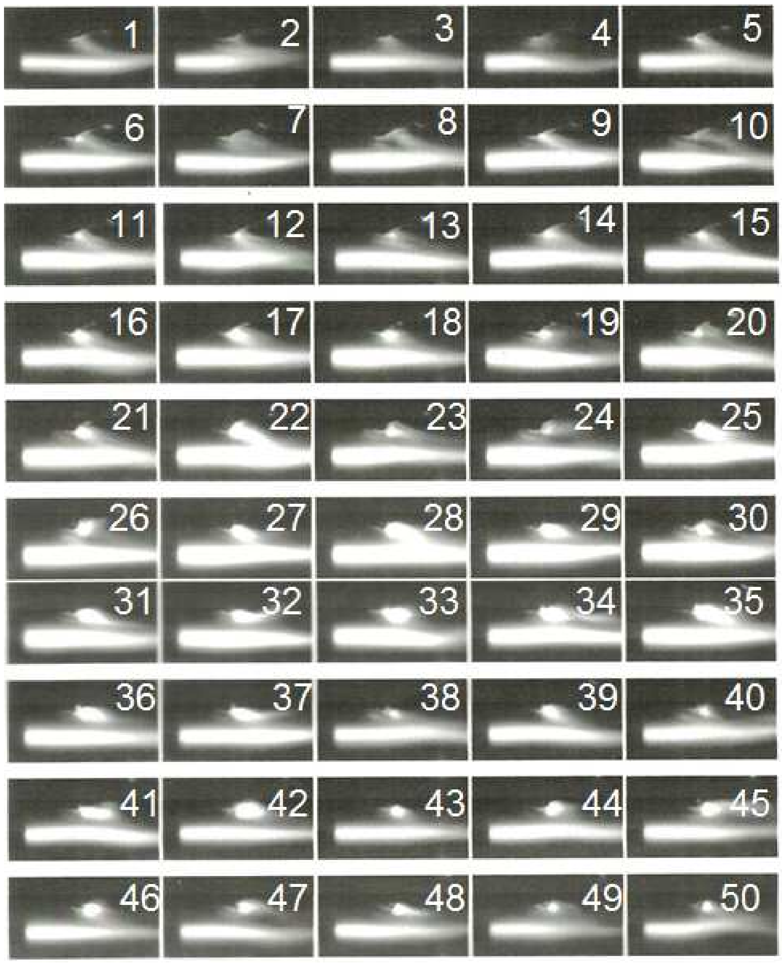

Figure A: Sequence of images depicting attachment of plasma jet and wire intermittently. Inter-frame time 0.0144ms.

It is clear from above sequence of images that arc is well attached with wire in very few images (22, 28). In most of the frame arc is not attached with wire.

(B) Feed rate 2m/min: In the following sequence of images, arc is not attached consistently.

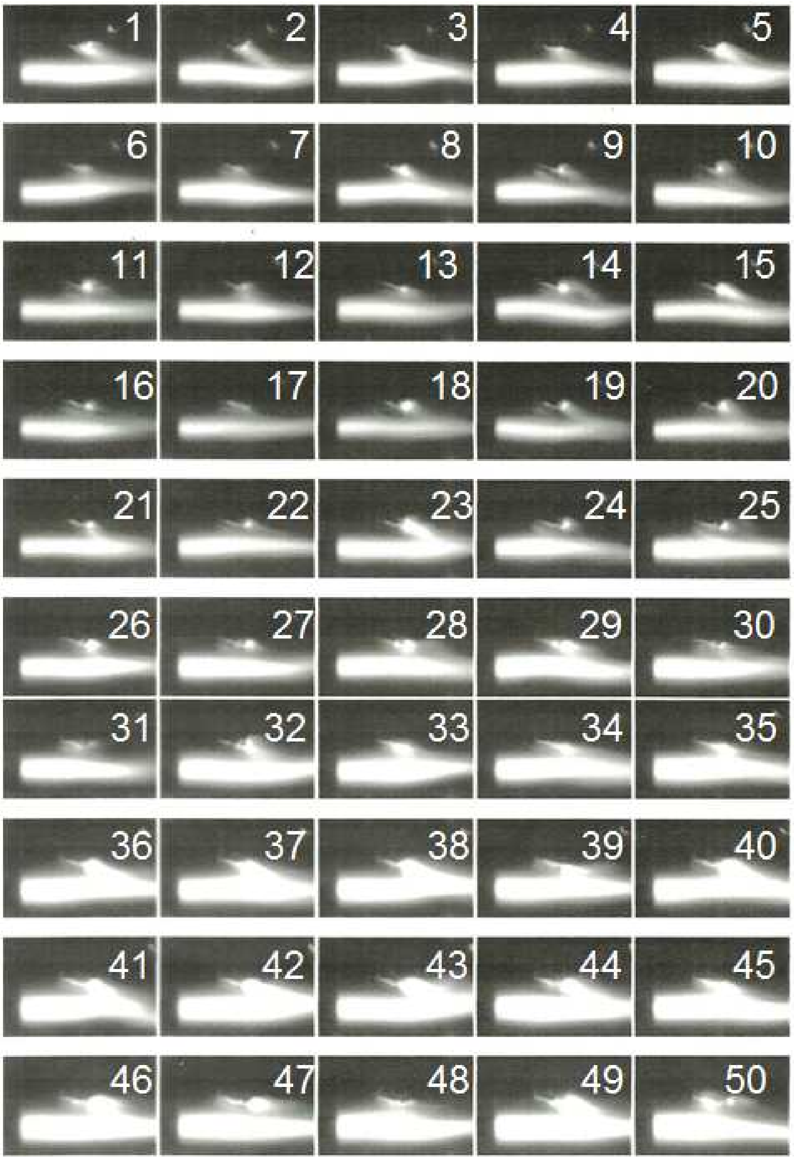

Figure B: Sequence of images depicting attachment of plasma jet and wire intermittently (42, 43, 44, 45 well connected, 21, 22, 24, 25 not connected)

(C)Feed rate 3m/min: It is clearly seen from figure C that at feed rate 3m/min arc is sustained between cathode and wire continuously over the period.

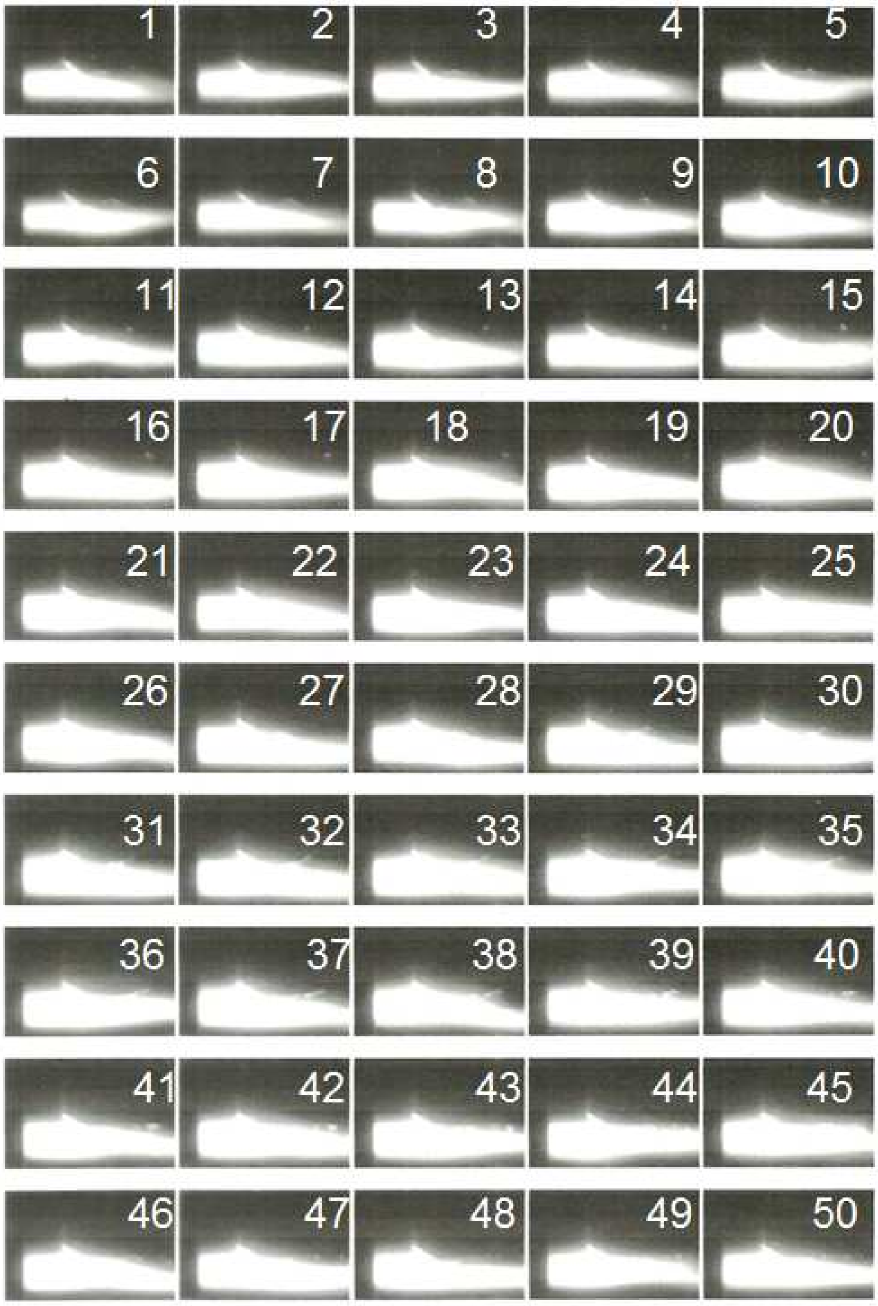

Figure C: Sequence of images depicting sustained attachment of plasma jet and wire (in all frames from 1to 50)

(D) Attachment process: Following figure shows images of the plasma jet with wire before attachment and after attachment. This image was captured usig spray watch system.

(a) **(b)** **(c)**

Figure D: (a) Pilot arc was on (b) During attachment (c) After wire is attached

Chapter-8

Investigation of Chemical Kinetics in Argon and Yttria-Argon Plasma

Outline of the Chapter

Chapter 8

Investigation of Chemical Kinetics in Argon and Yttria-Argon Plasma

8.1. Introduction

This chapter deals with the kinetics of the Argon plasma as well as Yttria-Argon plasma. Two types of chemical reactions named homogeneous (between plasma species) and heterogeneous (plasma and solid surfaces) have been reported by Grill [1]. Chemical kinetics of plasma species are presented in argon plasma under thermal non-equilibrium parameter ($\Theta=T_e/T_h$) ranging from 1 to 20, electron temperature ranging from 0 to 50000K and pressure ranging from 0.1 to 5 Atm. The data will be useful in understanding plasma synthesis processes over wide parametric range. Experimental investigation of chemical kinetics in Argon plasma and yttria-Argon plasma are presented. Identification of plasma species in argon and yittira argon plasma were done through in-situ emission spectroscopy. Formation of YO band in yttria argon plasma and possible mechanism behind synthesis of yttria nano particle have been explored. Dynamics of the plasma jet and inside kinetics were probed using and high speed camera, image analysis and voltage analysis. From emission spectroscopic study, dominant features of YI, YII and OI lines has been seen with particle feeding in plasma. Appearance of YO band is found between a distance of 3 to 6 cm from nozzle exit.

8.2. Computation of species density in argon plasma for non thermal equilibrium

The composition of the plasma depends strongly on its temperature. This is a result of the energy balance between the electrical energy dissipated and the heat losses [2]. The total energy content depends on the energy of the various particles (frozen energy) and on the chemical reactions among them (reactive energy). Therefore the thermodynamic properties (enthalpy, entropy, specific heat, and so forth) depend strongly on the composition of the plasma.

The plasma composition is calculated from the non-equilibrium Eggert - Saha equation, the equation of charge neutrality and Dalton's law of partial pressure. In Argon plasma, considering the dissociation of argon up to its third ionization state, the associated reactions and non-equilibrium Saha-equations are given in Table-8.2. Different notations used and corresponding atomic parameters are mentioned in Table-8.1. The reactions showing different species of argon, corresponding rate constants [3] are given in Table-8.2.

Eggert-Saha equation is derived through the minimization of the Gibbs free energy (for a given temperature and pressure). This in turn depends on the chemical potentials of the different chemical species present in the gas. At high temperatures *(T > 6000 K)* these chemical potentials can be calculated only from statistical thermodynamic considerations through quantities called partition functions and partition function is related to the internal energy levels of the different chemical species of the plasma.

Table-8.1: Notations used in dissociation of argon species and corresponding atomic parameters

Species index	1	2	3	4	5
Species	Ar	Ar^{+}	Ar^{++}	Ar^{+++}	e
Mass	m_1	m_2	m_3	m_4	m_5
Number density	n_1	n_2	n_3	n_4	n_5
Number of levels considered	426	416	124	124	57
Mass (amu)	39.948	39.948	39.948	39.948	5.49E-4

Table-8.2: Non-equilibrium Saha equations and their rate constants

Sl. No. (i)	Reaction	Saha Equation	Rate constant (R_i)	Reaction energy (Σ_i in cm^{-1})
1	$Ar = Ar^{+} + e$	$\frac{n_2.n_5}{n_1} = R_1$	$R_1 = 2.\frac{Q_2(T_h)}{Q_1(T_h)}\left(\frac{2\pi m_5 k_B T_e}{h^2}\right)^{3/2}.\exp\left(-\frac{\Sigma_1}{k_B T_e}\right)$	1,27,109.8
2	$Ar^{+} = Ar^{++} + e$	$\frac{n_3.n_5}{n_2} = R_2$	$R_2 = 2.\frac{Q_3(T_h)}{Q_2(T_h)}.\left(\frac{2\pi m_5 k_B T_e}{h^2}\right)^{3/2}.\exp\left(-\frac{\Sigma_2}{k_B T_e}\right)$	2,22,848.3
3	$Ar^{++} = Ar^{+++} + e$	$\frac{n_4.n_5}{n_3} = R_3$	$R_3 = 2.\frac{Q_4(T_e)}{Q_3(T_e)}\left(\frac{2\pi m_5 k_B T_e}{h^2}\right)^{3/2}.\exp\left(-\frac{\Sigma_3}{k_B T_e}\right)$	3,28,550.0
Independent species: e; Dependent species: Ar, Ar^{+}, Ar^{++}, Ar^{+++}				

Where Q_1, Q_2, Q_3 are partition functions, R_1,R_2, R_3 are rate constants, Σ_1, Σ_2, Σ_3 are ionization energies, n_1, n_2, n_3, n_4, n_5 are species densities. Partition function is defined to be the sum over the all states. For atoms, partition function is product of translational partition function and electronic partition function. Partition function for different species in argon plasma are given in table 8.3 and 8.4 respectively.

Table-8.3: Expression for partition function

SPECIES	Internal partition function	Translational Partition Function [V=volume of system]
A (Atom)	$Q_{\text{int}}^{A} = Q_{el}^{A}$	$Q_{tr}^{A} = V.\left(\frac{2\pi m_A k_B T_h}{h^2}\right)^{3/2}$
I (Ion)	$Q_{\text{int}}^{I} = Q_{el}^{I}$	$Q_{tr}^{I} = V.\left(\frac{2\pi m_I k_B T_h}{h^2}\right)^{3/2}$
D (Double Ion)	$Q_{\text{int}}^{D} = Q_{el}^{D}$	$Q_{tr}^{D} = V.\left(\frac{2\pi m_D k_B T_h}{h^2}\right)^{3/2}$
T (Triple ion)	$Q_{\text{int}}^{T} = Q_{el}^{T}$	$Q_{tr}^{T} = V.\left(\frac{2\pi m_T k_B T_h}{h^2}\right)^{3/2}$
e (Electron)	$Q_{\text{int}}^{e} = 2$	$Q_{tr}^{e} = V.\left(\frac{2\pi m_e k_B T_e}{h^2}\right)^{3/2}$

Table-8.4: Expression for internal partition function

SPECIES	Internal partition function	Expression
A (Atom)	Q_{el}^{A}	$Q_{el}^{A} = \sum_j g_{Aj} \exp\left(-\frac{E_{Aj}}{k_B T_e}\right)$
I (Ion)	Q_{el}^{I}	$Q_{el}^{I} = \sum_j g_{Ij} \exp\left(-\frac{E_{Ij}}{k_B T_e}\right)$
D (Double Ion)	Q_{el}^{D}	$Q_{el}^{D} = \sum_j g_{Dj} \exp\left(-\frac{E_{Dj}}{k_B T_e}\right)$
T (Triple Ion)	Q_{el}^{T}	$Q_{el}^{T} = \sum_j g_{Tj} \exp\left(-\frac{E_{Tj}}{k_B T_e}\right)$

Conservation of total charge (criteria of charge neutrality) is written as

$$n_5 = (n_2 + 2n_3 + 3n_4) \tag{8.1}$$

Total pressure (Dalton's law of partial pressures) are written as

$$n_1 = \frac{[p - (n_2 + n_3 + n_4 + n_5)k_B T]}{k_B T} \tag{8.2}$$

Now to get the composition of the plasma we need to solve five independent equations. Three equations are taken as the reactions mentioned in Table-8.2 and remaining two equations are the eq. (8.1) and (8.2). These five equations are solved for given range of temperature and pressure in order to get the composition of different argon species. Rate constants taken from NIST database were derived from minimization of Gibbs free energy. The different argon species and their chemical potential are given in table 8.5.

Table-8.5: Expression for chemical potential

Species	Expression for Chemical Potential		
	Potential	Translational (tr)	Internal (int)
e	μ_e	$-k_B T_e \ln\left[2\frac{k_B T_e}{p_e}\left(\frac{2\pi m_e k_B T_e}{h^2}\right)^{3/2}\right]$ +	0
Ar	μ_A	$-k_B T_h \ln\left[2\frac{k_B T_h}{p_A}\left(\frac{2\pi m_A k_B T_h}{h^2}\right)^{3/2}\right]$	$-k_B T_e \ln\left[Q_{\text{int}}^A (T_e) \exp\left(-\frac{E_A}{k_B T_e}\right)\right]$
Ar+	μ_I	$-k_B T_h \ln\left[2\frac{k_B T_h}{p_I}\left(\frac{2\pi m_I k_B T_h}{h^2}\right)^{3/2}\right]$	$-k_B T_e \ln\left[Q_{\text{int}}^I (T_e) \exp\left(-\frac{E_I}{k_B T_e}\right)\right]$
Ar++	μ_D	$-k_B T_h \ln\left[2\frac{k_B T_h}{p_D}\left(\frac{2\pi m_D k_B T_h}{h^2}\right)^{3/2}\right]$	$-k_B T_e \ln\left[Q_{\text{int}}^D (T_e) \exp\left(-\frac{E_D}{k_B T_e}\right)\right]$
Ar+++	μ_T	$-k_B T_h \ln\left[2\frac{k_B T_h}{p_D}\left(\frac{2\pi m_T k_B T_h}{h^2}\right)^{3/2}\right]$	$-k_B T_e \ln\left[Q_{\text{int}}^T (T_e) \exp\left(-\frac{E_T}{k_B T_e}\right)\right]$

where, E_A=0

E_I=Ionization Energy (single ion)

E_D=Ionization energy (second ion)

E_T= Ionization energy (triple ion)

When chemical reaction reaches equilibrium, minimization of Gibbs free energy gives:

Reaction 1	$\left(\frac{\mu_{A,tr}}{T_h}+\frac{\mu_{A,\text{int}}}{T_e}\right)-\left(\frac{\mu_{e,tr}}{T_e}\right)-\left(\frac{\mu_{I,tr}}{T_h}+\frac{\mu_{I,\text{int}}}{T_e}\right)=0$
Reaction 2	$\left(\frac{\mu_{I,tr}}{T_h}+\frac{\mu_{I,\text{int}}}{T_e}\right)-\left(\frac{\mu_{e,tr}}{T_e}\right)-\left(\frac{\mu_{D,tr}}{T_h}+\frac{\mu_{D,\text{int}}}{T_e}\right)=0$
Reaction 3	$\left(\frac{\mu_{D,tr}}{T_h}+\frac{\mu_{D,\text{int}}}{T_e}\right)-\left(\frac{\mu_{e,tr}}{T_e}\right)-\left(\frac{\mu_{T,tr}}{T_h}+\frac{\mu_{T,\text{int}}}{T_e}\right)=0$

Substituting values of chemical potential in reaction 1 gives:

$$-k_B\ln\left[2\frac{k_BT_h}{p_A}\left(\frac{2\pi m_A k_B T_h}{h^2}\right)^{3/2}\right]-k_B\ln\left[Q_{\text{int}}^A(T_e)\exp\left(-\frac{E_A}{k_BT_e}\right)\right]+k_B\ln\left[2\frac{k_BT_e}{p_e}\left(\frac{2\pi m_e k_B T_e}{h^2}\right)^{3/2}\right]$$

$$+k_B\ln\left[2\frac{k_BT_h}{p_I}\left(\frac{2\pi m_I k_B T_h}{h^2}\right)^{3/2}\right]+k_B\ln\left[Q_{\text{int}}^I(T_e)\exp\left(-\frac{E_I}{k_BT_e}\right)\right]=0$$

$$or,\ln\left(\frac{p_A}{p_I}\right)=-\ln\left[\frac{Q_{\text{int}}^I(T_e)}{Q_{\text{int}}^A(T_e)}.\frac{1}{p_e}.\left(\frac{2\pi m_e k_B T_e}{h^2}\right)^{3/2}.(2k_BT_e).\exp\left(-\frac{E_I-E_A}{k_BT_e}\right)\right]$$

$$or,\ln\left(\frac{p_I}{p_A}\right)=\ln\left[\frac{Q_{\text{int}}^I(T_e)}{Q_{\text{int}}^A(T_e)}.\frac{1}{p_e}.\left(\frac{2\pi m_e k_B T_e}{h^2}\right)^{3/2}.(2k_BT_e).\exp\left(-\frac{E_I-E_A}{k_BT_e}\right)\right]$$

$$\boxed{\frac{p_e p_I}{p_A}=\frac{Q_{\text{int}}^I(T_e)}{Q_{\text{int}}^A(T_e)}.\left(\frac{2\pi m_e k_B T_e}{h^2}\right)^{3/2}.(2k_BT_e).\exp\left(-\frac{E_I-E_A}{k_BT_e}\right)}$$

For argon plasma, E_I-EA=15.7596 eV

Similarly reaction 2 gives:

$$\boxed{\frac{p_e p_D}{p_I} = \frac{Q_{\text{int}}^D(T_e)}{Q_{\text{int}}^I(T_e)} \cdot \left(\frac{2\pi m_e k_B T_e}{h^2}\right)^{3/2} .(2k_B T_e).\exp\left(-\frac{E_D - E_I}{k_B T_e}\right)}$$

Densities of plasma species were computed for electron temperature range 300-50000K, pressure 0.1 - 5 atm and non-thermal equilibrium factor θ(=Te/Th) from1 to 20.

Variation of different species concentration with electron temperature at pressures 0.1, 1 and 4 atm under equilibrium Θ (T_e/T_h)=1 is presented in Figure 8.1.

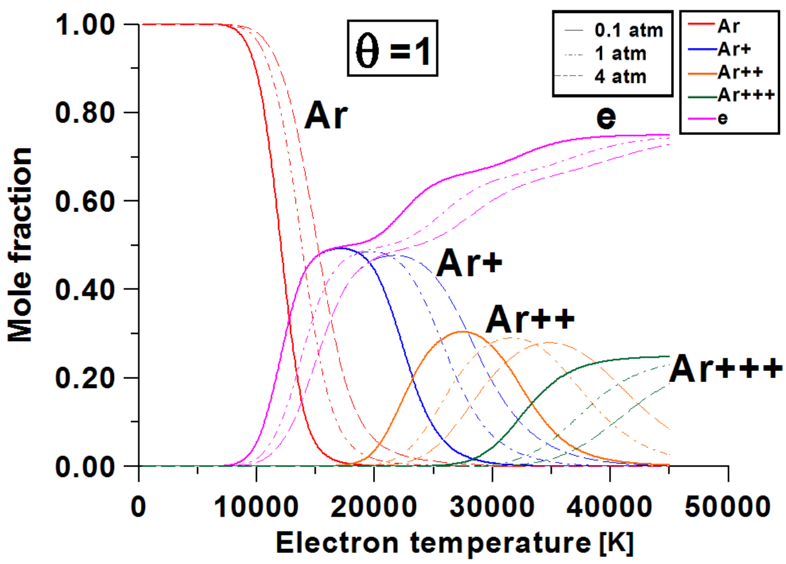

Figure 8.1: Concentration of different species in argon plasmas under equilibrium at pressure: 0.1 atm, 1atm and 4atm.

It is observed from Figure 8.1, that for a given electron temperature, as pressure increases, degree of ionization decreases. This is expected as mean free path between particles decreases with increase in pressure and particles do not get time to acquire sufficient energy for ionizing collision.

Initially Argon atom concentration is high. With increase in temperature, ionization takes place and density of Argon atoms falls down and concentration of Ar^+ and electron increases. On further increase in temperature, secondary ionization takes place and concentration of Ar^+ drops and concentration of Ar^{++} increases. At very high temperature around 20000 K, Ternary ionization starts and density of Ar^{+++} increases and Ar^{++} drops down.

Concentration of different species in Argon plasmas with pressure under under $\Theta(=T_e/T_h)= 5$ is presented in Figure 8.2.

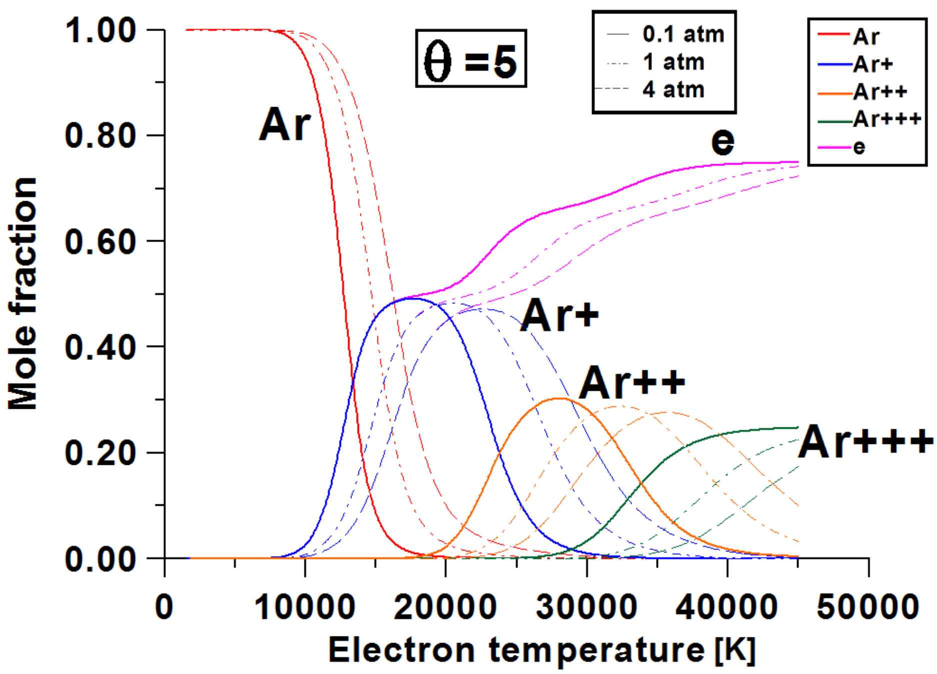

Figure 8.2: Concentration of different species in argon plasmas under non-equilibrium θ (T_e/T_h =5) at pressure 0.1 atm, 1 atm and 4 atm.

Comparing with corresponding results under equilibrium as shown in Figure 8.1, it is observed that sharper decrease in degree of ionization takes place with increase in pressure when degree of non-equilibrium increases. This can be explained from the fact that for same electron temperature, heavy species temperature is substantially low when degree of thermal non-equilibrium is high. This results in less effective ionizing collisions at higher thermal non-equilibriums.

Figure 8.3 shows concentration of different species in Argon plasmas with sub atmospheric pressure 0.1 atm under different degree of non-equilibrium $\Theta(=T_e/T_h)= 1$, 5 and 10. The effect of pressure is brought out in a more vivid manner in Figure 8.3 for slightly sub-atmospheric pressure plasmas like one considered in the present case.

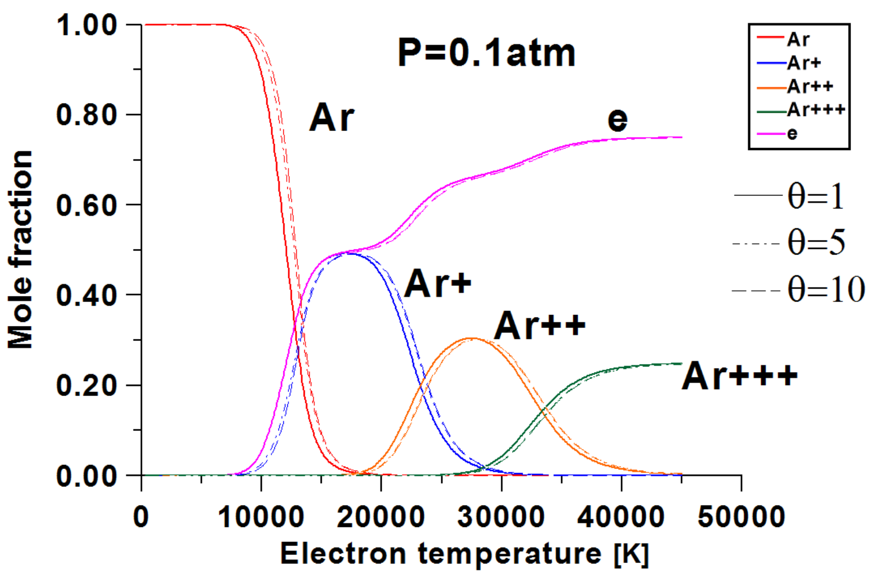

Figure 8.3: Concentration of different species in argon plasmas under different degrees of non-equilibrium θ=1, 5 and 10.

It is observed that for a given electron temperature, initially there is a sharp decrease in the degree of ionization with increase in thermal non-equilibrium. However, for further higher thermal non-equilibrium, the ionization scenario does not change much. This is primarily because at higher thermal non-equilibrium, it is energy of the electrons that primarily contribute in the ionization. Energy of bulky ions being very low at higher degree of thermal non-equilibrium, their effects are not that prominent.

8.3 Experimental investigation of chemical kinetics of Ar-Y_2O_3 plasma using emission spectroscopy and image analysis

Chemical kinetics in a low pressure dc arc argon plasma jet is investigated using optical diagnostics. Possible mechanism of nanopowder generation was established through emission spectra captured at different axial location using spectrograph. Multi-track assembly was setup to get the kinetics of plasma species at different axial location simultaneously. Reaction kinetics during powder feeding was investigated. Temperature was measured using Boltzmann plot technique. To explore the dynamics of the plasma jet macroscopically during powder feeding, images were captured using high speed camera synchronized with voltage signal. For investigation of intensity variation, intensity contours were drawn using image analysis in Matlab software.

8.3.1 Experimental details

Experimental set up for in situ probing of species is shown in Figure 2.5 of chapter3. Emission spectra originating from plasma were recorded. Sequence of plasma jet images synchronized with voltage signal was recorded using high speed camera. Voltage signal was measured using potential divider circuit. Image analysis was done to investigate intensity variation inside the plasma jet during powder feeding. Operating parameters are given in table 8.6.

Table-8.6: Operating parameters for investigation of chemical kinetics

Parameters	Value
Torch current	125-225A
Gas flow rate	22-32 lpm
Powder feed rate (rotation of disc per minute)	1-4 RPM
Plasma gas used	Argon
Powder	Y_2O_3

Powder feeder was calibrated for yttria powder. Amount of powder in one minute for different rotation speed was collected. Calibration curve for yttria powder is shown in Figure 8.4.

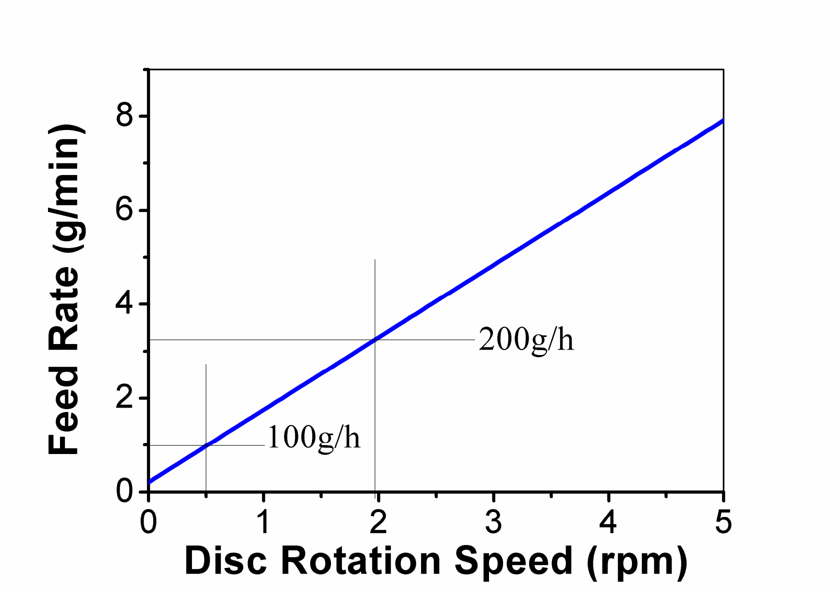

Figure 8.4: Powder feed rate vs disc rotation speed

Emission spectra for argon and argon-yttria were captured through multirack fibre set up assembly of spectrograph to get spectra at nine axial location simultaneously in the wavelength range 400-465nm. Emission line of Ar and Y were observed. Due to the limitation of resolution, YO band could not be resolved with multi-track set up, although could get some signature of band formation in the range 575 to 620 nm range [7]. For identifying formation of YO band, high resolution single track fibre assembly was used (resolution 0.05nm) and spectra were recorded at different location individually. Measurements were repeated to ensure the mechanism of YO formation.

8.4 Results

8.4.1 Emission spectra

(A) For pure argon: Emission spectra of pure argon plasma at currents 100A, 150A and 250 A are shown in following Figure 8.5. Prominent argon atomic lines were identified from 400-465nm wavelength range. These lines are marked as 1 to 12 in Figure 8.4. The absence of ionic lines of argon indicates that temperature of the plasma is below 10000K.

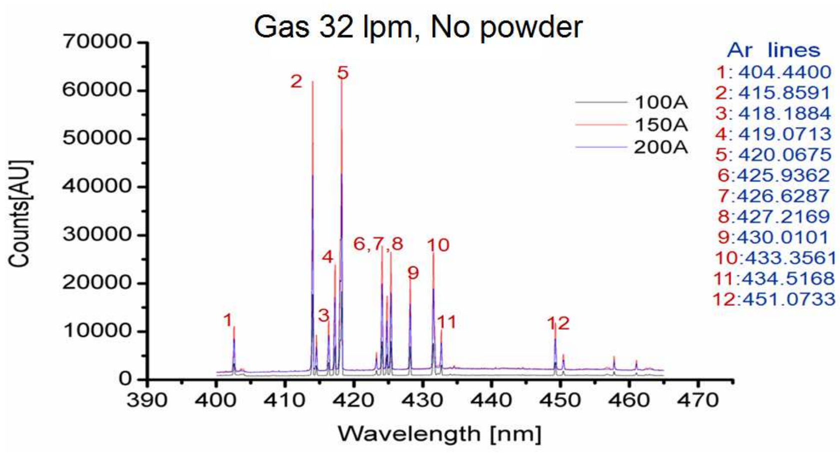

Figure 8.5: Emission spectra at nozzle exit of the plasma jet in pure Argon plasma

Emission spectra of Argon plasma obtained at different axial location of the plasma jet are shown in Figure 8.6. Only atomic lines of Argon were observed with the above defined operating parameters. Different axial locations marked as 1, 2, 3, 4, 5, 6, 7, 8, 9 denote the axial position from the nozzle. In the Figure 8.6, marking 1 denotes the fibre location at the tail of the plasma jet, while 9 denotes the nozzle exit. These lines were used to measure the plasma temperature using Boltzman plot technique [4]. Emission spectra could predict the temperature limit is less than 10000K, because no Ar^{+}, Ar^{++}, Ar^{+++} lines were identified in the emission spectra of pure argon plasma.

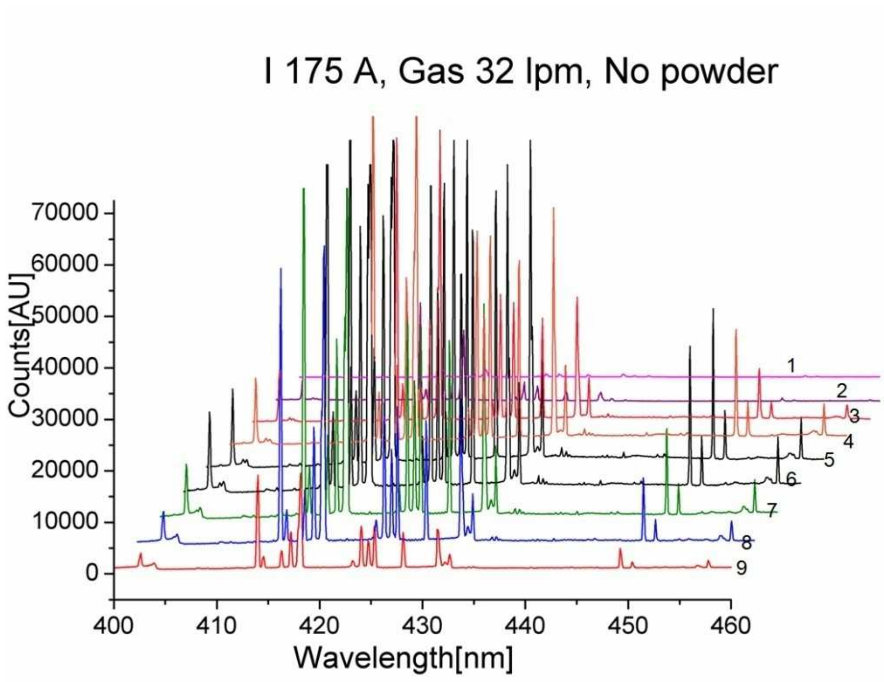

Figure 8.6: Emission spectra of pure argon at different locations recorded simultaneously

Composition of plasma species as computed in section 8.2, indicate the different atomic lines, singly ionized argon lines, doubly ionized argon lines and triply ionized argon lines, while in emission spectra only atomic lines of argon could be observed. The reason may be the temperature inside the chamber is below 10000K. Other possibility may be intensity of ionic lines is much less than the intensity of atomic line.

(B) For yttria-argon plasma

Plasma kinetics changes drastically as soon as Y_2O_3 powder is fed into the plasma. Emission spectra of Ar-Y_2O_3 plasma for different current are shown in Figure 8.7. It was observed during experiment that as soon as powder is fed into the plasma, intensity of argon lines goes down and formation of new lines were seen. It is clear from the Figure 8.7 that Argon lines diminish and YI and YII lines appear in the spectra.

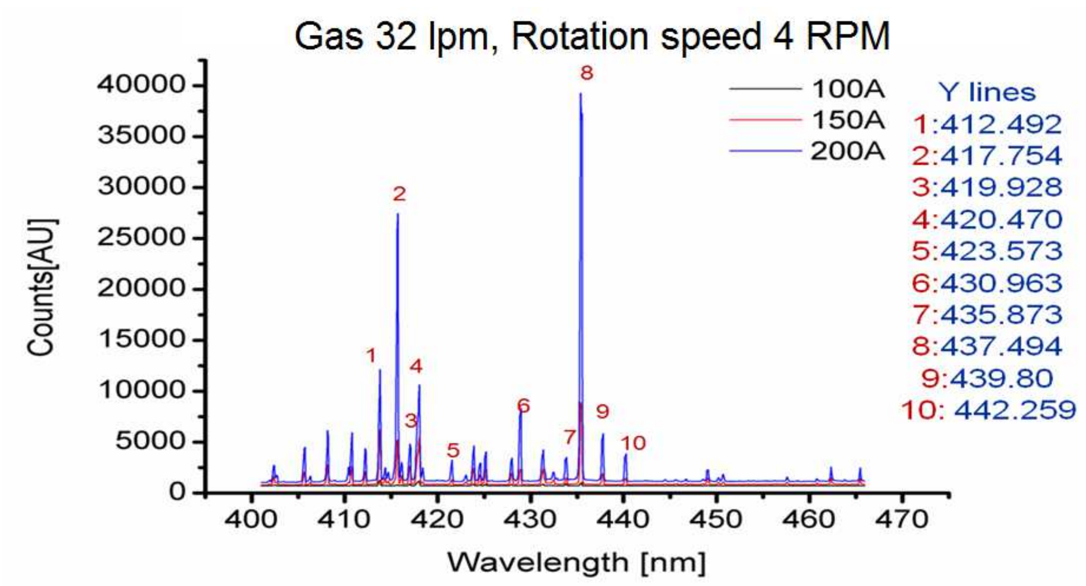

Figure 8.7: Emission spectra of Ar-Y_2O_3 plasma at different current

It may be possible due to the fact that the intensity of Y-II lines are very high as compared to argon lines. The emission spectra give information about dissociation of Y_2O_3 and formation of Y and Oxygen. YII lines marked on the Figure 8.7 may be used to measure the temperature using Boltzmann plot technique. Emission spectra recorded for different axial location are shown in Figure 8.8.

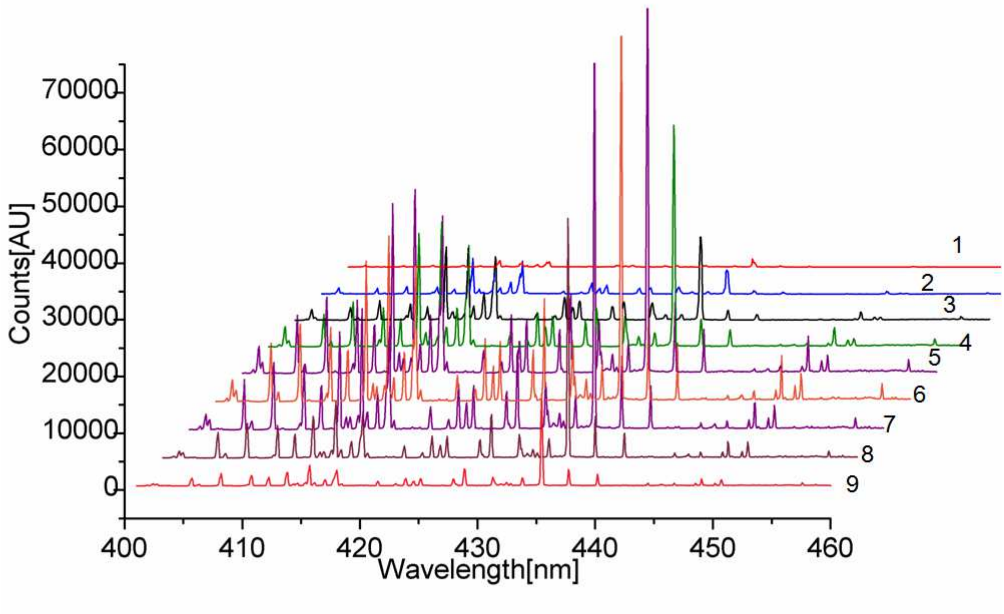

Figure 8.8: Emission spectra of Ar-Y_2O_3 at different axial location.

It is obvious from Figure 8.7 that even in the tail region also, argon lines are not visible. Argon lines were not observed due to very high intensity of YII line as compared to Argon lines. Kinetics of the plasma changes very fast during powder feeding.

(C) Formation YO band

In DC arc plasma torches, plasma temperature changes from 5000K to 30000K depending on the location and operating parameters. During nano synthesis, Y_2O_3 powder is fed into the plasma through powder feeder. Since temperature inside the plasma jet is greater than 3000K, powder starts melting, evaporated, and atomized. As the vapors move downstream, they undergo homogeneous nucleation due to facing of sharp temperature gradient in the plasma tail region. There were two assumptions for nanopowder synthesis: One assumption is that surface of Y_2O_3 melts and evaporates and nanopowder forms as it faces sharp temperature boundary. Second one assumes that Y_2O_3 breaks in Y and O at very high temperature. When temperature goes down it forms YO. YO acts as nucleation centre for homogeneous nucleation and growth for nanopowder generation [6]. Second mechanism of synthesis was observed in Figure 8.8. Appearance of strong YO band was seen after 6cm from the nozzle exit. A-X band of YO was also reported in Y_2O_3 nanopowder synthesis in inductively coupled plasma reactor by Dhamale et al. [7] and Patrick et al. [8].

Very interesting kinetics of YO formation over axial distance was observed. Formation of YO band over axial distance is shown in Figure 8.9. Image of plasma jet during powder feeding is shown in the inset. It is clear from the Figure 8.9 that initially Y_2O_3 break into Y and O. As temperature decrease, Y and O form YO after 6 cm from the nozzle exit. YO forms nucleation centre for formation of nano powder.

$$2Y_2O_3 + \text{Ar plasma} \longrightarrow 4Y + 3O_2 + Ar$$

$$Y + O \longrightarrow YO$$

Figure 8.9 shows a clear evidence of dissociated species of Y_2O_3 started appearing after 10 mm distance from nozzle exit. From 10mm to 30mm formation of band starts. YO band is clearly formed at 60mm from the nozzle exit. As distance from nozzle exit increases band intensity decreases.

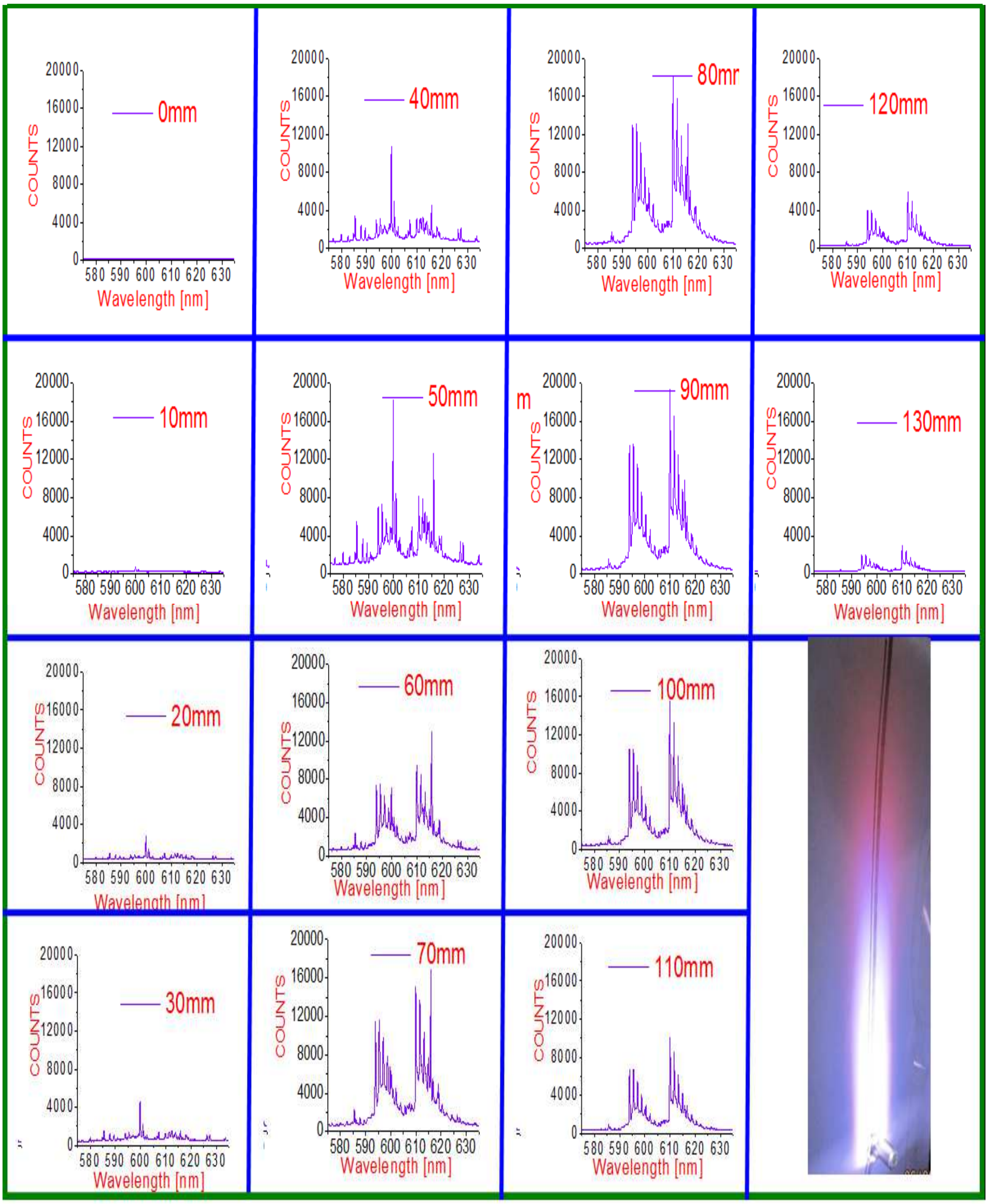

Figure 8.9: Emission spectra during Y_2O_3 powder feeding recorded at different locations from nozzle exit in the wavelength range of 575-630 nm.

8.4.2. Image analysis

Sequence of images of the plasma jet was analyzed using image analysis software Matlab [9]. Corresponding voltage signal were analyzed using Fast Fourier Transform.

(A) Effect of powder feed rate: Variation of jet structure and voltage signal with powder feed rate at constant current 175A and plasma gas flow rate 32 lpm is shown in Figure 8.10. Image and intensity contours are shown in Figure 8.10 a and b. Voltage and corresponding FFT signal are shown in Figure 8.10c and Figure 8.10d.

Feed Rate (RPM)	**Image**	**Contours**
0	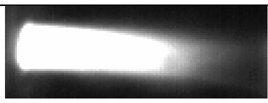	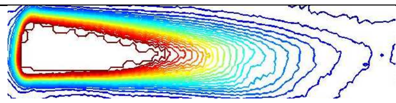
1	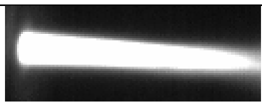	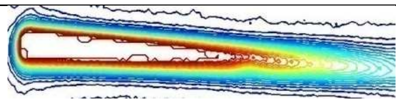
2	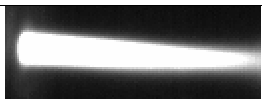	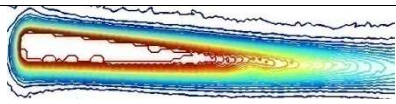
3	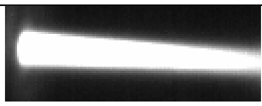	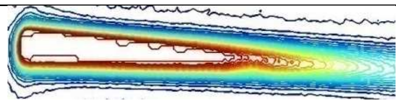
	(a)	**(b)**

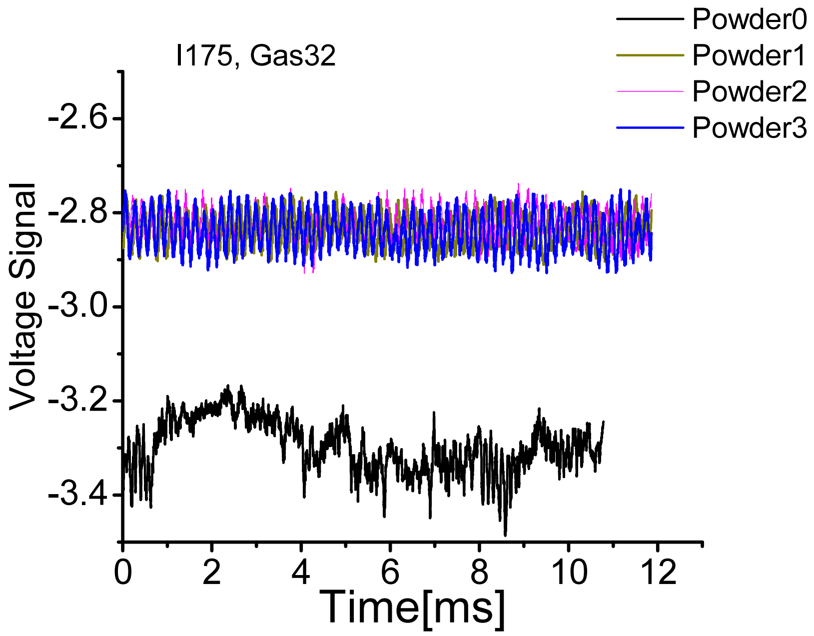

(c)

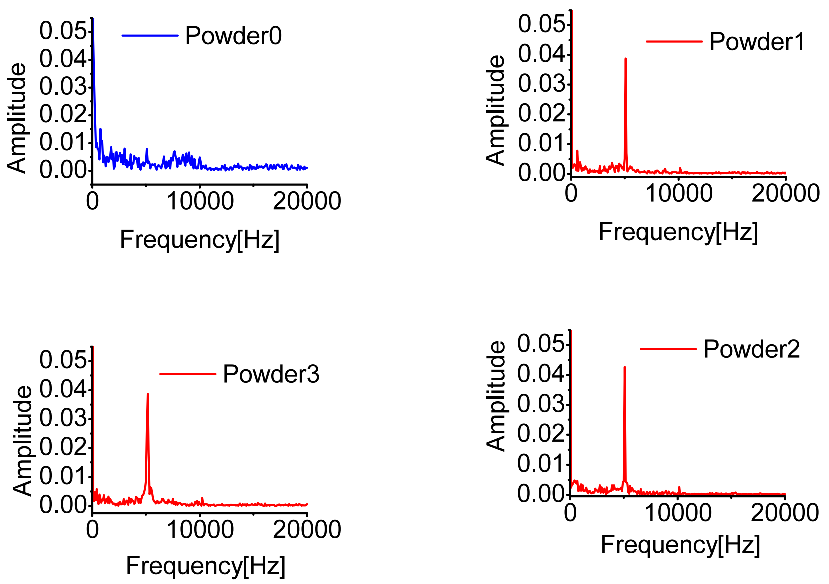

(d)

Figure 8.10: (a) Images of plasma jet (b) intensity contour (c) voltage signal and (d) FFT of voltage signal.

It was observed from Figure 8.10 that when there was no powder, luminous length of the jet was less while width was high. As soon as powder is fed to the plasma, jet shrinks and length increases. Intensity contour also depicts the same. When there is no powder, voltage signal is higher and fluctuating, while during precursor feeding, voltage reduced and almost sinusoidal. FFT of voltage signal shows appearance of a new frequency around 5500Hz in presence of powder, while it was not observed in absence of powder in this system. In absence of powder peak is very small.

(B) Effect of current

Images of the plasma jet, corresponding intensity contours, voltage signal and FFT of voltage signal for different currents are shown in Figure 8.11. Total gas (plasma + carrier) was 32 lpm.

Current	**Image and contours with no powder**	**Image and contours during powder feeding (4RPM)**
125A	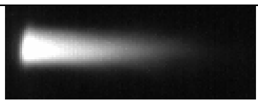	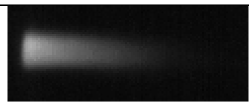
	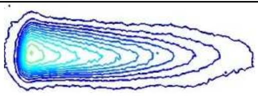	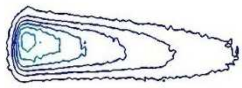
150A	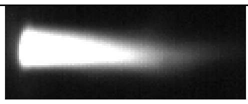	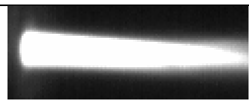
	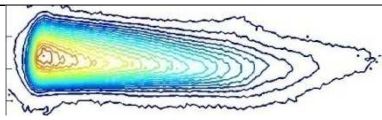	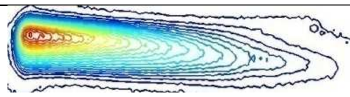
175A	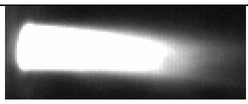	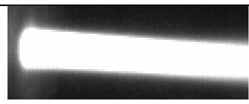
	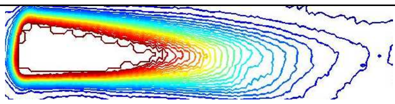	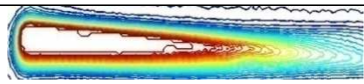
Voltage Signal at different torch current	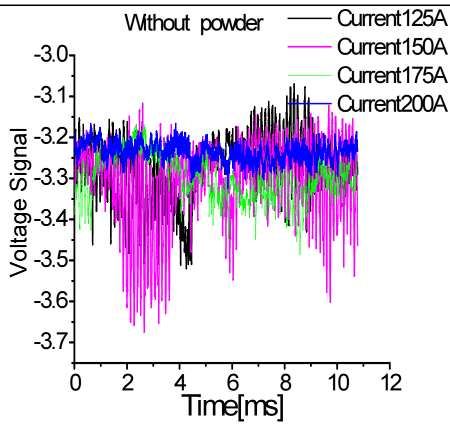	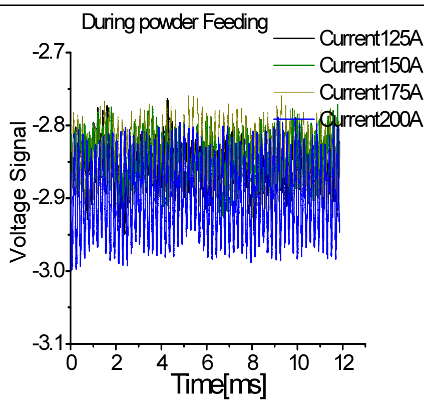

FFT of voltage signal at different torch current	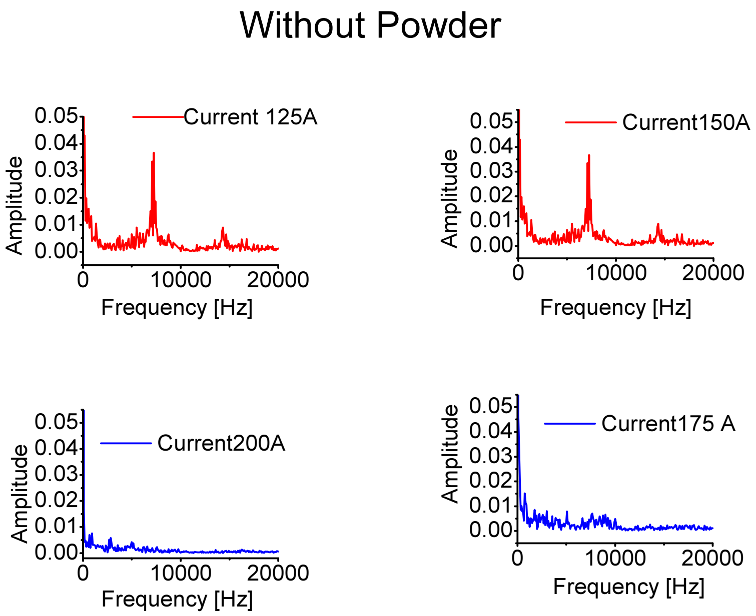
FFT of voltage signal at different torch current	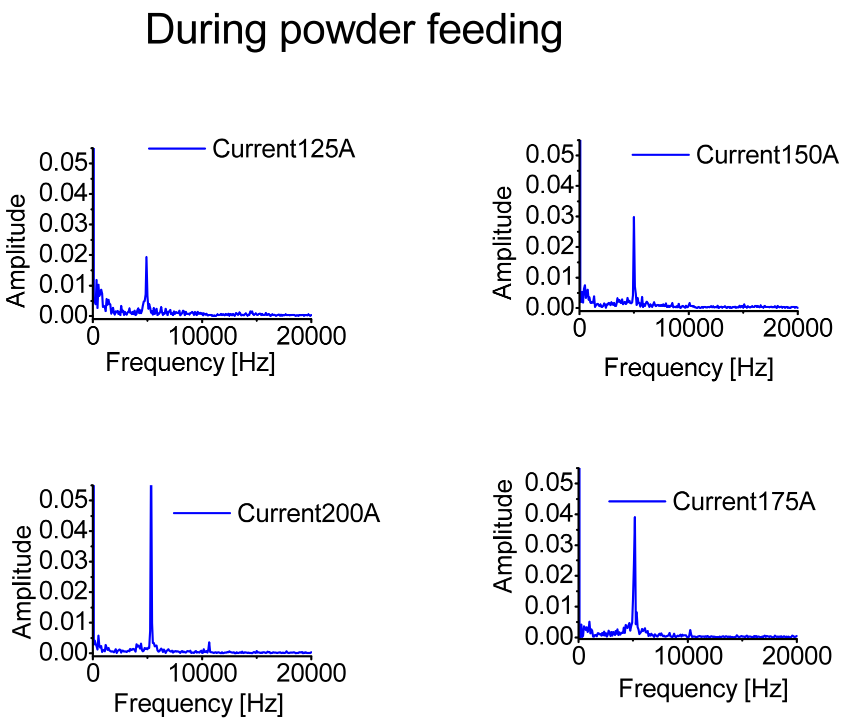

Figure 8.11: Effect of current during precursor feeding on plasma jet structure, voltage signal and FFT

At low current, it was observed that jet length is higher when there is no powder. As soon as powder is introduced in the plasma jet, heat transfer takes place, luminous length of jet decreases and temperature also decreases at low gas flow and current. After the introduction of powder loading, luminosity of the plasma jet is found to increases for higher gas flow rate and higher current. To see the variation inside the plasma jet, intensity contour of the plasma jet was plotted using matlab software. As discussed in our previous work in chapter5. Intensity variation gives rough estimation of temperature variation of the jet.

(C) Effect of flow rate

Images, corresponding intensity contours, voltage signal and Fast Fourier Transforms for flow rates 22 lpm, 27 lpm and 32 lpm at fixed current 150A are shown in Figure 8.12, 8.13 and 8.14 respectively. It was observed that when flow rate is low, luminous length of the plasma jet is very small. After feeding the powder it reduces as shown in Figure 8.13.

Measures	No powder feeding	During powder feeding (Rotation speed 4 RPM)
Image	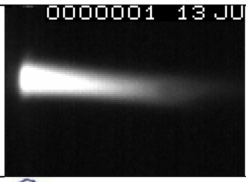	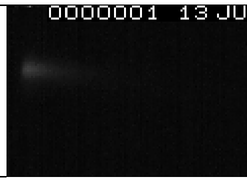
Intensity Contour	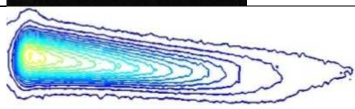	
Voltage Signal	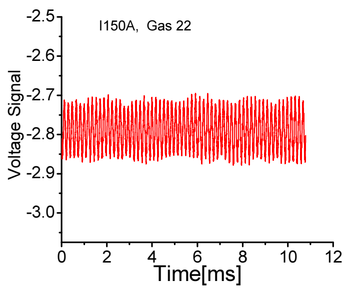	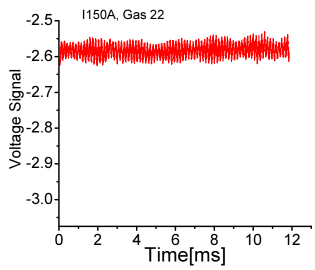
FFT signal	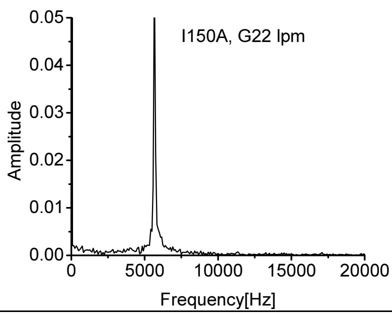	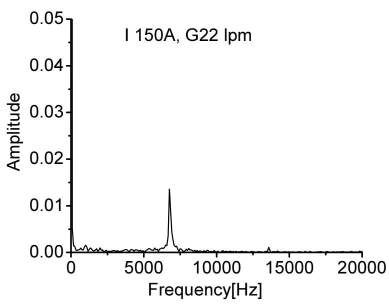

Figure 8.12: Images of the plasma jet, intensity contours, voltage signal and corresponding FFT signal at gas flow rate 22 lpm

Measures	No powder feeding	During powder feeding (Rotation speed 4 RPM)
Image	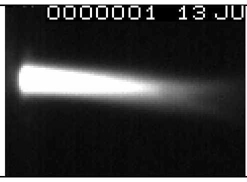	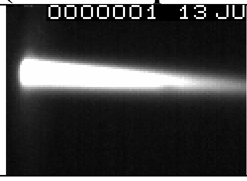
Intensity Contour	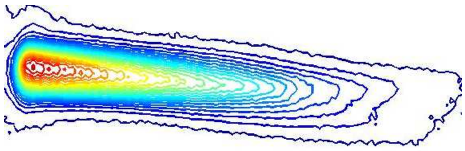	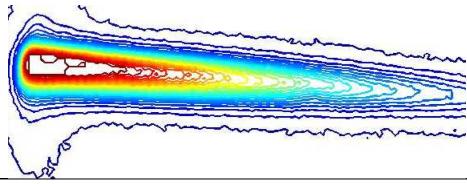
Voltage signal	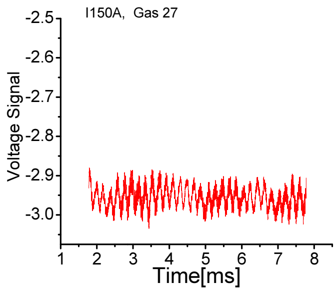	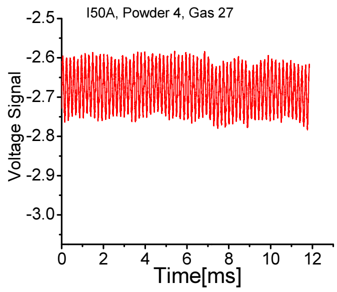
FFT of voltage signal	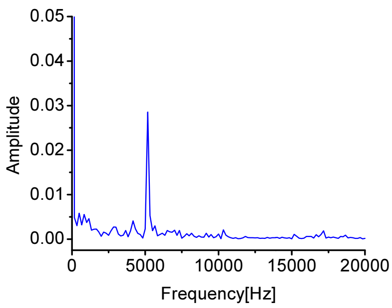	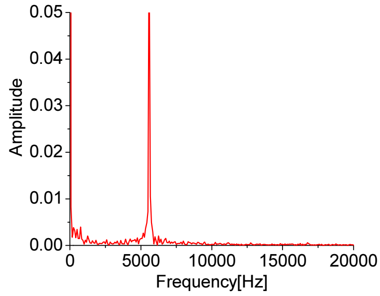

Figure 8.13: Images of the plasma jet, intensity contours, voltage signal and corresponding FFT signal at gas flow rate 27 lpm.

It is obvious from Figure 8.13 that as soon as gas flow rate was increased from 22 to 27 lpm, luminous length of the plasma jet increased and after feeding powder, length of the plasma jet increased significantly and amplitude of dominant frequency component was observed at 5500Hz frequency while at low frequency it was reduced. On further increasing the gas flow rate, jet length increased significantly as shown in Figure 8.14.

<table>
<tr><th>Measures</th><th>No Powder</th><th>During powder feeding (Rotation speed 4 RPM)</th></tr>
<tr><td>Image</td><td>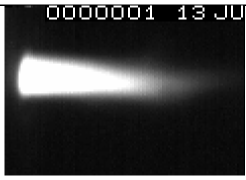
</td><td>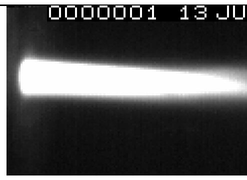
</td></tr>
<tr><td>Intensity Contours</td><td>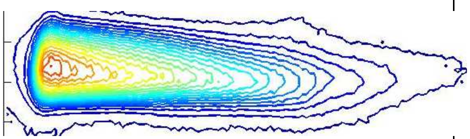</td><td>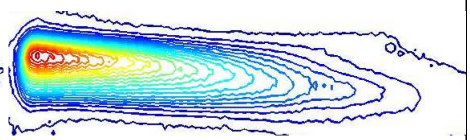</td></tr>
<tr><td>Voltage signal</td><td>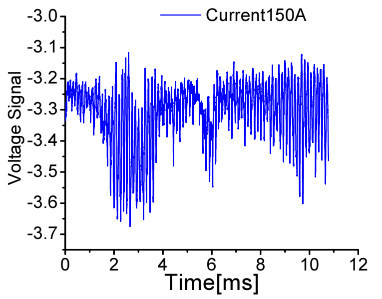
</td><td>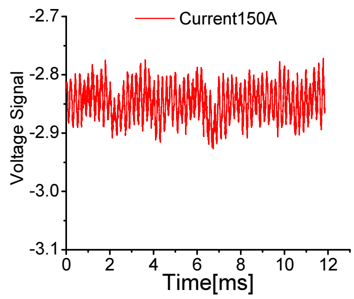
</td></tr>
<tr><td>FFT signal</td><td>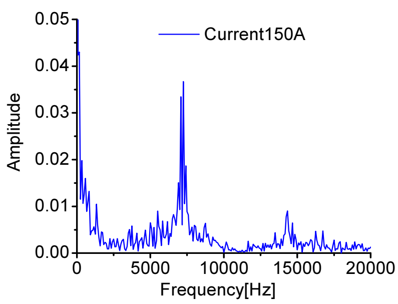
</td><td>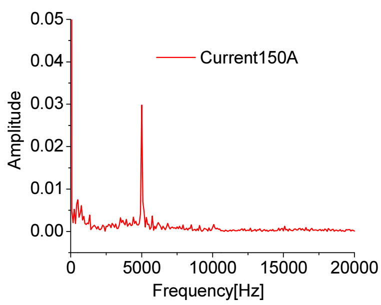
</td></tr>
</table>

Figure 8.14: Images of the plasma jet, intensity contours, voltage signal and corresponding FFT signal at gas flow rate 32 lpm

(D) Effect of low pressure

Sequence of images of the plasma jet at current 125A, 150A and powder feed rate 4RPM are shown in Figure8.15 and 8.16. It is evident of from Figure 8.14 and 8.15 that the plasma jet is quite stable generated in low pressure chamber. As current increases, amplitude in frequency space increases.

Current 125A, Powder Feed Rate 4 RPM and Gas 32 lpm

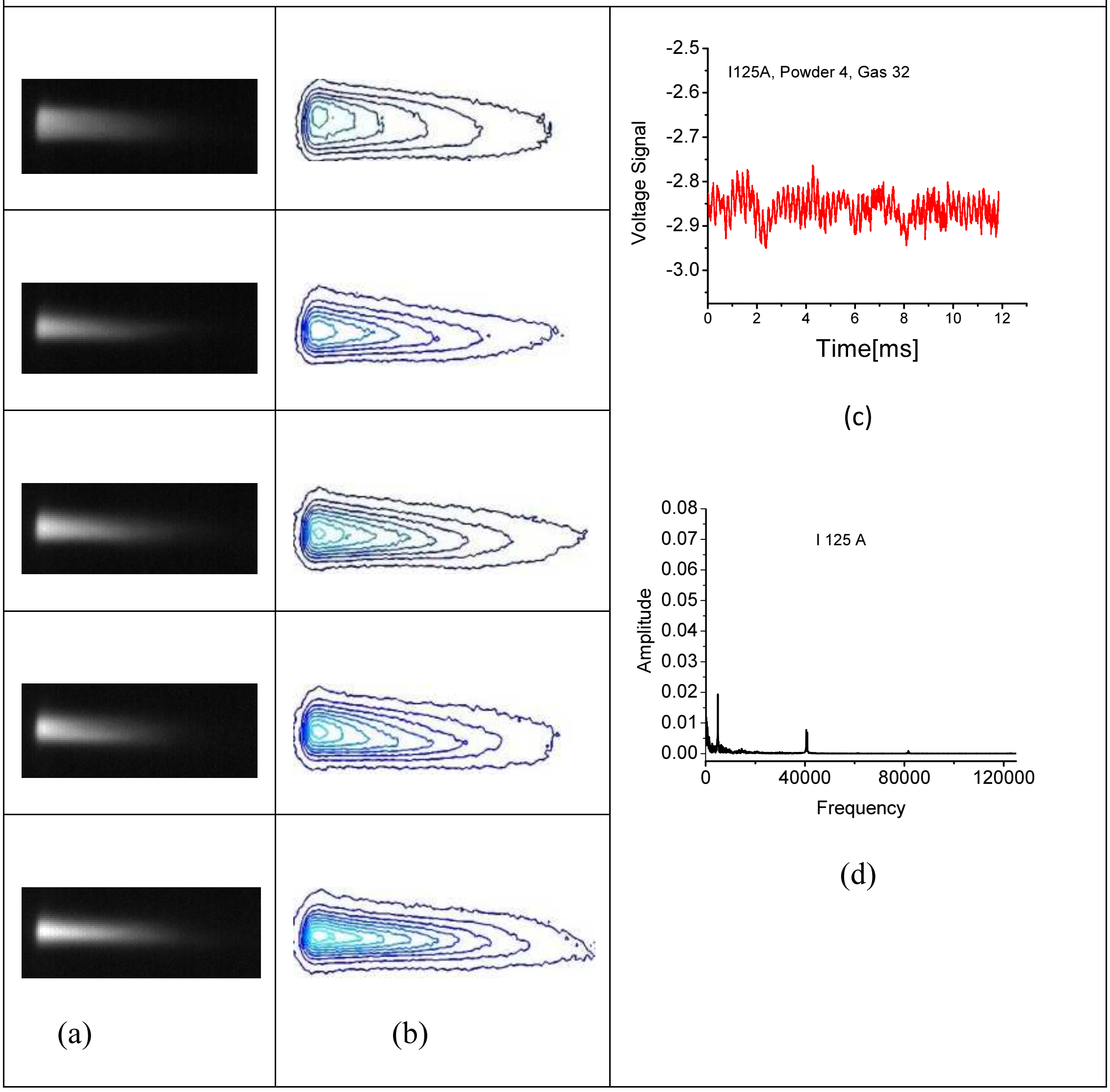

Figure 8.15: (a) Sequence of images of plasma jet (b) intensity contours (c) voltage signal and (d) FFT signal

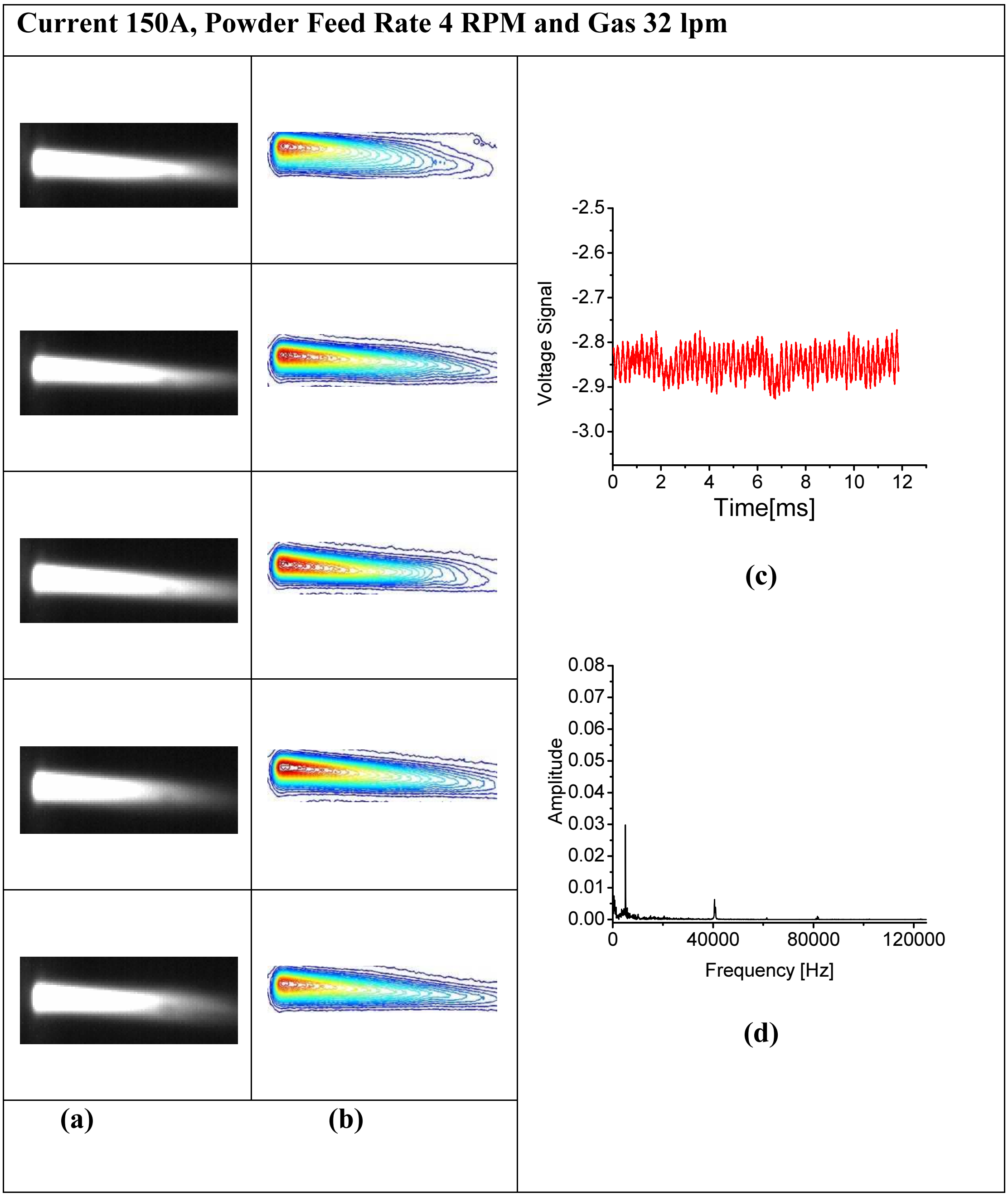

Figure 8.16: (a) Sequence of images (b) intensity contours (c) voltage signal and (d) FFT signal at current 150A.

8.5 Conclusions

Plasma species densities in the temperature range of 300-50000K, pressure 0.1 to 5 atm, and T_e/T_h from 1 to 20 were computed by solving 2T Saha equation, conservation of species and equation of pressure were computed. Computation of species composition revealed that species composition depend very much on temperature pressure and T_e/T_h. Species present at different axial location in the jet emanating from Argon and Yttria-Argon plasma were identified simultaneously using multi track fibre assembly setup in spectrograph. This type of detailed study was not reported earlier for a low pressure dc plasma spray system. It was observed that as soon as powder is fed into plasma jet, intensity of argon lines remains the same but that of Y lines are too high. One of the possible mechanisms of synthesis of Y_2O_3 nanopowder was established through emission spectroscopy. At very high temperature, Y_2O_3 breaks in Y and O and no YO was observed. As temperature falls down axially, YO band formation starts after 20mm from the nozzle exit and well resolved at 60mm from the nozzle exit. As an important outcome, the results support homogeneous nucleation theory [6] for formation of yttria nano particles and possibly removes the ambiguity about path ways followed in formation of nano-yttria in arc plasma. Composition of plasma species revealed that since there are no ionic lines of argon observed in emission spectra of pure argon plasma, temperature is less than 10000K.

Effect of powder on the structure of jet length was explored using image analysis. It was observed that plasma jet is quite stable in low pressure dc plasma reactor. At lower current, intensity of the plasma jet decreases while at higher current, intensity, and length of the plasma jet increase during powder feeding. Analysing of voltage signal using FFT tool gave us information of dynamics of plasma jet in a low pressure DC plasma reactor. It is observed that powder feeding in plasma jet significantly affect the system dynamics. Images recorded at different parameters provided optimized parameters for coating. Intensity contours show that for a lower current and low gas flow plasma power is not sufficient to melt the powder. As soon as the current increases it is sufficient to melt the powder and intensity suddenly increases that was observed in the intensity spectra also. These results will be useful for computing composition of Ar-Y_2O_3 plasma.

8.6 References

1. Grill, A., "Cold Plasma in Material Fabrication", IEEE press, New-York, ISBN 0-7803-1055 (1994).

2. Boulos, M. I., Fauchais, P., Pfender, E, "Thermal Plasmas, Fundamentals and applications", Vol1, Plenum Press, New-York(1994).

3. https://physics.nist.gov/PhysRefData/ASD/lines_form.html.

4. Griem, H. R. Plasma Spectroscopy McGraw-Hill (New York), (1964).

5. Meggers, W. F., Wheeler, J. A. The band spectra of Scandium, yttrium, and lanthanum monoxides, Bureau of Standards. J Res 6:239–275, (1931).

6 Dhamale, G. D., Tak, A. K., Mathe, V. L., Bhoraskar, Ghorui, S., "Nucleation and growth of Y_2O_3 nanoparticles in a RF-ICTP reactor: a discrete sectional study based on CFD simulation supported with experiments", J. Phys. D: Appl. Phys. 51, 439601 (2018)

7. Patrick D. Kee "Electronic state distributions of $YBa_2Cu_3O_7{-}x$ laser-ablated plumes", thesis, Air Force Institute of Technology Wright-Patterson Air Force Base, Ohio (2008).

8. G. D. Dhamale. V. L. Mathe . S. V. Bhoraskar .S. N. Sahasrabudhe . S. Ghorui, “Synthesis of nanocrystalline Y_2O_3 in a specially designed atmospheric pressure radio frequency thermal plasma”, J Nanopart Res, 17:416, (2015).

9. https://www.mathworks.com for image processing.

Chapter-9

Summary and Conclusions

Outline of the Chapter

Chapter 9

Summary and Conclusion

9.1. Summary and conclusion

Gas phase kinetics in arc plasma jets were investigated through experimental diagnostics like emission spectroscopy, high speed photography synchronized with voltage developed across torch and dynamic tools like FFT, phase portrait, Lypunov exponents of the voltage signal.

For the first time in arc plasma history, time resolved transient dynamics of anode arc root and its direct correlation with the voltage signal was captured. Direct proof of coexistence of multiple arc roots and revealing their formation, merging and extinction mechanisms were given. First concrete experimental proof of existence of current in the external plasma jet was given. Stability and structure in arc plasma jet were investigated. The first study revealing variety of interesting internal structures of high technological importance in the external plasma jets for Ar, N_2 and Air was given. Origin of such structures accounting interaction of plasma with self generated electric and magnetic field was explained. A new reliable image analysis technique for easy mapping of plasma temperature inside an external plasma jet was introduced. For the first time, highly reproducible unusually high electro-thermal efficiency, under certain cooling rates of anode boundary layer is reported. Onset of new arc dynamics driven by thermal state of anode boundary layer is established through observation of specific new frequency components in the arc voltage waveform. Vivid differences in the dynamics are revealed through phase space representations for the first time. An enhanced understanding of the evolution of spray particles from molten wire in wire arc plasma spray system and its behavior under flow driven environment of the arc plasma before deposition on the substrate is obtained through fast photography. A unique method, based on streak length generated by individual particles in CCD is established for determination of velocity of the particles getting deposited. Relation between particle velocity and instantaneous torch power is obtained. Chemical kinetics of plasma species are presented in argon plasma under thermal non-equilibrium parameter ($\Theta=T_e/T_h$) ranging from 1 to 20, electron temperature ranging from 0 to 50000K and pressure ranging from 0.1 to 5 Atm. The data will be useful in understanding plasma synthesis processes over wide parametric range. Chemical kinetics behind synthesis of yttria nano-paricles in gas phase nucleation process is explored through emission spectroscopy and high speed camera.

9.2. Future scopes

1. Comparative study of gas phase kinetics in thermal plasma systems: Arc torches, RF torches an underwater arc discharges.
2. Nucleation and growth study of yttria nanopowder in low pressure dc plasma reactor supported by emission study.
3. Thermodynamic and transport properties calculation for Ar-Y_2O_3 system.